Swansea University E-Theses

Electronic and structural properties of Au contacts on ZnO nanowires.

Lord, Alexander M

How to cite:

Lord, Alexander M (2013) *Electronic and structural properties of Au contacts on ZnO nanowires..* thesis, Swansea University.
http://cronfa.swan.ac.uk/Record/cronfa42804

Use policy:

This item is brought to you by Swansea University. Any person downloading material is agreeing to abide by the terms of the repository licence: copies of full text items may be used or reproduced in any format or medium, without prior permission for personal research or study, educational or non-commercial purposes only. The copyright for any work remains with the original author unless otherwise specified. The full-text must not be sold in any format or medium without the formal permission of the copyright holder. Permission for multiple reproductions should be obtained from the original author.

Authors are personally responsible for adhering to copyright and publisher restrictions when uploading content to the repository.

Please link to the metadata record in the Swansea University repository, Cronfa (link given in the citation reference above.)

http://www.swansea.ac.uk/library/researchsupport/ris-support/

Swansea University
Prifysgol Abertawe

Electronic and Structural properties of Au contacts on ZnO Nanowires

Alexander M. Lord

A thesis submitted to the University of Swansea in fulfilment of the requirements for the degree of Doctor of Philosophy

2013

ProQuest Number: 10807580

All rights reserved

INFORMATION TO ALL USERS
The quality of this reproduction is dependent upon the quality of the copy submitted.

In the unlikely event that the author did not send a complete manuscript
and there are missing pages, these will be noted. Also, if material had to be removed,
a note will indicate the deletion.

ProQuest 10807580

Published by ProQuest LLC (2018). Copyright of the Dissertation is held by the Author.

All rights reserved.
This work is protected against unauthorized copying under Title 17, United States Code
Microform Edition © ProQuest LLC.

ProQuest LLC.
789 East Eisenhower Parkway
P.O. Box 1346
Ann Arbor, MI 48106 – 1346

SWANSEA
LIBRARY
UNIVERSITY

Abstract

Zinc Oxide has emerged from an unspectacular past in the field of electronics to become one of the most widely researched materials for future devices. Here we investigate the growth and electrical properties of semiconducting ZnO nanowires for future application in the field of Nano-Devices and present a solution to control the behaviour of the electrical contacts.

ZnO nanowires (NWs) from initial growth experimentation and optimisation have been thoroughly characterised both structurally and electrically. Structural characterisation revealed the high quality of nanowires from vapour phase and hydrothermal growth that translated to similar measurements of nanowire resistivity. We have confirmed the results of atomic resolution dark field imaging with simulations that no Au catalyst contaminates ZnO nanowires, which makes the material more desirable than Silicon or GaAs. Within the limits of the dark field imaging the interface of the catalyst particle and the nanowire is abrupt, clean and intimate, with no Au diffusion, interfacial layers or roughness. Electron microscopy reveals the Au has an epitaxial relationship with the ZnO and is solid during growth. Using fabrication and contamination free nanoprobe measurements (four-probe scanning tunnelling microscope) in vacuum a transition from rectifying to Ohmic is dependent on contact size and not the materials or structural variations. We have shown this with the application of the nanoprobe on free standing as-grown catalysed ZnO nanowires. Using the most common nanowire growth methods the structure has been thoroughly characterised to allow the interpretation of electrical measurements of resistivity and Au end contacts.

A regime of size dependent contacts to ZnO nanowires provides the necessary knowledge and requirements to fabricate ZnO nanowire devices with controlled properties and function. This is a major hurdle for nanodevices overcome without complicated or difficult processing steps. A nanodevice can be fabricated from a substrate, with contacts, in one-step and with tailored interface properties by controlling the catalyst particle size.

Declarations and Statements

DECLARATION

This work has not previously been accepted in substance for any degree and is not being concurrently submitted in candidature for any degree.

Signed .... (A M Lord

Date ....12/4/13...

STATEMENT 1

This thesis is the result of my own investigations, except where otherwise stated. Where correction services have been used, the extent and nature of the correction is clearly marked in a footnote(s).

Other sources are acknowledged by footnotes giving explicit references. A bibliography is appended.

Signed .... (A M Lord)

Date ....12/4/13...

STATEMENT 2

I hereby give consent for my thesis, if accepted, to be available for photocopying and for inter-library loan, and for the title and summary to be made available to outside organisations.

Signed .... (A M Lord)

Date ....12/4/13...

NB: *Candidates on whose behalf a bar on access has been approved by the University (see Note 7), should use the following version of Statement 2:*

I hereby give consent for my thesis, if accepted, to be available for photocopying and for inter-library loans after expiry of a bar on access approved by the Swansea University.

Signed .... (A M Lord)

Date ....12/4/13...

Table of Contents

Abstract....2

Declaration and Statements....3

Table of Contents....4

Acknowledgements....13

Table of figures....14

Definitions and Abbreviations....17

1 Introduction....23

1.1 Nanotechnology....23

1.2 Single crystals and nanotechnology....24

1.3 Growing crystals....25

1.4 Incorporating single crystals into devices....26

1.5 Semiconductor devices and nanostructures....26

1.6 Research intensity of Nanostructures....27

1.7 ZnO Nanowires....27

1.8 Methods of ZnO nanowire growth....28

1.9 Properties of ZnO....28

1.10 ZnO Nanowire properties....29

1.10.1 Mechanical properties....29

1.10.2 Electrical properties....30

1.10.3 Electrical contacts....31

1.11 Scope....33

1.11.1 NW growth....33

1.11.2 Electron Microscopy....34

1.11.3 Nanoprobe....34

1.12 Objectives, results and achievements....35

2 Material properties and Fundamental Concepts........37
2.1 Crystalline ZnO: properties and growth........37
2.1.1 Crystal Structure........38
2.1.2 Lattice match........40
2.1.3 Silicon substrate for ZnO NW growth........41
2.1.4 Sapphire substrate for ZnO NW growth........42
2.1.5 Buffering ZnO growth from the substrate........44
2.2 Crystallographic analysis........45
2.2.1 Transmitted Electrons........45
2.2.2 Scattering of the electron beam........46
2.2.3 Diffraction of electrons........47
2.2.4 The Bragg Angle........47
2.2.5 The reciprocal lattice........48
2.2.6 Diffraction Patterns........48
2.3 Metal-semiconductor contacts........49
2.3.1 Fermi-Level pinning........52
2.3.2 Depletion Width........53
2.3.3 Conduction mechanisms across a Schottky barrier........54
2.3.4 Important Notes for Au contacts on ZnO........57
3 Literature Review........59
3.1 Zinc Oxide (ZnO)........59
3.2 NW growth methods........59
3.3 Vapour phase Growth methods........60
3.3.1 Vapour-Liquid-Solid Growth........60
3.3.2 Catalyst Free growth........62
3.3.3 Defects in NW growth........63

3.4 Problematic features of Catalysed NW growth 64
3.4.1 Locating the Au particle 64
3.4.2 Vapour-Liquid-Solid and Vapour-Solid-Solid growth 65
3.4.3 Au catalyst incorporation in NWs 66
3.5 Electrical properties of ZnO 67
3.5.1 Measuring NW bulk conduction properties 68
3.5.2 Nanoprobe measurement of NWs 71
3.6 Metal-semiconductor Contacts 72
3.6.1 Ohmic contacts on ZnO 75
3.6.2 Schottky Barriers on ZnO 76
3.7 Fabricating metal-semiconductor contacts 78
3.7.1 Contact layers to Nanowires 79
3.7.2 Fabricated contacts to individual Nanowires 81
3.8 Individual contacts to free standing NWs 83
3.9 Small contacts - experiment and models 87
3.10 Nanowire contacts research models and results 91
3.11 Literature Review Summary 93
4 Experimental technique 95
4.1 Zinc Oxide nanowire growth 95
4.1.1 Catalytic Au for NW growth 95
4.1.2 Non-catalysed nanowire growth 97
4.1.3 Nanowire characterisation 97
4.2 Nanowire growth experimental details 98
4.2.1 Catalysed NW growth sample preparation 98
4.2.2 Non-catalysed NW growth sample preparation 98
4.2.3 Vapour phase furnace technique 99

4.2.4 Experimental parameters from previous work 100
4.2.5 Process parameters 101
4.2.6 Hydrothermal nanowires 102
4.2.7 Au catalyst particles as electrical contacts 102
4.2.8 Au deposition for electrical contact fabrication 103
4.3 Scanning Electron Microscopy (SEM) 103
4.3.1 Secondary effects 104
4.3.2 Backscattered electrons 105
4.4 Secondary Electron Microscopy (SEM) experimental details 105
4.4.1 Equipment specifications 106
4.4.2 Sample examination technique 106
4.5 Transmission Electron Microscopy 107
4.5.1 Diffraction mode 108
4.5.2 Limitations of TEM 108
4.5.3 Aberrations 108
4.5.4 Imaging 109
4.5.5 Phase contrast of crystalline defects 110
4.5.6 Energy Dispersive X-ray (EDX) spectroscopy 110
4.6 Transmission Electron Microscope Experimental (TEM) details 111
4.6.1 Equipment specifications 111
4.6.2 Sample preparation 112
4.6.3 Sample imaging 112
4.6.4 Indexing diffraction patterns 112
4.6.5 Energy Dispersive X-ray (EDX) spectroscopy 116
4.6.6 Focussed Ion Beam (FIB) 116
4.7 Scanning Transmission Electron Microscopy (STEM) 117

4.7.1 Limits on resolution in STEM 119
4.7.2 Spherical aberration correction 119
4.7.3 High-Angle Annular Dark Field (HAADF) imaging 120
4.7.4 Atomic-scale HAADF 120
4.7.5 Comments on the detectability of single Au impurity atoms 122
4.7.6 Quantitative TEM/STEM simulations 122
4.8 Scanning Transmission Electron Microscopy Experimental details(STEM) 123
4.8.1 Equipment 123
4.8.2 Sample preparation 124
4.8.3 QSTEM simulations 124
4.9 Nanoprobe electrical measurements 125
4.9.1 Four-probe electrical measurements 125
4.9.2 Two-probe electrical measurements 126
4.10 Electrical measurements experimental details 128
4.10.1 Equipment specifications 129
4.10.2 Four-probe NW sample preparation 129
4.10.3 Two-probe NW sample preparation 130
4.10.4 Nanoprobe Preparation and sample loading 131
4.10.5 Probe Tip preparation 132
4.10.6 Nanoprobe 4-probe measurement technique 135
4.10.7 Nanoprobe two-probe measurement technique 136
4.11 Summary of the Experimental techniques 138
5 ZnO Nanowire Growth and Contact fabrication results 139
5.1 Previous work 139
5.2 Catalysed ZnO nanowire growth 140
5.2.1 Growth tapering 140

5.2.2 Thin nanowires with distinct Au catalyst particles 141

5.2.3 Short growth time for atomic imaging samples 143

5.2.4 Growth of nanowalls 144

5.2.5 Substrate lattice match 146

5.2.6 Catalysed growth conclusions 147

5.3 Non-Catalysed NW growth 149

5.3.1 Roughened α-Al_2O_3 for ZnO NW growth 150

5.3.2 Low density vertical NWs for two-probe measurement 150

5.3.3 Changing growth morphology and the sample temperature 151

5.3.4 Growth time and source vapour 152

5.3.5 Nanowire diameter 153

5.3.6 Base epitaxial growth layer 153

5.3.7 Metal and conducting substrates 154

5.3.8 ZnO Seed Layers and metal buffer layers 155

5.3.9 Au contact deposition 157

5.3.10 Metal-Semiconductor-Metal structure 158

5.4 Conclusions 159

5.5 Unusual structures 160

6 Electron Microscopy Analysis of ZnO nanowire structure 162

6.1 ZnO nanowire structure by imaging and diffraction 162

6.1.1 Indexed Diffraction patterns 164

6.1.2 Atomic Lattice imaging with high resolution HAADF 167

6.2 Metal contact structural analysis 170

6.2.1 Non-catalysed Au capped nanowires 171

6.2.2 Catalysed nanowire Au particle 172

6.2.3 TEM High Angle Annular Dark-Field (HAADF) imaging 175

6.3 Nanowire Compositional analysis 175

6.4 Catalytic Au contamination and the Au-ZnO interface by high resolution HAADF 176

6.4.1 Depth sectioning with HAADF STEM 179

6.4.2 Control Experiment of non-catalysed ZnO NWs 181

6.5 Au Catalyst Particle and the Growth Mechanism 181

6.6 HAADF Imaging Validation 182

6.6.1 Estimating intensity increases 184

6.6.2 The effectiveness of imaging with a small tilt off-axis 184

6.7 QSTEM: HAADF simulation 185

6.8 FIB cross-section Nanowire array analysis 187

6.8.1 Comparing three FIB sections of catalysed nanowire arrays 191

6.9 Conclusions 192

7 Nanoprobe Results 194

7.1 4-probe measurements 194

7.1.1 Experimental variation and technique 194

7.1.2 ZnO Nanowire Resistivity 196

7.1.3 Diameter dependence 199

7.1.4 Resistivity Magnitude variation 202

7.1.5 Four Probe experimental variations 205

7.1.6 Important experimental factors for future work 206

7.2 2-probe interface measurements 207

7.2.1 Non-Catalysed NWs with Deposited contacts 209

7.3 Catalyst Particle Interface (CPI) measurements 212

7.3.1 Schottky behaviour 214

7.3.2 Deviation from Thermionic Emission 216

7.3.3 The catalyst interface and CPI size dependence 218

7.3.4 Potential barrier and the Interface structure 219
7.3.5 Characteristic length scale and depletion region 221
7.3.6 Isolating the influences on the interface transport 223
7.4 Modelling Au-ZnO Catalyst Particle Contacts 225
7.4.1 Depletion regions 225
7.4.2 Transport mechanisms 226
7.4.3 Catalytic Au Contact modelling 227
7.4.4 Depletion region model optimisation 231
7.4.5 Depletion region fitting results 231
7.4.6 Summary of fitting results 234
7.4.7 Validity of the Model 235
7.5 Catalytic and deposited Au Contact comparison 240
7.6 Conclusions 244
8 Conclusions 247
8.1 ZnO nanowire growth 248
8.2 Transmission Electron Microscopy 249
8.3 Scanning Transmission Electron Microscopy 249
8.4 Four probe electrical measurements 250
8.5 Two probe electrical measurements 251
8.6 Further work 252
8.6.1 Further work: nanowire growth 254
8.6.2 Further work: TEM and HAADF-STEM 254
8.6.3 Further work: Four-probe measurements 255
8.6.4 Further work: Two-probe measurements 255
9 Appendix A – Growth parameter tables 257
9.1 Catalysed Growth Experiments 257

9.2 Non-Catalysed Growth Experiments 258

9.3 Appendix B – Matlab Code 260

10 References 267

Acknowledgments

I would like to thank Prof. Steve Wilks for providing such an interesting subject and invaluable support throughout the research. I would also like to thank Dr. Maffeis for help with all things nanowires and thesis related difficulties. Dr Quentin Ramasse and Dr Demie Kepaptsoglou provided a huge amount of expertise in analysing our nanowire samples with the SuperSTEM II microscope and the complex QSTEM simulations. Dr Alex Walton and Dr Mike Ward at Leeds University dedicated a lot of their time, effort and expertise into measuring and characterising the nanowires with the nanoprobe and TEM. Dr Juergen Köble enabled the delicate final measurement and helped to produce the final results on the nanoprobe in Omicron Germany. All of these people provided a huge amount of support analysing and collating the data for which I am very grateful.

Away from the research my family, most of all Sam, have provided the most welcome support and distractions to keep up my enthusiasm and make the end goal worthwhile.

Table of Figures

Figure 1. Czochralski method of growing large single Silicon crystals. Reproduced[8]. 25
Figure 2. A UHV Omicron Nanoprobe system similar to the one used for measurements. The four probe tips shown are located on the main stage in the hemispherical chamber. This equipment allows measurement of nanometre sized structures in a controlled atmosphere free from environmental effects with nanometre precision of probe tip movement. 30
Figure 3. The wurtzite structure displays the diatomic close packed layers 39
Figure 4. Schematic representation of the wurtzite ZnO structure with lattice constants *a* in the basal plane and *c* in the basal direction. The u parameter is the bond length or nearest neighbour distance b divided by c. α and β are the bond angles 109.47° in an ideal crystal. Reproduced [5]. 39
Figure 5. Growth habit of an ideal ZnO crystal. Reproduced[249] 40
Figure 6. Face-centred unit cell of Silicon (Reproduced[8]) and the Miller indices for three important planes of a cubic crystal, Reproduced[250] 41
Figure 7. The rhombohedral unit cell of Sapphire (Al_2O_3) and the larger hexagonal unit cell 42
Figure 8. **a)** Basal c-plane perspective of the sapphire unreconstructed rhombohedral unit cell. Reproduced[77]. **b)** Sapphire hexagonal unit cell showing the relevant directions and planes. Reproduced[78]. 43
Figure 9. Schematic diagram of the resulting epitaxial relationship of ZnO 0001 grown on Sapphire 0001. Reproduced[5]. 44
Figure 10. Diagram depicting the Bragg angle and the electrons initially in phase undergo different interactions and may suffer a phase change and either constructively or destructively interfere which depends on the interplanar spacing and wavelength of the beam. The spacing between different atomic planes and atoms affects the phase change and can provide information on this arrangement. Reproduced[251]. 48
Figure 11. Band diagrams showing for an n-type semiconductor a metal-semiconductor contact, in clockwise order, **a)** thermal equilibrium, **b)** reverse bias and **c)** forward bias. Reproduced[252]. 50
Figure 12. Typical rectifying I-V characteristics of a nanostructure showing the high current in forward bias and minimal current in reverse until the barrier is overcome and the breakdown voltage is reached. Reproduced[239]. 51
Figure 13. The diagram **a)** depicts the free semiconductor surface with surface states filled up to ϕ_0 that induces a readjustment of charge and surface band bending. **b)** the barrier height ϕ_b and built in voltage V_{bi} can be determined before an interface is formed with the metal although further adjustment of charge due to interface states can affect this. 53
Figure 14. Energy band diagram of a forward biased Schottky barrier indicating the energies at which Thermionic Field Emission and Field Emission occur through the barrier 56
Figure 15. Diagram showing the basic steps in nanowire growth by the VLS mechanism. The metal catalyst acts as a preferential site to capture vapour from the growth atmosphere which alloys with the metal catalyst. The alloy particle is liquid because the eutectic temperature can be significantly lower than the pure metal melting point. Within the alloy particle the concentration of the source element builds until it becomes saturated and precipitation occurs at the substrate interface which initiates crystal nucleation. Further supply of the source vapour continues this process and a crystal grows. Reproduced[253] 61
Figure 16. a) In-situ TEM images of the Vapour Liquid Solid (VLS) nucleation process and subsequent growth of a Ge NW. Initially the Au particle is solid, then as the temperature increases the particle alloys with Ge and melts, further condensation of Ge allows the NW to grow. Scale bar 20nm, reproduced[253]. **b)** TEM image of a ZnO nanowire growing from a ZnO seed particle by the Vapour Solid mechanism. The image shows the tilted angle of the growth due to the mismatch with the Si substrate, reproduced[120]. 62
Figure 17. **a)** Aberration corrected atomic resolution HAADF image of Au atoms (bright dots in two vertical lines) located at planar defects within a Si NW (background horizontal atomic rows), scale bar 5nm, reproduced[133]. **b)** Local Electrode Atom probe tomography of an InAs NW with a Au catalyst particle on top, the image shows the interface is abrupt but there is diffusion of Au (yellow) into the NW bulk, reproduced[137]. 66
Figure 18. The spread in resistivity of ZnO NWs across the literature, Reproduced[50].The graph was produced by Schenkler et al to compare the black symbols that indicate measurements from a review of the literature and the white symbols indicate their own measurements of vapour phase NWs. 69

Figure 19. The resistivity of Si NWs increases with decreasing diameter; the onset of the increase is more apparent in NWs of lower doping concentrations as the surface depletion consumes more of the NW. The interface and surface trap states bind charge carriers and deplete the NW near the surface; this induces band bending and a reduction of the conductive core to a size less than the physical diameter. Reproduced[154]. 71
Figure 20. Barriers heights of various metals deposited on ZnS, ZnSe, and ZnO. Reproduced[176]. 77
Figure 21. SEM image showing the n^+ doped ZnO layer formed to the top of a NW array grown on a p-type substrate. The inset shows the blue light emission and the device is represented in the schematic diagram. Reproduced[31]. 80
Figure 22. Circuits showing the interfaces of the CAFM setup and point contact to NW tip. Reproduced[157]. 83
Figure 23. I-V graph of an Au coated CAFM tip point contact, **a)** with Au deposited on ZnO NW and, **b)** I-V curve of an Au coated CAFM tip point contact on bare ZnO NW. Reproduced[188]. 84
Figure 24. The size of Au catalyst particle size affects the piezoelectric build-up of charge and the output to the AFM tip. A full particle which covers the entire facet leaks charge carriers and prevents the build-up of laterally separated static charge. 86
Figure 25. The depletion width for small contacts become dependent on the contact size when the contact becomes small. The diagram depicts the FWHM of the depletion layers for each contact size from 30nm (a) to infinite (e) for a circular contact pad on a planar semiconductor substrate. For low doping concentrations, as shown, the critical size of contact can be as large as 750nm diameter; however at smaller contact sizes the depletion region becomes comparable in size to the contact radius. Reproduced[60]. 89
Figure 26. **a)** Diagram depicting the numerical solution of the 3D Poisson equation of a NW with a top metal contact and a gated surface. In surface depletion mode the total depletion size extends into the NW depleting it of carriers, this is dependent on initial NW doping and the surface charge. When the surface is accumulated the depletion region becomes very small. Reproduced[201]. **b)** Current density against Voltage graph of Ge NWs with Au catalyst contacts on the NW tip. The decreasing NW diameter provides greater current density in both forward and reverse bias as the contacts become less rectifying. A significant change is not seen until the contact/NW become less then 50nm diameter. Reproduced[21]. 93
Figure 27. Schematic diagram depicting the Au catalysed nanowire growth. Adapted[24]. 96
Figure 28. Typical SEM images of the high quality nanowires achievable with, **a)** Au catalysed growth and, **b)** non-catalysed growth. 96
Figure 29. The Carbolite high temperature tube furnace used for NW growth. The main work tube was high purity alumina vacuum sealed at both ends to ensure the high purity gas flow of Ar/O_2, which flows from left to right, was not contaminated. The chamber pressure that was measured by a Pfeiffer Vacuum combination pressure sensor was maintained at a constant level by the two-stage Edwards rotary pump which is connected by a 1m long stainless steel bellows. A molecular sieve trap (not shown) was used to prevent backflow of oil vapour into the chamber. 98
Figure 30. Experimental arrangement of Furnace Growth experiments 99
Figure 31. The images show how the catalysed growth changes when the sample is located further away from the source, for the case of a sample location of, **a)** 9cm, **b)** 10cm, **c)** 11cm and **d)** 12cm from the furnace centreline. 100
Figure 32. Backscatter electron images, **a)** Au catalyst particles on top of ZnO nanowires and, **b)** deposited Au decorating the top facet of non-catalysed nanowires 102
Figure 33. Schematic of a Scanning Electron microscope indicating the important components. 104
Figure 34. Interaction volume of an electron beam with a thick sample. Reproduced [254] 105
Figure 35. Typical SEM stubs used for mounting NW growth substrates, shown here is the white ZnO growth product found on Sapphire. The S4800 Hitachi SEM used for sample characterisation. 106
Figure 36. Diagram showing the major components of a Transmission Electron Microscope. Reproduced[35]. .. 107
Figure 37. **a)** bright field TEM image of a catalyst assisted nanowire with a dense Au growth tip. **b)** HAADF image that shows the Au tip as a bright region because the dense heavy element Au scatters more electrons to high angles. 109
Figure 38. Photographs of the, **a)** FEI Tecnai TF20 field emission gun TEM used for the structural analysis and, **b)** the FEI Nova 200 a dual beam field emission gun SEM with a Ga^+ Focussed ion Beam. 111
Figure 39. **a)** Lattice image of a ZnO NW showing distinct lattice planes with Au deposited cap. **b)** the corresponding diffraction image which is rotated 90° with respect to the lattice planes due to imaging conditions. 113
Figure 40. Cropped diffraction image showing the measurements of three diffraction reflections which correspond to interplanar measurements of the reciprocal lattice 114

Figure 41. The final cropped diffraction pattern labelled according to the zone axis with the positive direction of 0001 chosen to be in the growth direction of the NW 115
Figure 42. **a)** Indexed diffraction pattern showing the ZnO NW is single crystal with 0001 growth direction that provides the hexagonal cross-section that was seen in SEM images. **b)** the 0001 planes labelled on the Lattice image 115
Figure 43. EDX-TEM analysis that can provide for example, **a)** a map of an area 100nm wide shows distinct diffusion of Zn (yellow) in to the Al (blue) of the Al_2O_3 substrate and, **b)** a compositional point scan of a ZnO nanowire which shows only the elements Zn, O and Cu that originated from the support grid. 116
Figure 44. FIB specimen milling from a planar wafer, **a)** the surface layer of NWs is protected by a beam deposition of Carbon-Platinum from a precursor gas injected near to the site, **b)** the ion-beam is then used to mill out a specimen of 100nm thickness, **c)** and several micrometres wide, **d)** the section is attached to a probe and transferred to a TEM grid. 117
Figure 45. **a)** Schematic diagram of a dedicated aberration-corrected STEM with the electron source at the bottom and the detectors at the top, reproduced [255]. **b)** diagram depicting the beam-sample interaction in a STEM and the dual process of HAADF imaging and EELS analysis, reproduced[207]. 118
Figure 46. Atomic resolution high angle annular dark field image of a ZnO nanowire and the interface with the Au catalyst particle. 120
Figure 47. Concept behind a through-focal series used for 'sectioning' of the crystal lattice to identify single atom impurities. Reproduced[140]. 121
Figure 48. The SuperSTEM II microscope is housed in a purpose built facility in Daresbury with vibration isolation to ensure the best resolution is achieved. 123
Figure 49. Example of the simulated HAADF image calculated by the QSTEM software and the line profile indicating the increase in image intensity with one Au atom located at the centre of a 7nm thick ZnO slab. .. 125
Figure 50. Schematic diagram of the four-probe electrical measurement technique which can be applied for measuring resistivity. Reproduced[256]. 126
Figure 51. Circuit diagram of an n-type semiconductor contacted by two electrodes and the band diagram which depicts one contact in forward bias and the other in reverse bias. The voltage drop across the two contacts and the semiconductor all contribute to the measured voltage. 127
Figure 52. Diagrams depicting the current – voltage characteristics of an ideal Ohmic contact and an Ideal Schottky contact. 128
Figure 53. **a)** Diagram depicting a 2-Probe measurement of low areal density vertical ZnO nanowires with Au tip. **b)** the nanoprobe in-situ SEM image of a two-probe measurement. One sample set had Au tips from the growth catalyst and the other had Au deposited onto bare non-catalysed nanowires. These measurements were compared to nanowires with no Au tips as a reference. 130
Figure 54. **a)** The nanoprobe system at Leeds University and the load lock where samples were mounted in a carousel and transferred into the main chamber with the transfer arm. **b)** The four probe tips mounted on the sample stage are controlled by fine- and coarse- piezo motors. The tips were etched and placed in the tip holder and mounted into the carousel for transfer into the main chamber. 132
Figure 55. In-situ SEM top-down image of a Four-probe measurement on a ZnO NW with the Nanoprobe. The bright regions on the substrate are Au tracks used for locating the tips vertically on the sample. 133
Figure 56. In-situ SEM images taken at 50,000x magnification depicting the difference between, **a)** DC etched tips and, **b)** AC etched tips which improve the ability to measure NWs less than 50nm diameter significantly reducing damage, the scale bar for both images is 1µm. 133
Figure 57. The DC etching apparatus used at Leeds University, the Tungsten wire is under DC current which is applied across the wire and the electrolytic solution which slowly etches the wire. 134
Figure 58. **a)** Current-Voltage graph depicting four-probe measurements and the corresponding outer probe measurement for a non-catalysed NW, the 1st and 4th probe measurements correspond to probe positioning on the nanowire. The 4th measurement had the inner probes closer together. **b)** an I-V measurement depicting an Ohmic linear I-V graph of a side-to-side two-probe measurement across a nanowire. 135
Figure 59. Images depicting the process of identifying a catalyst tipped NW and two-probe measurement, left-to-right fashion from the top-left. **a)** the NW with a 'bright' Au particle on the top facet is identified by SEM and BSE. **b)** the same NW is then identified in the Nanoprobe and the probe tips are brought in to test the contacts side-to-side across the NW. **c)** one probe is then raised above the NW and lowered onto the Au particle using a small applied bias and real-time current monitoring, once contact is achieved an I-V sweep is taken. The probe is then physically raised and lowered in similar fashion to repeat the measurement several times. **d)** probes are then removed and the catalyst particle is identified on top of the NW 137

Figure 60. Growth diminishes away from the source. **a)** the cooler region (~12cm from source centre of Experiment 35) along with a large amount of Au provided NWs of various lengths, mostly with Au particles at the tip. The sprawling base growth makes these ideal for electrical measurements on free standing NWs, however, **b)** a large number of Au nanoparticles were located on the undulating base growth. The base crystal growth provided electrical connection to ground on insulating substrates like sapphire. 141
Figure 61. SEM images depicting the change in NWs as the amount of Au catalyst was reduced. **a)** Long growth times with a thick (6nm) Au catalyst layer at low temperatures gave very long NWs (Exp. 35) with distinct Au tips as shown in **b)** a BSE image. **c)** less Au (4nm) produced smaller nanoparticles to initiate growth and then subsequently thinner NWs (Exp. 34), maintaining a low vapour pressure resulted in a high aspect ratio. **d)** growing for a short time produced NWs ≪20nm diameter, although they did not have time to grow as long. 142
Figure 62. SEM images depicting the critical influence of growth time. With all other parameters the same, **a)** Experiment 32 of growth time 30mins had very thin NWs just beginning to grow, **b)** Experiment 30 with only 5mins extra growth had NWs that are still thin but overall the growth is larger, **c)** and the fine wires sprout up, **d)** using more Au (~6nm) results in large Au particles and generally thicker NWs 144
Figure 63. **a)** High vapour pressure very near the source created thicker NWs with few Au tips and a substantial base growth layer (Experiment 23), **b)** simply by turning the sample to face upward reduced the base growth and individual NWs grew from the substrate, **c)** reducing the amount of Au gives excellent NWs but with very extensive walls Experiment 11, and, **d)** BSE image of Experiment 12 showed very little Au present on the nanowalls or the NWs that suggested at least in the latter stages of the experiment catalytic growth was not the dominant mechanism (2nm Au catalyst layer).. 145
Figure 64. The influence of the substrate on NW tilt. **a)** c-plane sapphire provided NWs tilted at 51.8° to the substrate consistent with the crystallographic misalignment of the substrate for NW growth, **b)** however this is easily overcome by using a lattice matched substrate such as GaN which provided vertically aligned NWs in high density arrays, these NWs though did not have Au particles at the tip, from experiment 7. 147
Figure 65. Drawing depicting the major influences on the catalysed growth product and the typical features that are displayed. 148
Figure 66. **a)** BSE image of Experiment 35 which showed the catalyst particle at various stages of dismount from the (0001) top facet of the NW. **b)** thin initial layers of Au catalyst provided more uniform arrays ideal for device fabrication, however there was no Au present on the NW tips which maybe a hindrance for contact formation. 149
Figure 67. **a)** Experiment 211 produced excellent NWs over a large area, similar experiments however do not always produce this quality, **b)** Experiment 198 showing equally good NWs of uniform length ~7µm and uniform diameter 100nm. 150
Figure 68. **a)** Low density vertical NWs allow good probe access along a cleaved edge, the NWs are long and vertical however other structures are evident that can interfere with measurements, it was difficult to avoid growing these when aiming for low density NWs by the catalyst-free method. **b)** the high density of growth in cooler regions and the tapering effect that can cause NWs to merge together 151
Figure 69. **a)** Crystal overgrowth occurred when the precipitation of ZnO increased, shown here is the effect of an increase of source material to 1g, NWs were of excellent quality, very long but many had grown in thickness rapidly due to the additional flux of ZnO with many NWs diameter 300nm. **b)** Growth in the cooler regions (~500°C) formed tapered NWs, increasing the pressure chamber also caused structures to grow in a three-dimensional sense merging together, shown here at the sample edge of Experiment 207 grown at pressure 2.8mbar. 152
Figure 70. **a)** Experiment 199 produced some excellent nanowires but only in small patches which allowed the inspection of the NW root, we can see here the hexagonal growth pattern of the crystal which developed into a NW, the NW may have sprouted when conditions in the chamber reached the correct balance. **b)** When high quality arrays of NWs grew the base growth was always a thick and uniform layer which did not appear to be formed of isolated crystallites and instead was one continuous layer from which NWs grew, the relationship with good NW growth suggested this layer is epitaxial. These NWs have had metal deposited on top of the NWs that grew from a solution seed layer on Si-Cr-W substrate... 154
Figure 71. **a)** Nicely aligned and very uniform NW array, grown using a solution derived seed layer on Si-Cr-W substrate, experiment 179. **b)** A thick base growth developed on the seed layers which was topped by dense NWs, the tungsten layer is also displayed on top of the Chromium and Silicon substrate. 155
Figure 72. **a)** SEM image which shows the best NWs achieved with buffer layer-seed layer combination with ~20nm Al and ~20nm ZnO plasma Ar-ion deposited with the inclusion of 10% O_2 during ZnO deposition and

post deposition 1hour anneal in air at 700°C. **b)** After annealing the PVD seed layer, large crystallites formed but the random orientation was difficult to control, this determined the alignment of the NWs 156
Figure 73. **a)** Excellent alignment was regularly achieved with the NWs located in the screw fixing region, many attempts were made to uncover the secrets of this but no attempt produced NWs of this quality over a large area. **b)** The cross-sectional SEM image shows a similar area, the base growth is substantial but growth quickly disappears suggesting some local roughening of the surface, this thick base growth always occurred with high quality well aligned catalyst-free NWs. 157
Figure 74. **a)** BSE image of a 10nm evaporated Au contact on ZnO NWs, the well aligned NW shows very little Au on the side whilst the tilted NW displays Au coating the uppermost faces. **b)** A deposition of 20nm Au on perfectly aligned NWs gives a substantial Au pad on top of the NW but still leaves some side deposition highlighted by the backscatter image. 158
Figure 75. **a)** The SEM image shows very long catalyst-free NWs with small metal particles at the tips. The metal was deposited by PVD, **b)** with closer inspection the metal can be seen to form a spherical particle on the NW tip and also to create a fluffy coating on the NW sides, this deposition was measured by SEM to be 170nm on planar Si. **c)** Increasing the deposition amount to approximately 500nm planar equivalent creates large particles at the NW tip which start to merge. **d)** Further deposition forms a complete film across the NWs. 159
Figure 76. **a)** 0001 lattice planes of a non-catalysed NW with single crystal defect free quality, **b)** a lattice image of a hydrothermal NW with the (0001) lattice and the $(10\bar{1}0)$ lattice aligned onto zone axis $[\bar{1}2\bar{1}0]$. 163
Figure 77. **a)** Bright field image of Non-catalysed NWs with uniform diameter, fringes from the thickness variation at the NW edges and overlapping NWs can be seen. **b)** Hydrothermal NWs with uniform diameter but considerable roughness/corrugation variation, strain contrast can be seen in the middle NW and the top NW is close to the Bragg angle. 164
Figure 78. **a)** Indexed diffraction pattern showing the ZnO NW was single crystal with 0001 growth direction giving a hexagonal cross-section as previously seen in SEM images. **b)** the 0001 planes labelled on the TEM lattice image. 164
Figure 79. **a)** Lattice image of a ZnO NW with beam parallel to planes of the $[2\bar{2}00]$ zone axis. **b)** diffraction pattern showing the zone axis configuration and the absence of the 0001 reflection. 165
Figure 80. **a)** Lattice image of catalysed sample 16 NW with a Au catalyst particle showing the (0001) lattice planes and abrupt interface. **b)** Diffraction pattern showing the zone axis, lattice spacing and growth direction as the non-catalysed sample. 165
Figure 81. **a)** Lattice image of a ZnO Nanobelt with a different growth direction to the NWs. **b)** diffraction pattern confirming the structure.. 166
Figure 82. **a)** lattice image of a hydrothermally grown NW showing considerable surface roughness but the lattice is unbroken to the surface. **b)** diffraction pattern indicating the [0001] growth direction and crystallographic equivalence to the other NWs 166
Figure 83 HAADF-STEM images at 100kV of a catalysed ZnO NW located on a major zone axis. **a)** a thin NW is located overhanging the carbon film. **b)** a 35nm wide scan of the wire reveals the (0002) lattice planes. **c)** a 20nm scan with a 5nm scale bar revealed the individual Zn atomic columns in the (0002) planes. **d)** a 10nm wide HAADF scan distinctly revealed the Zn atoms of the NW on the zone axis. **e)** high-resolution HAADF image of the individual Zn atomic columns of a [0001] orientated ZnO NW, the resolution allowed direct measurment of the atomic column spacing. 168
Figure 84. **a)** Wurtzite structure of ZnO. **b)** lattice structure facing the side facet of the Wurtzite structure of a [0001] grown ZnO NW looking down the $[01\bar{1}0]$ zone axis equivalent to the HAADF image, the horizontal axis is the equivalent of the a-axis in this image. The wurtzite crystal images were generated by the Diamond software.. 169
Figure 85. **a)** HAADF image under-focus on a nano-cluster below the NW, with a Z-number far greater than the ZnO NW appearing bright and with some crystalline structure. **b)** over-focus condition showing the intensity and structure of the foreign atom cluster was lost and the sensitivity to the focal point showed the necessity of focal sectioning... 170
Figure 86. **a)** TEM lattice image of the deposited Au cap, average pad thickness of the sample was 12nm, Au particles were seen on the NW side. **b)** a 20nm Au deposition with an average pad thickness of 19nm, the meniscus effect was very apparent as the Au deposition increased. c) image showing the polycrystalline nature of the Au cap... 171

Figure 87. **a)** Lattice image of a single crystal catalyst Au particle tip on ZnO NW with a growth meniscus and neck. **b)** ZnO NWs with catalyst particles of various sizes in various positions on the NWs 172
Figure 88. **a)** Lattice image showing the disordered growth meniscus at the edge of the Au particle. **b)** planes of various orientations in the Au particle suggested in this case the particle was polycrystalline........................ 173
Figure 89. **a)** Low magnification HAADF image of two non-catalysed NWs capped by a 20nm Au deposition. **b)** HAADF image of the Au cap and distinct Au clusters on the NW side facets, both images showed clearly the high Z-number clusters coated the sides of the NWs but they did not form a continuous layer. **c)** HAADF image of a catalysed NW with a bright high Z-number Au particle, the very abrupt interface with the NW and no Au on the sides. **d)** high magnifcation HAADF image achieving close to the best resolution of the microscope. .. 174
Figure 90. **a)** EDX spectra of the catalysed ZnO NW crystal. **b)** EDX spectra of the Au catalytic particle........... 176
Figure 91. **a)** Bright-field image of a 30nm diameter NW and the Au catalyst tip, the intimate relationship was evident but the interface region suffered from phase interference especially with two crystal orientations (displayed in the inset) of the Au particle which confused the image. **b)** corresponding HAADF image at higher magnification showed the (0001) of ZnO and a polycrystalline Au with a crystallite displaying {111} 177
Figure 92. High magnification HAADF images of the NW tip interface. **a)** two different orientations of Au are seen in the catalyst particle the interface is abrupt with no interfacial layer. **b)** magnifying further shows the individual atoms of Zn next to the abrupt Au interface 178
Figure 93. Graph showing the line intensity profile across the Zn columns to the abrupt Au interface and particle. The equal intensity of Zn atoms indicated the average Z-number of each column was the same and high Z-number impurities such as Au were not present. 178
Figure 94. On axis through-focal series. HAADF images of a ZnO NW oriented on the $\left[01\bar{1}0\right]$ zone axis and the ZnO-Au interface starting with focus on the NW centre through to the overfocus condition 15nm above. No bright spots were seen in the ZnO matrix near the interface or in the bulk. 179
Figure 95. Off axis through focus series. HAADF though focus images of a ZnO NW tilted away from channelling conditions. 180
Figure 96. **a)** HAADF image of a ZnO NW grown without Au catalyst and, **b)** HAADF image of a ZnO NW grown with Au catalyst. Both images were recorded in identical conditions, with both NWs oriented on the $\left[01\bar{1}0\right]$ zone axis. 181
Figure 97. **a)** bright-field image with phase contrast of the uninterrupted lattice planes of the Au particle joined to the ZnO NW. **b)** corresponding HAADF image highlighting the compositional difference and single crystal quality of both the tip and the NW. 182
Figure 98. **a)** Raw HAADF image of two overlapping NWs with bright spots apparent in the image. **b)** Bandpass filter of image enhances the spots of greater Z-number although in this case this is unlikely to be Au and more likely beam damage of the overlapping NW. 183
Figure 99. **a)** Unfiltered raw image showing the bright beam damage more clearly. **b)** line profile from the edge of the NW along the (0001) lattice plane and the distinct jump in intensity of the bright spot, also of note is the approximate linear increase of the intensity along the side facet of the NW and the increasing intensity relationship with thickness 184
Figure 100. HAADF image simulations of a slab 7nm thick, with one Au impurity atom placed at **a)** the entrance surface, **b)** middle and **c)** exit surface of the slab.. 186
Figure 101 HAADF image simulations of a slab 14nm thick, with one Au impurity atom is placed at **a)** the entrance surface, **b)** 3.5 nm from the entrance surface, **c)** in the middle of the slab, **d)** 10.5nm from the entrance surface and, **e)** at the exit surface of the slab. 187
Figure 102. **a)** Bright field span of sample Cat 34-3 and the lumpy nature of the base ZnO growth. **b)** Cat 36-3 the base growth segments and adjoining NWs are all one crystal with no obvious boundaries. 188
Figure 103 **a,** Au particles on sample Cat 34-3 with the bottom particle embedded in the ZnO and moire fringes from the overlapping crystalline materials, **b,** the corrresponding HAADF image of the same Au particle, **c,** EDX linescan of the particle and the Au element intensity, location identified by blue line in HAADF image 189
Figure 104. **a)** Lattice image looks at first like a boundary in the ZnO but the lattice planes continue uninterrupted across the entire ZnO layer of Cat 36-3. **b)** enlarged section of the ZnO lattice image showing a heavily faulted region with edge dislocations similar to this throughout the base growth of each sample. **c)** EDX linescan indicated in the lattice image across the interfacial layer, the blue Zinc line and red Aluminium line indicate more diffusion of the Zn into the Al_2O_3. 189
Figure 105. **a)** lattice image of a boundary within the interfacial layer of two different phases. **b)** corresponding EDX map shows yellow zinc diffusing more on the left side of the boundary... 190

Figure 106. **a)** Cropped FIB cross-section bright field image of Experiment 34 sample 3. **b)** cross-section of Experiment 36 sample 3 and, **c)** sample 4, all the scales bars are 1um. 191
Figure 107. **a)** Graph of six four-probe measurements on a non-catalysed NW of diameter 86nm. The inner probe separation is measured from in-situ SEM images and the error bars represent the uncertainty of these measurements i.e. the width of the probes in the SEM image. A linear fit is applied passing through zero obeying Ohm's law and no contact resistance. The gradient scaled by the cross-sectional area of the NW gives the resistivity 0.08Ωcm. **b)** graph showing individual measurements, blue data depicts the first in the series of the six four-probe measurements (blue circle in **a)**), black data the fourth measurement in the four probe I-V series (black circle in **a)**) and the red data is the two-probe I-V of the outer source tips. 195
Figure 108. **a)** In-situ SEM image of a non-catalysed NW indicating the position of the line profile. **b)** the line profile taken at 50% of the maximum gray value intensity. 196
Figure 109. Resistivity plot against NW diameter showing the multiple separation 4-probe measurement of 16 Catalysed, 14 Non-Catalysed and 10 hydrothermal NWs. The y-error bars indicate the standard error of the least squares linear fit and the x-error bars $\pm$2.5nm are omitted for clarity. The graph shows an increasing resitivity with decreasing diameter for all NW growth methods. 197
Figure 110. **a)** Diagram depicting the surface depletion resulting from trapped carrier electrons at the surface mid-band energy levels associated with surface states and defects, reproduced[18]. **b)** The radial band bending effect on a NW of surface trap states that occur as a result of Oxygen adsorption to dangling bonds and defect sites. **c)** Binding energy of Oxygen indicating loosely and tightly bound species. 200
Figure 111. **a)** Effective conduction diameter of a NW embedded in dielectric plotted against surface trap state density and n-type doping density, reproduced[18]. **b)** Diagram depicting the radial depletion of a nanowire by the surface interface trap states when embedded in a dielectric, the effect of the SiO_2 interface is proposed to be negligible on D_{eff}. 204
Figure 112. **a)** Resistance against separation graph of Hydrothermal NW showing a spread of data points around an Ohm's law fit average resistivity of 0.015 Ohm.cm, fit gradient resistivity of 0.016 Ohmcm and fit error of 0.0015 Ohm.cm. **b)** Resistance separation graph of a non-catalysed NW with increasing resistivity as the probe separation is decreased due to carbon deposition the average resistivity is 0.124 Ohm.cm the fit gradient resistivity of 0.113 Ohm.cm and fitting error of 0.007 Ohm.cm. **c)** Catalysed NW with increasing resistivity and average resistivity of 0.040 Ohm.cm, fit gradient resistivity of 0.034 Ohm.cm with fitting error of 0.0031 Ohm.cm. 205
Figure 113. Backscatter electron image at 45° of the actual NWs measured in two-probe experiments with distinct Au particle tips. A large aspect ratio is evident for all NWs measured in the two-probe configuration made possible by precise control of the probe tips. 207
Figure 114. Series of In-situ SEM images of sample non-catalysed 216a, a two-probe measurement of a bare non-catalysed NW and the corresponding I-V measurements. **a)** Firstly the probes are placed on the side, **b)** once good contacts are established one tip is placed on top and, **c)** then the tip is placed again on the side. The I-V graphs indicate in each instance a low-resistance contact is formed between the NW and both tips, the current scale is micro-amps. Measurements like these are highly dependent on clean probe tips. 208
Figure 115. Current-Voltage sweeps in two-probe configuration, **a)**, **b)** and **c)** correspond to catalyst-free NWs with Au contacts of thickness 52nm, 35nm and 19nm on NWs of diameter 110nm, 95nm and 92nm respectively. Nearly linear I-V were measured for all deposited contact thicknesses on NWs of diameters 40-300nm. Current data can only be compared qualitatively due to the difficulty in positioning the probe tips on the NW side below the interface in the top-down SEM view, and characterising the interface size. 209
Figure 116. The concept of a deposited Au contact presents the problem of thinning of the metal at the top facet edges. Under the reverse bias condition electrons maybe presented with a substantial barrier formed by Au-ZnO. Electrons seeking the path of least resistance find the barrier can be penetrated with enhanced tunnelling due to the local metal nano particle size and disordered agglomerate form of the deposited Au especially near the edges. These effects distort the contact size to much less than the characteristic length scale of the system, in this case the NW diameter. This allows tunnelling even with heavy deposition of Au on the top facet. 210
Figure 117. Current-Voltage sweeps in the two-probe configuration. **a)**, **b)** and **c)** correspond to catalysed NWs of diameter 73, 79 and 73nm with particles of diameter of 59nm, 47nm and 37nm respectively as depicted by the scaled 3-D drawings. Current data can only be compared qualitatively due to the difficulty in positioning the probe tips on the NW side below the interface in the top-down SEM view, and characterising the interface size. 213
Figure 118. **a)** Plot of the natural log of the current density J against the forward bias voltage V for each contact of Figure 115 and Figure 117, the rectifying contact of Figure 117a is the only curve to display a linear region

between 0.1-0.3V which is used with Thermionic Emission theory to estimate the barrier height by extrapolating to the y-axis. **b)** Forward bias current density plotted on a log-scale to show the much greater magnitude of current density on the two 'small' catalyst particle contacts. The deposited and 'large' Au particle contacts have very similar current density although the nature of the contacts varies the shape of the curve. 215
Figure 119. Graph showing the diameter dependence of Ge NWs. As the diameter decreases the zero bias conductance density increases and the contact becomes a less ideal exponential fit shown by the increasing ideality factor n for a generic temperature dependent exponential form, inset. Reproduced[19]. 218
Figure 120. **a)** Modelled contributions to the zero bias differential conductance of tunnelling and thermionic emission. For a diode of radius less than 100nm the tunnelling regime is substantial. **b)** The numerically calculated FWHM of the depletion region of several nanosized contacts on a planar semiconductor.Reproduced[60]. 221
Figure 121. Plot of the characteristic length scale of a diode with a radius below which the barrier FWHM (barrier width) no longer depends on the carrier concentration. Instead, independently the size and morphology of the contact forms a 'thin' barrier of FWHM equivalent to diode radius (Figure 120b) and tunnelling then becomes a substantial transport process. This concept is applied in this graph to ZnO for the bulk value of the dielectric constant and a measured value for 100nm diameter ZnO NWs. 222
Figure 122 Schematic diagram depicting the combination of depletion from surface effects and the metal contact of catalysed **a)-c)**, and, **d)** Au deposited catalyst free NWs. 224
Figure 123. Diagram depicting the model used to approximate the parabolic depletion width of small contacts. 227
Figure 124. The Graph shows the low bias experimental current voltage measurement of the 59nm Au contact (red dots) and the corresponding optimised fit for a trapezoidal depletion region approximation. The depletion shape provided the necessary current to match the data when applying Thermionic Field Emission and Field Emission as the dominant transport mechanisms through the barrier that has a large Schottky barrier height. 232
Figure 125. Graph showing the low bias experimental current voltage measurement of the 47nm Au contact (red dots) and the corresponding optimised fit for a trapezoidal depletion region approximation. This depletion shape provides the necessary current when applying Thermionic Field Emission and Field Emission as the dominant transport mechanisms and the change from trapezoidal to triangular shape represents the large increase in conductivity of the contact below the characteristic length scale when edge effects increase. 233
Figure 126. Graph showing the low bias experimental current voltage measurement of the 37nm Au contact (red dots) and the corresponding optimised fit for a trapezoidal depletion region approximation. The transition to pure Ohmic behaviour is a result of the reduced depletion size which encourages more tunnelling across the contact. 234
Figure 127. The band diagram for a highly doped n+ region near the interface for an n-type contact. The Fermi level is below the conduction band but tunnelling can still occur due to the extreme band bending near the interface, the potential barrier becomes virtually transparent to tunnelling current. 240
Figure 128. End-bonded model for Ge NWs in the presence of strong Fermi-level pinning which fixes the barrier to 0.59ev regardless of contact or NW size. The contact covers the entire NW diameter and when the is decreased the combined effect with surface states increases the depletion width along the NW. Reproduced[19]. 241
Figure 129. **a)** Small-bias conductance density of the deposited ZnO-Au contacts against Au contact diameter, the graph shows a similar relationship to Figure 13. **b)** the major difference however is the current density of the Catalysed NWs increases in similar manner but independent of a change in NW diameter with the two smallest contacts on NWs of diameter 79nm and 73nm. 242
Figure 130. **a)** The conductance density of the deposited contacts with a surface related estimated fit proportional to the inverse of the diameter, a similar fit has been used to explain surface related electron-hole recombination in Ge NWs[21] however this could also apply to surface leakage from the contact and NW bypassing the potential barrier in reverse bias which provides more Ohmic like conduction[199] and, **b)** a linear like increase of conductance with diameter. 243

Definitions and Abbreviations

Symbol	Definition
Ø	Diameter
A	Area, amps
a	Diode radius
Å	Angstrom
A^{**}	Modified Richardson Constant
C_C	Chromatic Aberration coefficient
C_S	Spherical aberration coefficient
d	Diameter, interplanar spacing
D_{eff}	Effective conductive diameter
e, q	Electron charge
E_0	Incident energy
E_0	Tunnelling Parameter
E_{00}	Tunnelling parameter
E_c	Conduction band minimum energy
E_F	Fermi level energy
E_{FS}	Fermi energy level in semiconductor
E_g	Energy bandgap
E_V	Valence band maximum energy
h	Planck's constant
$\hbar$	Reduced Planck's constant
hkil	Miller indices
I	Current
J	Total Current Density
J_{FE}	Field emission current density
J_{ms}	Current density from metal to semiconductor
J_r	Recombination current density
J_{r0}	Zero bias recombination current density
J_s	Saturation current density
J_S^{cnst}	Constant Saturation current
J_{sm}	Current density from semiconductor to metal
J_{TE}	Thermionic emission current density
J_{TFE}	Thermionic field emission current density
k	Boltzmann constant
L	separation
l_c	Characteristic Length Scale
m_e	Electron mass
m_r	Relative electron mass
n	Ideality factor
n^+	High n-type carrier concentration
N_d	Doping Density
n_i	Intrinsic carrier concentration
N_t	Density of trap states
R	resistance
sccm	Standard cubic centimetre
T	Temperature
T_R	Vertical resolution limit
V	Voltage
V_a	Applied Voltage
V_{bi}	Built-in Voltage
V_d	Diffusion potential
V_s	Surface potential
W	Depletion Width
Z	Atomic Number
α	Convergence angle, a-plane
β	Collection angle
$\Delta\phi$	Phase shift
ε_0	Permittivity of free space
ε_{SR}	Semiconductor Relative permittivity
θ	Scattering angle
θ_B	Bragg Angle
λ	Mean free path
ξ	Fermi-level relative to CBM
ρ	Resistivity
σ	Scattering cross-section
τ	recombination lifetime
Φ_0	Charge neutrality Level
Φ_b	Barrier height
Φ_e	Effective barrier height
Φ_M	Metal Work Function
Φ_s	Surface energy barrier height
X_S	Semiconductor electronegativity
Ω	Ohm

AC	Alternating Current
ADF	Annular Dark Field
AFM	Atomic Force Microscopy
BF	Bright Field
BSE	Backscatter Electron
CBED	Convergent Beam Electron Diffraction
CBM	Conduction Band Minimum
CCD	Charge couple device
CPI	Catalyst Particle Interface
CVD	Chemical Vapour Deposition
DC	Direct Current
DI	De-ionised
DoF	Depth of Field
EDX	Energy Dispersive X-ray spectroscopy
EELS	Electron Energy Loss Spectroscopy
FE	Field Emission
FEG	Field-emission gun
FFT	Fast Fourier Transform
FIB	Focussed Ion Beam
FWHM	Full width at half maximum
HAADF	High Angle Annular Dark Field
IPA	Isopropanol Alcohol
MBE	Molecular Beam Epitaxy
MOVPE	Metal Organic Vapour Phase Epitaxy
NW	Nanowire
PVD	Physical Vapour Deposition
SDD	Silicon Drift Detector
SE	Secondary Electrons
SEM	Scanning Electron Microscopy
STEM	Scanning transmission electron microscopy
STM	Scanning Tunnelling Microscopy
TE	Thermionic Emission
TEM	Transmission Electron Microscopy
TFE	Thermionic Field Emission
UHV	Ultra High Vacuum
VLS	Vapour Liquid Solid
VSS	Vapour Solid Solid
YAG	Yttrium aluminium garnet

Chapter 1

1 Introduction

Nanotechnology presents the possibility of novel devices that are vastly superior to current electronic devices, for example, Spintronics can provide memory devices that take advantage of the magnetic moment of single electrons. In terms of electronic devices electrons are the smallest element of electric charge that produce the current in present day devices. However the transfer of this charge is still not fully understood and is highly dependent on the material properties and the device structure as a whole, including most importantly the electrical contacts. To enhance the properties of materials single crystals can provide highly reproducible, predictable and superior properties to other material forms. Nanotechnology looks to combine the materials of highest quality that are enhanced when of a nanoscale size and incorporate them into high performance applications. Crystals require precise growth environments to produce the defect free qualities that are important and the properties that are required. Amongst these single crystal materials ZnO has emerged from an unspectacular past in the field of electronics to become one of the most widely researched materials for future devices. Here we investigate the growth and electrical properties of semiconducting ZnO nanowires (NWs) for future application in the field of Nano-Devices and present a solution to control the behaviour of the electrical contacts. These terms are now explained in full.

1.1 Nanotechnology

Nanotechnology is a very diverse field and definitions vary, from a broad description of working at the nanoscale, or exploiting materials with a nanoscale dimension, to

"'Nano-technology' mainly consists of the processing of, separation, consolidation, and deformation of materials by one atom or by one molecule."[1]

Sections of most sciences have undergone a rebranding as Nanotechnology, a good example is Colloid Science which has been studied for centuries, Perrin in 1909 provided experimental support for the kinetic theory of matter by producing small quantities of monodisperse gums.[2] Recent interest in Nanotechnology has breathed new life into these

Sciences and made them fashionable once again. Other advances are very much a product of Nanotechnology, such as Buckminster fullerenes initially synthesised in 1985 for which Harold W. Kroto, Robert F. Curl and Richard E. Smalley were awarded the 1996 Nobel prize in Chemistry.[3] The origin of another wonder fullerene carbon molecule known as nanotubes stretches as far back as 1952 in Russia[4] but nanotechnology has embraced this modern material which exhibits extraordinary electronic and mechanical properties. There is great interest in incorporating nanostructures into nanoscale electronics and nanotubes are already incorporated into macro-scale products to improve strength and electrical conductivity.

1.2 Single crystals and nanotechnology

Bio-nanotechnology, nanomedicine, colloids, materials and semiconductor devices are important fields within nanotechnology; all use single crystals which are amongst the most crucial of building blocks for enhanced performance. Devices which can take advantage of single crystals provide properties much improved on those of poly-crystalline or amorphous materials, nanotechnology takes this a step further and uses single crystals of nanometre scale.

A single crystal can be large, metres in length, or small and measured in nanometres invisible to the naked eye. The fundamental characteristic is the atomic lattice is continuous or unbroken throughout. This distinguishes polycrystalline materials which consist of many small crystals called crystallites segmented by many grain boundaries. The dissimilar atomic bonding at the boundaries and misalignment of the overall lattice can have severely detrimental effects on physical and electrical properties.[5] Amorphous materials have no long range atomic order, a common example is glass.

Single crystals of an appreciable size however are difficult and time consuming to produce with highly controlled laboratory-like conditions required to produce defect free crystals.[5] However, as high quality crystals provide very well defined properties industry has produced large dislocation free commercial crystals of Silicon and GaAs for decades and they are the basis for solid-state electronics[6].

Much of the high purity processing is the cornerstone of the semiconductor industry which controls the enhanced electrical properties with addition of atomic impurities. Control at

the atomic and nanoscale is standard fabrication procedure in modern devices using planar structures. However the future requires small nanometre sized crystals which are readily produced and sometimes consist of only a few atomic layers[7], but the properties are far more difficult to measure and tailor.

1.3 Growing crystals

Crystal growth has three main processes categorised[6] according to the phase changes that take place:

- Solid growth, solid-solid transitions
- Melt growth, liquid-solid transitions
- Vapour growth, gas-solid transitions

Solid growth such as annealing or sintering is less common and growth from the melt includes processes such as directional freezing and crystal pulling. Vapour phase growth can be categorised as sublimation, vapour transport or gas phase reactions.[6]

Sublimation occurs for some materials which is a transition from solid to vapour and back again solely due to temperature changes with no intermediate liquid. This is similar to vapour phase growth except a carrier gas transports the vapour to the growth site. Gas-phase growth occurs as a direct precipitation from chemical reactions of vapour species, the by-product of a chemical reaction and the atmospheric conditions.[6]

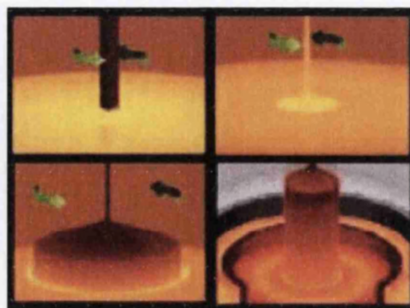

Figure 1. Czochralski method of growing large single Silicon crystals. Reproduced[8].

Silicon crystal growth is the most well established industrial process producing vast quantities of large crystals of 300mm diameter and metres in length. The boules are cut along specific crystal planes by a saw and polished into thin wafers ready for device

fabrication. The crystals are generally grown by the Czochralski method, or crystal pulling method, a type of melt growth (Figure 1).[8]

1.4 Incorporating single crystals into devices

Single crystals are typically used as the main components in electronic and electro-mechanical devices. A common example is quartz which is used in piezoelectric applications as resonators for timing, frequency control and frequency selection[9]. Metals are also grown as single crystals, improving strength for applications such as turbine blades. The electronic industry mainstay of Silicon is grown, processed and then incorporated as part of many devices.

It is sometimes desirable or required to grow single crystals *in situ* as part of the device, such as organic thin film semiconductors initiated by growth nucleation sites specifically chosen to pattern individual single crystals.[10] These examples highlight two different assembly processes which involve single crystals, bottom-up and top-down.

In many instances high quality, high-performance semiconductor devices such as field-effect transistors (FET) require only very small single crystals[11], to realise performance enhancement the crystal size is decreasing. The technology is now close to a fundamental size limit which is a major reason for the great amount of research focussed on nanoscale structures as device alternatives.

1.5 Semiconductor devices and nanostructures

Semiconductor devices are traditionally thought of as planar devices incorporating heterostructures of semiconductor layers. The combination of these layers can be used to fabricate devices such as lasers and transistors, a common example are those devices that rely on electric-field effects on the conduction properties of the material. To improve the speed and performance of electronic components the fundamental device structures such as FETs have to be scaled down to incorporate more devices into smaller and smaller areas. Lasers are required to function at smaller and smaller wavelengths to increase the information that can be packed onto storage mediums. These expressions of Moore's law are the driving forces behind nanotechnology research as nanostructures with dimensions as small as one atom, such as graphene[7], or tens of nanometres, quantum dots[12], nanotubes[13] and NWs[14] can all potentially provide major advances. However the properties

of these new materials are very different from the known bulk material equivalent, with the measurement and characterisation of properties still continuing.

Planar devices have material properties that can be tailored specifically for the device requirements, such as precise doping of silicon from p-type to n-type. These well-defined properties then allow repeatable electrical contacts to be formed over relatively large surface areas which average out interface irregularities. However, on the nanoscale in structures as small as 10nm individual dopant and impurity atoms become far more influential[15–17], along with the surface properties[18] and the very small electrical contacts[19–21].

1.6 Research intensity of Nanostructures

Research into nanostructures includes many materials such as Carbon, Si, GaAs, InAs, ZnO, GaN, ZnSe, and Ge and so on. Carbon is the most widely studied due to the tremendous properties that are theoretically predicted for the single crystal carbon structures such as buckyballs and nanotubes. Among the many semiconductor compounds Zinc Oxide (ZnO) has one of the most diverse ranges of nanostructure growth morphologies including nanocombs, nanosprings, NWs, nanorods, nanobelts, nanotubes, nanocages and nano-tetrapods.[22,23] A variety of methods have been used to grow these single crystals but vapour transport[24] and hydrothermal[25] methods are most common for synthesising widely researched one dimensional structures such as NWs.[5]

One-dimensional structures have been at the forefront of nano-crystal research activity. These structures raise the possibility of investigating fundamental phenomena in low-dimensional systems, for example Ohm's law which can even apply at the atomic scale[26], and to take advantage of the enhanced properties such as much reduced resistivity and metal-like current capacity[26] or piezoelectric coupling[27]. Carbon nanotubes are a prime example alongside ZnO NWs of the incredible possibilities these building blocks provide.[28,29]

1.7 ZnO Nanowires

A Zinc Oxide NW is essentially a defect-free individual single crystal which at present is incorporated into prototype research based devices either using single NWs[30] or vertically aligned arrays[31]. Manipulating and positioning single NWs in order to fabricate useful

devices is difficult, requiring multiple difficult fabrication steps which are very time consuming.

Vertical arrays of NWs have the advantage that the bottom-up design philosophy can be followed with NWs grown straight onto device ready substrates. Vertical arrays of NWs are important for enhanced devices such as light emitting diodes[31], field emitters[32–34], photon detectors[35] and piezoelectric coupling devices[36]. The most important materials for NW arrays to be compatible with are Silicon and metallic conducting layers which have a very large crystallographic mismatch with ZnO.

1.8 Methods of ZnO nanowire growth

Several very different methods exist for ZnO nanostructure growth with the main focus of research concentrated on vapour phase[37] and hydrothermal reactions[38]. Other less popular methods include electrodeposition, sol-gel and polymer assisted growth.[23]

Vapour phase growth often uses either the generation of Zinc (Zn) vapour by evaporation of ZnO/Zn source powders or the chemical reaction of precursor gases. Carbothermal reduction of ZnO powder and subsequent catalysed vapour liquid solid (VLS) growth is amongst the most popular of techniques due to the relative simplicity of the setup.[5] VLS and also catalyst-free vapour solid growth (VS) most crucially provide a means to grow high quality vertical arrays of NWs on 'large' area substrates without exposing the product to solutions which may alter the surface properties.

1.9 Properties of ZnO

ZnO has recently emerged as a viable material for many device applications due to unique properties such as a direct band gap of 3.37eV and an extremely large exciton binding energy of 60 meV [5,39] that allows near-band-edge exciton emission at room temperature. ZnO is very resistant to high energy radiation and provides many wet etch options which can aid device fabrication and compatibility with other materials. Nanotechnology also seeks materials that provide novel biomedical devices and ZnO can provide biocompatible electro-mechanical coupling and functionalised sensing for many of these applications.[40] Very simple growth technology of high quality ZnO results in cheaper devices compared to similar semiconductors such as GaN.[5]

ZnO is naturally an n-type semiconductor but the origin of this intrinsic doping is still debated. The natural electron doping carrier concentrations of up to $10^{21}cm^{-3}$ are usually attributed to deviations in the stoichiometry, Oxygen vacancies and Zn interstitials, or hydrogen incorporation. The bulk resistivity of ZnO is high at 59800Ωcm but with intentional doping thin films can exhibit resistivity as low as 10^{-4}Ωcm.[5,41] Permanent P-type doping has proved more difficult and is one major drawback of ZnO although recent advances in nanostructures display good possibilites.[36,42]

Hydrothermal, vapour phase and Czochralski (crystal pulling) methods are all successfully used for ZnO bulk crystal growth.[5] For research and device purposes ZnO thin films have received much attention using numerous growth methods of Radio Frequency (RF) magnetron sputtering, molecular beam epitaxy, pulsed laser deposition and chemical vapour deposition all of which can provide single crystal films.

1.10 ZnO Nanowire properties

The one dimensional morphology of NWs and the properties of ZnO provide significant advantages in applications such as room temperature UV lasing[43], gas or chemical sensing[44] and field effect transistors[45]. The less common property of high electromechanical piezoelectric coupling of ZnO NWs present applications in transducers, actuators and sensors amongst others.[46] The reason for this diverse range of applications using ZnO nanostructures is much improved over bulk and macro-scale ZnO due to the enhanced function.

1.10.1 Mechanical properties

The mechanical properties of nanostructures are difficult to assess due to the problems in applying testing methods, such as bending for the Young's modulus. However some techniques such as Atomic Force microscopy (AFM) allow the manipulation of individual structures, or the use of electric fields to induce bending due to the piezoelectric properties of ZnO.[23] The enhanced piezoelectric response of the NWs due to the defect free crystal lattice allows the application to electro-mechanically coupled devices such as nanogenerators.[29,47] However these improved properties are greatly influenced by the surface properties, effects are most apparent for NWs much less than Ø100nm, which

results in a Young's modulus much greater than the bulk, the surface dominates this improvement.[48]

1.10.2 Electrical properties

Electrical properties of nanostructures are equally difficult to assess with one favoured technique of FET fabrication using lithography which allows measurement of the transconductance and calculation of the NW mobility and carrier concentration[49], typically with field effect electron mobility of $80cm^2/Vs$ at concentrations of 10^{17}-$10^{18}cm^{-3}$.[18,23] However, the charge associated with the surface acts much like a FET gate effect on the bulk electrical properties of the NWs influencing the carrier density of the material.[18] This surface effect is increased due to the large surface-to-volume ratio of quasi-one dimensional nanostructures. Analysing and quantifying the surface effect and divulging the bulk properties is very difficult which is expressed in the "eight" orders of magnitude in measured resistivity (10^{-3}-$10^{5}\Omega cm$) for ZnO NWs across recent literature.[50]

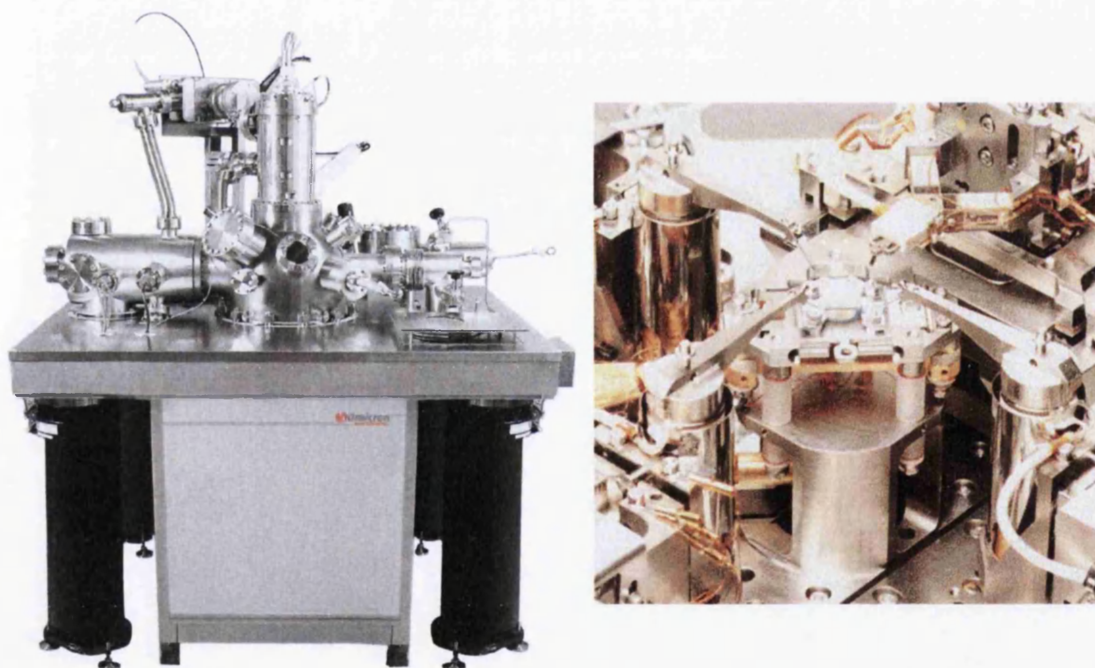

Figure 2. A UHV Omicron Nanoprobe system similar to the one used for measurements. The four probe tips shown are located on the main stage in the hemispherical chamber. This equipment allows measurement of nanometre sized structures in a controlled atmosphere free from environmental effects with nanometre precision of probe tip movement.

Bulk property measurements of ZnO NWs use various techniques, in most of these an unknown error arises from the intermediate processing steps which interfere with the NW surface, for example e-beam lithography or Focussed Ion beam deposition.[41,51] One technique bypasses the 'fabrication' process and allows direct measurements of as-grown

NWs, a Scanning Tunnelling microscope (STM) with four-independent moveable tips, known as the Nanoprobe, which is housed in UHV (Figure 2). Only one reported measurement by Lin et al has been performed with a similar system on ZnO NWs with a resistivity value of 0.25Ωcm.[52] Here we complete a comprehensive dataset of four probe measurements on 40 NWs of different growth methods, results are discussed in Chapter 7.

Nanotechnology and Nanoelectronics can produce high performance devices from lasers[53] to electro-mechanical actuators[29] but they are highly reliant on the electrical contacts[19]. The contacts need to be investigated along with the material properties of the nanostructures to take full advantage of the enhanced properties. Electrical contacts are dependent on the materials used and the interface structural quality[21,54,55] which are yet to be fully understood or controlled especially at the nanoscale. The fundamental concepts behind electrical contacts are introduced in Chapter 2 and Chapter 7 reveals the nanoprobe measurements of ZnO NWs that isolate the contact behaviour formed by Au on the NW tips.

1.10.3 Electrical contacts

Electrical contacts formed to nanostructures have to overcome the inherent small contact area. For planar and macro-scale devices interface inhomogeneity's are averaged out over the large contact area which allows established fabrication techniques to repeatedly form contacts for devices. However, as NWs maybe as small as 10nm diameter, or smaller for nanotubes, the contact area is limited even when deposited on the structure side. The typical schemes for ZnO, Ohmic contacts of Ti/Au and Al, or Au, Ag and Pt for rectifying contacts have all been applied to ZnO NWs with some success.[5,29,36,56,57] AT the typical sizes studied here (diameter <100nm) the contact behaviour becomes dependent on the NW diameter[21] and not only on the metal and semiconductor properties. The scale of the structures can also lead to single dopant or impurity atoms altering the potential energy landscape at the contact interface[16]. Today electrical contacts on planar devices are still proving difficult to theoretically predict; nanosized contacts may prove to be an even greater challenge.

Although there is well established theory for Schottky barriers[55](these concepts are explained further in chapter 2), deviations are mostly nanoscale effects such as edge current crowding, barrier inhomogeneity, impurities and surface adsorbates which all have substantial influence. For nanoscale systems these effects become even more dominant

when the surface, bulk and contact properties all become one entwined system[19,21,54] and all are highly dependent on preparation methods. A prime example to ease these fabrication difficulties is the catalyst particle that resides on top of vapour phase grown NWs which provides individual ready-made contacts to the NW tips, the array as a whole can use the growth substrate as a back contact. Here we have a bottom-up semiconductor device complete with contacts, although little is known about the electrical behaviour of the metal-NW interface and the NW-substrate interface.

A major hurdle is the difficulty in approaching and contacting the free standing vertical NWs <100nm diameter and measuring only the catalyst particle interface. One study achieved this with a probe tip installed in a Scanning Electron Microscope (SEM) and found the Au catalyst interface to Ge NWs[21] to become more conductive as the NW diameter reduces below 50nm. However it is also known the Au catalyst particle on ZnO NWs can vary considerably in size independently from the size of the NW[58] but this anomaly has not been considered in theoretical or experimental analysis of NW contacts. Here we consider this behaviour through growth experiments (Chapter 5), structural analysis at an atomic level (Chapter 6) then building on this knowledge, electrically through measurement and theory (Chapter 7). The range in proportions of catalyst particle an NW diameter is applicable to many NW materials during high temperature growth, for example GaAs[59]. Formation of metallic nanodots or nanocontacts on planar substrates results in less than ideal Schottky behaviour and this effect becomes more dramatic as the scale is reduced. Tunnelling, edge effects, and leakage currents all can contribute to deteriorate the rectifying barrier.[60–63]

Investigations here aim to complete our understanding of Au-NW contacts in the regime where the contact is smaller than the NW diameter (Chapter 6 for TEM analysis). This was achieved by initially tailoring the growth procedure to produce NWs suitable for devices or electrical measurement of individual NWs. Atomic analysis was then conducted using advanced transmission electron microscopy techniques to examine the bulk and interface structure to confidently allow the correct analysis of the electrical measurements. Nanoprobe experiments initially revealed the true 'bulk' NW resistivity (Chapter7), over a range of diameters from 40nm to 160nm, comparing NWs of different growth methods. Au contact properties were then measured with the nanoprobe over a range of Au catalyst particle sizes from 37-59nm and compared to Au contacts deposited onto catalyst-free

vapour-solid grown NWs. The results that are fully discussed in Chapter 7 have significant impact on many devices currently being investigated for the future electronics market.

1.11 Scope

This thesis spans many techniques which combine in a thorough investigation of Vapour Phase ZnO NWs grown with and without Au catalyst and those grown by a hydrothermal method (Chapter 5). The structural properties were examined at atomic levels (Chapter 6) and bulk electrical properties measured, together they allowed the analysis and modelling of the first measurements comparing ZnO NWs with fabricated and as-grown catalyst Au contacts (Chapter 7). The results reveal behaviour which depends directly on the nanometre size of the contacts and the NWs. Measurements were performed with Transmission Electron Microscopy (TEM), high resolution Scanning Transmission Electron Microscopy (STEM)[15] and the most comprehensive use of the Nanoprobe[64] on NWs.

To correctly characterise and interpret the contact measurements it was necessary to relate NW growth phenomena to detailed Electron Microscopy inspection of the NWs and the electrical interfaces. Possibilities such as Au diffusion into the NW, large variations in properties across growth methods, and crystallographic defects can all greatly affect the mechanisms attributed to the results. Therefore great care was taken to analyse the NWs down to the atomic level before narrowing the applicable theories and refining traditional models.

1.11.1 NW growth

To compare NWs across growth methods ZnO NWs were grown by carbothermal Chemical Vapour Deposition (CVD) and high-pressure high-temperature hydrothermal processes. The techniques are described in Chapter 4 and the results are shown in Chapter 5. Vapour-phase methods were used with and without a metal catalyst, the products were compared and then NW structures tailored for the measurement experiments, in particular to obtain:

- Vertically aligned high quality defect free NWs
- Density control to allow probe access
- As-grown Au catalyst particle and post-growth fabricated electrical contacts
- NWs suitable for high resolution electron microscopy analysis

1.11.2 Electron Microscopy

Electron microscopy was used to characterise individual NWs and cross-section samples of NW arrays from the optimum growth experiments. Individual NWs were transferred to suitable support grids for TEM and STEM analysis as discussed in Chapter 4.

TEM analysis studied the composition and crystallographic properties of the individual NWs both for defects, crystal orientation and the interface formed by the Au contacts. These results (Chapter 6) formed the preliminary work for high resolution STEM which aimed to:

- Identify any Au incorporation into catalysed ZnO NWs
- Study the interface with the catalyst particle at an atomic level to reveal any interface diffusion, interfacial layers, abruptness and crystallographic relationships
- Compare results to NWs grown without catalyst
- Ensure accurate imaging and interpretation of results with simulations of individual Au atoms within the ZnO matrix performed with the QSTEM simulation suite[65]

1.11.3 Nanoprobe

Firstly the nanoprobe was employed to extensively study the bulk electrical conduction properties of NWs grown by the vapour phase techniques, with and without Au catalyst, and those grown by the solution based method. A comprehensive set of multiple four-probe measurements on individual ZnO NWs is presented in Chapter 7 which allows comparison of electrical properties across growth methods and NW size. Using the detailed electron microscopy it was possible to confidently apply appropriate theories to the four probe bulk measurements and the two-probe measurements taken of as-grown and deposited Au contacts on vertical free standing NWs. The main aspects of the work are:

- Multiple Four probe measurements on a total of 40 NWs of Catalysed, Catalyst-free, and Hydrothermal growth methods
- Two-probe current voltage measurements of the local Au-ZnO NW interface
- Modelling of the contact behaviour combining well established theory of Schottky contacts with nanoscale effects to determine the interface transport properties

1.12 Objectives, results and achievements

The main objectives of the work were:

- Vapour phase NWs with and without catalyst for device fabrication, dense vertical arrays of long NWs on electronic device compatible substrates with a top contact
- Vapour phase NWs with as-grown and fabricated Au contacts for free-standing electrical measurements, low density NWs orthogonal to the substrate with identifiable contacts
- Thorough crystallographic and compositional characterisation of Vapour phase and hydrothermal NWs, with and without Au contacts
- Atomic compositional analysis of Au catalysed NWs to reveal Au impurities and inspect the structure of the interface
- Refine the known electrical conductivity properties of ZnO NWs and compare various growth methods and analyse the effect of morphology
- Refine our understanding of electrical contacts to NWs and analyse relationships with NW diameter, contact thickness and contact diameter

The main results were the equivalence electrically of NWs from different growth methods with bulk properties that are dominated by the surface, the Au catalysed NW contact behaviour, from Ohmic to rectifying, can be controlled by the contact size. The main achievements of this research are summarised below:

- High quality, high density vertical NW arrays on a range of conducting substrates
- Fabricated top contacts either individually to each NW or one complete layer formed to the entire array
- Density control of vertical Au catalysed NWs with the ability to choose whether Au catalyst particles were present on the NW tips
- Thorough TEM and EDX characterisation of Vapour phase and hydrothermal NWs which revealed single crystal defect free NWs
- TEM analysis of as-grown and fabricated Au contacts
- Atomic resolution STEM analysis which reveals no Au impurities within the NWs and an abrupt interface with the catalyst particle providing an intimate contact

- STEM analysis was justified by multislice simulations which reveal contrast increases of up to 20% from one Au impurity within ZnO – this result makes ZnO different from most Au catalyst-assisted semiconductor NWs which can suffer from substantial Au incorporation
- Successful application of the Nanoprobe technique to NWs as thin as diameter 40nm with multiple four probe resistivity measurements on each NW at different separations, in total 40 NWs were measured, this is the largest known dataset for any nanostructure using the Nanoprobe, results show the resistivity is diameter dependent increasing as the NWs become thinner, the three growth methods produce equivalent NWs and the magnitude of resistivity can vary by 2 orders of magnitude due to the shifting balance of doping and surface properties
- Fabricated Au contacts on vertical vapour phase NWs with Au thickness from 10-60nm are dominated by an Ohmic surface conduction mechanism which produces linear, near Ohmic I-V characteristics regardless of NW size, free standing NWs were measured by the two-probe technique using the Nanoprobe
- Similar experiments of Au catalysed NWs with distinct Au particles on the top facet show contact size dependent transport behaviour, contacts above 50nm are rectifying, as the particle reduces to below 40nm the contact becomes Ohmic because a contact size-reduced depletion region leads to transport dominated by edge tunnelling

Chapter 2

2 Material properties and Fundamental Concepts

This chapter introduces the fundamental concepts that are crucial to the experiments carried out.

a) The production of NWs is crystal growth and is expressed by the science of Crystallography. This subject defines specific crystal structures which determine the properties of a material and provides insight into the rules governing crystal growth. The aim of single crystal growth is a perfect crystal which is free from defects. When crystal growth is considered as the building up of a structure one atom at a time we can start to appreciate the complexity of the subject and the difficulty in controlling the process. This is relevant to the results presented of NW Growth (Chapter 5) and Electron Microscopy Analysis (Chapter 6).
b) The crystals grown are analysed by electron microscopy (Chapter 6), in particular transmission electron microscopy which is governed by fundamental laws of physics. The electrons which traverse through the crystalline material undergo specific deflections which can reveal many details of the sample.
c) The electrical measurements and all electrical devices rely on electrical contacts (Chapter 7). We must form electrical contacts to the NWs in order to measure their properties. Therefore this chapter also details the background of metal-semiconductor contacts.

2.1 Crystalline ZnO: properties and growth

A large amount of the recent interest in ZnO is due to the large exciton binding energy of 60meV which promises to allow efficient room temperature emitters and very low threshold lasers.[53] Spintronics is also a modern application of ZnO due to the possibility of ferromagnetism at room temperature[5] which has been shown with Mn doping[66]. A large piezoelectric coupling coefficient of ZnO has also led to great interest in energy harvesting applications.[29] All of these properties and possibilities are rooted in the crystal structure of the NWs.

The properties of bulk ZnO that are of interest to the materials investigated in this thesis are listed below, in particular for wurtzite structure ZnO:

Physical property		Electrical Property	
Lattice constants [5,23]	a=3.25Å c=0.521Å	Relative dielectric constant[23]	8.66
Density[23]	5.606g/cm^3	Band gap[5,23]	3.3-3.4 eV direct
Melting Temperature[5,23]	2248 K	Intrinsic carrier Concentration[23]	<10^6 cm^{-3}
Young's Modulus[5]	111.2 GPa	Exciton Binding energy[5,23]	60 meV
Thermal Conductivity[5]	~1.3 W/mK	Electron relative effective mass[23,67]	0.24
		Hole relative effective mass[23]	0.59
		Richardson constant[68,69]	32x10^4 A/m^{2}K^2

2.1.1 Crystal Structure

Zinc Oxide is an inorganic II-VI semiconductor compound of Zinc and Oxygen which crystallises into three possible structures, wurtzite, zinc blende and rock salt. The wurtzite structure is a hexagonal crystal with two interpenetrating hexagonal close packed (HCP) sub-lattices one of each atom with four like atoms forming a tetrahedron. This structure results in each anion surrounded by four cations and vice versa, see Figure 3. The cubic forms of ZnO are the zinc blende structure and the rarely observed rock salt structure.[5,67]

Under normal ambient conditions the thermodynamically stable phase is wurtzite which is used for most applications. The wurtzite unit cell due to the symmetry of the hexagonal arrangement is defined by two lattice constants *a* and *c*, as shown in Figure 4, the third lattice constant in the basal plane is equal to *a*. Wurtzite ZnO belongs to point group 6mm or C_{6v} and space group C_{6v}^4 or $P6_3mc$. The lattice constants a=3.252Å and c=5.213Å with

ratio c/a~1.6 is close to the ideal wurtzite structure of ratio 1.633.[5]

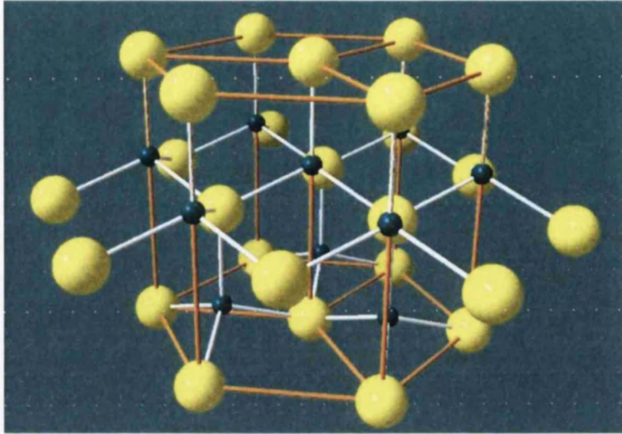

Figure 3. The wurtzite structure displays the diatomic close packed layers

Figure 4 shows the structure consists of triangularly arranged atoms which alternate as diatomic close-packed (0001) planes. The stacking sequence of the (0001) plane is *AaBbAaBa* in the ⟨0001⟩ direction and possesses no inversion symmetry which is the source of the crystallographic polarity. The crystal is Zn polarity when the bonds are along the c direction from cation Zn^{2+} to anion O^{2-} and the bonding is largely ionic. [5,70] This indicates the direction of the bonds in (0001) wurtzite basal planes differ from those of $(000\bar{1})$.[5,67]

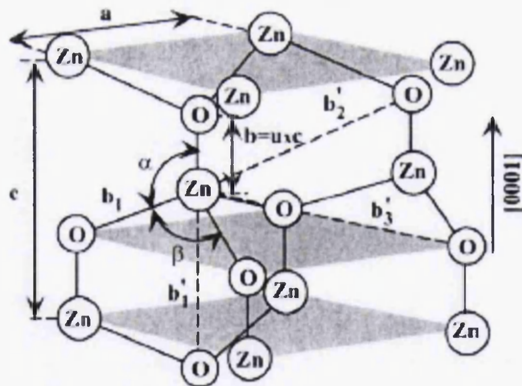

Figure 4. Schematic representation of the wurtzite ZnO structure with lattice constants *a* in the basal plane and *c* in the basal direction. The u parameter is the bond length or nearest neighbour distance b divided by c. α and β are the bond angles 109.47° in an ideal crystal. Reproduced [5].

The lack of inversion symmetry and polarisation of the bonds results in the piezo- and pyro-electric properties. The polar surfaces of ZnO, most commonly the (0001), are an important feature of the typical growth structures possible with ZnO. The polar planes terminate in positive Zn lattice sites (0001) and the other in negative O sites $(000\bar{1})$ creating charged surfaces. This results in a normal dipole moment and spontaneous polarisation along the c-

axis as well as divergence in surface energy. The divergence in surface energy can induce in some materials massive surface reconstruction or faceting to maintain a stable structure. However, ZnO $\pm(0001)$ polar surfaces are exceptions being atomically flat or with single atomic steps. Examination on the atomic level by detailed Scanning Tunnelling Microscopy (STM) studies revealed O islands on the Zn terminated plane.[71] The stability of the (0001) polar surface makes growth along [0001] desirable. [5,72]

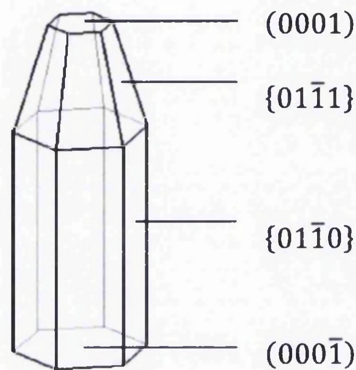

Figure 5. Growth habit of an ideal ZnO crystal. Reproduced[249].

ZnO exhibits three fast growth directions $\langle 2\bar{1}\bar{1}0\rangle$, $\langle 01\bar{1}0\rangle$ and $\pm[0001]$ which compete in the growth environment. The dominant direction and crystal morphology are determined by the relative surface activity of each crystal facet. In the correctly balanced conditions, after an initial period of nucleation and growth, the structure will develop into a well-defined 3-D object with low index crystallographic faces. Structures tend to maximize the $\{2\bar{1}\bar{1}0\}$ and $\{01\bar{1}0\}$ facets as these are non-polar with lower surface energy than the $\{0001\}$ facets. This produces the well-known NW crystal morphology which is an elongated hexagonal shape growing along [0001] (Figure 5).[5,72] Nanobelts are a prime example of a structure dominated by the polar $\{0001\}$ facets and thus exhibit strong deformation to minimise the polar surface area which can result in nanorings and nanohelixes as the structure attempts to interface the two polar surfaces.[46,73]

2.1.2 Lattice match

To grow crystals from the gas phase a target substrate is usually necessary. The substrate provides a preferable nucleation site for growth which is the seed of the structure. This is the most crucial stage in the growth development and is largely influenced by the substrate. Usually a substrate with similar crystal structure to the desired product is used, however in some instances this is not possible for compatibility reasons, e.g. high temperature growth,

Silicon based devices. A large crystal lattice mismatch of the desired growth with the substrate results in a high strain energy which is unstable. To reduce the system energy lower strain growth forms develop and the original structure and morphology is lost. ZnO NWs are the product of the [0001] fast growth direction, however when using poorly matched substrates such as Si the NW growth is not the boundary with lowest energy. This can cause NWs to lose coherence with the substrate and point in random directions or produce entirely different structures.[35]

The ZnO wurtzite crystal structure and cubic Silicon inevitably creates a large lattice mismatch which makes high quality NW growth difficult. To eliminate the lattice mismatch growth has been extensively studied on hexagonal substrates such as GaN with 1.8% mismatch and SiC with 3.5%.[5] GaN has a wurtzite crystal structure like ZnO and very similar lattice constants which make it a much better choice for vertically aligned growth on a conductive substrate which is suitable for electronic devices, rather than Silicon or metals.[23]

Silicon on the other hand is very cheap, recyclable, abundant and one of the most important semiconductors. When using Silicon the influence of the substrate structure on the resultant growth must be removed. This allows the desirable properties of Silicon, such as well-defined doping, to be used in conjunction with the NWs.

2.1.3 Silicon substrate for ZnO NW growth

The atomic structure of silicon is displayed by the diamond cubic lattice structure with each silicon atom having four bonds to each of its four nearest neighbours. This forms the tetrahedral relationship shown by the dark spheres in Figure 6.[74,75]

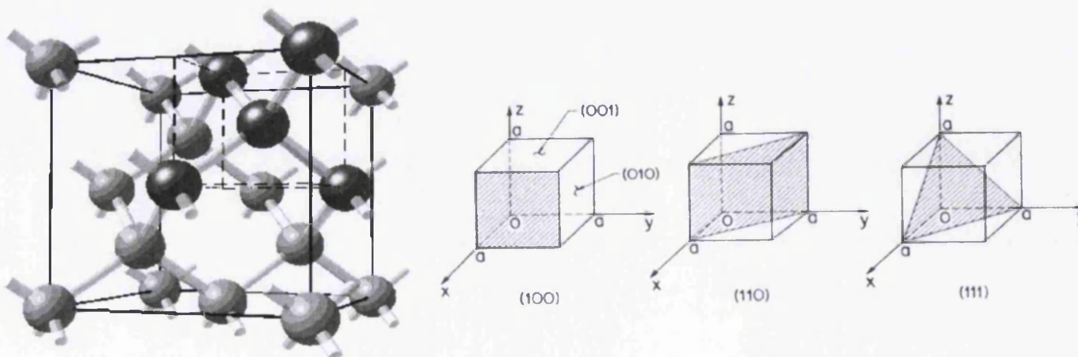

Figure 6. Face-centred unit cell of Silicon (Reproduced[8]) and the Miller indices for three important planes of a cubic crystal. Reproduced[250].

The lattice constant of Silicon is the cube side length a=0.543nm shown in Figure 6.[5] The three most important planes of low miller indices associated with cubic crystals are shown in Figure 6. This cubic system is also relevant to metals such as Au, W, Nb and Cr used as substrates in growth experiments.

Lattice mismatch is a simple calculation comparing the two lattice constants of each unit cell,

$$\text{mismatch} = \frac{(a_{ZnO} - a_{substrate})}{a_{substrate}} \times 100$$

where a_{ZnO} and $a_{substrate}$ are respectively the lattice constants of ZnO and the substrate. ZnO NWs grown on Silicon are generally tilted with dramatically longer growth in a diagonal direction; this is consistent with incoherent fast growth directions.[5,35]

2.1.4 Sapphire substrate for ZnO NW growth

The epitaxial growth of ZnO on sapphire substrates has been widely investigated both on the a–plane and c-plane of sapphire as it is inexpensive compared to GaN and SiC. The atomic structure of sapphire is displayed by the structure of Chromium sesquioxide Cr_2O_3 with two molecules in the rhombohedral unit cell, four Al^{3+}ions and six O^{2-} ions, Figure 7. Rhombohedra can be considered as a cube stretched along one diagonal and having six identical faces and when viewed from above the three fold symmetry becomes apparent. From the Bravais lattice rhombohedral unit cell it is difficult to visualise the larger hexagonal unit cell which contains 12 Al and 18 O atoms which is more appropriate for comparison to ZnO.[76]

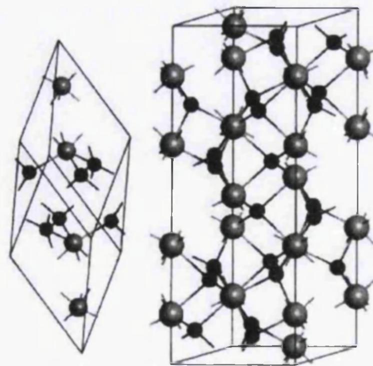

Figure 7. The rhombohedral unit cell of Sapphire (Al_2O_3) and the larger hexagonal unit cell

The rhombohedral unreconstructed cell of sapphire (Figure 8a) viewed along the [0001] direction is the basal c-plane perspective. The oxygen anion positions can be approximated so they form a hexagonal closed packed lattice with a=4.757Å and c=12.983Å.[77] The planes and directions of the hexagonal unit cell are also shown (Figure 8b). The unit cell consists of six close-packed (0001) planes of O anions sandwiching 12 planes of Al cations occupying two thirds of the octahedral interstices with a slight shift along the c-axis. The crystal has largely ionic bonding and the (0001) surfaces are oxygen terminated. All common planes employed for epitaxy are non-polar including (0001).

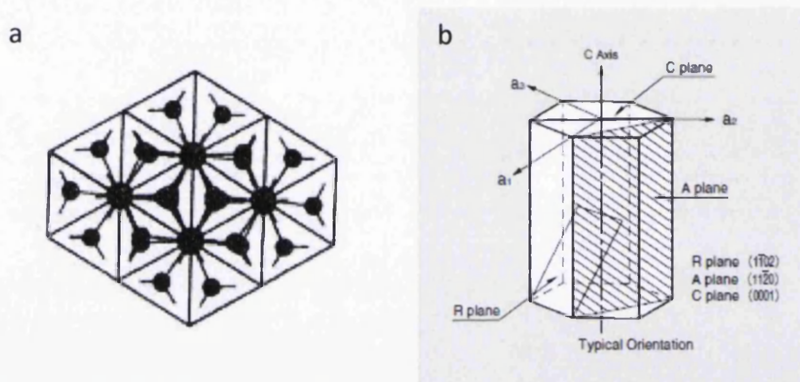

Figure 8. **a)** Basal c-plane perspective of the sapphire unreconstructed rhombohedral unit cell. Reproduced[77]. **b)** Sapphire hexagonal unit cell showing the relevant directions and planes. Reproduced[78].

Sapphire substrates are commonly used for the epitaxial growth of ZnO primarily on the (0001) basal c-plane and the $(11\bar{2}0)$ a-plane. The large c-plane lattice mismatch even after reducing by a 30° in-plane rotation is $\sim$18% and ZnO films display a large proportion of mosaicity, high residual carrier concentrations and low mobility.[5] The rotation occurs for the ZnO axis relative to the Sapphire axis to reduce the induced strain. In the idealised case ZnO$[11\bar{2}0]$ || $[11\bar{2}0]$$Al_2O_3$ but due to preferential bonding of Zn to sapphire O in-plane rotation domains are seen and the ZnO m-plane $(10\bar{1}0)$ normal aligns with the normal of the sapphire a-plane $(11\bar{2}0)$ shown in Figure 9.[5,79] These problems are eliminated by growing the films on the a-plane such that ZnO(0001) || $(11\bar{2}0)$$Al_2O_3$ and ZnO$\langle 11\bar{2}0\rangle$ || $[0001]$$Al_2O_3$.[18,19]

The *a* lattice parameter of ZnO relates by nearly exactly a factor of four to the sapphire c-axis, giving a mismatch of 0.08%.[37] Therefore ZnO NWs can grow epitaxially from the $(11\bar{2}0)$ a-plane and display very good vertical alignment. The mismatch can be calculated with sapphire $c = 12.99$Å and ZnO $a = 3.252$Å multiplied by a factor of four. In comparison

the mismatch of the sapphire c-plane to ZnO c-plane can be calculated with $a = 3.252Å$ for ZnO and $a = 4.757Å$ for sapphire ~32% before the in-plane rotation.[5]

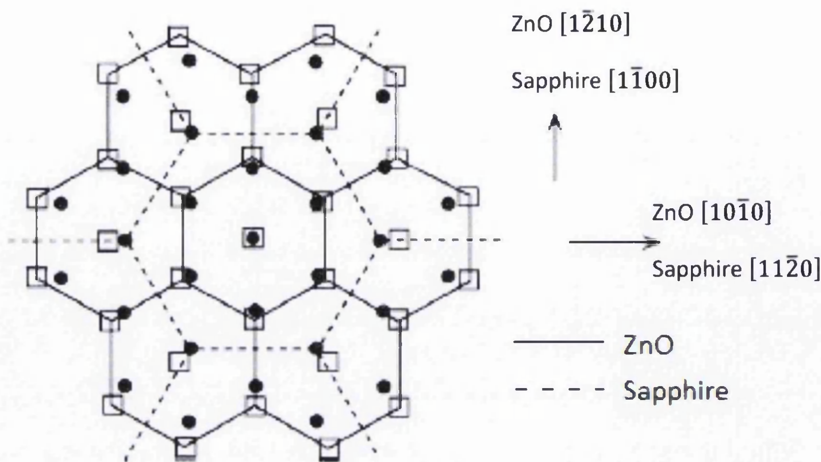

Figure 9. Schematic diagram of the resulting epitaxial relationship of ZnO (0001) grown on Sapphire (0001). Reproduced[5].

The problems associated with poorly matched substrates can affect the properties of the NWs displayed by a reduction of buckling and mechanical strength.[81] Sapphire is an insulating material which is not appropriate for many electronic devices therefore growth has been extensively studied on better matching substrates such as GaN. Also ZnO itself has been used as a buffer layer on sapphire and silicon to provide an exact lattice matched substrate to ensure alignment of the epitaxial growth of NWs.[81–83]

2.1.5 Buffering ZnO growth from the substrate

ZnO used as a buffer layer can provide an exact lattice matched substrate to ensure alignment of the epitaxial growth of nanorods or NWs.[84,85] To buffer the crystal growth from the substrate a very thin seed layer or much more substantial buffer layer can be formed depending on application and growth method. A seed layer aims to deposit a thin (~10nm) layer of very small ZnO crystallites which can physically align the (0001) planes with the flat substrate regardless of crystallinity.[83] A buffer layer aims to form a much thicker film (>50nm) again c-axis orientated but some crystalline relationship may exist at the substrate-layer interface. Seed layers are usually preferred for hydrothermal nanorod growth[81] with easy patterning and vertical growth on any substrate[86]. Regardless of the growth method used the product must be inspected for crystallographic structure and quality, this cannot be assumed.

2.2 Crystallographic analysis

There are a number of ways to inspect the structure of crystals which use electrons or x-rays. The most common methods are X-ray Diffraction (XRD) and Transmission Electron Microscopy (TEM). XRD is most useful for analysing bulk or powder samples, such as thin films. In this instance x-rays directed at the sample interact with the crystal structure and the diffracted x-rays are detected. TEM is only useful for 'thin' samples usually <100nm thickness which can be suspended on a small grid which makes it very applicable for studying nanostructures.

TEM is very appealing as the sample is directly imaged and displayed on a screen during analysis and the sample can be rotated to align features and crystal planes with the beam. The image is formed after the electron beam passes through the sample and some electrons interact with the crystal lattice. These interactions determine the image that is formed with the post-specimen optics defining the electrons that are collected. Interactions and scattering are extremely complex and a brief introduction is provided here.

2.2.1 Transmitted Electrons

Electrons incident on a thin sample can undergo one of three major interactions[87]:

1. Pass straight through the sample undeflected and with no energy loss
2. Pass through the sample and be deflected by the specimen lattice with no energy loss, this is known as elastically scattered
3. Lose a significant amount of energy and probably deflected from its original trajectory, known as inelastically scattered, which can result in a secondary emission such as secondary electrons or x-rays

The unscattered electrons are separated from those that are scattered by more than a selected angle defined by the objective aperture. The objective aperture is inserted into the back focal plane and is a key component to forming an image in a TEM. The three limits on TEM resolution (diffraction, spherical aberrations and chromatic aberrations) are all highly dependent on the objective aperture angular size. For normal imaging the objective aperture is chosen as a compromise to balance these effects and to allow the assumption that no energy is lost by the collected electrons. For lattice images of crystalline materials a

large aperture allows phase contrast where the diffracted beam and unperturbed beam interfere revealing the fine structure of the atomic lattice.[87,88]

The number of unscattered electrons dictates the brightness and so thicker or dense heavy element regions appear darker. The electrons are scattered over an angular range depending on the mass and density of the sample. Crystalline materials diffract the electrons in well-defined particular directions and cancel in others. Most of the scattered electrons will travel in specific directions at twice the Bragg angle θ_B. The intensity and direction of unscattered and diffracted electrons is dependent on the orientation of the crystal presented to the beam and the thickness of the sample. The undeflected electrons makeup the bright field image while the scattered or diffracted electrons are the dark field image.[87,88]

2.2.2 Scattering of the electron beam

Electron scattering occurs when the primary electron beam interacts with the specimen. Scattering can occur with virtually no energy loss, elastic scattering, or with a significant measureable loss, inelastic scattering. The probability of a scattering event is usually expressed as a scattering cross-section σ, or mean free path λ. The scattering cross-section is the area which scattering particles present to the incoming electron. The mean free path is the average distance between scattering events.[88–90]

One scattering event whilst passing through the sample is termed single-, more than one is plural-, and many is multiple-scattering. Electrons that have not been scattered or singularly-scattered are of most interest in TEM/STEM analysis and imaging. For most TEM analysis the mean free path is roughly equal to the sample thickness.[89,90]

Elastic scattering occurs with a deflection to the electrons path but with no detectable energy change. This Rutherford scattering is from Coulombic interaction with a specimen atom and results in an intense forward peaked energy distribution such that an electron beam with incident energy E_0 has probability of being scattered through an angle θ of

$$p(\theta) \propto \frac{1}{E_0^2 \sin^4 \theta}$$

Scattering by a single atom occurs according to this equation. As the beam energy increases scattering to higher angles decreases which is important for diffraction and dark-field

analysis as well as the contrast of bright-field imaging. The specimen itself also dictates the number and type of scattering events that occur.[89,90]

Inelastic scattering occurs with some appreciable energy loss and possibly some change in direction. These energy losses are the basis for a number of analytical techniques such as Electron Energy-loss Spectroscopy (EELS) and Energy Dispersive X-ray spectroscopy (EDX).[88,90]

2.2.3 Diffraction of electrons

Diffraction patterns are the spatial variation in electrons after scattering events on passing through the specimen. The pattern gives information about the arrangement of atoms within the sample. Elastically scattered electrons are the major contributor to the signal of diffraction patterns. However in a specimen of many atoms there is strong interaction of scattered electrons from different atoms and so the atomic arrangement dictates the pattern. This pattern is regular for crystalline materials which we consider here and is a measure of the crystal structure. Diffraction is described by Bragg's law.[88,90]

2.2.4 The Bragg Angle

Bragg's law describes the distribution of scattered electron waves that are in phase. The waves in phase will lead to a strong local electron beam. Waves out of phase will not reinforce and may cancel. The primary electron beam interacts with the sample and if the path lengths of the scattered electrons differ by an integral number of wavelengths n they will be in phase. This leads to the relation $2d\sin\theta = n\lambda$ where d is the interplanar/column spacing of the atoms and can be expressed in Miller indices, n is the order of diffraction for which only the first order is usually considered and θ is the Bragg angle. The Bragg angle is the angle of scatter relative to the lattice column at which constructive interference of diffracted electrons from successive lattice planes occurs, it is not the divergence angle emerging relative to the sample. To gain the most crystallographic information the sample is aligned with the beam near parallel to the lattice planes of interest i.e. crystallographically on-axis. θ is usually very small and $\sin\theta \sim \theta$ and in practice only the planes near parallel to the beam will show strong diffraction. This simplifies diffraction patterns greatly, however, the accuracy of lattice measurements using this condition is only within a few degrees as diffraction can occur at up to five degrees from the Bragg angle.[90]

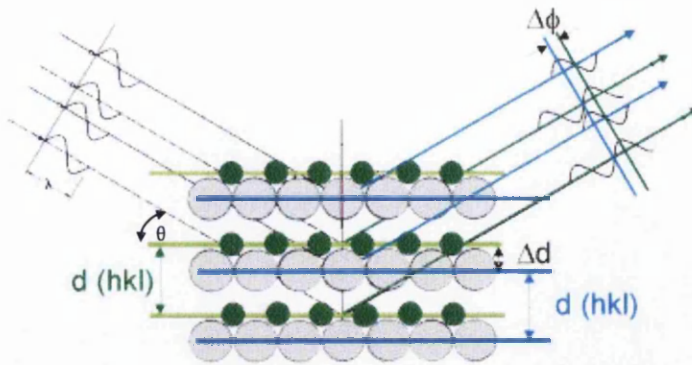

Figure 10. Diagram depicting the Bragg angle and the electrons initially in phase undergo different interactions and may suffer a phase change and either constructively or destructively interfere which depends on the interplanar spacing and wavelength of the beam. The spacing between different atomic planes and atoms affects the phase change and can provide information on this arrangement. Reproduced[251].

2.2.5 The reciprocal lattice

From geometric considerations the electron diffracted through the angle of 2θ will be a distance r from the unperturbed trajectory on the TEM image with $r \propto 1/d$. The constant of proportionality is the camera constant which is dependent on camera length allowing d to be calculated directly from diffraction patterns. The digital diffraction images produced by a modern TEM generally are expressed in terms of the reciprocal lattice which gives the spacing as $1/d$ and units nm^{-1}. The reciprocal lattice provides a powerful way of constructing a scaled diffraction image of a unit cell section by expressing the dimensions of the structure in the reciprocal form. Or alternatively a diffraction pattern of a single crystal specimen is the equivalent of a magnified planar section through the reciprocal lattice normal to the beam direction.[88,90]

2.2.6 Diffraction Patterns

In the case of single crystal materials the perfect planar structure diffracts electrons at repeating separations from which the exact formation of the unit cell can be calculated. Polycrystalline materials may feature diffraction patterns from several grains of different orientations and so the pattern can form rings. Certain planes in crystalline materials diffract in such a way that destructive interference will occur, these are forbidden reflections and do not usually appear in diffraction patterns. Diffraction patterns can be gained from very small regions of the specimen which allows individual grains or nanostructures to be analysed.[89,90]

Diffraction of electrons is used to identify defects within crystalline specimens. Crystal planes parallel to the beam will diffract most strongly and those tilted to the beam will not

diffract as much and appear brighter in the image. Buckled or strained samples will for this reason show dark regions or contours and subsequent fringes. Defects have various contrast mechanisms in bright and dark field images and are discussed with the TEM image analysis.[87,89,90] The high quality NWs produced with the aid of the aforementioned techniques allowed further electrical analysis.

2.3 Metal-semiconductor contacts

Electrical devices and measurements are entirely dependent on the behaviour of the electrical contacts formed. The contact formed at the NW tip with the top Au contact is of fundamental importance for array devices and not limited to ZnO NWs. The behaviour of a contact is a result of the interface formed between the metal and the semiconductor surfaces and material properties.

Metal-semiconductor contacts have great importance in direct current and microwave applications and in analysis of fundamental physical properties and so have been extensively studied.[68] Figure 11 shows the energy band diagrams of an ideal metal-semiconductor interface. A built-in voltage V_{bi} appears at any interface of two materials with different work functions/electron affinities where ϕ_m and ϕ_s are the work functions of the metal and semiconductor respectively, and χ_s is the electron affinity of the semiconductor. The mobile electrons in each material have different potential energies and redistribute around the junction to bring equilibrium. For these two interfacing materials the energy bands are offset at the junction (E_c and E_v denote the potential energy of the semiconductor conduction band minimum and valence band maximum). Both the built in voltage at the junction and the resulting band offset are related directly to the potential energy barrier formed which is a material constant, ϕ_b see Figure 11a. Therefore, metal-semiconductor interfaces are classified as *heterojunctions* in qualitative terms although this is usually used to refer to a junction between two different semiconductors.[75]

Schottky assumed the shape of the potential barrier is determined by a uniform space charge due to ionised impurities, this conforms fairly well to practice. For this reason, metal-semiconductor contacts are usually referred to as Schottky barriers and those with intentional rectifying behaviour as Schottky diodes. The impurities can be dopants or stoichiometric variations, for n-type semiconductors shallow donors provide the charge

carriers.[55]

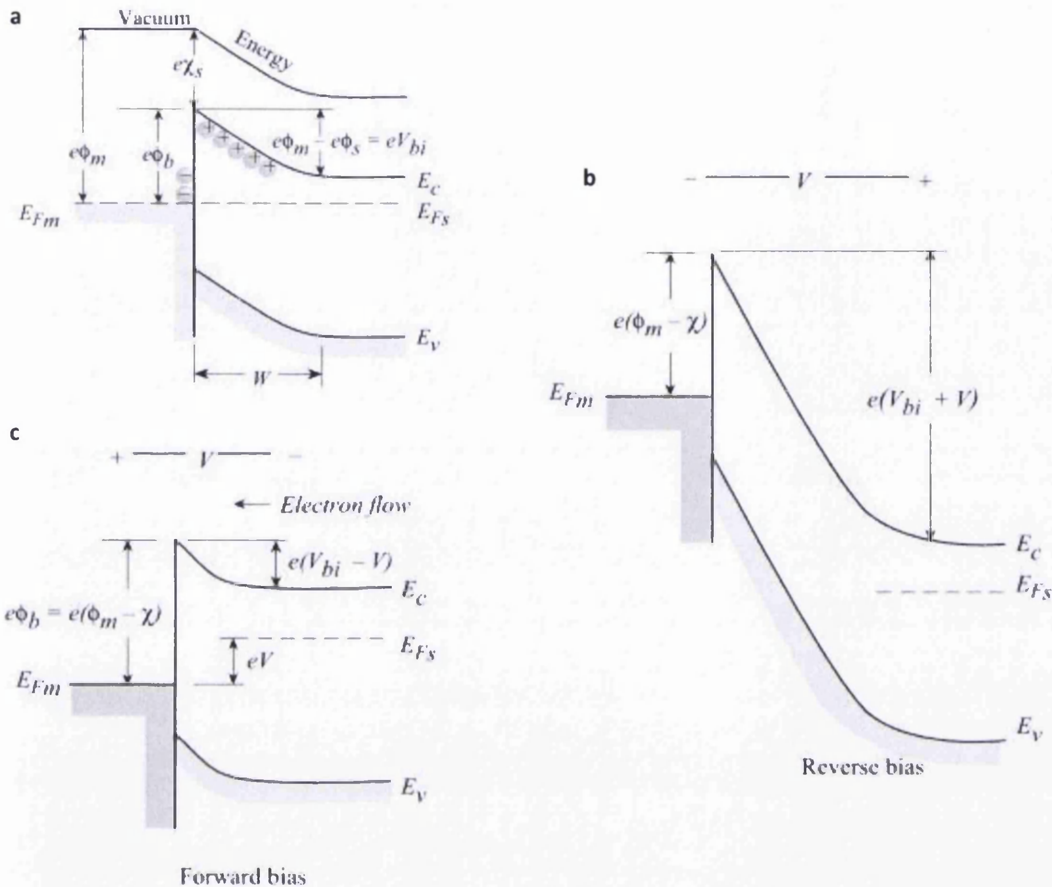

Figure 11. Band diagrams showing for an n-type semiconductor a metal-semiconductor contact, in clockwise order, **a)** thermal equilibrium, **b)** reverse bias and **c)** forward bias. Reproduced[252].

There are two main categories of metal-semiconductor contacts, rectifying contacts known as Schottky diodes and low resistance Ohmic contacts, depending on characteristics of the interface. Schottky diodes are similar in I-V characteristics to a P-N junction but differ as they operate with a single carrier (majority) type. Ohmic contacts have linear I-V characteristics. [75,91] Discussion here is centred around the majority charge carriers of electrons due to the n-type characteristics of ZnO.

Figure 11a shows the metal to n-type semiconductor contact in thermal equilibrium where the barrier for the electron on the metal side is ϕ_b and on the semiconductor side is V_{bi}. This simplified model represents the ideal case with no surface states affecting the interface charge equilibrium. There is charge redistribution when the metal and semiconductor are brought together with electrons passing from the semiconductor into the metal. This leaves

a negative charge on the metal surface and positive charge in the semiconductor (Figure 11a). Uncompensated donors in the semiconductor leave a space-charge known as a depletion region known which extends a distance W from the junction and is represented by the upward band bending in the diagrams. It is evident the barrier height relative to the Fermi level (E_{FS} and E_{FM} for semiconductor or metal respectively) must be $\phi_b = \phi_m - \chi$ where ϕ_m is the metal work function and χ is the semiconductor electron affinity, this is known as the Schottky-Mott theory.[55]

Applying a negative voltage V to the metal with respect to the semiconductor (positive voltage to semiconductor) lowers the Fermi level of the semiconductor below the metal Fermi Level Figure 11b, increasing the potential across the contact and extending the depletion region. Both of these effects increase the electric field at the contact. Electrons from the semiconductor are prevented from moving through the contact due to the increased energy barrier in the depletion layer.[75,91]

The forward bias is shown in Figure 11c, applying a positive bias to the metal raises the semiconductor Fermi level. This reduces the barrier for electrons on the semiconductor side. In all situations the barrier height to electrons on the metal side is constant if ignoring image force lowering, tunnelling, interface states and interfacial variations. The decrease in electric field across the contact in forward bias occurs only in the semiconductor interface region due to the much greater resistance of the depletion region and the semiconductor material compared to the metal.[75,91]

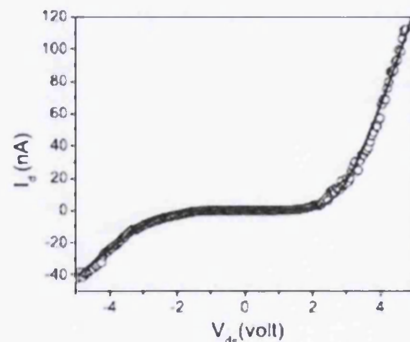

Figure 12. Typical rectifying I-V characteristics of a nanostructure showing the high current in forward bias and minimal current in reverse until the barrier is overcome and the breakdown voltage is reached. Reproduced[239].

The result of the much greater resistance to electrons from the semiconductor in reverse bias gives much less current across the contact and produces rectifying I-V characteristics, Figure 12. The depletion region that is constant at zero bias extends further into the semiconductor with increasing reverse bias and contracts under forward bias which compensates the positive charge near the interface. The remaining positive charge in all bias cases is the space charge depicted by the upward band bending in Figure 11. In the zero-bias condition depletion regions can extend up to micrometres into the semiconductor which dramatically reduces its conductivity.[75,91]

Ideal surfaces have surface states where the crystal lattice is terminated. Surface states can result in energy states within the bandgap which are drawn from the valence or conduction band reducing the density within these bands. These states must be filled by electrons if the surface is to remain electrically neutral. Below this neutral level the states are donor-like(positive when empty) and above acceptor-like (negative when filled).[55] These surface states can be thought of as the free dangling bonds at the surface due to unpaired electrons which can act as a donor giving up its electron or as an acceptor and accept an electron.[55] Due to these inner-band states the surface can act as a trap removing carriers from the bulk, Figure 11a.[92] Dangling bonds, surface defects and adsorbed ions can all cause energy levels in the band gap and when these are filled the result can be surface depletion or accumulation.[93] The presence of these states and surface charge can result in Fermi-level pinning which can greatly affect contact barrier formation which no longer is determined by the metal and semiconductor work functions.[94]

2.3.1 Fermi-Level pinning

Negative charge trapped at the semiconductor surface must be balanced by a positive charge in the space charge region. The surface charge is defined by the position of E_{FS} with regards to the surface charge neutrality level ϕ_0. The charge neutrality level is the level to which surface states need to be filled with electrons to render the surface neutral. Surface states are assumed to be filled up to E_{FS}, in the 'absolute-zero' approximation. At zero bias the Fermi level in the semiconductor E_{FS} coincides with the Fermi level of the metal and is constant throughout the barrier region. When the charge neutrality is below the Fermi level the surface states must hold a net negative charge which increases the built-in voltage,

increases the barrier height and depletion width. When ϕ_0 is above the Fermi level the surface states hold a net positive charge decreasing ϕ_b and V_{bi} (see Figure 13) The occupancy of the surface states creates a dipole with an image charge in the metal. As the surface states are occupied further the effect on V_{bi} increases and drags E_{FS} towards ϕ_0 and when the density of states is high enough they become approximately equal.[95] In this situation the Fermi level is constant throughout the semiconductor and band bending at the surface is due to surface states inducing charge redistribution. The barrier height then becomes approximately

$$\phi_b \approx E_g - \phi_0$$

where E_g the semiconductor band gap, and the barrier is pinned by the high density of surface states.[55] E_{FS} is pinned to ϕ_0 , and the barrier has become independent of the metal. In simple terms if the density of surface states is high enough they have an overriding influence on the band bending and the barrier formed. Energy states can also occur due to the union of the metal and semiconductor and are known as interface states that can similarly pin the barrier.

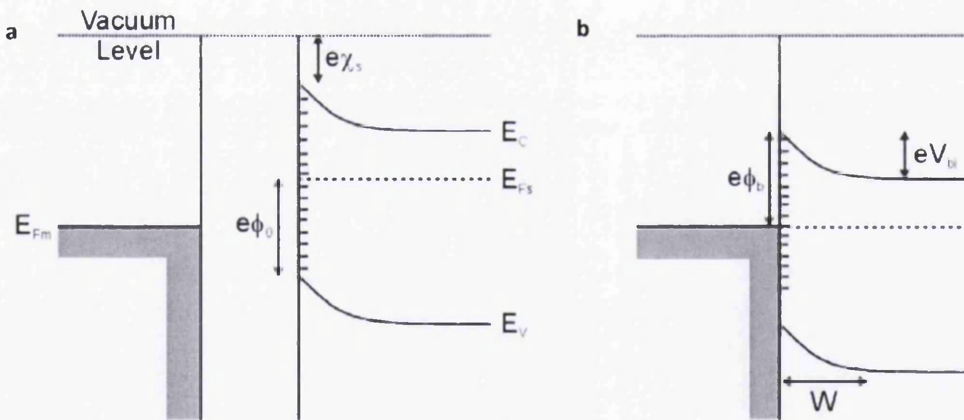

Figure 13. The diagram **a)** depicts the free semiconductor surface with surface states filled up to ϕ_0 that induces a readjustment of charge and surface band bending. **b)** the barrier height ϕ_b and built in voltage V_{bi} can be determined before an interface is formed with the metal although further adjustment of charge due to interface states can affect this.

2.3.2 Depletion Width

The potential barrier induces a region in the semiconductor depleted of n-type charge carriers. In conventional diodes the width of the barrier is expressed as

$$W = \sqrt{\frac{2\varepsilon_{sr}\varepsilon_0(V_{bi} - V)}{qN_d}}$$

Where ε_{sr} is the relative permittivity of the semiconductor, ε_0 the permittivity of vacuum, V_{bi} is the built in voltage, q the charge of an electron and N_d the doping concentration. qV_{bi} is the energy between the conduction band minimum in the semiconductor bulk and the barrier maximum i.e. a measure of band bending at zero bias. The depletion width is normally discussed for a Schottky barrier in terms of the zero-bias width, used from here onwards unless stated as 'bias-dependent'.

2.3.3 Conduction mechanisms across a Schottky barrier

There are four mechanisms, described below, for charge carriers to traverse the barrier and must satisfy the total current density of electrons from semiconductor to metal

$$J = J_{sm} - J_{ms}$$

The barrier from the metal side is constant and the current density from metal to semiconductor J_{ms} is included as a thermally excited contribution to provide zero current at zero bias, although under forward bias the dominant electron flow is from semiconductor to metal.

Thermionic emission - electrons are thermally excited to an increased energy and they can surmount the barrier. The current density can be expressed by the saturation current and the current from applied forward bias

$$J = A^{**}T^2 \exp(-q\phi_b / kT)[\exp(qV / kT) - 1]$$

In reality the barrier height determined from experimental data must be considered an effective barrier height ϕ_e and thermionic emission requires a fitting parameter known as the ideality factor n. In such cases we have

$$J = A^{**}T^2 \exp(-q\phi_e / kT)\exp(qV / nkT)[1 - \exp(-qV / kT)]$$

Where T is the temperature, q is the electron charge, k is the Boltzmann constant, A^{**} is the modified Richardson constant and n is the ideality factor which can be used for diodes exhibiting non-ideal thermionic emission i.e. $n>1$. Values of n deviating from unity can indicate a variety of reasons for non-uniform behaviour such as bias dependence of the

barrier height, image force lowering, barrier inhomogeneities, tunnelling and interfacial layers. The calculated barrier height must be considered as the 'effective barrier height' and not the true interface potential difference. The divergence from the ideal is especially prominent in the case of spatially confined contacts or with interfacial variations such as defects. The modified Richardson constant takes into consideration the effective mass of electrons in the semiconductor. A^{**} can be calculated however it is not always a well-defined quantity and maybe more appropriately measured from J-V characteristics over a range of temperatures.

Tunnelling – electrons in the conduction band at energy levels below the top of the barrier quantum-mechanically tunnel when the depletion width is small. Figure 14 depicts the energies at which the two-categories of tunnelling occur, other influences such as indirect tunnelling and scattering are not considered. Tunnelling that occurs at raised temperatures so that most electrons tunnel at energies above the Fermi level, (E_m) above the conduction band minimum, is known as Thermionic Field Emission (TFE). Padovani and Stratton[96] derived expressions for TFE combined with the normalisation of Crowell and Rideout[97], beyond that of simple barrier lowering, for the forward bias the general tunnelling term is of the form

$$J = J_s \exp\left(\frac{V}{E_0}\right)\left[1 - \exp\left(-\frac{qV}{kT}\right)\right]$$

where $E_0 = E_{00}\coth\left(\frac{qE_{00}}{kT}\right)$ and the saturation current for the particular tunnelling mechanism, in this case TFE is

$$J_s = \frac{A^{**}Tq\exp(q\xi/kT)\{\pi E_{00}(\phi_b - V + \xi)\}^{1/2}}{k\cosh(qE_{00}/kT)}\exp\left(-\frac{(\phi_b + \xi)}{E_0}\right)$$

The important terms in the expression are discussed in more detail in Chapter 7 with the data analysis for clarity. However ξ is the semiconductor Fermi-level and the important tunnelling parameter $E_{00} = \frac{h}{4\pi}\left(\frac{N_d}{m^*\varepsilon_{ZnO}}\right)^{1/2}$ is dependent on the donor concentration N_d, m^* is the electron mass in the semiconductor and the permittivity of ZnO is ε_{ZnO}, the value E_{00} is

very important in the TFE term.

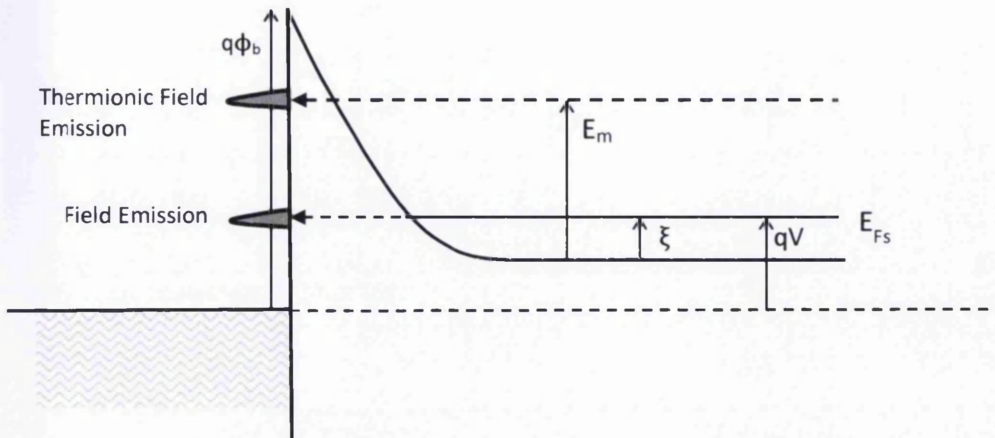

Figure 14. Energy band diagram of a forward biased Schottky barrier indicating the energies at which Thermionic Field Emission and Field Emission occur through the barrier.

Field Emission – this process takes place generally when the depletion region is very narrow and is important for degenerate semiconductors where the Fermi level E_{Fs} is located in the conduction band (ξ is positive as in Figure 14). Padovani and Stratton[96] derived expressions with relatively simple terms which are readily applied. In forward bias the field emission generally applies at low temperatures[96], although the form can still be applied with highly doped semiconductors[68] or large electric fields both of which induce very narrow depletion regions. The expression by Padovani and Stratton used in the general tunnelling form is

$$J = J_s \exp\left(\frac{V}{E_{00}}\right)\left[1-\exp\left(-\frac{qV}{kT}\right)\right]$$

Where

$$J_s = \frac{2\pi q A^{**} T E_{00} \exp(-\phi_b / E_{00})}{k\left[\ln\{2\left(\frac{\phi_b - V}{\xi}\right)\right]\sin\left[\frac{\pi kT}{2qE_{00}}\ln\{2\left(\frac{\phi_b - V}{\xi}\right)\right]}$$

TFE and FE are both tunnelling terms and require the semiconductor Fermi level to be in the conduction band or very near to it. TFE applies at raised temperatures when the majority of the electrons in the conduction band (CB) are at energy levels above the band minimum. The terms for TFE and FE assume a Gaussian distribution of electrons centred either at the

Fermi-level, in the case of FE, or at a greater thermally excited energy (TFE). We can still assume a large quantity of electrons reside near the CBM under ambient conditions and are available for tunnelling by FE if the depletion region is very narrow.

E_{00} and the ratio qE_{00}/kT provide criteria for determining the tunnelling transport mechanism. E_{00} can be considered as the diffusion potential such that the transmission probability of an electron at the CB minimum at the depletion edge is exp(-1) (~37%). For $qE_{00}/kT \gg 1$ field emission dominates, when $qE_{00}/kT \sim 1$ thermionic field emission is appropriate and E_0 is used as the tunnelling parameter and in the final case $qE_{00}/kT \ll 1$ thermionic emission characterises the transport mechanism.[55] A more specific criteria is $qE_{00}/kT > 2.7$ for an Ohmic tunnelling contact, then $E_0 \approx E_{00}$ (only 1% error) and J_s for TFE begins to break down as $\cosh(qE_{00}/kT)$ becomes large and we must turn to field emission.[98]

Recombination in the space charge region - recombination in the depletion region originates from mid-bandgap energy levels and can increase with surface defect states. The term is described as

$$J_r = J_{r0}\{\exp(qV/2kT) - 1\}$$

where $J_{r0} = qn_iW/2\tau_r$. A large depletion region, a large intrinsic carrier concentration n_i, or a small recombination lifetime τ all increase recombination. Recombination is most important with large barriers at low temperatures and at low bias. Recombination in the neutral region generally occurs as hole injection in semiconductors with small bandgaps and is not considered further here.

2.3.4 Important Notes for Au contacts on ZnO

The contacts experimentally investigated in this work were Au catalyst particles at the tip of NWs and compared to evaporated Au on catalyst-free NWs. A Schottky barrier is usually formed between Au and ZnO with planar contacts typically with barrier heights of 0.6-0.7eV and ideality factors 1.05-1.6.[5] High quality contacts are highly dependent on the preparation methods which usually involve fabrication in vacuum. The main reasons for divergence of interface behaviour from 'ideal' thermionic emission are due to interfacial layers, tunnelling, surface states, contaminants and diffusion of the metal into the semiconductor. Contacts formed on the Oxygen terminated $(000\bar{1})$ can also exhibit lower barrier heights because the

surface polarity and surface states are different to Zn terminated (0001). High donor density levels can also have a major impact on tunnelling increasing transmission though the barrier by compressing the depletion region. The carrier concentration of ZnO NWs varies between 10^{17} cm^{-3} and 10^{18} cm^{-3} within an array sample and across growth methods.[18]

Chapter 3

3 Literature Review

3.1 Zinc Oxide (ZnO)

ZnO has been of interest mostly due to the n-type electrical properties and its strong piezoelectric response. It is a semiconductor compound which is most commonly grown in the wurtzite structure. Industrial applications take advantage particularly of the direct bandgap in the near ultraviolet and the piezoelectric properties.[5] The greatest use of ZnO is in particle form as a material additive in paints, ointments, sealants, plastics, cements and ceramics which take advantage of the high refractive index, high thermal conductivity and broad UV protection. More recently, ZnO NWs have received much attention in the field of Nanotechnology.

3.2 NW growth methods

ZnO NWs are single crystals and can be grown by various methods which all require precise control of the reactants and the growth conditions. Crystal growth can among others occur by reactionary methods such as Metal Organic Vapour Phase Epitaxy (MOVPE) or physical deposition methods such as Molecular Beam Epitaxy (MBE). The most common methods for NW growth are vapour phase methods[24,37,43] and solution based hydrothermal growth[99]. Although template assisted growth is possible this is generally not useful for upright arrays of NWs. The objective here and for many devices is to grow NWs orthogonal to a surface.[29,36,53,100] Vapour phase and hydrothermal techniques can provide relatively simple methods to achieve this. The process of growth however is very complicated at an atomic level and control of the refined growth environment is necessary. Even then in lab based facilities crystal growth is rarely precise.

Planar substrates allow the use of standard semiconductor processing techniques to create heterostructure formations and also incorporate NWs from lab-based methods. The combination of techniques allows fabrication of electrical and actuator devices taking advantage of the nano-enhanced properties, such as large surface area[101] or increased elasticity[102]. Growing single crystal NWs in the desired morphology to fabricate devices

requires a suitable crystallographic relationship with the substrate. In this sense a substrate of the same crystal structure and orientation as the desired NW is preferable. ZnO NWs of wurtzite structure grow along [0001] and to aid this process hexagonal substrates such as Al_2O_3 or GaN are commonly used. Sapphire cut on the a-plane provides an epitaxial relationship of ZnO(0001) ‖ $(11\bar{2}0)Al_2O_3$ and with c-plane GaN ZnO(0001)‖(0001)GaN which are ideal for the alignment of the growing crystal.

3.3 Vapour phase Growth methods

Vapour phase furnace growth is a common method due to the relative simplicity in experimental setup. The Chemical Vapour deposition (CVD) apparatus most commonly used is relatively simple compared to those of similar methods such as MOVPE which relies on chemical reactions at the substrate surface. A common method with CVD growth uses a tube furnace loaded with a ceramic tube through which controlled gases flow at a specific pressure. The ZnO NW precursors are a solid source of ZnO and Carbon catalyst. High furnace temperatures >900°C and the reaction of the carbon catalyst cause dissociation of the Zn and O, the Zn evaporates and the gas flow carries the vapour to the cooler region where it is deposited on the sample. However pinpointing the relationship of parameters on growth quality is not always obvious and infrequently exact. To appreciate this we need to look at NWs as crystal growth, where atom by atom the structure is developed and any slight deviation in conditions greatly affects this balance. Growth investigated here occurs by Vapour phase transport initiated via a catalytic or nucleation process usually known respectively as the Vapour liquid solid (VLS) or Vapour-solid (VS) process. Both methods can produce high quality nanostructures, in this case NWs, and are mainly distinguished by the local growth temperature and the use of a metal catalyst.

3.3.1 Vapour-Liquid-Solid Growth

The Vapour Liquid Solid (VLS) mechanism of NW growth was first proposed by Wagner and Ellis in 1964[14] who produced silicon "whiskers" of 100nm diameter and this technique still commands full attention at the forefront of science and nanotechnology[24,43,103–105]. The VLS method (Figure 15) is now widely used in the growth of one dimensional nanostructures mainly using inorganic semi-conductor materials such as Si, Ge, GaN, GaAs, ZnS, CdSe and oxides like ZnO and MgO.[106] Among these GaN, ZnO, GaAs and CdSe have received much

attention due to their direct band gaps which are attractive for optical and optoelectronic applications.

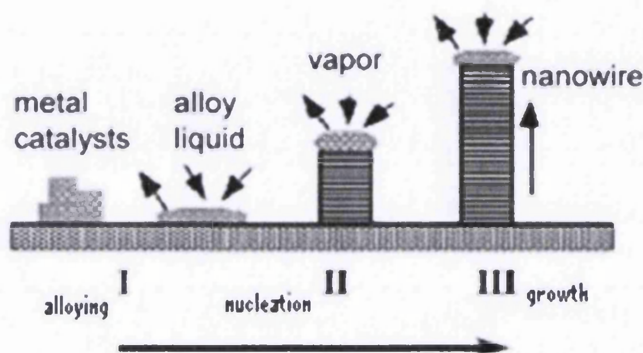

Figure 15. Diagram showing the basic steps in nanowire growth by the VLS mechanism. The metal catalyst acts as a preferential site to capture vapour from the growth atmosphere which alloys with the metal catalyst. The alloy particle is liquid because the eutectic temperature can be significantly lower than the pure metal melting point. Within the alloy particle the concentration of the source element builds until it becomes saturated and precipitation occurs at the substrate interface which initiates crystal nucleation. Further supply of the source vapour continues this process and a crystal grows. Reproduced[253].

Relating the initial description given by Wagner and Ellis the metal catalyst on the substrate melts at high temperatures forming nano-droplets or clusters.[22] These droplets are governed by the thermodynamic limit on radius of metal liquid clusters at high temperature[37] which is defined as

$$R_{min} = \frac{2\sigma_{LV} V_L}{RT \ln s}$$

Where σ_{LV} is the liquid-vapour surface free energy, V_L is the molar volume of liquid, and s is the vapour phase supersaturation.

In particular for ZnO NWs, Zn and CO/CO_2 vapour is produced by carbothermal reduction of the ZnO source and carried in the gas flow, in this case Ar/O_2, to the reaction site.[24] The carbothermal reduction of ZnO uses graphite and high temperatures to initiate the reaction of the oxygen which allows evaporation of Zn. This reaction occurs at a much lower temperature (~900°C) than the ZnO decomposition temperature. The Vapour-Liquid-Solid transition occurs when the vapours condense on the catalyst surface and form an alloy

droplet, an alloy of the metal catalyst and source material. The catalyst alloy liquid eventually becomes supersaturated with the elemental source species which forms on the liquid surface and precipitates out, see Figure 16a.[107]

NW growth initially occurs at the solid substrate – liquid interface where ZnO precipitates following oxidation[107] and crystal nucleation. The continuation of this process causes the alloy droplet to escape the surface on top of the growing NW. The growth may continue as long as the tip continues to catalyse growth and the reactants are available.[35] After the growth and cooling the NW typically has a solid alloy particle at the tip. This particle on the wire tip was until recently used to identify the growth solely as the VLS process. The VLS method produces high quality single crystal NWs of very uniform diameter which can be as thin as 10nm and with length >1μm.[106]

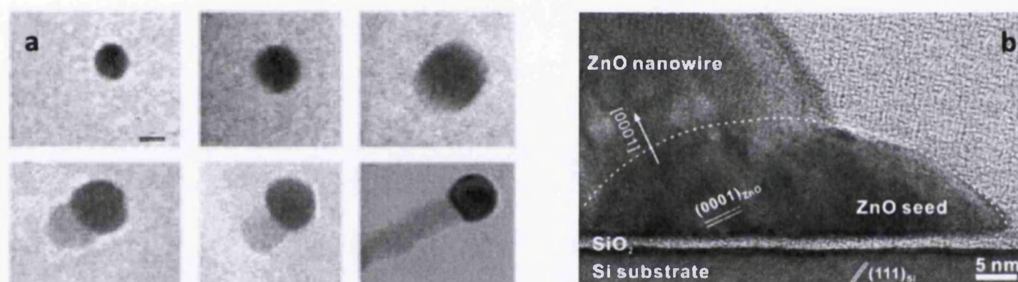

Figure 16. a) In-situ TEM images of the Vapour Liquid Solid (VLS) nucleation process and subsequent growth of a Ge NW. Initially the Au particle is solid, then as the temperature increases the particle alloys with Ge and melts, further condensation of Ge allows the NW to grow. Scale bar 20nm, reproduced[253]. **b)** TEM image of a ZnO nanowire growing from a ZnO seed particle by the Vapour Solid mechanism. The image shows the tilted angle of the growth due to the mismatch with the Si substrate, reproduced[120].

3.3.2 Catalyst Free growth

ZnO NW growth without a specific catalyst occurs at temperatures much lower than catalysed growth, typically the growth sample is located in the temperature range ~600°C.[36,108–110] The growth is induced by a process of crystal nucleation on the intended substrate via a vapour solid mechanism. This can be encouraged by providing preferential nucleation points on the substrate, achieved either by surface roughness[111] or by a crystal seed layer[36,83,112]. A seed layer is made up of relatively small crystallites of the same composition as the desired growth, Figure 16b. The all-important functionality of the layer is to provide the crystallographic basis for subsequent growth and act as a buffer to any

substrate mismatch[113–115]. This requires the seed layer to be crystallographically orientated in such a way to produce the desired growth crystal orientation, morphology and alignment.[116] Seed layers tend to be composed of small crystallites <30nm diameter and generally produce a rough film on the substrate.[83] Therefore it is likely nucleation is initiated with both elements of roughness assisted- and seeded- growth. High quality p-type NW arrays for device fabrication were grown by Lu et al including a phosphor source in the growth precursors with similar solution based drop-cast seeding method to the one used here.[36]

Catalysed and vapour solid modes compete during catalyst-assisted vapour phase growth of NWs.[117,118] The balance is governed by the temperature and Zn supersaturation in the growth atmosphere.[119] VS growth usually dominates at higher vapour saturation which requires higher temperatures to evaporate more Zn than is necessary for catalysed growth. Metal catalysts are often undesirable and so seeded or 'self- catalysed' growth models propose growth nucleation can occur due to the condensation of Zn and Zn suboxides.[119–121] Zinc vapours may at lower temperatures condense on the surface and quickly oxidise leading to a segregation of ZnO and a self-catalysed growth process.[121,122]

High Zn vapour saturation and high oxygen concentrations aid the evaporation and subsequent oxidation of Zn vapour without the catalytic effect of a metal tip. However catalysed growth is complicated by the dual processes of catalysed and VS competing at the same time. Although VS NWs can be distinguished by the lack of growth tips.[119]

Using ZnO powder as the source requires high source temperatures to reach the saturation required for metal catalysed growth >900°C. A much higher source temperature >1050°C is required for VS growth with low substrate temperatures 500-600°C.[36,121] High quality NWs are produced by both growth modes, however growing without a catalyst removes the additional metal which may contaminate or interfere with the NW array properties. Even when using a catalyst the VS mode still contributes particularly to the NW diameter and the growth that forms as a base layer.[58,117,119]

3.3.3 Defects in NW growth

Mismatch with the substrate can induce strain in the growing crystal leading to misalignment and defects.[22] The relationship with the substrate greatly affects the crystal

quality in the layers immediately adjacent[123] which can lead to defects such as stacking faults and dislocations within the base layer growth that is present with most NW arrays.[124] Even the small mismatch of ZnO with GaN can lead to in-plane compressive strain which affects the epitaxial growth of the ZnO layers and NWs.[123,124] Crystal Defects within the NWs may greatly impact the properties, possibly dominating over the desired qualities. However, the defects formed in the base layer are not thought to transmit to the NWs which are generally observed to be defect free[37,123], although with crystal growth this cannot be taken for granted and we investigate this with cross-sectional TEM in Chapter 6.

3.4 Problematic features of Catalysed NW growth

The interaction of the dissimilar catalyst metal and the semiconductor NW material is complex and leads to some undesirable features of the growth method, these are briefly discussed below and investigated in full by experimentation, in Chapter 5 and by microscopy analysis in Chapter 6.

3.4.1 Locating the Au particle

Catalysed growth depends on the relationship between the Au particle that captures the source vapour and precipitating out ZnO in the form of a NW. There is not a simple relationship however between the particle and the NW size, with large variations occurring.[58,117,125] Large diameter NWs can be found with very small Au particles on the tip, and in many cases the Au particle can be found falling off the top facet or even on the NW side.[58] Au particles can be found on the NW stems, roots and on the base growth. The role these particles play in the growth and the relationship with NW nucleation is unclear. However Kodombaka et al used in-situ TEM growth of Si NWs grown by the VLS method to show the Au particle decreases in size as growth proceeds and the speed of growth is independent of NW diameter, eventually the Au droplet disappears due to diffusion processes.[126] Therefore it was necessary here to pinpoint the catalyst particle and the relationship with the NW before selecting electrical and microscopy analysis samples. Secondary Electron Microscopy (SEM) and Backscatter Electron (BSE) imaging provided the means to locate the Au particle (Chapter 5). This was especially important for electrical measurements which investigated the electrical relationship between the catalyst particle and the (0001) growth facet (Chapter 7).

3.4.2 Vapour-Liquid-Solid and Vapour-Solid-Solid growth

The validity of the VLS model[14] has been debated recently for many semiconductor-metal growth schemes[127] because the basis of the VLS mechanism revolves around eutectic melting of the system formed by alloying of the metal and semiconductor.[127] Au-Si is the model case where the alloying in the catalyst particle can drive the melting temperature down to temperatures as low as 363°C. Increasing the temperature and locally increasing the source vapour concentration (i.e. from the gas phase) creates an imbalance in concentration gradients and the alloy becomes unstable and precipitates Si.[127]

The VLS mechanism has been used to describe the growth of many nanostructures. However, recent evidence of growth of nano-materials including Ge[128], ZnO[125], GaN[129], ZnSe[130] and others have been shown to occur with solid catalyst particles well below the eutectic melting points. In particular for ZnO NWs there is thought to be no alloying of Zn and the Au particle and as such no eutectic melting.[125] For pure Au the melting of a 33nm nanoparticle can only occur when the temperature reaches 1031°C (bulk 1064°C).[125,131] This is far higher than the local growth temperature during ZnO NW growth which is usually 800-900°C for catalysed growth. The growth mode has therefore in some instances been labelled Vapour-Solid-Solid (VSS). In this process the catalyst particle is solid throughout and no alloying or bulk melting occurs. However as high temperatures near the melting point of the metal are involved there may be a surface liquid layer on the particle which can result in surface diffusion of Zn and the growth of a crystal.[125,132] For VSS growth to be possible an epitaxial relationship between the solid particle and growing crystal is vital.[58,103,125]

An important process for VSS growth is lateral propagation of ledges at the catalyst-NW interface, this phenomena has been observed in real-time TEM of growing Si NWs.[103] The steps nucleate at the NW edge and are driven by the diffusion of the vapour species around the catalyst surface along the concentration gradient which is relieved at the NW interface. This process also occurs with VLS catalysis, albeit with longer periods between ledge nucleation which precedes very rapid propagation, a result of a large concentration build up in the liquid alloy droplet.[105] Catalyst particles provide excellent control over the growth however which was optimised by Wen et al to switch from VLS to VSS and grow a Ge interface at the tip of a Si NW with 'near atomic' abruptness, this overcomes the usual broad composition gradient when using catalytic growth to form NW heterostructures.[105]

The quality of the interface between ZnO NW and the Au particle has not been studied although a solid Au particle was revealed by Kirkham et al.[125] Atomic scale analysis is conducted here to reveal the crystallographic relationship of the ZnO NW and the catalyst particle and whether any interfacial layers, alloying or metal diffusion occurs. This would greatly affect the electrical properties of the interface and so here the role of the Au catalyst and the interface with the ZnO NW are examined in detail by Transmission Electron Microscopy (TEM) and high resolution Scanning Transmission Electron Microscopy (STEM) in Chapter 6.

3.4.3 Au catalyst incorporation in NWs

High temperatures provide kinetic energy to atoms increasing the atomic vibrations which can cause diffusion of one material into the other at interfaces of dissimilar materials. For Silicon NW growth this has been investigated extensively and revealed a high solubility of Au within Si NWs.[15,105,133,134] These stray atoms, within structures that might only be 50 atoms across, may drastically alter the properties by creating deep level gap states which trap charge carriers.[135] Impurities have also been found in Au catalysed GaAs[136] and InAs[137] NWs. The Au atoms are most frequently found at defect sites within the bulk of the Si NWs[133] but can also decorate the surface[134].

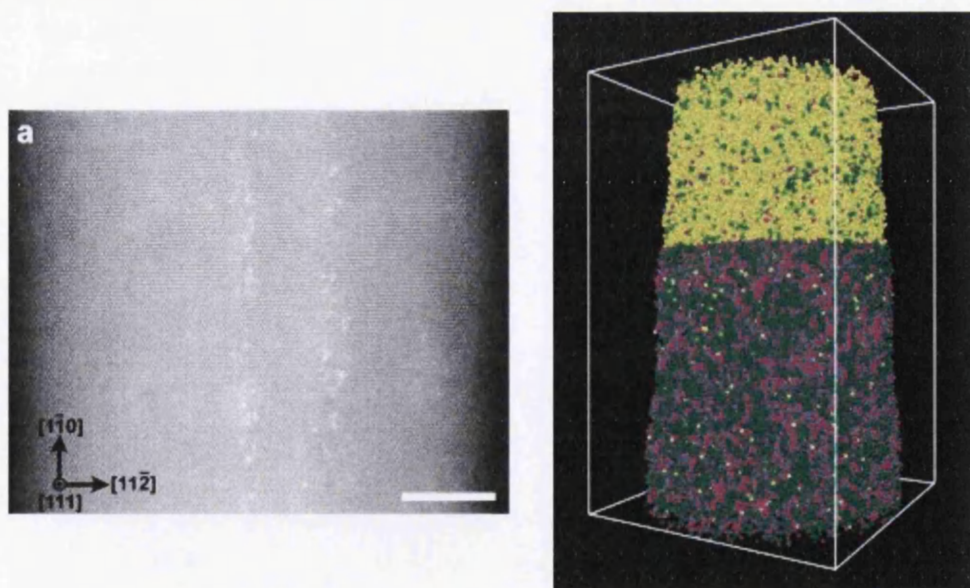

Figure 17. **a)** Aberration corrected atomic resolution HAADF image of Au atoms (bright dots in two vertical lines) located at planar defects within a Si NW (background horizontal atomic rows), scale bar 5nm, reproduced[133]. **b)** Local Electrode Atom probe tomography of an InAs NW with a Au catalyst particle on top, the image shows the interface is abrupt but there is diffusion of Au (yellow) into the NW bulk, reproduced[137].

Two very modern techniques have been pioneered recently which allow the detection of single impurity atoms within a host structure. The advent of spherical-aberration corrected Scanning Transmission Electron Microscopy (STEM) allows the atomic resolution of High Angle Dark Field Imaging (HAADF).[138–140] Large Z-number atoms strongly scatter the incoming electron beam creating more imaging intensity, this technique is ideal for imaging single Au atoms within lower Z-number host materials (Figure 17a) and a number of 'tricks' can allow detection in more demanding materials such as GaAs[136]. Atom probe tomography uses the extremely sensitive nature of mass spectrometry to detect single atoms evaporated from a NW (Figure 17b). The structure of the NW is digitally reconstructed atom by atom with time of flight calculations[141] and the atomic composition of a NW is achieved.[15,137]

These studies highlight the complex interplay between the catalyst particle and NW interface. The near interface behaviour and catalyst diffusion dynamics in ZnO NWs has not been investigated so it was necessary here to further our understanding of the structure and allow accurate electrical characterisation. The catalyst behaviour was studied by aberration corrected STEM (Chapter 6) to reveal the true structure and quality of the NWs and the interface formed with the catalyst particle.

3.5 Electrical properties of ZnO

The excitement that has surrounded ZnO for electronic devices is largely due to its large exciton binding energy of 60meV which has been applied to efficient room temperature emitters and very low threshold lasing applications. ZnO is a semiconductor with single crystals showing conductivities almost always greater than $10^{-3}(\Omega cm)^{-1}$ and has a wide direct band gap of 3.3-3.4eV at room temperature.[5,142] Due to the large exciton binding energy and relatively easy crystal growth ZnO has many optoelectronic and electronic applications. Although the difficulty in obtaining high quality p-type conduction has held back many applications but recent advances are being made.

Undoped ZnO is an intrinsic n-type semiconductor with electron densities as high as 10^{21}cm^{-3}.[5] The semiconductor doping is thought to be due to the presence of intrinsic or extrinsic defects usually attributed to native defects such as the Zn-on-O antisite, the Zn interstitial and the O vacancy.[143] Alternatively, First principle studies based on density

function calculations suggest hydrogen occurs in ZnO only in the positive charge state and is responsible for the n-type conduction.[144] Hydrogen is considered the most likely impurity due to its universal presence in and around growth processes and its high mobility in ZnO allows easy diffusion.[5,145] The origin of the n-type conductivity is still debated but the necessity to divulge this information is apparent in the difference between commercially available undoped bulk ZnO with resistivity as high as $10^5\Omega cm$[41,146] and ZnO NWs often in the range of $0.019\text{-}0.15\Omega cm$[41,51].

P-type doping of ZnO NWs is required for many nanodevices. Synthesis of p-type ZnO has proved to be very difficult but high quality p-type NWs have recently been achieved.[42,147] P-type NWs doped with phosphorus were grown by Xiang et al on a-plane sapphire, although the p-type conductance was only stable for two months.[42]

More recently p-type NWs have been grown by Yuan et al via the VLS method and were doped with nitrogen from a N_2O source during growth.[147] Before p-type doping the n-type NWs had an FET device derived electron concentration of $6.1x10^{18}cm^{-3}$, mobility of 19.5 cm^2/Vs and resistivity of $8x10^{-3}$ Ωcm. When a small amount of nitrogen was introduced the electron concentration decreased to $8.9x10^{17}cm^{-3}$, mobility to 0.39 cm^2/Vs and resistivity $2.9\Omega cm$. Increased nitrogen concentration during growth resulted in p-type NWs with hole field effect mobility of 10.5 cm^2/Vs and a hole concentration of $1.2x10^{18}cm^{-3}$ and a resistivity of $0.08\Omega cm$. The p-type NWs remained p-type for five months and during this time the hole concentration increased by one order of magnitude due to adsorption of O atoms on the surface, exposure to vacuum removed this additional hole concentration.

3.5.1 Measuring NW bulk conduction properties

The problems of measuring the properties of nanostructures was made evident in a recent review of resistivity measurements on ZnO NWs that revealed a spread of 8 orders of magnitude 10^{-5} to 10^3 Ωcm across the literature, Figure 18.[50] The majority of the included measurements employed the four-probe technique and should have been free from contact resistance in the measured values, however the fabrication technique is the key to this spread.

Experiments using the lithographically patterned four-probe technique have shown 3 ZnO NWs to have a spread in resistivity of $0.019\text{-}0.15\Omega cm$.[41] The patterning techniques such as

e-beam lithography can suffer from unknown levels of carbon beam induced deposition and surface modification[148] from resist contamination and exposure to harsh solvents[93]. These effects can temper surface states and shell depletion, pacifying surface effects which may alter the measured bulk properties[17]. Other patterning techniques using FIB[149] also suffer from similar problems along with additional ion implantation and sample damage. The heavy ions typically Ga+ used for FIB patterning are a known n-type dopant of ZnO.[150] Recent attempts[51,92] which measure a total of 4 NWs using FIB patterned electrodes gave values of 0.022-0.046Ωcm which represent one four probe measurement on each NW.

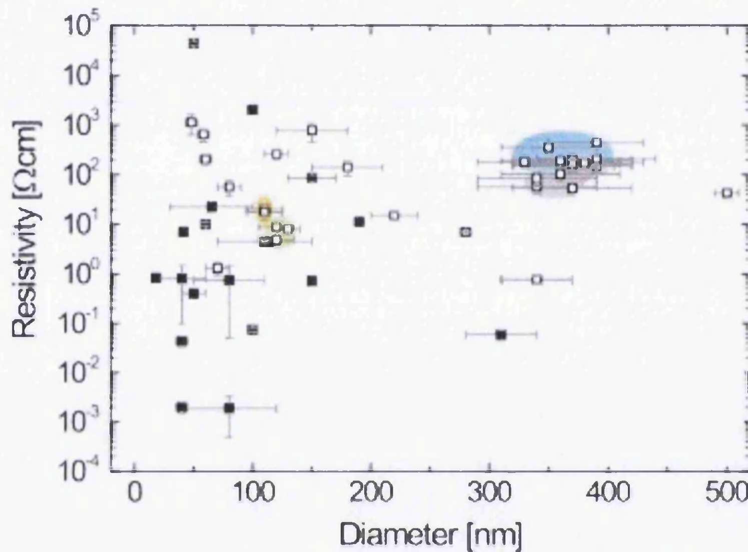

Figure 18. The spread in resistivity of ZnO NWs across the literature, Reproduced[50].The graph was produced by Schenkler et al to compare the black symbols that indicate measurements from a review of the literature and the white symbols indicate their own measurements of vapour phase NWs.

Hong et al attempted to characterise the electronic properties of vapour phase NWs grown with and without Au catalyst on different substrates by fabricating 327 FET devices.[18] The growth techniques which produced corrugated surface NWs exhibited strong emission in the visible range due to an increase in surface defect trap states. The n-type carrier concentration on substrates similar to those used here ranged from 7.68×10^{17} to $1.26 \times 10^{18} cm^{-3}$. The surface defects lead to a trapping of negative charge carriers which depletes the NW near the surface and reduces the effective conductive diameter of the NW. The extent of this effect depends on trap state density and initial doping concentration. Crucially the devices were coated with PMMA to remove the influence of water and air during measurements which may also have the effect of inducing or passivating surface states. The dramatic effect surface passivation can have on the measured NW properties

was shown by coating a ZnO NW FET device with polyimide which increased the mobility from 75 cm^2/Vs to over 1000 cm^2/Vs.[151] In these fabricated device configurations with patterned contacts the ZnO surface is inevitably changed to a state that is far from its native as-grown condition.

There are many studies which look at the importance the surface of NWs has on the electrical properties for example:

- Undoped Ge NWs are dominated by surface state hole accumulation[17].
- ZnO NWs are dominated by surface state induced depletion layers[18], which can be altered by exposure to different atmospheres such as dry or humid air[94]. Exposure to ethanol releases the adsorbed Oxygen and frees trapped charge carriers increasing the conductivity[93].
- Surface states of InAs NWs have a capacitive effect in FET devices and the intrinsic properties can only be extracted by charge neutralising the surface or passivating the charged states.[152] Eliminating surface states through surface passivation creates a dramatic recovery of band edge emission[153].

However the most complete study by Bjork et al revealed the balance between doping concentration, NW size and resistivity of Si NWs.[154] The effect observed was a sharp increase of NW resistivity with decreasing NW diameter caused by deactivation of donor atoms due to the dielectric mismatch with the surroundings. This reduced carrier density to 50% in the thinnest 15nm diameter NWs, see Figure 19. The interface states on the surface and trapped charge carriers in the native oxide reduce the conductive core to a diameter less than the physical size. The size of the conductive core is dependent on doping concentration which dictates the extent of surface depletion and the effect on resistivity. A contributing effect is the dielectric mismatch of the NW with the surrounding air which increases the donor ionisation energy of the phosphorus impurities. This effect was displayed by coating the NWs with a dielectric material (Al_2O_3) that reduced the dielectric mismatch and the charge trapping effect; this was shown not to be a result of surface defect passivation as the trap density is governed by the core-native oxide interface. There is little spread in the measured resistivity of each doping density other than the increase with decreasing diameter. The extent of the surface depletion has well-defined behaviour with

the doping concentration which indicates similar trap densities for each NW. The NWs were measured by the four-point technique with electron-beam lithographically patterned contacts, contamination levels and the effect they may have on the Si NWs are unknown however the oxide layer may have buffered the NWs from this effect. The spread in NW resistivity for the 20nm diameter NWs was at least a factor of 30 across the doping range shown. The increase in resistivity isn't apparent above 30nm diameter which is partially an effect of high doping levels. The study however relies on calculations to estimate the NW doping concentration from the resistivity of the NWs greater than 30nm in diameter and no doping variations within a growth experiment is considered. The NWs grown by CVD were n-type doped with different proportions of gas precursor. Any variation in growth experiments may result in NWs of different doping densities from the same growth batch although this is ignored.

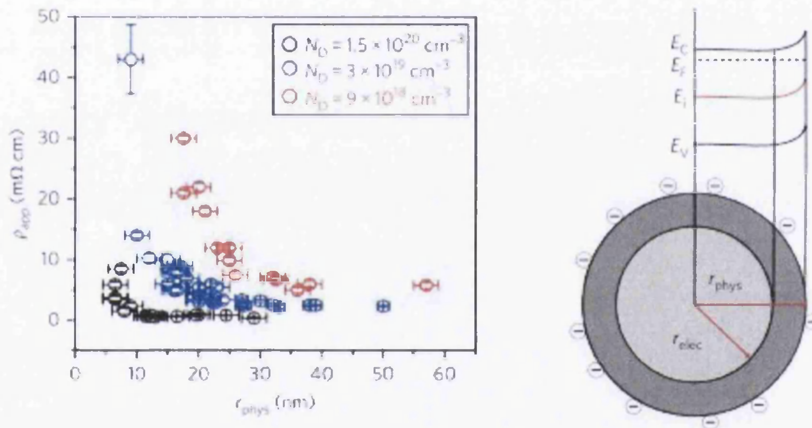

Figure 19. The resistivity of Si NWs increases with decreasing diameter; the onset of the increase is more apparent in NWs of lower doping concentrations as the surface depletion consumes more of the NW. The interface and surface trap states bind charge carriers and deplete the NW near the surface; this induces band bending and a reduction of the conductive core to a size less than the physical diameter. Reproduced[154].

We show here the resistivity of ZnO NWs is a property determined by the extent of surface depletion and varies independently of controlled doping and growth method. This is possible with the use of the UHV nanoprobe to complete a comprehensive set of four-probe measurements with multiple measurements on each wire that are completely free from contact fabrication processing. The results are described in Chapter 7.

3.5.2 Nanoprobe measurement of NWs

Electrical measurements on nanostructures such as NWs[41], Nanotubes and Tetrapods[155] are extremely challenging due to their size and the problem of forming reliable electrical contacts. One method is to form electrical contacts using patterning lithography

techniques[51,92,156] and metals deposition. There are many examples of these techniques providing good electrical measurements of all morphologies and materials. However the technique itself introduces contamination and subjects the structure to multiple processing steps and exposure to harsh solvents. The surface dominated properties of the structures can be greatly altered by surface modification or passivation and possibly alter the resisitivity[17]. Patterned contacts on single structures are limited to the two-dimensional horizontal configuration. Other techniques such as C-AFM[157] and nano-manipultors[158] can provide electrical measurements but are essentially limited by the number of contacts.

A modern technique combines the precise fine piezo control of STM with the clean environment of UHV and the positional control of four independent probe tips control aided by in-situ SEM imaging. The Nanoprobe is a multi-probe STM technique which is essentially an STM with four independent probe tips and an in-situ SEM for real-time imaging. This allows four probe electrical measurements on structures as small as 30-40nm and even in a 3-D configuration, for example free standing NWs. The only reported measurement using a nanoprobe on NWs revealed a resistivity of 0.25Ωcm which represents a single four-probe measurement of a ZnO NW.[52] The nanoprobe is used extensively in this thesis and the results are described in Chapter 7 that details the complete set of four-probe measurements of 40 ZnO NWs and further two-probe contact measurements of free-standing NWs.

3.6 Metal-semiconductor Contacts

Metal-semiconductor contacts are highly important in all semiconductor devices. This has led to intense theoretical and experimental research since before 1900. Although some of the theory, such as metal work function determining the Schottky barrier height, still does not fit experiment exactly the thermionic emission theory is well established and highly applicable to many planar contact systems. It wasn't until the work of Schottky[159] and independently Mott[160] that any headway was made with the theoretical analysis of experimental rectifying contacts. The models of drift and diffusion across the barrier were challenged by Bethe[161] in 1942 with the theory of thermionic emission (TE) of electrons into the metal. However, Schottky made the assumption that a space charge region of ionised impurities at the interface between metal and semiconductor creates the potential energy barrier. This still conforms to observations to this day and so they became known as Schottky barriers. They are typically represented by an energy band diagram which takes a

parabolic shape and the main characteristic is the electric current has an 'easy' direction when a negative bias is applied to the semiconductor. This raises the Fermi level with respect to the metal and electrons experience a much smaller barrier which is expressed by an exponential rise in current as the applied bias increases.

When TE does not provide an exact fit small deviations can be accommodated by an ideality factor which alters the exponential shape slowing the current increase with bias. Along with the Schottky barrier height the ideality factor is used to express the nature and quality of contacts, values close to one are achievable for vacuum formed contacts on clean surfaces. Deviation from TE can be due to a bias dependence or variation of the barrier height, and recombination of electrons and holes in the depletion region due to thermal generation of electron-hole pairs and defect states in the bandgap. Typical problems are barrier inhomogeneities, edge effects, interfacial defects and interfacial layers such as those formed by oxides. These oxide layers can even form in UHV conditions, the extent of this is difficult to predict, and even more so the effect on the final contact formed. Compositional characterisation of the deposited contact interface can be difficult to achieve and relate to the electrical characteristics. Regular symptoms of deviation from TE in I-V characteristics are reverse bias leakage, non-exponential forward bias, large zero-bias differential conductance and reverse bias breakdown. The main transport phenomena that can be attributed to these features is tunnelling where electrons quantum mechanically tunnel through 'thin' regions of the barrier. The curvature of the bands in the depletion region increases according to Poisson's equation in relation to carrier doping. At electron doping levels in n-type semiconductors greater than $\sim 5 \times 10^{17} cm^{-3}$ the barrier near the top becomes thin enough for tunnelling to occur.[55] The emission of electrons into the metal can occur at energies much lower than the barrier height when the barrier is thin which makes the contact more conductive.

The increased band bending that leads to tunnelling can be explained by increased semiconductor doping, high electric fields or low barrier heights and is usually theoretically described as Thermionic Field Emission (TFE) or Field Emission (FE). The accepted expressions for these terms which are still used today were derived by Padovani and Stratton in the seminal paper "Field and Thermionic-Field Emission in Schottky barriers" (1966)[96]. Field-emission is described at low temperatures where the overriding condition is

the Fermi-level of the semiconductor must reside above the conduction band minimum (CBM). Tunnelling at the Fermi energy level is the main contribution to current i.e. no thermally excited electrons contribute. For the Fermi-level to reside above the CBM doping must be very high, and the semiconductor is then known as degenerate, typically of concentration >10^{19}cm^{-3} for Silicon, although it is less for materials with a lower effective electron mass.[55] Tunnelling near the CBM can occur if the barrier is extremely narrow. At higher temperatures which include thermally excited electrons tunnelling occurs at energy levels greater than the CBM and Fermi level, then tunnelling is known as thermionic field emission. TFE describes tunnelling at energy levels above the CBM and below the barrier height up to temperatures where TE dominates and electrons easily surmount the top of the barrier. The probability of tunnelling depends on the potential barrier formed and for large barrier heights the barrier must be very thin. This concept is used to form Ohmic contacts using a thin degenerately doped layer of the semiconductor at the interface which distorts the barrier and allows tunnelling of electrons from the semiconductor 'bulk' where the Fermi level maybe below the CBM.[162] Tunnelling can then occur with moderate 'bulk' doping and at moderate temperatures. In non-degenerately doped semiconductors not employing highly doped surface layers the Fermi level is below the CBM. Tunnelling is then possible at the next available energy states which occur at the CBM, with very thin barriers the mechanism then is both FE and TFE but not FE alone in the strict sense.[162] The extreme band bending necessary to allow this combination of FE and TFE can also occur due to high electric fields.

These theories are applicable to infinite planar contacts, and so the potential barrier is considered uniform and constant throughout. In reality most large contacts suffer from barrier inhomogeneities which have been described by Tung[163,164] as patches of low Schottky barrier height where the interface structure may vary and create saddle points in the potential energy field. This altered field is considered to be the culprit of leakage currents and even singular patches can lead to large deviations of ideality factor.

However, spatially confined contacts, which is the case for the majority of semiconductor devices such as transistors, experience effects at the contact edge which crowd the field lines, this is known as edge effect.[165] The semiconductor experiences a larger electric field density in these edge regions which can be expressed by a reduction in barrier height[63] or by

a compression of the barrier width[55]. These effects are traditionally counteracted by using a guard ring such as a p-type layer under the edge of the metal contact which eliminates the high field and puts a reverse bias p-n junction in parallel with the Schottky barrier.[55,163] Another method uses surface preparation to control surface charge, this can provide near ideal forward voltage characteristics and much greater reverse breakdown which highlights the influence of the surface at the contact edge.[165,166] However the edge effects can be accentuated in the case of surface accumulation which increases the field of the local depletion region, the accumulation of surface charge in an n-type semiconductor can be the result of positive surface charges.[165]

Small contacts expose the semiconductor surface around the contact edge which may influence the I-V characteristics through surface leakage via surface states. The dangling bonds of the free semiconductor surface may contribute as an Ohmic like conduction path experimentally observed by Dickie[167] when exposing the silicon surface to benzene and by Dupont-Ferrier[168] by exposing $ErSi_2$ contacts on clean Silicon to Oxygen during STS and I-V measurement. These effects become more crucial as the contacts are scaled down.

To examine these topics further we now look at experimental contacts to ZnO and then compare these to contacts to ZnO nanostructures before highlighting recent work which aims to uncover the secrets of nanocontacts to nanostructures.

3.6.1 Ohmic contacts on ZnO

An Ohmic contact is defined as having linear and symmetric I-V characteristics ideally with little parasitic resistance. Parasitic resistance or contact resistance is a major problem for electrical devices as this can lead to thermal stress and contact failure. Low contact resistance can be achieved with surface treatment to reduce the barrier height or increase the surface carrier concentration to allow increased tunnelling. Thermal annealing can induce surface roughness and structural degradation of the interface which is a possibility as high temperatures are impossible to avoid when growing NWs by vapour transport. This is investigated with electron microscopy in Chapter 6. However non-alloyed low resistance contacts on ZnO have not been extensively studied until recently for potential applications in nanodevices and solar applications.[5]

Al is common for Ohmic contacts which take advantage of the low barrier height of Al on ZnO and aided by Al acting as an n-type dopant. Non-alloyed Al and Al/Pt Ohmic contacts were formed on n-type ZnO with linear I-V characteristics and contact resistivity's of $8\times10^{-4}\Omega cm^2$ and $1.2\times10^{-5}\Omega cm^2$ respectively.[169] The Pt overlay on Al resulted in a dramatic decrease in resistivity because it prevents a surface oxide layer. Ti/Al[(170)] provided an Ohmic barrier on undoped ZnO with contact resistivity as low as $9\times10^{-7}\Omega cm^2$ when annealed at 300°C, while Ti/Au contacts[171] on Al doped ZnO ($2\times10^{18}cm^{-3}$) with contact resistance of $1.2\times10^{-5}\Omega cm^2$ showed thermal degradation at temperatures exceeding $300°C$. Similar behaviour was seen with In contacts[172] with contact resistance of $7\times10^{-1}\ \Omega cm^2$. Ohmic contacts[173] formed with Ru yielded a resistance of $2.1\times10^{-3}\Omega cm^2$ which improved to $3.2\times10^{-5}\Omega cm^2$ after annealing at $700°C$ for 1 minute with no degradation seen. One common result of alloying or growth of an interface is unintentional doping of the ZnO in the near interface regions which locally increases carrier concentrations and narrows the depletion region.

Al was used to form Ohmic contacts[174] with epitaxial ZnO film grown on sapphire. Another useful scheme for Ohmic contacts[175] to ZnO bulk was used when depositing single layers of Ti(250Å)/Au(1000Å). The specific resistivity of $3\times10^{-4}\Omega cm^2$ increased when the contacts were annealed at temperatures exceeding 350°C. Voids exposing the underlying ZnO were seen at temperatures of 600°C, the Ti and Au formed intermetallic compounds and removed oxygen from the ZnO surface as the temperature increased. Unusually the surface polarity (O or Zn terminated) had no influence on the contacts formed. Annealing of contacts highlights the effect of alloying, interfacial compounds and surface reconstruction on the contact properties; however this is difficult to assess on a nanometre scale. For planar contacts thin sections can be made using a focused ion beam for TEM cross sectional analysis to map interdiffusion of elements by EDX and examine the interface crystal structure, see Chapter 6 for an example of a NW array section. This option is not so applicable to small contacts which are difficult to isolate and section, we show in Chapter 6 that NWs provide the ideal test beds to examine the entire interface structure and composition.

3.6.2 Schottky Barriers on ZnO

Mead reported[176] in 1965 on various metals deposited by condensation on cleaved ZnO and measurements of potential barrier height showed the materials to behave as materials

without surface states. The measured barrier heights have a linear relationship with electronegativity, this is interpreted as an interface with no surface states within the band gap. Metals applicable for Ohmic contacts with low barrier heights are In, Al and Ti, Figure 20. Metals on ZnO which form large barrier heights are Au, Ag, Pt and Pd and provide suitable Schottky barriers. For ionic semiconductor materials, e.g. ZnO which have little overlap between adjacent atoms, surface states can occur just above the valence band and just below the conduction band.[177] When a metal is placed in intimate contact with the semiconductor the barrier height is very approximately proportional to the metal work

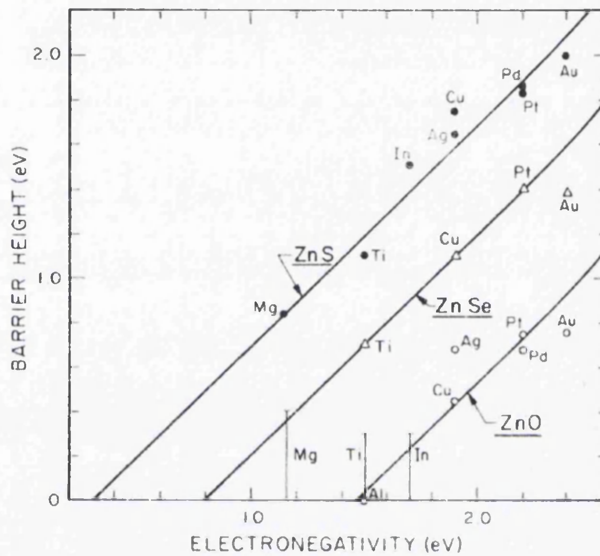

Figure 20. Barriers heights of various metals deposited on ZnS, ZnSe, and ZnO. Reproduced[176].

function, for example 5.3eV, 4.4eV, 5.7eV , 5.2eV and 4.5eV for Au, Ag, Pt, Pd and Cu respectively,[176] which is displayed in Figure 20. For more covalent materials the barrier height is nearly independent of the metal.[177] However Schottky barriers are not an exact science as shown by a selection of the literature.

One study which formed Schottky contacts[178] by depositing Au on the $(000\bar{1})$ plane of ZnO wafers were shown to improve significantly with plasma cleaning at 525°C of the ZnO surface prior to deposition. The plasma cleaning results in a highly ordered and stoichiometric surface. The improved Schottky barrier of height 0.6eV and ideality factor of 1.03 compared favourably to those prepared on the 'as received' wafer which exhibited large leakage currents and ideality factors greater than 2. A 40nm Ti layer was used as the back Ohmic contact on the (0001) surface.

Liang et al made Schottky barriers formed with Ag evaporated onto ZnO film which produced a barrier height estimated at 0.84eV.[174] Other results for Ag on ZnO (0001) have shown values of barrier heights in the region of 0.65-0.69eV and ideality factors of 1.3-1.8.[5] Ag deposited on the (0001) c-plane surface of hydrothermally grown single ZnO crystals was also shown to form Schottky contacts.[179] These interfaces typically showed signs of degradation after heating at temperatures as low as 100°C even in vacuum.

In comparison to the two previous examples Polyakov et al fabricated Au and Ag Schottky contacts formed on n-type ZnO (0001) that had SBH in the range of 0.65-0.7eV, ideality factors of 1.6-1.8 and saturation current densities for HCl cleaned surfaces of $10^{-5}Acm^{-2}$ and those cleaned by solvents of $8\times10^{-7}Acm^{-2}$.[180] All contacts degraded with temperatures as low as 92°C.

Most Schottky contact materials for ZnO show an ideality factor much greater than one, this is thought to be due to tunnelling, increased surface conductivity and influence of deep level recombination centres.[5] Common metals for Schottky formation are Au, with barriers typically of 0.6-0.71 eV and ideality factor between 1.05-1.8, and Pt with large barrier heights greater than 0.7eV.[5]

Although the interface of a ZnO NW and the Au catalyst is formed at high temperature a great advantage is that Au is inert and little reaction occurs with the O_2 atmosphere which is required for ZnO growth. The actual characteristics of the NW-Au particle interface and any potential alloying are not at present known, we detail this interface at the atomic level with high resolution electron microscopy in Chapter 6. The variability in contacts is largely due to the fabrication methods and the problems are summarised next.

3.7 Fabricating metal-semiconductor contacts

During fabrication, contacts are sometimes heat-treated to promote mechanical adhesion and alloying. Even at low temperatures ~ 200°C metallurgical changes take place and contact layers can inter-diffuse and the interface becomes blurred and far from an abrupt metal-semiconductor contact. Rectifying contacts exhibit changes in I/V characteristics and Ohmic contacts vary in contact resistance. However, it can be difficult to correlate changes in I/V behaviour with metallurgical changes.[55]

Barrier height can be controlled in a limited way by metal choice but this maybe constricted by other requirements such as thermal cycling or mechanical stress. The only precise way of producing a thin effective barrier is too produce a thin highly doped layer near the semiconductor surface by ion bombardment. For contact formation Semiconductor surfaces are required to be clean, the process usually requires vacuum and deposition of metals in UHV although a thin oxide can in some instances be accommodated. Exposure to air results in adsorption of atmospheric gases and reactions at the surface.[55] All of these issues are examined in the I-V characteristics of contacts to ZnO NWs in Chapter 7.

3.7.1 Contact layers to Nanowires

For device purposes contacts to entire NW arrays are required and these contacts are required to be Schottky or Ohmic depending on the application. Usually the substrate contact is required to be the large scale Ohmic back contact. However control over the top layer contact is more difficult due to the irregular formation of the NW forest. It was discussed above that introducing a highly doped n^+ region narrows the barrier width that allows increased current flow with reduced resistance. When doping is of a sufficient level, the barrier becomes almost transparent to electron tunnelling and the contact exhibits Ohmic behaviour. This concept was used by Ham et al to form an Ohmic contact with Al doped ZnO film deposited onto bare NW tips grown by MOCVD on a p^+ substrate to form a p^+-n junction for LED (Light Emitting Diode) emission purposes.[31] The device is shown in Figure 21.

The Al-doped ZnO film was characterised as being 400nm thick with a carrier concentration of $9.7\times10^{18}cm^{-3}$ and an electron mobility of $6.9cm^2/Vs$ and was deposited by radio frequency magnetron sputtering using a 3% Al (by weight) doped ZnO target. To complete the Ohmic contact Indium contacts were simply deposited on the Al doped ZnO film. It was shown that the Al doped film had the same hexagonal crystal structure as the ZnO NWs with both growing along the c-axis. The Al doped ZnO film was mostly deposited near the tips of the NWs which formed a good n-n^+ junctions with good interfacial contact and no crystal mismatch. The Fermi level of the Al doped film was close to the conduction band creating a thin barrier at the interface with the metal contacts. The perfect lattice match of the interfaces and low density of interfacial defects reduced the leakage current under reverse bias and increased carrier injection in forward bias compared to fabricated film based

structures. The NW inserted device improved electroluminescence emission and carrier injection.

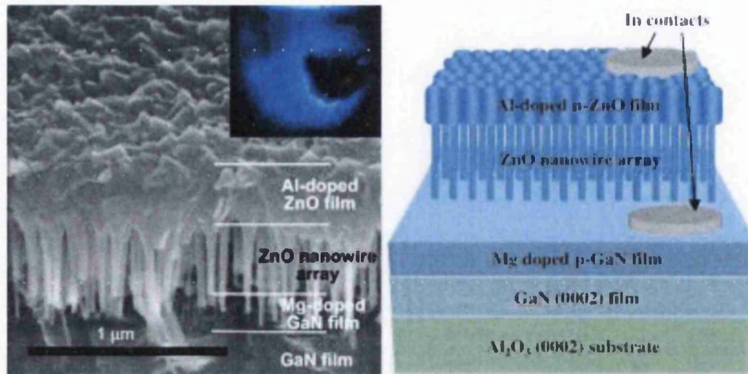

Figure 21. SEM image showing the n+ doped ZnO layer formed to the top of a NW array grown on a p-type substrate. The inset shows the blue light emission and the device is represented in the schematic diagram. Reproduced[31].

Top contact films are important for light emitting heterojunction devices such as lasers and LEDs. Taking advantage of new advances in p-type doping of ZnO NWs an electrically pumped waveguided laser device was fabricated using p-type NWs and a n-type substrate.[53] The film was grown by MBE and the NWs by CVD and the top contact was formed by sputtering ITO on to the NWs. However to prevent ITO deposition far down the NW sides and onto the n-type substrate PMMA was spin coated through the NWs before deposition. The diode device exhibited stable room temperature UV lasing.

Alternatively Yu et al used Pt to form a Schottky barrier on top of a dense Nanorod array.[181] The film of dense rods grown on SiC was used as a highly sensitive gas sensor in the reverse biased condition. Exposure to H_2 gas modulated the carrier density and the reverse bias I-V characteristics. The model presented was based on a charged 'hemisphere on a post' which considered the metal on the nanorod tips as a charged hemisphere removed a distance from the substrate. This enhanced the electric field which influenced the reverse bias I-V characteristics with longer, thinner nanorods inducing greater electric fields and the device exhibited lower breakdown voltages.

For these multilayer heterojunction based devices they require a base contact, usually the substrate. This limits the possible materials to those which are similar in crystalline structure to ZnO, conducive to NW growth and of good electrical properties. However, it is a distinct possibility for insulating materials such as sapphire to rely on the base growth of the NWs as

a conductive layer. This layer can form a large area back contact composed of ZnO and can be grown as film such as nanowalls[182] or deposited as a buffer layer[183].

However as discussed in section 3.3.3 the base layer can have many defects such as stacking faults and dislocations especially when there is a crystallographic mismatch with the substrate.[124] Also NWs grown with a catalyst may find many catalyst particles littered around the base growth which may cause substantial depletion of charge carriers.[58] To assess the possibility of using the base growth as a conductive layer we examine the structure and presence of Au catalyst in the base layer with cross-sectional electron microscopy in Chapter 6.

3.7.2 Fabricated contacts to individual Nanowires

There are not many published examples which investigate contacts to the top of vertical free standing NWs. Those that do comprise of conducting AFM (CAFM) measurements of bare and metal deposited ZnO NWs, C-AFM measurements of NWs for piezoelectric output and single probe measurements of Ge NWs grown by Au catalyst. There are many examples of flat lying NW devices with patterned contacts particularly as nanostructure n-channel FETs which are now briefly discussed.

Schottky barriers were created by Lao et al with Au contacts deposited on ZnO nanobelts and ideality factors of ~3 were achieved.[184] The Nanobelt device was shown to have a current of $0.5\mu A$ at $1.5V$, 100 times greater than seen with wet-synthesised nanorods on chrome and Au electrodes by Harnack et al[185]. The ideality factor of the nanorod devices again showed a large deviation of the ideality factor from unity. Asymmetric contact properties were cited to explain unusual characteristics attributable to an insulation layer between the electrode and semiconductor.

Niobium can form Ohmic contact to ZnO and was used by Cha et al for a single NW FET. Contacts were formed by sputtering and e-beam lithography lift-off of a 200nm Nb layer.[45] With Niobium having a work function of 4.3eV compared to the electron affinity of 4.35eV of ZnO Cha et al fabricated two single ZnO NW FETs with near Ohmic contacts. The gate electrodes used the metal scheme of Chrome/Au deposited across the NW. Using the four-point method the resistivity of the NWs was found to be ~7.5Ωcm. The devices with the n-type NW channel operating in enhancement mode showed field effect mobility of 928

cm^2/Vs. The NWs of diameter 60nm spanned the channel length ~1μm. Field effect mobility values were all a factor of six or greater than the best reported ZnO NW FETs.

Heo et al showed Pt Schottky diodes patterned to MBE grown NWs had low ideality factors of 1.1 and very low reverse currents of 1.5×10^{-10}A at -10V.[186] The Ohmic contacts on either end of the flat NW were fabricated by an e-beam lift-off scheme of Al/Pt/Au and annealed for 1min at 300°C. The Pt/Au gate contact patterned across the NW was of 1μm width which created a Schottky contact of area ~$10^6 nm^2$. Exposure to UV modulated the I-V to exhibit linear behaviour.

In the study of patterned Au as a Schottky barrier contact Das et al only achieved a SBH of 0.4eV at 300K which was confirmed by X-ray Photo-Spectroscopy (XPS) studies.[187] The low barrier height was attributed to image force lowering, tunnelling, surface defects states, barrier inhomogeneities, Fermi level pinning, trap states and edge leakage due to high electric field at the contact periphery. UV photoelectron spectroscopy measurements revealed the Fermi-level was 0.2eV below the conduction band and tunnelling which is insensitive to temperature variations must have been a major factor even when the temperature was elevated to 523K. Ionised interface states were considered to be the major cause of Fermi-level pinning and the low Schottky barrier height. The ionised states at the interface may have originated from injected hot electrons but may also be a result of exposure to air during fabrication.

One study by Kim et al aimed to characterise the unwanted contact potential found at metal – semiconductor NW interfaces.[57] Annealing a metal/semiconductor interface can reduce the contact resistance but this does not overcome oxide layers and differences in work function of the metal and semiconductor. By making four contacts of Ti(30nm)/Au(50nm) by e-beam lithography single ZnO NW FETs were fabricated and the I-V characteristics were recorded by two- and four- probe methods. The difference in the two- and four-probe measurements showed that the majority of voltage drop occurred at the Ti/ZnO contacts. Carrier mobility was estimated at $40cm^2/Vs$ and concentration at $5x10^{18}cm^{-3}$. The conductivity was shown to decrease with temperature, which is consistent with semiconductor materials, and displayed depletion mode characteristics. The four-probe method showed a linear relationship with temperature and an activation energy of 2.4meV

whilst the two-probe method had an activation energy in the linear region of 27.6meV. The thermal energy at room temperature of 25meV was used to conclude the carriers were injected by thermionic emission. The larger activation energy of the two-probe measurements was attributable to the potential barrier between Ti/ZnO. At lower temperatures the transport mechanism changed from thermionic emission to tunnelling because the barrier height is insensitive to temperature variations. The low activation energy of the four-probe method indicated the Fermi level is just below the conduction band which provides the high conductivity and depletion mode behaviour.

These results show the complexity of forming good and reliable contacts to nanostructures. In the flat lying configuration contacts are formed across the side of the structure. This provides a relatively large contact area which is always desirable for a well-defined contact. This is not possible for free-standing contacts which are limited by the nanostructure cross sectional area. Measurement in this configuration is also far more demanding and relies on a good and isolated physical connection to the top contact, however the nanoprobe provides a solution to this problem (Chapter 7).

3.8 Individual contacts to free standing NWs

To realise the full potential of optoelectronic and electronic applications of ZnO Nanowires high quality contacts to vertical NW arrays are needed. Therefore, a number of studies have specifically investigated Schottky and Ohmic contacts to individual NWs.

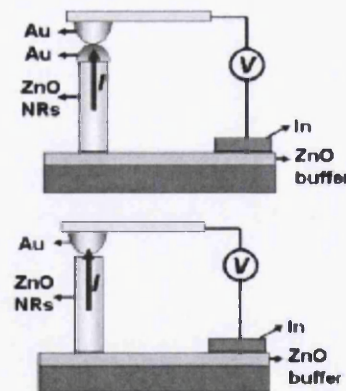

Figure 22. Circuits showing the interfaces of the CAFM setup and point contact to NW tip. Reproduced[157].

One such study by Park et al (2003) fabricated metal contacts to ZnO NW arrays by simply evaporating the metal onto vertically aligned ZnO NWs.[157,188] The NWs had been grown by catalyst free metal-organic vapour phase epitaxy (MOVPE) along the c-axis and thus had no

catalyst tip. A ZnO buffer layer 20-30nm thick was deposited prior to growth to provide a conducting layer. The electrical properties of the NW-top contact were probed by CAFM with an Au conducting tip as shown in Figure 22.

The metal film thickness deposited on the ZnO NW tip (0001) surface was in the range of 10-15nm for Au and compared to a different scheme of Ti (10nm)/Au (5nm). The samples deposited with Ti/Au were annealed between 300-500°C for 30 seconds. The Au only layer interface appeared abrupt by TEM imaging; the Au was not structurally uniform or single crystalline due to the room temperature deposition. The Au crystallites were preferentially deposited on the top NW surface. The likely formation of titanium Oxides at the Ti/ZnO interface was used to argue for greater donor concentration near the junction. An n^+ near interface region may form when an increased density of Oxygen vacancies are formed in the ZnO which lowers the contact resistivity. The process of oxidation is promoted by annealing and the contact resistivity is lower for greater annealing temperatures. [56]

The deposition of only Au formed a Schottky barrier with a reverse bias breakdown voltage of -8V and a leakage current. In comparison contacting a bare NW which exhibited -3V breakdown, see Figure 23. The Au coated CAFM tip with a work function 5.1eV formed a Schottky contact and had nonlinear and rectifying I-V characteristics. The built-in potentials of the NW-ZnO and Indium-ZnO were thought to be negligible, although as the current must pass from CAFM tip though the NW, base layer and the base contact the measured currents are very small (Figure 23). We suspect the results are dominated by the conduction process through the defective base layer.

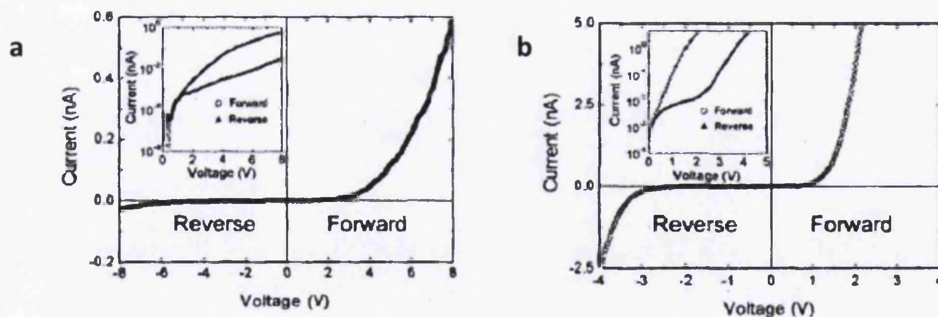

Figure 23. I-V graph of an Au coated CAFM tip point contact, **a)** with Au deposited on ZnO NW and, **b)** I-V curve of an Au coated CAFM tip point contact on bare ZnO NW. Reproduced[188].

Park et al report the Schottky barrier was much improved by the Au deposited on the NW because there is little contact potential between the Au coated AFM tip and Au coated NW. However we can see from Figure 23a and b the current is an order of magnitude less for the coated NW than for a bare NW. The improved rectifying behaviour was stipulated to be due to a greater and more well-defined interface area, uniformly spreading the electric field. The ideality factor calculated was estimated at 7-9. We suggest the high ideality factor values were most likely due to the small contact with the AFM tip, multiple interfaces and the long conduction path that scatters charge carriers especially when the base layer maybe defective.

Similar experiments by Scrymgeour et al using CAFM with probe tips coated with Ti-Pt and conducting diamond were performed on bare ZnO Nanorods.[189] Both coatings gave non-linear I-V characteristics i.e. non-Ohmic contact. To form Ohmic characteristics and appreciable currents (μA) the Nanorods were annealed in H_2/N_2 gas, then coated with photoresist (PR) and the top NW facets were exposed by etching. 3nm Ti and 50nm Au were deposited to provide an Ohmic contact which increased the current by several orders of magnitude. Annealing the contacts creates a highly doped subsurface which provided good Ohmic contact i.e. an n^+ layer. A strong piezoelectric response was correlated to the more resistive nanorods by compressing the NWs with the AFM tip. The photoresist and gas annealing processes alter the NW surface which in turn affects the electrical properties of the structure and the interfaces.

Measurements by C-AFM on as-grown arrays of ZnO NWs typically have small nano-ampere currents at bias up to 10V. A study by Shao et al[(190)] aimed to emulate the Nanogenerator experiments and devices which are discussed next. The Pt AFM tip on the bare NWs had Schottky behaviour of ideality factor 3 and only 15nA at 10V.[190] The convoluted effect of the multiple interfaces again results in the small currents and the non-ideal I-V characteristics were attributed to tunnelling through the point contact.

The most high profile devices that rely on individual top contacts to vertical ZnO NW arrays are the series of Nanogenerators developed by Wang's group at Georgia Institute of technology. The initial break through experiments did not categorically test the top contact but instead showed when the AFM tip traverses across the NW the deformation of the

piezoelectric crystal creates static charge.[29] The charge is then compensated once the AFM tip reaches the negatively biased compressed side where the probe tip-NW Schottky barrier is in the forward bias condition and current can pass easily. The output was as great as -20mV per deflected NW.

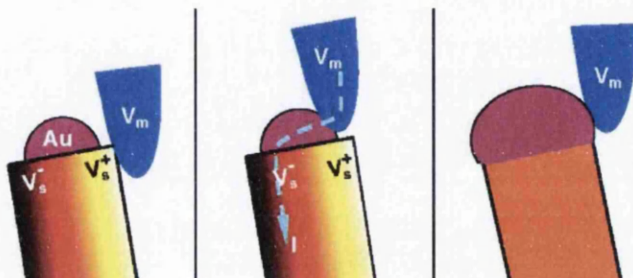

Figure 24. The size of Au catalyst particle size affects the piezoelectric build-up of charge and the output to the AFM tip. A full particle which covers the entire facet leaks charge carriers and prevents the build-up of laterally separated static charge.

The Au catalyst particle on the top facet which was assumed to form a large Schottky barrier that can help or hinder the build-up of lateral electrostatic charge.[29] The NWs of ~50nm diameter were shown to have a variety of Au catalyst particle sized tips. A large Au particle which covers the entire end facet leaks charge to the compressed side which destroys any potential build up. Therefore the Pt CAFM tip was proposed to work best on NWs without a Au tip or with a Au tip smaller than the NW diameter. These types of contacts allowed piezo-charge build up and an output was registered when the CAFM tip contacts the Au (Figure 24). The study provided evidence for the variation of Au catalyst particle size and location on the NW. The hemispherical Au does not often cover the entire end facet and some particles can be found on the sides of the NWs. The measurement method required the output to be measured via the base layer connected by silver paste to the AFM circuit.

The follow up device took advantage of NWs grown by vapour methods without a catalyst and included phosphorus source to create a p-type nanogenerator.[36] The intention of the device was to create a positive potential output developed on the extended side of the NW (an n-type NW has negative charge carriers which screen the positive charge on the deflected side when physically deflected, a p-type NW has positive carriers which screen the negative compressed side[191,192]). This avoided the need for the tip to contact the compressed side which created maximum voltage spikes of 50-90mV. The Pt coated AFM tip provided the large Schottky barrier which is necessary for the charging process but without the Au catalyst.

Modelling by Gao et al of the n-type Nanogenerator predicted a voltage output of 0.3V per NW.[191] The discrepancy with experiments is partially due to the very small contact area between the AFM probe and the NW which may have created a very high contact resistance. The measurements were conducted through the Au contact, NW base layer and the Ag paste contact to the base layer. This provides potential for charge scattering and the capacitance of the NW array system is far greater than the capacitance of a single NW, this consumes the majority of charges produced. The influence of the base layer on the measurement of the top contact is overcome here by the use of the nanoprobe in Chapter 7.

The measurements discussed in the recent sections reveal non-ideal characteristics and provide some insight into the difficulties in contacting Nanostructures, especially in vertical arrays. The role between the catalyst particle that rides on top of the growing crystal is complex[58,117] but provides the ability to produce desirable nanostructures such as NWs. The catalyst particle when residing on the NW tip also provides a readymade electrical contact, and for electrical devices this fabrication pitfall can be bypassed. However, characterisation of this interface is limited and the precise quality and electrical behaviour is unknown although it was suspected the interface properties are mostly dependent on the catalyst material and interface structure. To cover this we examine the interface with electron microscopy in Chapter 6.To provide comparison, confidence and fabrication options in parallel we investigated NW growth without metal catalysts using post-growth metal contact deposition, Chapter 5. To gain further understanding of the small contacts to NWs it was necessary to consider appropriate models for nanoscale contacts. The majority of these models, until recently, were concerned with nanocontacts on planar substrates and we cover these next and apply the most appropriate results in Chapter 7.

3.9 Small contacts - experiment and models

Small contacts are often considered to suffer from large tunnelling currents, surface leakage, poor reverse bias characteristics, edge leakage and barrier inhomogeneity to explain the I-V characterises which are far from ideal and very different from the planar equivalent. These arguments have greater influence when the contacts decrease to below 100nm diameter, in this regime, single dopants atom, structural and point defects, impurities and interfacial layers can drastically alter the potential barrier formed. A single

barrier saddle point created in an inhomogeneous Schottky barrier can dominate the entire contact.

A Schottky contact is formed when a metal comes into contact with a semiconductor. The two features of this barrier that have an overriding influence on the current transport are the barrier height and the depletion region width. The value of the barrier height as discussed is not an exact science for most metal-semiconductor schemes however for certain clean and intimate contacts the barrier height is found within a range of values, typically 0.6-0.7eV for Au-ZnO,[5] and in the case of strong Fermi level pinning the SBH is well defined, 0.59eV for Au-Ge[193]. In these cases of large SBH the transport mechanism becomes dependent on the depletion width which for planar contacts is highly dependent on the semiconductor doping and SBH.

However as contacts are scaled down the contact size becomes the dominant factor on the extent of the depletion region. This relationship was explicitly modelled by Smit et al for small circular contact pads on planar substrates.[60] The Poisson equation was numerically solved for the contact shape and the transmission coefficient was obtained with a fully quantum mechanical calculation. Tunnelling was shown to become the dominant transport mechanism for contacts below a critical size. This was expressed by a depletion layer that no longer depends on material properties and scales with the contact as shown, Figure 25. The Poisson equation formed did not take into consideration the additional potential formed at the contact edge or at the semiconductor surface. Tunnelling occurs as a direct result of the contact scale. This depletion effect was shown in a follow-up paper by Smit et al on small contacts to provide, in contrast to planar contacts, much greater experimental current densities at low bias.[61] Contacts of diameter ~20nm exhibited near linear I-V characteristics and zero bias differential resistance 10^4 times smaller than planar equivalents. This increase can only be due to increased tunnelling from a much reduced depletion region. An interesting observation for the smallest diodes on highly n-type substrates (0.01Ωcm Si) was the forward bias current was smaller than the reverse bias current, reversing the operation of the diode. This was explained by Smit et al by considering the diode as a point contact and suggesting Fowler-Nordheim tunnelling played a role at the diode's edge under forward bias.[61]

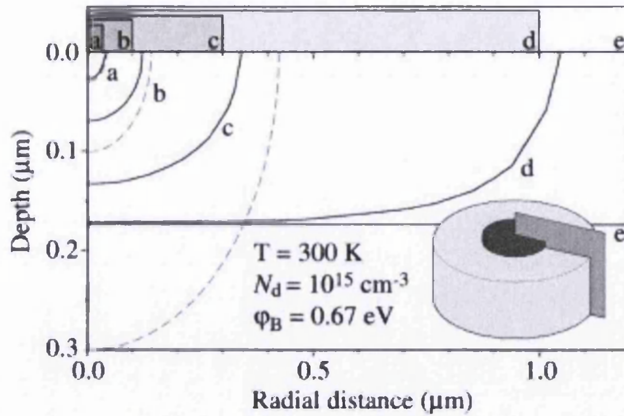

Figure 25. The depletion width for small contacts become dependent on the contact size when the contact becomes small. The diagram depicts the FWHM of the depletion layers for each contact size from 30nm (a) to infinite (e) for a circular contact pad on a planar semiconductor substrate. For low doping concentrations, as shown, the critical size of contact can be as large as 750nm diameter; however at smaller contact sizes the depletion region becomes comparable in size to the contact radius. Reproduced[60].

Similar studies have revealed depletion scaling depending on contact morphology (linear, cylindrical and spherical)[194] and a similar relationship to Smit with contact radius for disc-shaped metals on planar substrates[195].

Edge effects are expected to become more influential for small contacts as the surface area becomes a dominant factor over volume. The band bending that occurs at contact edges has been directly measured by Carroll et al with STM.[63] The edge effect was also modelled as an annular region around a central contact region for small Schottky diodes[196] and a similar model was used by Carroll to explain the easy tunnelling that occurred for the STM experiment as the tip traversed the edge regions of a small contact. Carroll et al modelled this annulus as a region of low SBH, however it may equally be considered as a region of high field and narrow depletion width[55]. The depletion region should be a smoothly varying function[163] across the contact, however to simplify the analysis an 'average' effect is considered for the annulus and central regions i.e. a stepped depletion.

Experimental measurements of nanocontacts on planar substrates frequently show much greater current densities than the planar equivalent. Au contacts on n-type Si measured by STM tips had current densities as large as 10^6 Acm^{-2} for contact area of 10^{-12} cm^2 compared to a bulk contact of area $0.5cm^2$ and current densities of 10^{-2} Acm^{-2}. The reduced depletion region was again shown to be the important feature.[197]

Smit et al conducted STM measurements of many $CoSi_2$ islands on Si from 6000nm^2 to less than 200nm^2.[16] The spread in zero-bias conductance density was seen to increase dramatically with decreasing contact size. The contacts and interfaces were epitaxial and monocrystalline as they were formed in vacuum by annealing of Cobalt on the Si surface. Barrier inhomogeneities were ruled out because the epitaxial contact formation does not create variations in atomic arrangement and defects at the interface; this was previously confirmed by separate BEEM studies which revealed a constant barrier height. The deviation in contact behaviour which increases with decreasing size is explained by the random distribution of dopant atoms. The local distortion of the barrier by one dopant atom has an increasing effect as the contact becomes smaller. Samples of lower doping concentration did not exhibit the spread in conductance, but again the conductance increases with decreasing diameter due to the depletion scaling effect and increased tunnelling. The effect of the local barrier lowering was estimated to be roughly as large as it Bohr radius (~3nm for Si) and the effect was expected to be much less pronounced in thicker barriers. The smaller effective Bohr radius of ZnO of 2.34nm[(198)] means this barrier distortion effect will be reduced and the effect on the conductance spread will also be reduced. ZnO NWs are normally of doping density slightly lower than the Si used in these experiments ($1x10^{18}cm^{-3}$ in ZnO NWs compared to $2x10^{18}cm^{-3}$ in the silicon substrate) which may again reduce this effect. The measurements on the $CoSi_2$ contacts showed the increased spread in conductance with decreased diameter was not apparent until the contacts area $<1000nm^2$. The contacts measured here which display a change in rectifying nature are all $>1000nm^2$.

However increased conductance with decreasing diameter can also be a symptom of an increased surface effect. Surface conduction or leakage is a common explanation. Smit bypassed this argument by annealing the contact islands in hydrogen. This may have minimised the surface effect but it may not have removed it completely. Surface transport mechanisms have been investigated by exposing the surfaces to different gases or treating the surface in some way to passivate or charge the surface around the contact. Surface states can provide a conduction path between islands[168] or an Ohmic-like conduction path for point contacts on clean Si. When Dickie et al removed the surface states of the Si surrounding the point contact changed from Ohmic to strongly rectifying[167]. Song et al revealed by exposing the surface to gases and modifying the surface states a change was

seen in the surface conductance for nanocontacts of $ErSi_2$ on Silicon[62,199]. This technique was used by Song et al to reveal the additional surface conduction path which had a significant contribution to the overall contact conductance. However the contacts were still tunnelling dominated when the surface effect was suppressed. The contacts measured here are all prepared equally and the change in I-V characteristics must be attributed to an effect other than surface conduction.

The surface surrounding a small contact can also affect the depletion region. A surface accumulation layer suppresses the depletion region which originates from the metal contact at the contact edge.[165] A surface depletion allows the depletion region from the contact to extend further along the surface of the semiconductor. In the case of minimal surface charge or minimal surface depletion the contact depletion layer is similar to that described by Smit, Figure 25.

3.10 Nanowire contacts research models and results

The behaviour of electrical contacts to NWs is different to that of contacts to planar semiconductor surfaces. The constricted semiconductor morphology reduces the contact area and changes the extent of the depletion region and enhances the effect of the surface. A recent review by Leonard and Talin highlighted results on NWs and nanotubes.[19] NW contacts can be categorised as either end-bonded or side-bonded. Side bonded contacts are those which are used in NW FET devices, on flat lying NWs with patterned contacts.[18] End-bonded contact is an appropriate term for catalyst particle-NW interfaces and contacts that are deposited or reacted with the NW end. They end abruptly at the NW end which constricts the contact area to that of the NW cross-section. This introduces two factors that are unusual for planar contacts, the contact size is very small and the depletion region is constricted to the NW structure.

By depositing Ni on one end of a flat lying Si NW an end bonded contact was formed by annealing the sample which formed NiSi. The compound migrated along the NW forming a NiSi-Si junction hundreds of nanometres away from the Ni.[54] The contact formed a Schottky barrier with height similar to planar contacts and a current of 10^{-7} Amps at 1V bias.

Hu et al numerically investigated metal NW contacts by solving the Shockley equations for energy band diagrams.[200] The total current through the contacts was considered as

Thermionic emission(TE) and Thermionic field emission (TFE), although TE was found to be very small compared to TFE. A barrier height of 0.4eV and a doping of $5x10^{17}cm^{-3}$ was assumed. It was shown that as the NW diameter decreased the depletion region increased into the NW. However this increase was not substantial until the NW decreased below 20nm diameter. The effect was explained by a field fringing effect outside of the NW that increases as the NW size decreases and reduces the field density in the NW. Subsequently, the contact depletion width then extends further into the NW reducing the calculated current and increasing the contact resistivity. For NWs near to 100nm the effects were not significant.

By solving the 3D Poisson equation of a gate surrounded NW Sarpatwari et al revealed for a NW with a depleted surface and a metal end contact the overall depletion regions combine and extend into the NW, Figure 26a.[201] When the surface of the NW was considered to be accumulated the depletion region was compressed to the contact and the effective barrier height was reduced.

A similar result was previously found by Leonard and Talin investigating single probe measurements of freestanding Ge NWs with Au catalyst particles.[21] A large barrier which results from pinning at the Au-Ge interface and surface state depletion was shown by solving the Poisson equation for an end-bonded NW that the depletion region extends further into the NW. The effect was most prominent for NWs less than 50nm diameter. The I-V measurements with a single probe tip in contact with the Au catalyst tip showed an increasing low bias conductance for NWs less than 50nm diameter and weakening rectifying behaviour. The current density at both forward and reverse bias increased for the smaller (<50nm diameter) NWs, see Figure 26b, with the reverse bias almost equal to the forward bias for the smallest 37nm diameter NW. The effect is less considerable for larger NWs. The increasing low bias conductance with decreasing NWs diameter and the increasing depletion width was explained by surface enhanced recombination currents. The surface effect provided a $(\text{diameter})^{-1}$ relationship with low bias conductance and a diameter dependent recombination time. It was argued all other transport mechanisms are suppressed by the large barrier height and increasing depletion width.

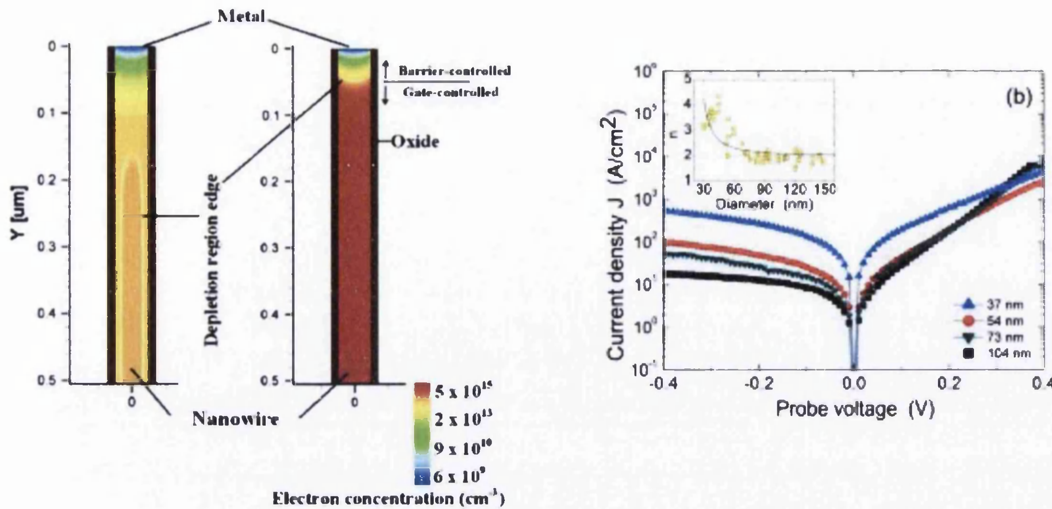

Figure 26. **a)** Diagram depicting the numerical solution of the 3D Poisson equation of a NW with a top metal contact and a gated surface. In surface depletion mode the total depletion size extends into the NW depleting it of carriers, this is dependent on initial NW doping and the surface charge. When the surface is accumulated the depletion region becomes very small. Reproduced[201]. **b)** Current density against Voltage graph of Ge NWs with Au catalyst contacts on the NW tip. The decreasing NW diameter provides greater current density in both forward and reverse bias as the contacts become less rectifying. A significant change is not seen until the contact/NW become less then 50nm diameter. Reproduced[21].

The models of these end-bonded contacts all assume the contact is the same diameter as the NW. This assumption spreads the depletion width across the entire NW width where it can combine with the surface depletion found on the side of some NWs. This argument is appropriate for some NWs, such as Silicon NWs[126], where the Au catalyst covers the entire end facet, however this is not the case for ZnO NWs[58]. These measurements reveal the need for investigation of Schottky contacts to the end facets of NWs in the size range of 50-100nm diameter where the contact is smaller than the NW diameter which we complete here in Chapter 7.

3.11 Literature Review Summary

We have discussed the different growth modes that are applicable to ZnO NWs and highlighted the VLS and the new VSS growth mechanisms that both may be applicable to catalyst-assisted ZnO NWs. Due to variability in crystal growth we have identified the need to examine the Au catalyst particle and its relationship with the NW. To fully understand the properties of this interface and the effect it may have structurally and electrically on the NW it must be examined at an atomic level. Only one technique is capable of revealing the atomic structure of the interface and simultaneously detecting any Au diffusion into the NW which may also greatly hinder electrical properties. The unique technique is atomic

resolution HAADF-STEM. In Chapter 6 we show results from the SuperSTEM II microscope analysing the Au-ZnO interface and reveal the structure and behaviour of the Au catalyst at the interface. The analysis is confirmed by Multislice calculations using Qstem[65] which fully justifies the imaging results by simulating the electron beam interaction with a single Au atom in ZnO.

Also highlighted in this chapter were significant discrepancies in the electrical properties of ZnO NWs such as the significant spread in resistivity measurements revealed by Schlenker et al, their work shows the need to clarify the electrical properties of ZnO NWs.[50] With the aim of doing this and ensuring accurate measurements we must consider ZnO NWs as structures with a surface sensitive nature and a surface dominated morphology that all fabrication processes can modify and affect the measured properties. To overcome this problem which is common for nearly all published resistivity measurements on NWs the fabrication process must be removed. This is achieved here by using the nanoprobe equipment which allows measurements of nanostructures by the four-probe technique free from any processing. The difficulty in measuring electrical properties also extends to contact measurements, especially of free standing NWs. The nanoprobe allows the possibility of isolating the top-contact interface (such as with a catalyst particle) from the effects of the NW-base growth, NW-substrate and substrate-back contact effects which can disrupt the I-V signal[202]. A common symptom of these problems is the measurement currents of only nano-amperes at large voltages up to 10V. We overcome this with the nanoprobe which allows local measurement of the NWs and the top contact when they are still part of the original array. This is extended to the analysis of fabricated and as-grown Au contacts and the size-dependent behaviour of Au catalysed contacts on ZnO NWs which defines a regime different to that revealed by Leonard et al[21]. The contacts here do not cover the entire end facet which presents I-V behaviour different to those contacts of Leonard et al.

Chapter 4

4 Experimental technique

This chapter summarises the experimental principles and relevant theory that are important to understand each technique and the equipment specifications and procedures. A description of the growth technique is included followed with the experimental details. The NWs product of the growth experiments were characterised by two main techniques of Electron Microscopy (EM) and nanoprobe electrical measurements. The EM covers Scanning Electron Microscopy (SEM) for initial assessment of the growth quality and morphology, Transmission Electron Microscopy (TEM) to analyse the crystal structure quality, morphology and composition and finally high resolution Scanning Transmission Electron Microscopy (STEM) to assess the atomic composition of the vapour phase grown NWs and the interface with the Au catalyst particle. This data allowed the correct assessment of the electrical measurements performed with the nanoprobe. The measurements covered bulk resistivity of 40 NWs with the four-probe technique and the two-probe technique to measure the deposited Au and catalyst particle Au interface properties.

4.1 Zinc Oxide nanowire growth

Growth experiments covered the vapour phase growth of ZnO NWs with and without a catalyst. Both techniques are similar and use the same experimental apparatus which harnesses a controlled atmosphere of a rough vacuum level. Here we use a tube furnace to achieve this environment along with the high temperature necessary for evaporation of the source material of ZnO. Chapter 2 discusses the importance of the crystallographic substrate match with the desired growth crystal structure and morphology. For this reason α-Al_2O_3, GaN and ZnO seed layer were preferred for high quality growth. The processes for the two growth mechanisms are summarised followed by the experimental details.

4.1.1 Catalytic Au for NW growth

The gold layer which coats the substrate melts and separates at the high growth temperature in the tube furnace, typically ~900°C, forming nano-droplets or Au clusters.[23] Zn and CO/CO_2 vapour is produced by carbothermal reduction of the ZnO source[24] and carried in the gas flow, in this case Ar/O_2, to the reaction site. This preferentially condenses

on the Au droplets/particles covering the surface of the substrate in the slightly colder region of the furnace.

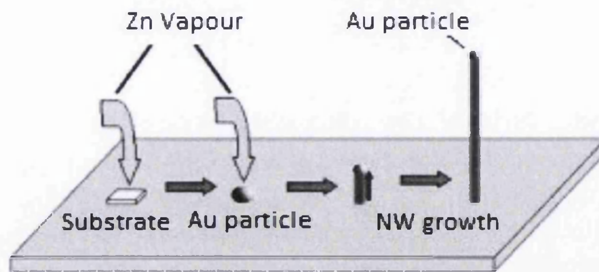

Figure 27. Schematic diagram depicting the Au catalysed nanowire growth. Adapted[24].

The Au acts as a catalyst and preferred site of deposition for source atoms until the liquid/particle surface is supersaturated as depicted in Figure 27.[103,126] The zinc forms on the surface of the catalyst and oxidises by the low concentration of CO/CO_2 and O_2.[107] NW growth initially occurs at the solid substrate – catalyst interface where Zn precipitates followed by oxidation of the Zn and growth ledge formation.[103,107] Continuation of this process allows the alloy droplet to escape the surface and rides on top of the growing NW which continues as long as the catalyst remains on the NW tip and the reactants are available. A NW produced by this method typically has a solid catalyst particle at the tip which is used as the feature to identify the catalyst growth process. A typical image of a Au catalysed ZnO NW array is shown in Figure 28a and further details with examples are discussed in Chapter 5.

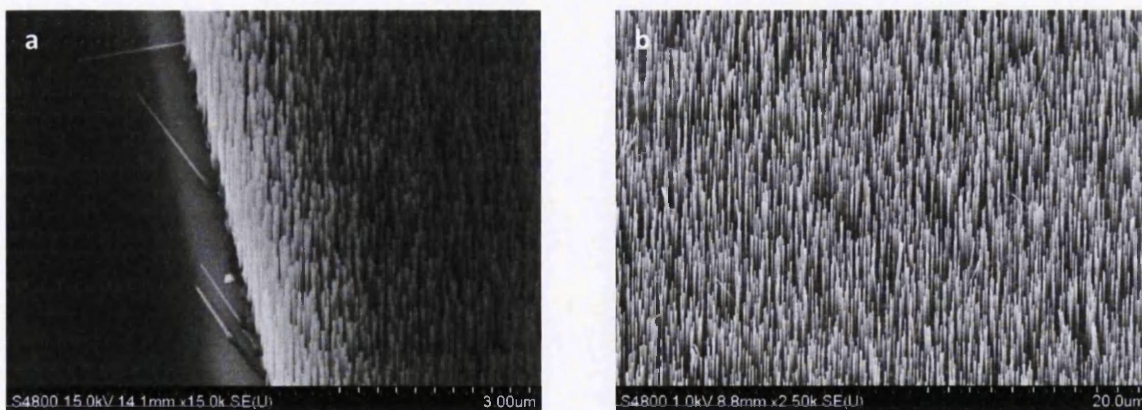

Figure 28. Typical SEM images of the high quality nanowires achievable with, **a)** Au catalysed growth and, **b)** non-catalysed growth.

4.1.2 Non-catalysed nanowire growth

Non-catalysed growth is broadly categorised as a vapour-solid (VS) growth mode that usually dominates at a higher vapour supersaturation than catalysed growth.[119] A narrow bore quartz tube used in this study helps increase the vapour saturation and the relatively high furnace temperatures (1050°C) also produce high vapour concentrations.[112]

Metal Catalysts are often undesirable and so catalyst free growth is frequently more appropriate and the models propose growth nucleation occurs due to the condensation of Zn and Zn suboxides.[119] Vapour is transported downstream to the substrate at ~500-600°C where Zinc vapours condense/oxidise on all surfaces leading to a build-up of ZnO. Observation shows ZnO is deposited on all surfaces in this region of the furnace suggesting no preferential catalytic effect influences the deposition of ZnO. High Zn vapour concentration and high oxygen concentration aid the oxidation of Zn vapour adsorbing to the growth surfaces. A typical image of non-catalysed ZnO NW arrays is shown in Figure 28b and further details with examples are discussed in Chapter 5.

4.1.3 Nanowire characterisation

NWs were grown specifically for experimental purposes, e.g. contact measurements. Therefore experiments focussed on achieving control of the growth product and characterising it for specific requirements. The elements that were important to both are listed below. A number of parameters were changed throughout the experiments but control over the product is mostly achieved with the following:

- catalyst thickness
- substrate material - crystal structure, lattice matching and surface morphology
- temperature of the growth region
- Source-Sample distance

The NWs growth were characterised by the following:

- Length
- Diameter
- Cross-section shape
- Coverage
- Alignment
- Termination
- Branching/kinking

4.2 Nanowire growth experimental details

Vapour phase NWs were grown by two methods at the Multidisciplinary Nanotechnology Centre at Swansea University. The growth experiments were performed in a high temperature tube furnace with and without Au catalyst on planar substrates. High-temperature high-pressure hydrothermal NWs were provided by Alex Walton at Leeds University for electrical measurements, the growth method is briefly stated.

4.2.1 Catalysed NW growth sample preparation

Samples were thoroughly scrubbed with acetone and a cotton swab, then sonicated in acetone, ethanol and IPA, then rinsed in de-ionised (DI) water and dried with N_2. Au was then deposited with a dedicated Au Edwards plasma sputter that was calibrated to deposit 1nm Au every 4 seconds.

4.2.2 Non-catalysed NW growth sample preparation

Single crystal sapphire substrates for roughness-assisted growth were cleaned similar to the catalysed NW substrates and then etched in 1M NaOH (as reported by Ho et al) for various amounts of time.[111] After etching, the substrates were rinsed thoroughly with DI water, then ethanol sonication and further rinse and dry. Etching was performed with stirring at room temperature.

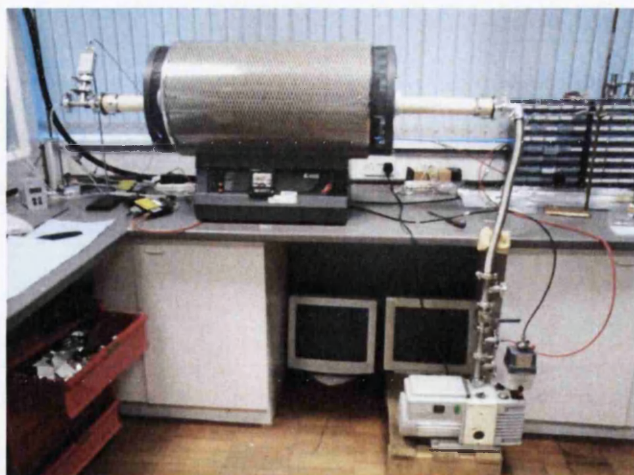

Figure 29. The Carbolite high temperature tube furnace used for NW growth. The main work tube was high purity alumina vacuum sealed at both ends to ensure the high purity gas flow of Ar/O_2, which flows from left to right, was not contaminated. The chamber pressure that was measured by a Pfeiffer Vacuum combination pressure sensor was maintained at a constant level by the two-stage Edwards rotary pump which is connected by a 1m long stainless steel bellows. A molecular sieve trap (not shown) was used to prevent backflow of oil vapour into the chamber.

Metal substrates were created by Sputter deposition of metals onto Silicon substrates. To ensure good adherence to the substrate the Silicon was solvent cleaned, oxidised with Piranha solution and etched with HF acid to remove the oxide. Samples were then transferred into the Physical Vapour Deposition (PVD) system for metals deposition. A thin 25-50nm layer of Cr was found to benefit the adherence of subsequent metal layers. To initiate the growth on substrates other than those of roughened sapphire a ZnO seed layer was employed, either deposited by solution methods described in section 4.2.4 or from a pure ZnO source using PVD. No optimum procedure for the PVD seed layers were found, therefore it is only briefly discussed in Chapter 6.

4.2.3 Vapour phase furnace technique

Vapour phase NWs were grown in a tube furnace, see Figure 29. This was performed in a controlled atmosphere as previously reported by the author in his MRes thesis.[203] A high purity Alumina tube is inserted into the furnace with vacuum fittings to seal the open ends. These fittings allow the controlled flow of high purity Argon and Oxygen with the aid of Mass flow-controllers and the continuous evacuation of the chamber to maintain a constant pressure (1-30mbar depending on experiment).

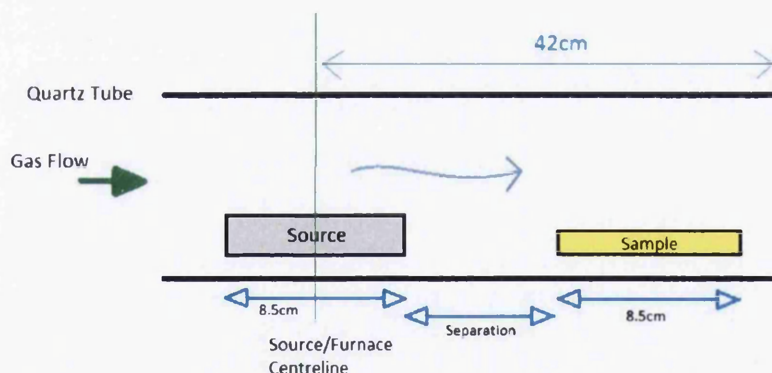

Figure 30. Experimental arrangement of Furnace Growth experiments

The sample boat and source boat including the carbothermal source mix of ZnO (Alfa Aesar 99.99%) and Carbon (sigma Aldrich 99.99%) 325mesh were placed in a Quartz tube and inserted into the Alumina tube, Figure 30. The assembly was evacuated and then heated at ~50°C/min to 200°C and held under vacuum for 20mins, the furnace was then ramped up to the growth temperature (~900-1100°C). Whilst at 200°C dwell the flow of Argon and Oxygen was established. On completing the growth time the experiment was allowed to

cool under a steady gas flow and the samples were then removed and immediately inspected with Scanning Electron Microscopy (SEM). Figure 31 shows how the growth changes as the sample is moved further from the source boat, this example is of catalytic NW growth.

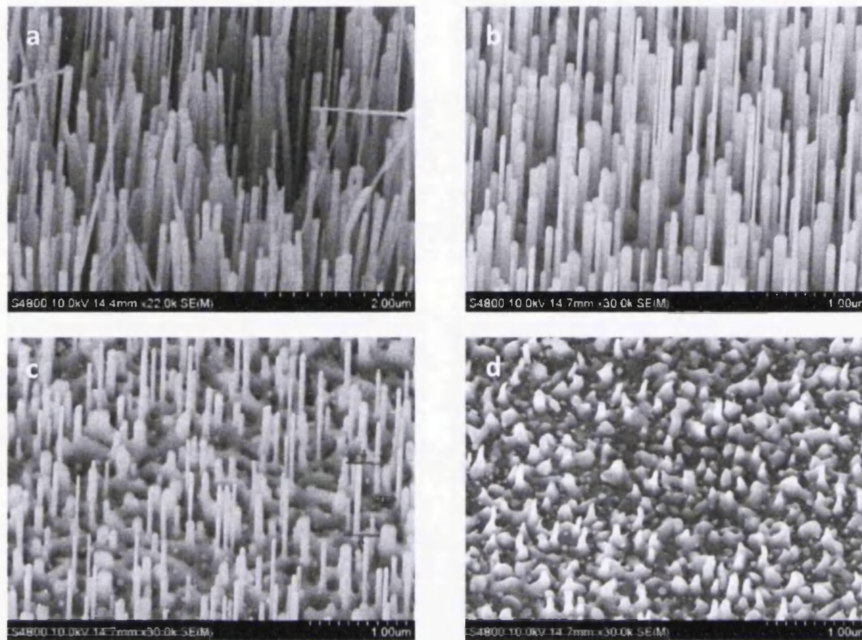

Figure 31. The images show how the catalysed growth changes when the sample is located further away from the source, for the case of a sample location of, **a)** 9cm, **b)** 10cm, **c)** 11cm and **d)** 12cm from the furnace centreline.

4.2.4 Experimental parameters from previous work

Previous work by the author[203] established optimum parameters for catalysed growth and non-catalysed growth, these were the basis for all growth experiments (significant deviations from these settings will be explained) :

- Catalysed growth – furnace temperature 950°C, substrate temperature 850°C, pressure 30mbar of gas flow 49sccm Ar and 1sccm O_2, growth time of 30mins
- Non-catalysed – furnace temperature 1050°C, substrate temperature 650°C, pressure 1.6mbar, gas flow 100sccm Ar and 10sccm O_2, growth time 60mins

The previous work covered aspects of NW growth such as source and substrate temperature, chamber pressure, source and sample boat separation and seed layer. To avoid repetition only appreciable advances are discussed here. Seed layers were produced in similar fashion by dissolving 0.11g of Zinc Acetate into 100ml of ethanol, stirring, and then drop coating onto the clean substrate. Upon annealing the sample at 350°C ZnO was formed

and by repeating this process a continuous layer was formed, in all cases here 2 cycles each of a 20μl drop were used on 7x10mm samples (e.g. Silicon). Growth was previously observed to reduce as the sample was moved further from the source. There is an optimum point from the source where NWs grow well, although this (after many experiments), varied by 1cm from growth to growth when the experiments were working as intended. Some experiments here concentrated on growing NWs on non-lattice matched substrates such as metal layers or other experiments concentrated on a particular NW density and morphology. Many experiments were completed for the purpose of transferring to TEM or Nanoprobe substrates for measurement. In these cases only the best vertically aligned high-quality NWs were used. Previous experiments revealed a large effect of turbulence on the growth and so most experiments used a flat smoothed Alumina boat to reduce unpredictable eddy currents around the samples.

4.2.5 Process parameters

The experimental parameters which could affect the resultant growth that were considered in detail were:

Catalyst thickness – the resulting Au nanoparticle size and quantity is expected to drive the mean NW diameter and areal density of growth

Substrate material – growth depends on substrate material and crystallinity, the crystal structure can determine the growth direction and also the subsequent material composition

Substrate Surface morphology – surface roughness can affect the growth nucleation and alignment

Source quantity – the amount of source material can be varied, this is kept at equal weight ratio 1:1 ZnO and Carbon

Source particle size – the surface area of the carbon particles can influence the evaporation rate of Zn and so this can be controlled by varying the particle size

Turbulence and boat shape – the low pressures and high gas input results in a very fast flow which induces heavy ZnO deposition on regions that catch the flow

The particular experiments covered here were,

Catalysed NWs:

SWANSEA LIBRARY UNIVERSITY

- vertically aligned NWs on sapphire
- NWs grown on GaN for comparison
- Au thickness, furnace and sample temperature, and source material weight – to control the density and morphology and to encourage the presence of Au particles on the NW tips

Non-catalysed NWs:

- Seed layer for aligned growth on metal layers deposited on Silicon <111>
- Roughening of Sapphire according to the research of Ho et al[111] that details the low level etching of polished Sapphire for vertical non-catalysed NW growth – these NWs were intended for Nanoprobe measurement

4.2.6 Hydrothermal nanowires

Hydrothermal NWs obtained from Alex Walton of Leeds University were used only for the four-probe electrical measurements. These NWs were grown at 140°C and 4bar pressure in a pressure bomb. After growth a viscous fluid was obtained which contained NWs of varying morphology. The liquid was drained and the NWs were rinsed thoroughly and then dried by centrifuge. The NWs had a range of surface roughness from smooth to corrugated which was thought to be a growth feature.

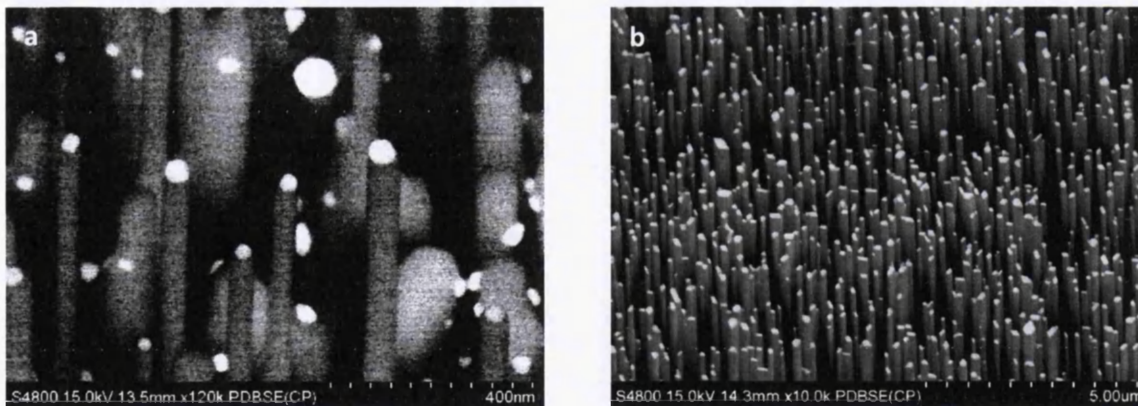

Figure 32. Backscatter electron images, **a)** Au catalyst particles on top of ZnO nanowires and, **b)** deposited Au decorating the top facet of non-catalysed nanowires.

4.2.7 Au catalyst particles as electrical contacts

Catalysed NWs were grown specifically with prominent Au particles at the top facet. The substrate was initially solvent cleaned and then Au sputter deposited at 10^{-3}mbar. NW growth occurred at ~900°C in a flowing atmosphere of Argon and Oxygen at 30mbar. The

furnace was cooled under vacuum and the NWs removed for SEM examination. The samples were stored in air until the Nanoprobe measurements. A typical backscatter electron image from the SEM instrument discussed later is shown in Figure 32a, further details are discussed in Chapter 5 and Chapter 6.

4.2.8 Au deposition for electrical contact fabrication

Au was evaporated onto vertical catalyst-free NWs at $\sim 10^{-5}$mbar using an Edwards thermal evaporator and observed in TEM to characterise the Au thickness and crystallinity. The NW array was secured at a constant known height above the source basket. The chamber was evacuated by diffusion pump for one hour before deposition. The NW arrays had been exposed to air for a substantial amount of time and previously undergone SEM examination. The thickness of the deposition was assessed by TEM of the NW tips. A quantity from 6cm-37cm of 0.2mm Au wire was loaded into the basket according to the deposition required. Chapter 5 and Chapter 6 discuss the results in detail and a typical backscatter electron image is shown in Figure 32b.

Scanning Electron Microscopy (SEM), Transmission Electron Microscopy and Scanning Transmission Electron microscopy (STEM) were used to analyse the NWs. The aspects of each technique that are important to the study are summarised along with the experimental details.

4.3 Scanning Electron Microscopy (SEM)

Scanning Electron Microscopy (SEM), depicted in Figure 33, is used to study the interaction of an electron beam with the surface of a sample and can be used for 'large' bulk samples. The electron source is a very sharp tungsten tip which creates a very high electric field when a potential is applied to it across vacuum. The electric field is great enough to cause a field emission current of tunnelling electrons into free space. The emission of electrons is independent of temperature ('cold') which provides the name cold field-emission gun (cold-FEG). The field emission source offers high resolution (~1nm) and excellent performance over a wide range of accelerating voltages 0.5-30kV. High probe currents are possible with small probe sizes but the biggest advantage is the resolution at low voltages. The beam is scanned across the sample in a raster pattern and simultaneously secondary electrons and secondary effects are detected.

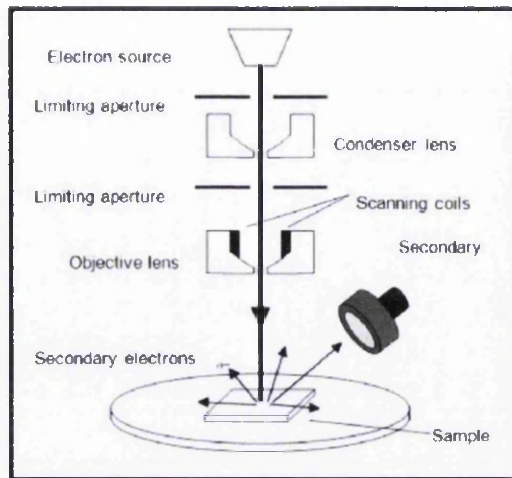

Figure 33. Schematic of a Scanning Electron microscope indicating the important components.

There are terms that are important to all electron microscopy techniques but the function may vary slightly for each, in particular to SEM they are:

- Condenser lens – or spot size demagnifies the beam from the source and affects the resolution.
- Objective aperture – controls the convergence angle which is a compromise between signal strength, depth of field (DoF) and resolution. A smaller aperture reduces signal, increases the DoF but results in worse resolution. Small apertures produce a large depth of field by constricting the convergence angle but reduce the overall signal. This can be overcome when a large depth of focus is needed at low magnifications by increasing the spot size. The DoF can also be increased by increasing the working distance from the objective aperture to the sample.[87]
- Objective lens – focusses the beam to the sample, the beam size at the sample controls resolution

4.3.1 Secondary effects

Primary electrons incident on a 'thick' sample interact and may undergo an energy loss which can produce a number of secondary effects shown in Figure 34. Normal imaging in a SEM relies on the detection of secondary electrons (SE) which are usually electrons from or near the surface of the sample which have been excited to a point that they can escape, typical images are shown in Figure 28. These electrons are abundant and are typically low energy and originate from an area similar to the beam. For this reason SE give the best

resolution as they are the most localised. Relaxation of excited atoms can produce x-rays, Auger electrons or visible light. Backscattered electrons (BSE) are another secondary effect but are in fact primary electrons that have re-emerged from the sample. BSE usually escape with most of their initial energy and are considered to have higher energy than other detected electrons. The detection of BSE forms another imaging technique.[90]

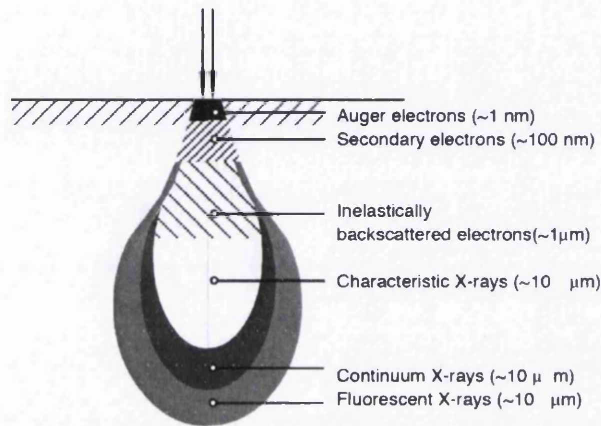

Figure 34. Interaction volume of an electron beam with a thick sample. Reproduced [254].

Generally interactions are inelastic with primary electrons losing significant energy and either coming to a halt in the sample or they are re-emitted. The origin of each signal is dependent on the beam energy and the sample atomic number which determines the interaction volume and secondary effects.

4.3.2 Backscattered electrons

Some primary electrons will be backscattered by the sample after an inelastic interaction. These electrons do not penetrate deep into the sample and generally have a broad energy range. The electrons of greatest energy are of the most use for BSE imaging as they have undergone less scattering. BSE imaging gives compositional information with large Z number materials backscattering more frequently than low Z number materials. Typical examples of Au on ZnO NWs are shown in Figure 32.

4.4 Secondary Electron Microscopy (SEM) experimental details

SEM was used to examine the products from each growth experiment, particularly the morphology, alignment and areal density. The Hitachi S4800 SEM was used in the Multidisciplinary Nanotechnology Centre at Swansea University.

4.4.1 Equipment specifications

The SEM used in this study was the Hitachi S4800 Cold field emission gun SEM, accelerating voltage 0.5-30kV, magnification up to 800kx, SE resolution 1-2nm, equipped with YAG BSE backscatter detector of resolution 3nm, Oxford instruments 50mm^2 EDX detector and STEM detector.

4.4.2 Sample examination technique

Planar samples were mounted to an aluminium stub with carbon pads, solvent based silver paint or mechanical clips. A selection of sample stubs is shown (Figure 35) with typical growth products on planar samples. A stub is attached to the sample shuttle and placed in the SEM air lock. Here the chamber is evacuated to a level close to the chamber pressure of 10^{-3}mbar. Once this pressure was reached the load lock door was opened and the shuttle transferred into the main chamber.

The SEM was then controlled from the flight deck control system to adjust beam focus, magnification, astigmatism, working distance, sample tilt, beam current and beam voltage. For high resolution imaging a short working distance (1-5mm) was used with the upper Secondary Electron (SE) detector. For analytical work, such as backscatter electron (BSE) imaging, a large working distance was used and typically with higher accelerating voltage of 15-20kV. When the sample was located at a large working distance SE imaging was best with a combination of the upper and lower SE detectors. BSE imaging required a dedicated detector to be manually wound in to locate the detector near the sample which restricted the sample tilt range.

Figure 35. Typical SEM stubs used for mounting NW growth substrates, shown here is the white ZnO growth product found on Sapphire. The S4800 Hitachi SEM used for sample characterisation.

4.5 Transmission Electron Microscopy

Transmission Electron Microscopy (TEM) studies the interaction of a high energy electron beam with a thin sample, usually less than 100nm thick. Some principle components are above the sample such as the electron source and a condenser system which collimates the electron beam. Below the sample is an objective lens, which gives the first focused image, and then further along the optical axis comes a projector system to magnify the image onto a viewing system, Figure 36.[87]

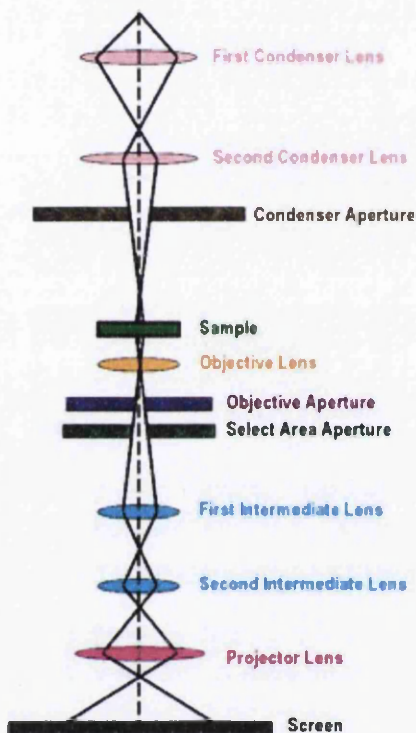

Figure 36. Diagram showing the major components of a Transmission Electron Microscope. Reproduced[35].

The two condenser lenses are similar in effect to a SEM with additional alignment coils to columnate the beam and an aperture to provide control of the beam intensity. Demagnification of the source beam occurs in the first condenser lens before the second condenser lens projects the beam and gives control of the illuminated area and the convergence angle. A condenser aperture which is generally between the lens and sample provides additional control of the convergence angle and beam intensity. [87,90]

Electrons that exit and diverge from the sample are magnified by the objective lens (50-100x). An objective aperture controls the angular range of electrons that contribute to the signal, e.g. eliminating diffracted electrons. It is then possible to introduce a selected area

(diffraction) aperture in the back focal plane to select a specific area of the image or for electron diffraction analysis.[87]

Generally the beam diameter at the specimen is much larger for a TEM than in STEM/SEM. Although most TEM microscopes now have the ability of a scanning mode used for High Angle Annular Dark Field Imaging (HAADF) and Energy Dispersive X-ray (EDX) analysis.[87]

4.5.1 Diffraction mode

Electrons that are diffracted by the specimen in parallel directions are focussed to the same point by the objective lens. It is the well-defined diffraction of electrons by crystalline materials that produces diffraction patterns governed by the Bragg angle, described in Chapter 2.[87,90]

To obtain diffraction contrast a beam close to parallel is necessary that provides even illumination of the sample and similar diffraction conditions to create diffraction spots in the image. The smallest area of illumination is 0.5-1μm in diameter because spherical aberrations begin to interfere with the beam. The selected area aperture may then be used to obtain a diffraction image from a smaller area e.g.250nm diameter.[90]

4.5.2 Limitations of TEM

Modern TEM microscopes often have a FEG which provides high brightness from a sharp tungsten tip. The most advantageous feature of these sources is the very well defined energy spread of electrons which can be as low as 0.3eV and produces a very fine beam.

However, diffraction is a detrimental process that occurs throughout the microscope and not only in the sample. The effect of diffraction in lenses is reduced in electron microscopes which use electromagnetic lenses and have no refractive index difference with the surrounding vacuum. Aberrations and apertures however have a significant effect.[90]

4.5.3 Aberrations

Electron microscopy suffers from two lens aberrations:

- Chromatic aberrations resulting from electrons of different energy/wavelength due to an energy spread in the emitted beam
- Spherical aberrations from lens inhomogeneity.

A lens will focus electrons of different wavelength to different points along the optical axis. The best solution is a monochromatic electron source which produces a beam of very low energy spread and reduces the chromatic aberration coefficient C_c to a minimum. Other options include cold-field emission sources such as the one used at Leeds University. In the case of a TEM fitted with a monochromator the beam can have an energy spread of 0.15eV, while a cold-FEG source around 0.3eV and a FEG of 0.7eV.[204]

Electrons in a parallel beam that are far from the optical axis must travel further than the electrons near the optical axis when passing through a lens. This results in electrons focusing at different points along the optical axis and is known as Spherical aberration. Apertures of small diameter which restrict electrons to a very narrow path can reduce the effect. Recently spherical aberration correction has been implemented in dedicated STEM microscopes that improve the resolution to less than a single atom, discussed in section 4.7.

4.5.4 Imaging

Bright-field images are obtained with a small objective aperture centred on the optical axis which removes diffracted electrons from the image. Dark regions have a weaker signal because they scatter more electrons which indicates they are thicker or more dense, see Figure 37a. Removing the objective aperture and allowing diffracted electrons to interfere is the basis for lattice imaging. The phase contrast in a lattice image provides the ability to view atomic planes and anomalies in the crystal structure, see Figure 39a.

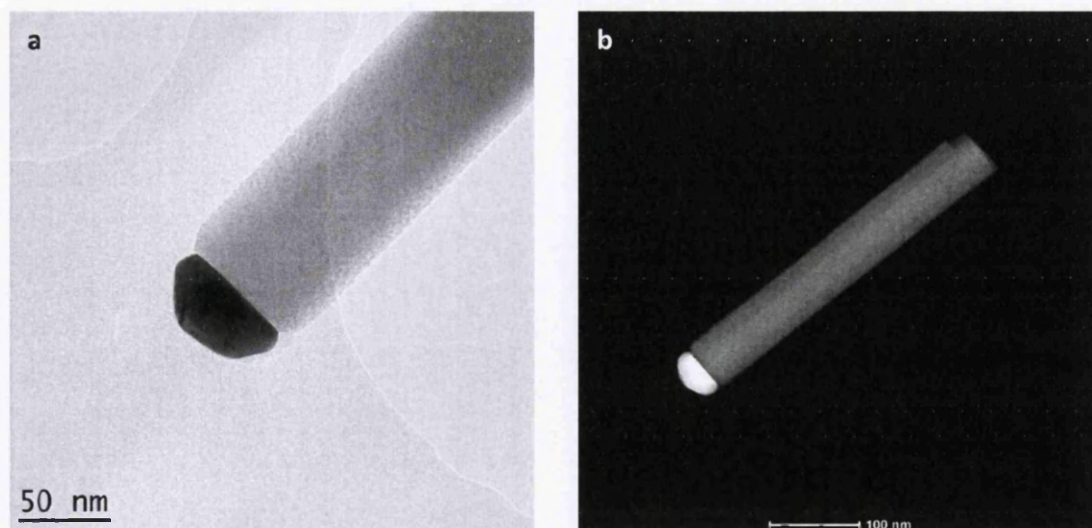

Figure 37. **a)** bright field TEM image of a catalyst assisted nanowire with a dense Au growth tip. **b)** HAADF image that shows the Au tip as a bright region because the dense heavy element Au scatters more electrons to high angles.

High Angle-Annular dark field (HAADF) imaging in STEM mode or in a dedicated STEM uses an annular detector to collect electrons that are incoherently scattered to relatively large angles. The atomic number of the specimen greatly influences the Rutherford-like scattering which is the basis for this technique.[205] The scattering to high angles occurs with an approximate intensity relationship with the square of the atomic number. This relationship produces images with atomic columns and regions of greater Z number that are bright, see Figure 37b. The technique contains little diffraction contrast which makes the images relatively simple to interpret compared to phase contrast images.[90]

4.5.5 Phase contrast of crystalline defects

Planar defects are defects such as stacking faults, displacement faults, and grain or phase boundaries. Displacement faults characteristically have fringes that run parallel to the fault and sample surface intersection. These fringes are caused by interference of electrons diffracted above and below the defect. The defects can be distinguished because the fringes and contrast differences may disappear when the sample is tilted. Boundaries will likely show disorientated or discontinuous lattice planes. Dislocations are surrounded by locally bent planes overlapping the defect which leads to strong diffraction. A sample orientated such that it is not diffracting strongly can show a dislocation as a dark line or region due to the increased diffraction in the defect locality.[90]

4.5.6 Energy Dispersive X-ray (EDX) spectroscopy

Relaxation of electrons in an excited atom can result in the emission of an x-ray. The emitted x-ray is unique in energy to that electron shell transition in that specific element. Energy Dispersive X-ray spectroscopy (EDX) detects the energy and intensity of these x-rays which provides the spatial dispersion and identification of elements present in the sample.

Incident electrons interact with not only the surface atoms but also deep into the sample and the interaction volume can be micrometres in diameter. EDX of thick samples provides information not only of the surface but deeper into the bulk and the signal is highly delocalised. This is a great advantage of the thin specimens used in TEM-EDX analysis where the interaction volume is constricted to the solid volume.

4.6 Transmission Electron Microscope Experimental (TEM) details

TEM was used to inspect the crystal structure and composition of individual NWs and cross section samples of NW arrays. A focussed Ion beam (FIB) was used to mill out sections of catalysed NW arrays to inspect the base growth and catalyst behaviour. The equipment was accessed at Leeds University as part of the Leeds EPSRC Nanoscience and Nanotechnology equipment facility (LENNF) and was operated by Michael Ward.

4.6.1 Equipment specifications

The TEM used in this work shown in Figure 38a was a FEI Tecnai TF20 FEGTEM which operates at 200keV, 1000k magnification, with STEM/TEM mode, HAADF imaging with an Oxford Instruments INCA 350 EDX system/80mm X-Max SDD detector and Gatan Orius SC600A CCD camera. The microscope has spatial resolution of approximately 0.2nm and STEM-HAADF resolution of 0.5nm with beam energy spread of 0.7eV. A selected area aperture was used for diffraction pattern imaging selecting an area of diameter 250nm on the sample.[206]

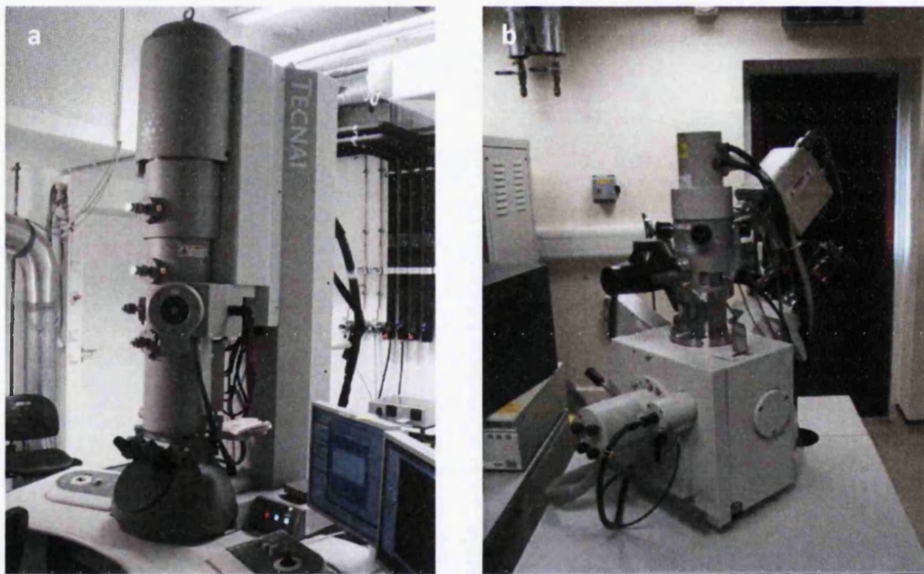

Figure 38. Photographs of the, **a)** FEI Tecnai TF20 field emission gun TEM used for the structural analysis and, **b)** the FEI Nova 200 a dual beam field emission gun SEM with a Ga^+ Focussed ion Beam.

The FIB shown in Figure 38b is a FEI Nova 200 NanoLab high resolution Field Emission Gun Scanning Electron Microscope (FEGSEM) with precise Focused Ion Beam(FIB) with etch and deposition capabilities.[206]

4.6.2 Sample preparation

NWs were directly transferred to holey carbon coated copper TEM grids by rubbing the vertical NW array with the coated side of the grid. TEM analysis was performed without baking the grid and no contamination problems were observed at 200kV. NWs tended to lie flat on the grid on a side facet. Cross-sectional samples prepared by FIB were mounted onto a TEM grid using the FIB beam deposition of carbon platinum glue from the injected precursor gas.

4.6.3 Sample imaging

The grid sample was loaded into the microscope and the vacuum was allowed to stabilise before imaging. The samples were rotated within the microscope to allow the structure of interest to be manipulated until the atomic planes were close to parallel with the beam. Large tilt angles were possible which allowed the viewing of more than one zone-axis when required. Patient alignment of the sample aligns the columns of atoms such that clear well-defined diffraction and lattice images were obtained.

Typically lattice images were obtained of the NWs on the grid to inspect the crystal quality, see Figure 39a. To identify the crystal structure diffraction patterns were obtained in diffraction mode using a selected area aperture, see Figure 39b. High Angle Annular Dark Field (HAADF) imaging and Energy Dispersive X-ray (EDX) analysis were performed with the microscope in STEM mode.

4.6.4 Indexing diffraction patterns

The sample was rotated until the beam was parallel to the two planes perpendicular and parallel to the growth direction in the lattice image. This orientated the atomic columns sufficiently for spot diffraction patterns to be obtained. The area of illumination was large such that a near parallel beam was achieved and the selected area aperture magnified an area of approximately 250nm.

In the case where the material is known the procedure for indexing a spot pattern is taken from Edington[88] and displayed in Figure 40 for the NW and raw diffraction pattern displayed in Figure 39b.

1. Measure the distance from central spot of the transmitted undeflected beam to three diffraction spots forming a parallelogram. In the diffraction pattern the image displays units in the reciprocal lattice and the measured distance is $1/d_{hkil}$. The fairly large size of the spots and the imprecise measurement to the centre spot limits the accuracy but this is sufficient for comparing to standard data.
2. Using known interplanar spacing's for the material correlate the d spacing measurement to actual d values to obtain the {hkil} for each of the spots
3. Each spot represents a plane and so the angle between two planes is measured as the angle subtended by the centre spot and the two diffraction spots. These lines are parallel to the normal direction of each plane.
4. The normal of each plane is translated as a crystallographic direction
5. Bragg diffraction suggests the electron beam is parallel to the reflecting planes and it can be assumed the zone axis is the same as the beam direction.

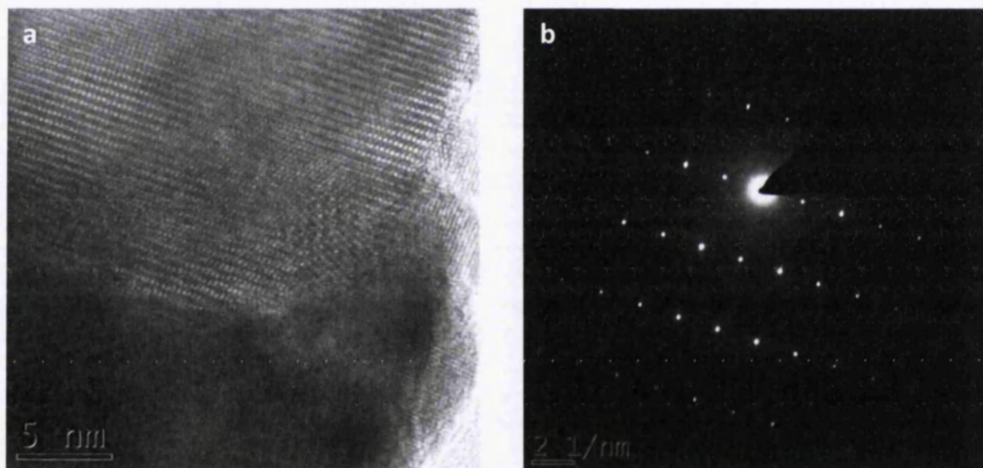

Figure 39. **a)** Lattice image of a ZnO NW showing distinct lattice planes with Au deposited cap. **b)** the corresponding diffraction image which is rotated 90° with respect to the lattice planes due to imaging conditions.

The procedure will be followed for one example Non-catalysed ZnO NWs - Sample 179-4. The distances shown in Figure 40 correspond to 10 manually measured plane spacing's for b=3.932nm^{-1} (std. dev.=0.008 nm^{-1}) , a=3.444 nm^{-1} (std. dev.=0.006 nm^{-1}) and c=1.886 nm^{-1} (std. dev.=0.007 nm^{-1}) that give the distances of 1/c~0.530nm (std. dev.=0.002nm), 1/a~0.290nm (std. dev.=0.0006nm), and 1/b~0.254nm (std. dev.=0.0005nm). The diffraction image is rotated through an angle of ~90° with respect to the bright field image in Figure 39a due to the lenses and magnification used. The value of 0.53nm is reasonably

close to 0.521nm of the c axis spacing of the ZnO wurtzite unit cell but may indicate some strain or slight errors are present in the microscope.[5]

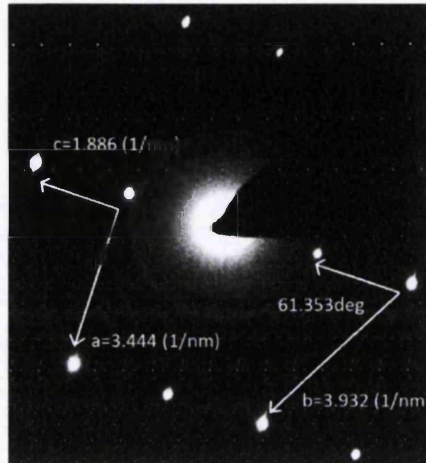

Figure 40. Cropped diffraction image showing the measurements of three diffraction reflections which correspond to interplanar measurements of the reciprocal lattice

Estimating errors in the manual measurement of diffraction images are difficult due to uncertainties in microscope, beam and sample alignment. To ensure results are accurate as possible the camera is calibrated using a gold standard (a known diffraction pattern is taken from a gold sample), in a well aligned microscope. The measurements of the rings are then used to work out the relative dimensions of the pixels on the CCD, for a given magnification (camera length). Assuming this is done correctly, there will be errors introduced by the measuring inaccuracies and any misalignment of the microscope, x-ray diffraction is more suited to detecting small changes in lattice parameters.

The ratio of the distances (b=3.932nm^{-1}, a=3.444nm^{-1} and c=1.886nm^{-1}) can be used to compare to standard diffraction patterns of the hexagonally close packed structure.[88] Here c/a=0.548, the standard result is c/a=1.09 for the $[2\bar{1}\bar{1}0]$ zone axis beam configuration in which the 0001 reflection is forbidden and the c measurement is to the 0002 reflection spot. The ratio of c/a=1.09 is approximately twice the experimental measurement which indicates a forbidden reflection appears due to double diffraction or multiple scattering.[88] From the diffraction spot spacing and comparing to the standard result we can see the c distance corresponds to {0001}, the b distance is the spacing associated with $\{01\bar{1}1\}$ and the a distance is the spacing for $\{01\bar{1}0\}$.

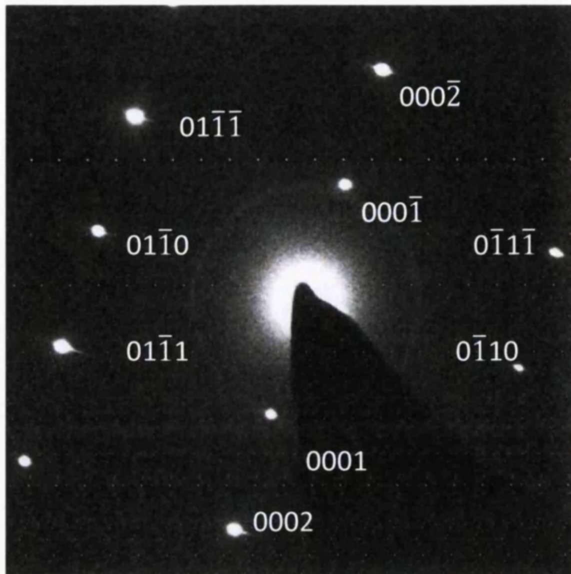

Figure 41. The final cropped diffraction pattern labelled according to the zone axis with the positive direction of 0001 chosen to be in the growth direction of the NW

This is confirmed by the 10 angle measurements between b and c which the average measure is 61.353° (std. dev. 0.603°) close to the theoretical value of 61.38°.[88] Therefore the spot to the right hand side of the central spot in Figure 40 is part of the {0001} group of directions and arbitrarily labelled 0001, and then the other spots are labelled accordingly. Rotating the diffraction image in order for the planes to match the bright field lattice image (Figure 39a) and indexing of the diffraction spots is then complete Figure 41.

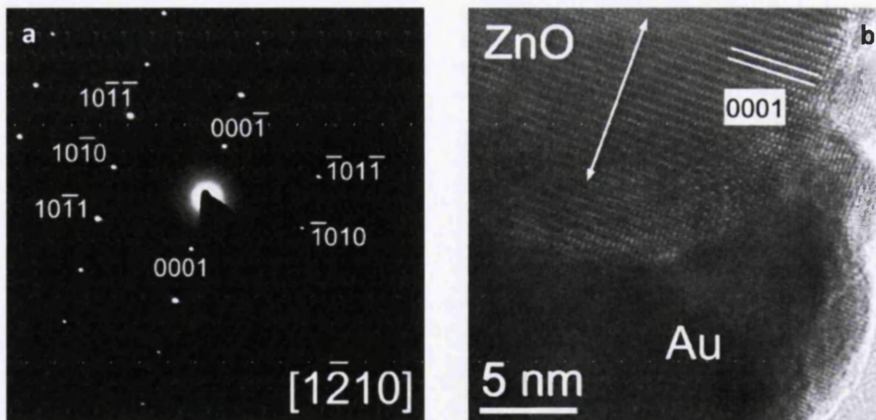

Figure 42. **a)** Indexed diffraction pattern showing the ZnO NW is single crystal with 0001 growth direction that provides the hexagonal cross-section that was seen in SEM images. **b)** the 0001 planes labelled on the Lattice image

The beam direction parallel to all of these planes is the zone axis $\left[2\bar{1}\bar{1}0\right]$ which is part of a crystallographically equivalent family of directions in the basal plane. $\left\langle 2\bar{1}\bar{1}0\right\rangle = \left[2\bar{1}\bar{1}0\right],\left[\bar{1}2\bar{1}0\right],\left[\bar{1}\bar{1}20\right]$ are used to express the basal plane unit vectors of the

hexagonal system. Using symmetry we can express the diffraction pattern as shown with an alternative appropriate zone axis and label the corresponding lattice image Figure 42.

4.6.5 Energy Dispersive X-ray (EDX) spectroscopy

The EDX detector was inserted and operated when the TEM was in STEM mode. A typical example of an EDX area map of ZnO growth on sapphire substrate is shown in Figure 43a and a typical EDX spectra of a ZnO NW is shown in Figure 43b, the full results are discussed in Chapter 6. Maps can be produced showing the compositional variation of the sample but the accuracy is no better than 1% with the best TEM setup.

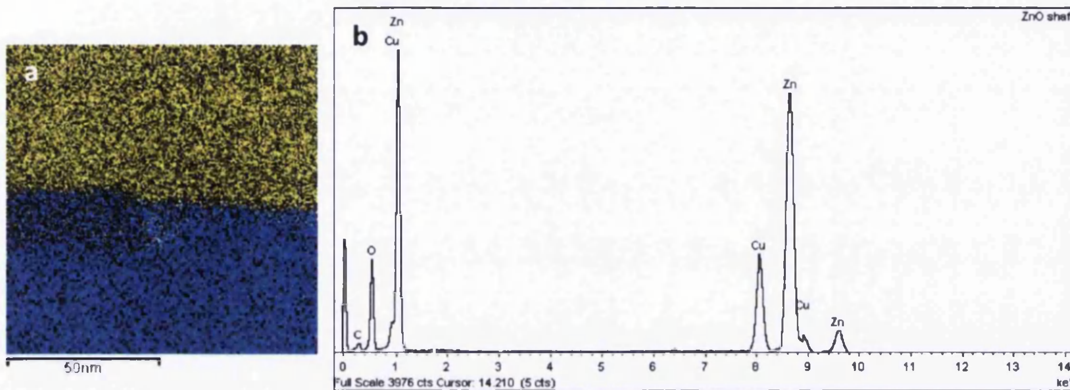

Figure 43. EDX-TEM analysis that can provide for example, **a)** a map of an area 100nm wide shows distinct diffusion of Zn (yellow) in to the Al (blue) of the Al_2O_3 substrate and, **b)** a compositional point scan of a ZnO nanowire which shows only the elements Zn, O and Cu that originated from the support grid.

4.6.6 Focussed Ion Beam (FIB)

This technique uses Gallium ions formed into a beam which can be tailored and focussed in a similar way to electrons in a SEM. Secondary electrons are emitted from the sample as the ion beam scans. The large Ga+ ions obliterate the sample where they are focussed and are used to create very fine TEM sections <100nm thick but several microns long.[90] This technique was used to create sections of NW arrays. A metal-organic precursor was used to protect the area of interest before the ion-beam milling. This was also used to mount the section onto the needle and the TEM grid. The diagrams in Figure 44 show the technique of the following process:

1. A 50nm Platinum layer was used to coat the sample surface
2. In the dual beam FIB system a metal-organic precursor was injected near to the site of interest and an initial layer of amorphous carbon and Platinum crystals were deposited with the electron beam

3. A fine layer of 300nm was built into a more coarse layer of 2µm thickness with ion-beam deposition
4. This protective layer allowed the milling and thinning of a cross section of 100nm thickness and several micrometres wide
5. Once the final thinning of the specimen was achieved with a more gentle ion beam the section is cut out
6. A micro-manipulator was then used to transfer the section on a needle to a TEM grid where it was adhered with the carbon deposit.

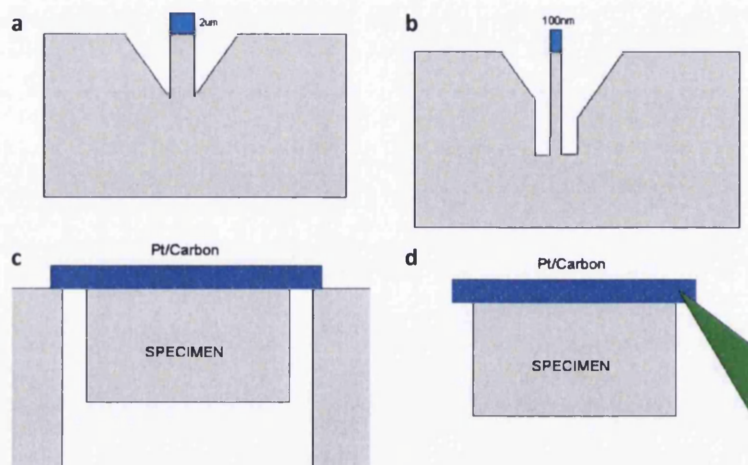

Figure 44. FIB specimen milling from a planar wafer, **a)** the surface layer of NWs is protected by a beam deposition of Carbon-Platinum from a precursor gas injected near to the site, **b)** the ion-beam is then used to mill out a specimen of 100nm thickness, **c)** and several micrometres wide, **d)** the section is attached to a probe and transferred to a TEM grid.

4.7 Scanning Transmission Electron Microscopy (STEM)

Dedicated STEM microscopes have become popular analytical tools because of the superb resolution they can achieve. They do not require a projection system to magnify the beam which allows more space for other detectors. To access this space the microscope is assembled with the electron gun on the floor, the microscope is assembled 'up-side down' relative to a TEM as shown in Figure 45a.

The beam formed at the sample is highly convergent and is scanned across the sample similar to SEM. The signal is measured at each scan point and digitally recorded. This signal maybe detected for example by a bright field or annular dark field detector, EDX, electron energy loss (EELS) or light detectors. The magnification is determined by the size of the scan collected pixel by pixel and not the microscope lenses. A major difference in the beam forming optics is the objective aperture lies before the specimen and directly determines

the convergence angle and the beam current focussed on the specimen, this is similar to the condenser aperture in a TEM. A collector aperture is used to define the collection angle and the electrons that contribute to a bright field image or EELS spectrum as shown in Figure 45b.[89]

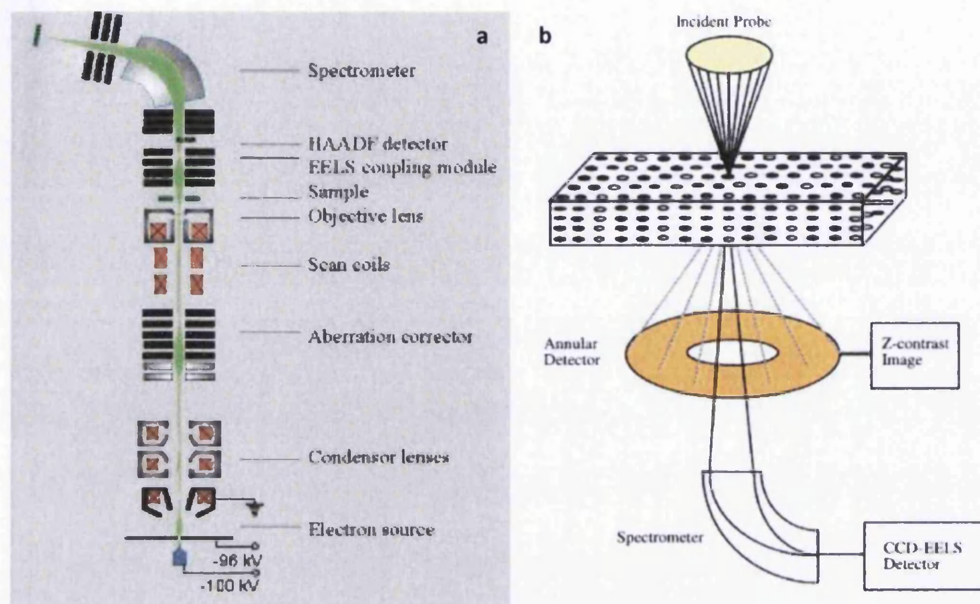

Figure 45. **a)** Schematic diagram of a dedicated aberration-corrected STEM with the electron source at the bottom and the detectors at the top, reproduced [255]. **b)** diagram depicting the beam-sample interaction in a STEM and the dual process of HAADF imaging and EELS analysis, reproduced[207].

A cold-field emission source provides the high brightness source from a very small area that is required for atomic resolution imaging.[207] The beam is focussed to a fine point on the sample and for analytical measurements it may be concentrated in one position for many minutes increasing the problems of beam deposited contamination. For these reasons dedicated STEM's use cold field emission sources in a UHV environment. The high brightness fine beam provides the best resolution and allows analysis of very small areas on the sample which can be scanned over a wide region. The advent of aberration correction has reduced the beam size even further.[89,90] For diffraction, EDX, EELS and other analysis a very small probe size achieves very high current density which provides a strong signal from a small region of the sample.[87]

Chromatic aberrations are reduced in a STEM as there are no lenses below the specimen unlike the projector system in a TEM.[87] A STEM excels with a low energy beam which improves contrast over the traditional TEM high kV (200-300kV) microscopes. A high kV is

traditionally favourable as it gives a brighter image, more penetration and better resolution.[87] But with the high brightness source used in a dedicated STEM and recently with aberration correction it is possible to achieve the best resolution of all using low accelerating voltages (60-100kV). The lower energy beam allows the analysis of low contrast samples such as biological specimens and also increases the impact of analytical signals of low concentration species.[207]

4.7.1 Limits on resolution in STEM

For high resolution work the three limits on resolution are the gun chromatic aberrations, spherical aberrations and the diffraction limit. The diffraction limit set by the objective aperture $\propto 1/\alpha$ and becomes insignificant as the convergence angle α is increased, this is compared to spherical aberrations which follow α^3.[89] A convergent beam focuses the beam to a small spot. This can limit resolution as the larger convergence angle introduces electrons far from the optical axis which are strongly subjected to spherical aberrations. For a STEM with convergence angle 10mrad, and no spherical aberration correction, the resolution limit presented by diffraction and spherical aberration is approximately 0.25nm. To overcome this and form sub-angstrom probe sizes the spherical aberration coefficient must be reduced to approximately zero which allows a very large convergence angle and a very small probe size.

4.7.2 Spherical aberration correction

Spherical aberration correction is achieved by producing the negative of the microscope aberration. The image aberration is measured and translated into adjustments of the beam in terms of beam offsets, tilts and defocus by the octupole and quadrupole currents.[208] This produces the negative of the microscopes aberrations before the objective lens which focusses all electrons to one single point and produces the extreme resolution.[208] Another very important effect is the great increase in brightness at the focal point which contributes to the possibility of sub-angstrom imaging. The first dedicated STEM spherical aberration corrector was demonstrated by Krivanek in 1997 [(138)] using a quadrupole-octupole corrector. By altering the microscope and improving the quadrupole –octupole design of the mark II Nion corrector the probe size was decreased below 1Å. Spatial resolution of 1Å was achieved with SuperSTEM I even at low voltages of 100kV. The introduction of the corrector itself introduces further order aberrations which the next generation of microscopes, for

example SuperSTEM II can correct up to the fifth order which improves the resolution to 0.8Å.[209]

4.7.3 High-Angle Annular Dark Field (HAADF) imaging

HAADF or Z- contrast imaging utilises an annular detector to collect high angle Rutherford and thermally diffuse scattering.[89,210] SuperSTEM II used for analysis here has an inner semi-angle of 79mrad and outer angle of 195mrad operated at 100kV. The angular range is large enough to exclude most diffracted or Bragg scattered electrons and the image has little dynamical diffraction contrast which can greatly limit electron analysis.[207,211] The resolution can be a factor of two better than coherent images with the spatial resolution only limited by the size of the focussed probe.[211]

4.7.4 Atomic-scale HAADF

HAADF is employed in this thesis specifically to investigate the diffusion of Au catalyst into ZnO NWs because the HAADF technique can display the presence of large Z-number atoms within the NW matrix.[15] Direct atomic analysis is possible with HAADF as it does not use the interference effect of diffracted and undiffracted electrons like bright field phase contrast imaging.[207] Figure 46 shows a typical HAADF image captured with SuperSTEM II of a ZnO NW.

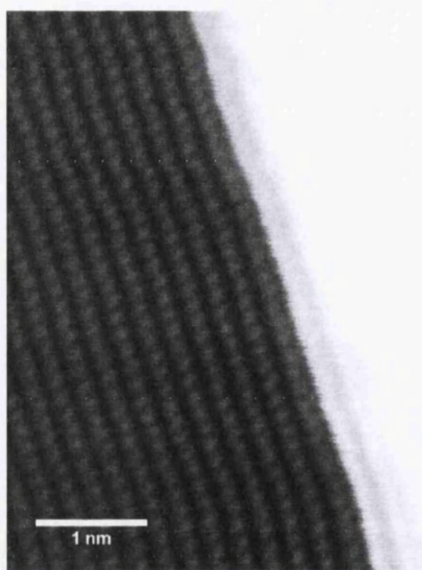

Figure 46. Atomic resolution high angle annular dark field image of a ZnO nanowire and the interface with the Au catalyst particle.

Once a sub-angstrom probe size has been formed scattering within the sample can degrade resolution. Very thin samples are required to increase the relative intensity of single impurities and to reduce beam spread. Crystalline materials on a zone axis orientation imaged with HAADF-STEM display sequentially illuminated atomic columns in which the intensity depends on the average atomic number.[207] The intensity of the atomic columns in thin specimens is dominated by the composition which is used to reveal impurity atoms which are otherwise hidden in the lattice.[15,207]

One of the great advantages of Spherical aberration correction is the ability to use large convergence angles that decrease the depth of field. This reduced depth of field improves the vertical resolution and STEM can be used for 3-D data sets. Combined with HAADF imaging it is possible to localise in three dimensions single large Z-number atoms.[140] Van Benthem et al propose a vertical resolution limit of $T_R \approx 2\lambda/\alpha^2$ and for a third-order aberration corrected STEM operated at 300kV with $\alpha = 23$mrad and $T_R \sim 7$nm.[140]

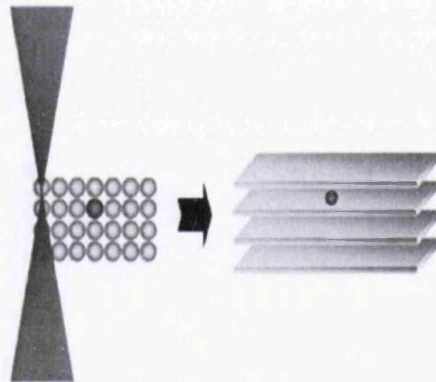

Figure 47. Concept behind a through-focal series used for 'sectioning' of the crystal lattice to identify single atom impurities. Reproduced[140].

The fifth order correction of SuperSTEM II allows even greater convergence angles and sub-angstrom probe sizes at low kV. Therefore at 100kV and a convergence angle of 30.5mrad a similar vertical resolution is achieved with the benefit of reduced beam damage and contamination. The excess intensity in the region of a high Z-number atom within a lower Z-number matrix makes it possible to locate the vertical position with a precision far better than the resolution limit.[140] By sectioning the region around an atom with a through-focal series of images the intensity profile can determine the position to within $\pm$0.5nm.

4.7.5 Comments on the detectability of single Au impurity atoms

In spite of the large atomic weight difference between Au (Z_{Au}=79) and the ZnO host matrix (Z_{Zn}=30 and Z_O=8), detecting single impurity atoms in crystalline ZnO NWs can prove a difficult challenge. Electron beam channelling along crystallographic directions can for instance influence the recorded intensity so much that heavy substitutional dopants atoms become 'invisible'. Inclining the sample away from perfect zone axis alignment is a well-known 'trick' to reduce channelling and enhance the contrast of impurities. It was applied very successfully in a recent study to detect single Au atoms in GaAs NWs of similar diameter to the ZnO NWs of interest here[136], even though the atomic weight ratio Z_{Au}/Z_{Ga}=2.55 was lower than the detectability criterion proposed by Voyles et al for a point defect impurity of $Z_{dopant}/Z_{host} \geq 3$. (in the case of an uncorrected electron microscope[212]). With Z_{Au}/Z_{Zn}=2.63 the detection of Au in ZnO was also favourable. Interstitial impurities are expected to be clearly visible if the sample is viewed along a crystallographic direction with large enough distances between columns [134,213]. Even with application of these techniques it was necessary to conduct HAADF image simulations to reveal the expected excess intensity that may occur from single Au atoms embedded within the ZnO matrix.

4.7.6 Quantitative TEM/STEM simulations

The QSTEM software[65] written by Koch offers simulation of HAADF-STEM images (also TEM and ADF images) using the Multislice algorithm. The Multislice algorithm is a numerical integration of the Schrodinger equation and the solution provides the wavefunction of electrons incident on a crystalline sample after interaction with the atomic lattice. The sample was 'cut' into thin slices parallel to the surface which can then be treated as two-dimensional slices which simplifies the scattering processes. Integration was performed over the slice thickness and this was repeated for each subsequent slice and eventually the wavefunction at the exit surface of the sample was calculated. The software was able to take into consideration beam aberrations and probe characteristics.

By constructing the atomic crystal formation of the sample of interest the software calculated the interaction of the beam with the lattice and simulates a HAADF image that would be expected for the specific microscope. In this manner it was possible to substitute in individual foreign atoms and simulate any excess HAADF intensity that may have

occurred. Simulations were performed by Quentin Ramasse and Demie Kepaptsoglou at the SuperSTEM laboratory. An example of the simulation results is given in Figure 49.

4.8 Scanning Transmission Electron Microscopy Experimental details(STEM)

STEM imaging and analysis was performed at the SuperSTEM site at Daresbury by Quentin Ramasse.

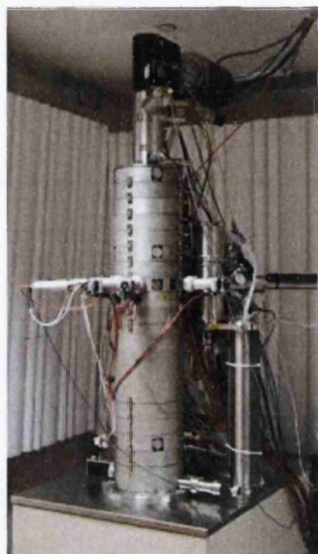

Figure 48. The SuperSTEM II microscope is housed in a purpose built facility in Daresbury with vibration isolation to ensure the best resolution is achieved.

The microscope used was the SuperSTEM II fifth-order aberration corrected microscope, Figure 48. High Angle Annular Dark-Field (HAADF) simulations were performed by Quentin Ramasse and Demie Kepaptsoglou. Samples were prepared at the Multidisciplinary Nanotechnology Centre at Swansea University and screened with TEM by Michael Ward at Leeds University. STEM Imaging concentrated on very thin catalysed ZnO NWs with distinct Au catalyst particle tips although non-catalysed NWs were imaged for comparison.

4.8.1 Equipment

The SuperSTEM II Nion Ultrastem 100 microscope was operated at 100keV for imaging. The microscope is equipped for full spherical aberration correction to the fifth-order with a Nion QO corrector to sixth-fold astigmatism $C_{5,6}$. A UHV Enfina EELS spectrometer is also fitted. The facility and microscope are designed to minimise structural and mechanical vibrations and the microscope is designed to minimise the influence of external magnetic fields on the beam. Beam damage was reduced by short dwell times during scans, in most cases damage

was negligible. An accelerating voltage of 100keV was used as contamination was not significant during any analysis. The probe-forming optics were configured to provide ~100 pA of beam current with a 31 mrad beam convergence semi-angle, for an estimated probe size of 0.8 Å. The inner and outer radii of the HAADF detector were calibrated at 79 mrad and 195 mrad, respectively. HAADF and bright field imaging were performed simultaneously.

4.8.2 Sample preparation

NWs were directly transferred from NW arrays to holey carbon film coated TEM copper grids. Each grid was baked at 120°C overnight at 10^{-6}mbar to remove loosely bound gaseous species and water. The grids were loaded into the microscope and left to thermally stabilise which was crucial for atomic scale imaging. NW arrays were grown specifically for STEM-HAADF analysis particularly those grown by catalytic methods. For ideal analysis NWs were required to be thin, ~15nm diameter, with a distinct catalyst particle at the tip. This maximised the intensity of any signal from Au contaminant atoms within the NW bulk or surface even at low voltages. Non-catalysed NWs of similar diameter were required for comparison. The non-catalysed NWs were taken from Non-catalysed growth experiment 202 and the catalysed NWs were taken from Catalysed growth experiment 31. Specimens were initially rotated to the most accessible zone axis to allow single atomic columns to be resolved and imaged.

4.8.3 QSTEM simulations

To confirm the validity of the HAADF imaging of Au atoms in ZnO image simulations were performed using the multi-slice method as implemented in the QSTEM Software Suite[65]. The software used measured experimental parameters for the probe convergence, detector geometry and aberration coefficients. The chromatic aberration coefficient was set to Cc=1.3 mm and the native energy spread of the cold field emitter of the instrument was ΔE=0.30 eV. Thermal diffuse scattering effects were simulated using a total of 15 frozen phonons in the simulations. Finally, partial coherence effects (due to finite probe size or instabilities for instance) were incorporated in the simulations by convolution of the simulated images with a Gaussian of 0.08 Å full-width at half-maximum.

Slabs of ZnO of various thicknesses were created for the simulations aligned along the $[01\bar{1}0]$ zone axis and with a flat entrance and exit surface. Single Au atoms were then substituted for Zn atom at various depths within the slab (along the beam propagation direction), without any additional relaxation of the lattice. While a crude approximation to a Au substitutional impurity, this model provided a good estimate of the additional contrast heavy Au atoms were expected to generate when inserted within the host matrix, see Figure 49.

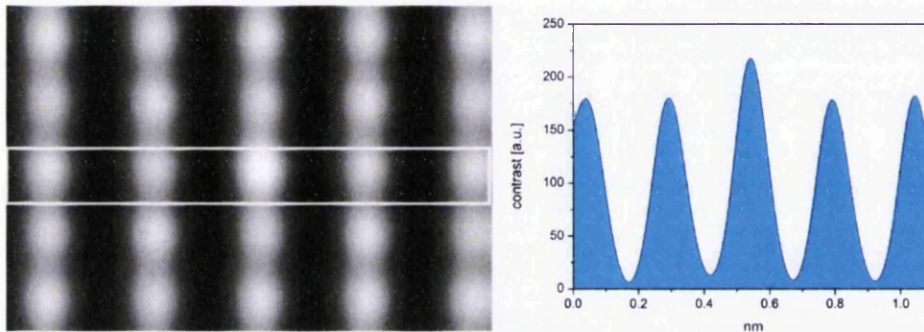

Figure 49. Example of the simulated HAADF image calculated by the QSTEM software and the line profile indicating the increase in image intensity with one Au atom located at the centre of a 7nm thick ZnO slab.

4.9 Nanoprobe electrical measurements

Once the NWs had been thoroughly characterised structurally and compositionally it was possible to apply the nanoprobe technique to measure the resistivity of NWs from three growth methods. The four-probe measurements building on the structural analysis enabled a comparison of deposited Au contacts on non-catalysed NWs and catalyst particle Au contacts using the nanoprobe in a two-probe configuration. This was performed with the NWs in the as-gown free-standing vertical configuration. This was possible due the precise positioning of the probe tips and the good contacts made between the probe tips and NWs. The principles of the four-probe technique and the two-probe technique are described in this section followed by the experimental details, an image of the microscope is shown in Figure 54a.

4.9.1 Four-probe electrical measurements

Four-probe electrical measurement is required to remove the contact resistance associated with metal-semiconductor contacts (see Chapter 2) that can dominate two-probe measurements, however the technique can be applied to most materials not just

semiconductors. Two outer probes act as the current source whilst the 'inner' probes measure the voltage and Ohm's law is used to calculate the intrinsic resistivity of the material measured, as shown in Figure 50. The resistivity is calculated from the measured resistance of the inner probe voltage against the outer probe current scaled by the cross-sectional area A and inner probe separation L.

$$\rho = \frac{R * A}{L} = \frac{V_{inner} A}{I_{outer} L}$$

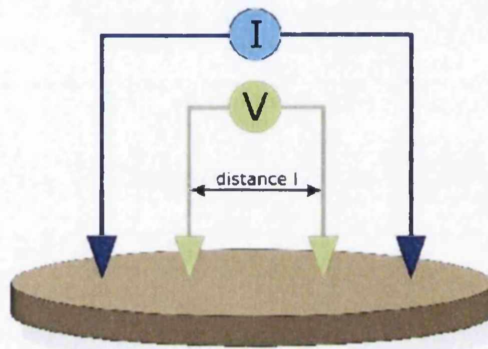

Figure 50. Schematic diagram of the four-probe electrical measurement technique which can be applied for measuring resistivity. Reproduced[256].

The essence of this technique is to supply a controlled current through the sample and measure the voltage with two separate probe tips at a known separation. Using the inner probes for voltage measurement removes the error of probe resistance, spreading resistance and most crucially the contact resistance of each probe with the sample. The contact resistance is removed from the measurement as this does not affect the voltage drop across the sample or across the inner measuring probes but the technique is only valid when four equal contacts are formed. The four-probe technique is most useful in the case of low-resistance materials when the contact resistance associated with the metal probe-semiconductor can be greater than the sample itself. This is always a major issue with two-probe measurements, although these can be improved by Ohmic contacts.

4.9.2 Two-probe electrical measurements

The two-probe technique can suffer greatly from contact resistance that may dominate the measurement of a sample. However the measurement technique is useful when the structure of interest is a contact itself, e.g. metal deposited on a semiconductor. The two-

probe technique can be used to investigate the properties and behaviour of the contacts created on the semiconductor, for example Ohmic or rectifying. Fabricated metal contacts or probes in direct contact with a semiconductor form a metal-semiconductor interface which may form a rectifying potential barrier or an Ohmic contact, the principles governing metal-semiconductor contacts are discussed in detail in Chapter 2. Ohmic contacts still have a contact resistance which may be great enough to contribute to the measured resistance and this is the reason for the four-probe technique.

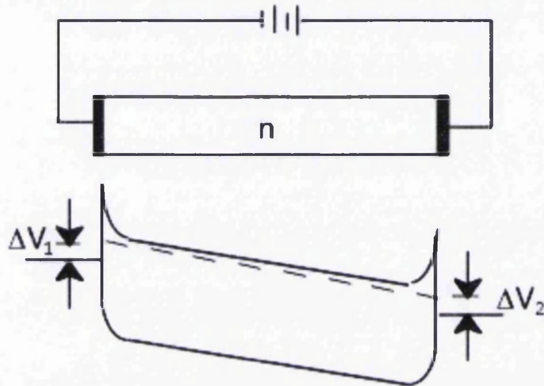

Figure 51. Circuit diagram of an n-type semiconductor contacted by two electrodes and the band diagram which depicts one contact in forward bias and the other in reverse bias. The voltage drop across the two contacts and the semiconductor all contribute to the measured voltage.

Figure 51 shows the circuit diagram that represents two-probes in contact with a semiconductor and the band diagram with one contact in forward bias and the other in reverse bias. The diagram depicts the potential drop across each contact as different i.e. the contacts are unequal. The inequality can represent two Ohmic contacts, one of high resistance the other of low resistance, or the contacts can be Schottky barriers. For two back-to-back Schottky barriers little current is measured but in the case of one Schottky and one Ohmic contact the current flow is dictated by the Schottky barrier. The total potential drop is a sum of the potential drop across each contact and the semiconductor.

A metal in contact with an n-type semiconductor generally induces a depletion region which extends from the surface into the bulk of the semiconductor. In this region charge carriers have moved from the conduction band into the metal to find thermal equilibrium and charge readjusts across the interface. This leads to band bending, a potential energy barrier at the interface and region of positive uncompensated donors in the semiconductor near the interface. This barrier can be small or large, and the characteristics of the potential barrier determine the carrier transport that can make an appreciable contribution to

current flow once a bias is applied to the contact. These processes are thermionic emission for high temperatures with wide barriers, recombination for high intrinsic carrier concentrations and a small bandgap, or tunnelling for narrow barriers that maybe a result of high doping or high electric fields (these are discussed in detail in Chapter 2). The depletion region in bulk contacts is determined by the material properties. However, in small nanometre sized contacts the scale of the contacts can govern the extent of the depletion region which becomes small and tunnelling becomes more important.[60]

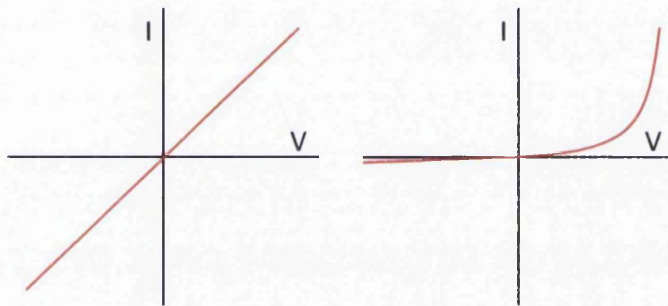

Figure 52. Diagrams depicting the current – voltage characteristics of an ideal Ohmic contact and an Ideal Schottky contact.

A Schottky contact is the result of a significant barrier that has an easy forward and hard reverse bias characteristic. This is shown in a sketch of a typical I-V measurement for an Ohmic and rectifying contact in Figure 52. An Ohmic contact may have a large barrier height and a thin depletion region that allows significant tunnelling, or alternatively the conduction band aligns with the metal Fermi level and no barrier to charge flow is present i.e. the metal work function is less than semiconductor electron affinity. Ohmic contact is represented by a linear I-V characteristic as current flows equally in forward and reverse bias and ideally provides negligible resistance to current flow compared to the specimen. The most useful fabrication technique of Ohmic contacts uses thin barriers that can be easily tunnelled through. Traditionally an Ohmic tunnelling contact was only achievable with heavy doping of the near interface semiconductor region but we investigate here nanoscale contacts dominated by tunnelling without degenerate doping in Chapter 7.

4.10 Electrical measurements experimental details

ZnO NWs grown with and without Au catalyst by the vapour phase technique, and hydrothermal NWs were measured in UHV with the four-probe method. These

measurements were intended to reveal the 'bulk' conduction characteristics of several NWs from the three growth methods. The results of these measurements were used to validate the comparison of Au contacts on catalytic and non-catalytic vapour phase NWs by the two-probe method in UHV using the Nanoprobe. Four-probe measurements were conducted at Leeds University by Alex Walton and the Author. Two-probe measurements on Au deposited non-catalysed NWs were conducted at Leeds University by Alex Walton and the Author and Two-probe measurements on bare non-catalysed NWs and Au tipped Catalysed NWs were conducted at Omicron Germany by Juergen Köble, the Author and Nathan Smith.

4.10.1 Equipment specifications

The Omicron UHV Nanoprobe comprises 4 individual STMs guided by a high resolution Gemini FEGSEM. By guiding the four STM tips with the SEM it is possible to form reversible, non-destructive electrical contacts to an individual nanostructure. It has a liquid Helium flow cryostat allowing measurements to be taken at 25-450 K. The electrical measurements were conducted with a Keithley 2601 source meter with a measurement range of picoamp to Amp. The nanoprobe at Leeds had a manual switch box for switching source and measurement tips, whereas in Omicron a HP multiplexer 3488A was used.

The NP used on the Omicron site was similar to the Leeds model but with an improved Gemini column. This provided 3nm resolution SEM over 5nm resolution in Leeds. This improved imaging of fine details such as Au catalyst particles on NW tips. The NP also included in the load lock a homemade field emission tip cleaning process that placed a high voltage on the etched W tip. This removed oxides and contamination but did not alter the tip shape, sharpness or flexibility.

4.10.2 Four-probe NW sample preparation

Suitable NWs were grown specifically for each experiment performed. Four-probe measurements required long NWs of several microns in length to allow multiple probe positions. The diameter of the NWs was tailored to ensure the full range of ~40-100nm diameter was covered for each NW type. Catalysed and non-catalysed vapour grown NWs were measured along with high-pressure high temperature hydrothermal NWs.

NWs were directly transferred to Au patterned insulating SiO_2 substrates that were patterned with photoresist using photolithography. Linear photoresist tracks of 10-20um in

width and spacing of 10um or 30um were formed before Au was deposited and the resist lifted off. This process formed Au tracks covering ~5mm^2 over the sample with a connecting electrical contact pad at either end. Substrates were then solvent cleaned and crucially Piranha etched to remove any traces of the patterning process. The piranha clean was essential to avoid significant beam deposition in the nanoprobe. NW coated substrates were then transferred into the nanoprobe and the NWs lying between the Au tracks were measured.

4.10.3 Two-probe NW sample preparation

Two-probe samples required low density vertical NWs to allow easy probe access without contacting other NWs, Figure 53. Very long NW >5um proved to be very flexible and difficult to measure precisely. Therefore short NWs <3um long and ~Ø80nm were most suitable to provide some rigidity and ample top facet surface area to place the probe. Catalysed NWs with Au particles at the tip were compared to catalyst-free NWs with deposited Au of various thicknesses. Au was deposited by evaporation onto the NWs. The morphology and structural properties of the evaporated and catalysed Au contacts were characterised by SEM, TEM and STEM.

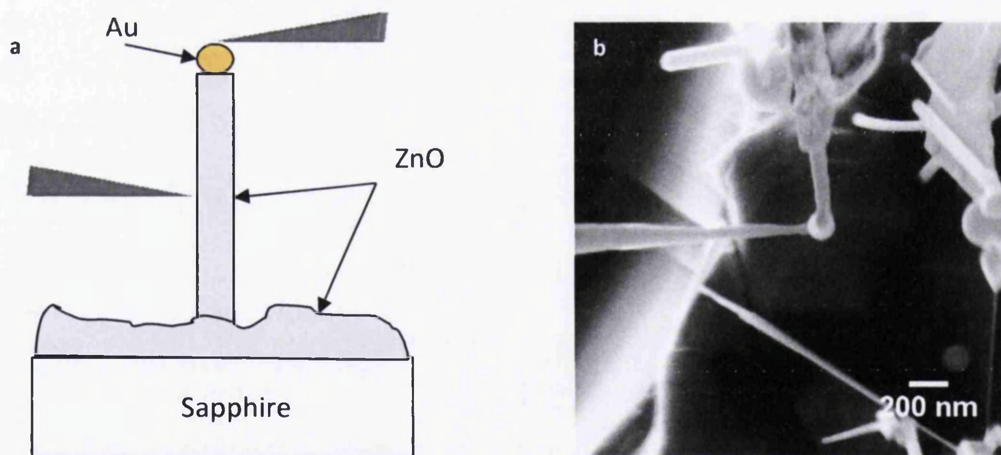

Figure 53. **a)** Diagram depicting a 2-Probe measurement of low areal density vertical ZnO nanowires with Au tip. **b)** the nanoprobe in-situ SEM image of a two-probe measurement. One sample set had Au tips from the growth catalyst and the other had Au deposited onto bare non-catalysed nanowires. These measurements were compared to nanowires with no Au tips as a reference.

NWs were grown at a suitable density for probe access to ensure no additional current path was formed by inadvertently touching another NW, Figure 53b. Looking at NWs in the top-down perspective the in-situ SEM can resolve catalyst particles on the top facet which ensures reliable measurement and contact to the Au. The actual ZnO NWs for each Catalysed I-V sweeps are of similar diameter (~70-80nm) but the particle size varies. NWs for the non-catalysed NWs covered a large range of diameters (40-250nm) and Au thickness (10-50nm).

The majority of NWs were difficult to measure in the free standing two-probe configuration because good contacts were sometimes difficult to establish. This was the main difficulty with the technique. However for some NWs good contacts were easy to establish probably due to relatively highly doping allowing good Ohmic contacts to be formed.

4.10.4 Nanoprobe Preparation and sample loading

The NW coated substrates were loaded into the load lock (Figure 54a) of the Nanoprobe and pumped down until the vacuum pressure of 10^{-10}mbar was reached. The substrate was then transferred to the main chamber with the transfer arm. Tips were transferred in similar fashion onto the main stage (Figure 54b) using the tip and sample carousel. Using SEM imaging and the piezo control the tips were positioned close to the surface. The final approach used the tunnelling feedback technique when the sample had Au tracks. The Au tracks were of similar thickness to the NW diameter and so the tips could then be moved laterally into position onto a NW, Figure 55. It was possible to approach directly onto a NW without the feedback loops by careful manual control of the coarse and fine piezo-steppers which have nanometre precision. This control allowed manipulation and measurement of NWs in flat and vertical configurations. Once the tip touched the NW it was seen to glow in the SEM image even in the absence of an applied potential. Experiments were conducted at 25°C/298K and 10^{-10}mbar or better which takes approximately one hour of pumping once the sample was loaded into the main chamber even though samples were not baked before or during experiments. The SEM provides a top-down view of the flat sample as shown in

Figure 55.

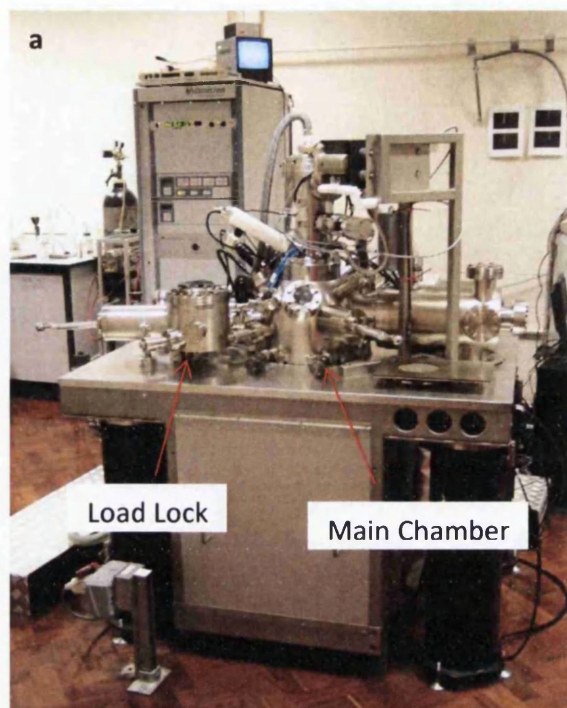

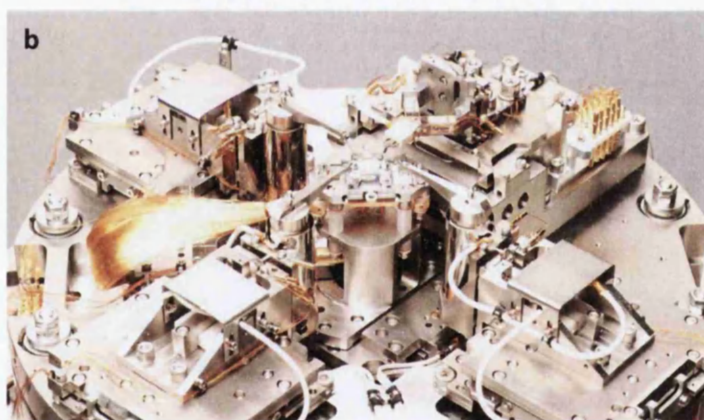

Figure 54. **a)** The nanoprobe system at Leeds University and the load lock where samples were mounted in a carousel and transferred into the main chamber with the transfer arm. **b)** The four probe tips mounted on the sample stage are controlled by fine- and coarse- piezo motors. The tips were etched and placed in the tip holder and mounted into the carousel for transfer into the main chamber.

4.10.5 Probe Tip preparation

The probe tips in the nanoprobe are fine 0.38mm Tungsten wire which was cut to length and then etched to provide a sharp tip. Tips were not required to be atomically sharp like STM but the length, flexibility and sharpness of the point all contributed to a good tip. More rigid blunt tips proved to be the best for four-probe measurements because these allowed pressure to be exerted at the contact and were robust enough to withstand many measurements. These tips were etched under a DC current, Figure 56a. More flexible tips

were required to measure very thin NWs (diameter 40nm) in the four-probe configuration and for the two-probe measurements to avoid disrupting the Au contact and damage to the NWs. These tips were etched under an AC current, Figure 56b.

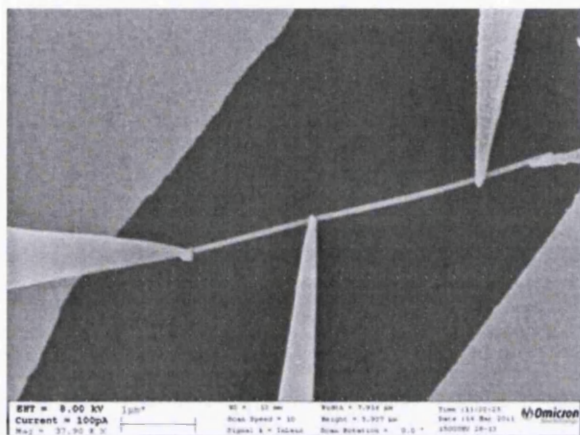

Figure 55. In-situ SEM top-down image of a Four-probe measurement on a ZnO NW with the Nanoprobe. The bright regions on the substrate are Au tracks used for locating the tips vertically on the sample.

Tungsten wire tips that were DC etched in Potassium Hydroxide solution will be referred to as 'DC tips', Figure 57. Tips prepared at Omicron required more preparation and will be referred to as 'AC tips'. Typically for AC etched tips the wire was first mechanically drawn, then AC etched to thin the wire further which provided the longer flexible tip and then a final DC etch to give the very small nanometre radius apex. AC tips were essential for probing NWs thinner than 50nm because the flexibility eliminated wire damage. Flexible tips bend when pushed onto a NW which allowed good adjustment of the contact without cutting or crushing the NW.

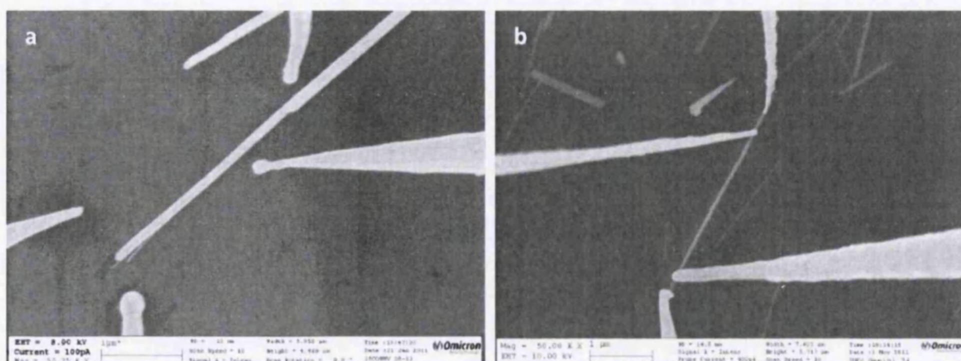

Figure 56. In-situ SEM images taken at 50,000x magnification depicting the difference between, **a)** DC etched tips and, **b)** AC etched tips which improve the ability to measure NWs less than 50nm diameter significantly reducing damage, the scale bar for both images is 1µm.

After loading the tips it was necessary to remove oxides and other contamination by cleaning them in the nanoprobe. DC etched tips at Leeds University were cleaned by touching two tips together and passing a current between the two until the resistance was negligible. Care was taken to avoid excessive melting of the tips and to ensure contamination was removed from all over the tip surface. AC etched tips in Omicron Germany were initially cleaned in the load lock by filament field emission using a high voltage, this had the advantage of maintaining the sharp tip and avoided melting which can alter the tip shape. The field emission clean also had the effect of cleaning more of the tip and not only the local high resistance point where the tips touch together. This may have removed more of the etching contaminants which may cause beam deposition onto the sample and tips. The DC etch procedure within both tip preparation methods is the same and so only the AC procedure is stated.

The AC etch procedure at Omicron to etch tungsten nanoprobe tips:

- Tungsten wire 0.38mm, ~12mm long
- Fast AC etch procedure (NaOH), removed contamination and reduced the diameter of the tip to a more conical shape
- DC etching (NaOH) with homebuilt electronics that has an automated threshold switch monitoring the current to stop the etching procedure on time
- Brief cleaning with distilled water
- Vacuum field emission annealing at roughly 1100°C to remove residual contamination

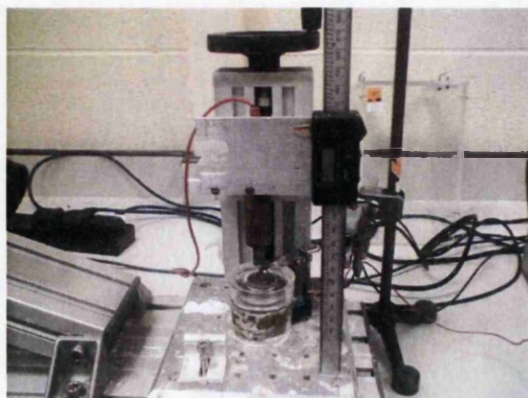

Figure 57. The DC etching apparatus used at Leeds University, the Tungsten wire is under DC current which is applied across the wire and the electrolytic solution which slowly etches the wire.

4.10.6 Nanoprobe 4-probe measurement technique

The four probe technique involved positioning the four clean tips onto a NW and taking current-voltage measurements. The current between each of the four tips was tested for a magnitude of 10^{-7}-10^{-6}Amps which was typical for good contacts on ZnO NWs, see Figure 58a for an example of the current-voltage characteristics of a four-probe measurement and the corresponding outer probe two-probe measurement. The tips were adjusted until a good contact was formed and the current scaled approximately according to tip separation. The scaling of the current was important as it indicated four approximately equivalent contacts which are necessary for a legitimate four-probe measurement. Once four good contacts were established a four-probe measurement was performed with an applied voltage sweep across the outer probes, usually $\pm$0.5-1V, and the voltage across the inner probes was measured. The resistivity can then be calculated as

$$\rho = \frac{R * A}{L} = \frac{V_{inner} A}{I_{outer} L}$$

The outer probes were then kept in position and the separation between the inner probes was changed. Usually measurements started with a wide separation and then reduced with one probe in its initial position. However, it can be beneficial to use a more random inner probe positioning to investigate any unusual effects, for example if the structure is inhomogeneous.

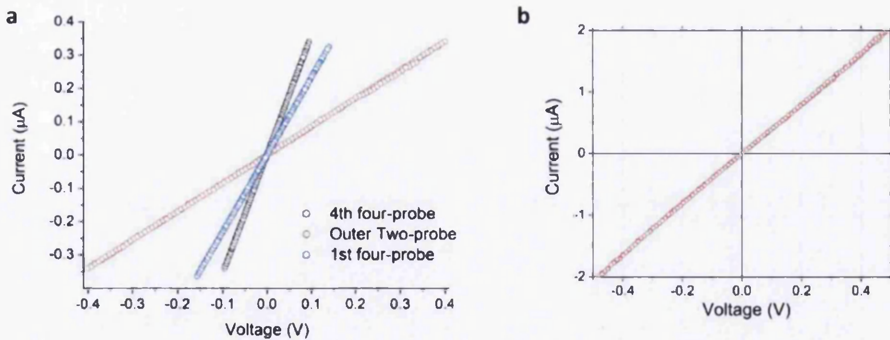

Figure 58. **a)** Current-Voltage graph depicting four-probe measurements and the corresponding outer probe measurement for a non-catalysed NW, the 1st and 4th probe measurements correspond to probe positioning on the nanowire. The 4th measurement had the inner probes closer together. **b)** an I-V measurement depicting an Ohmic linear I-V graph of a side-to-side two-probe measurement across a nanowire.

Multiple measurements, usually five or six, were completed on each wire. The majority of measurements were conducted with NWs transferred in flat lying configuration to simplify

tip positioning and contact formation. Four-probe measurements on free standing NWs and on NWs detached from the substrate were attempted but good contact on all four tips was difficult to achieve.

4.10.7 Nanoprobe two-probe measurement technique

Measuring catalysed Au-ZnO contacts were the more involved electrical experiments as it was required to initially pinpoint the catalyst particle. The particle is known to on occasions fall off the top facet and many can be found either on the NW side or at the base.[58,117] Therefore it was necessary to locate NWs with suitable catalyst particles on the top facet with BSE and SEM. Then using a series of images at increasing magnification the same NWs were located with the in-situ nanoprobe SEM. Catalyst particle interfaces (CPI) were measured in Omicron Germany to take advantage of the better resolution of the SEM which could resolve the Au particles and determine whether the particles were in place on top of the wire before and after a measurement. Deposited Au interfaces were measured at both nanoprobe sites with AC and DC etched tips. AC etched tips allowed fine adjustment, manipulation and positioning on the NW.

Two-probe measurements allowed the measurement of free standing vertical NWs as part of the original array which investigated the electrical contacts formed by the Au-NW interface at the tip of individual NWs. The optimum procedure to contact the NWs was to turn off the tip approach feedback loops and rely on manual piezo control. This required the tips to be lowered very carefully to the height of the NW without crashing into the substrate or other NWs – operator skill was essential. Ohmic contacts formed at the probe-ZnO NW side contact made these measurements possible and avoided the requirement for an intermediate contact material, see Figure 58b for an example of the side-to-side Ohmic contact achieved on a NW before measuring the Au contact. An I-V sweep was typically performed $\pm$0.5-1V and the shape of the output provided many characteristics of the contact along with the current for which a typical magnitude was micro-amps, consistent with the four-probe measurements of ZnO NWs. Results are discusses in detail in Chapter 7.

The Two-probe measurement method of CPI's is performed as depicted in Figure 59 as follows:

1. Identified suitable NWs with SEM and BSE imaging, this step also allowed measurement of the Au particle and NW diameter
2. Local 'landmarks' were used to identify the same NW with the in-situ SEM and then the probe tips were brought in side-to-side on the NW
3. Contacts were then tested with I-V sweeps, a good contact provided linear I-V and micro-amps current, good Ohmic contacts on the NW side were essential to minimise the effect of side contact resistance in the Au contact measurement
4. One tip was raised above the NW and lowered under a small 100mV applied bias until a current spike was observed
5. The Au NW contact was then measured with an I-V sweep, the top probe tip was then raised and lowered again in similar fashion and the measurement repeated several times
6. Tips were then removed and the catalyst particle was identified atop of the NW

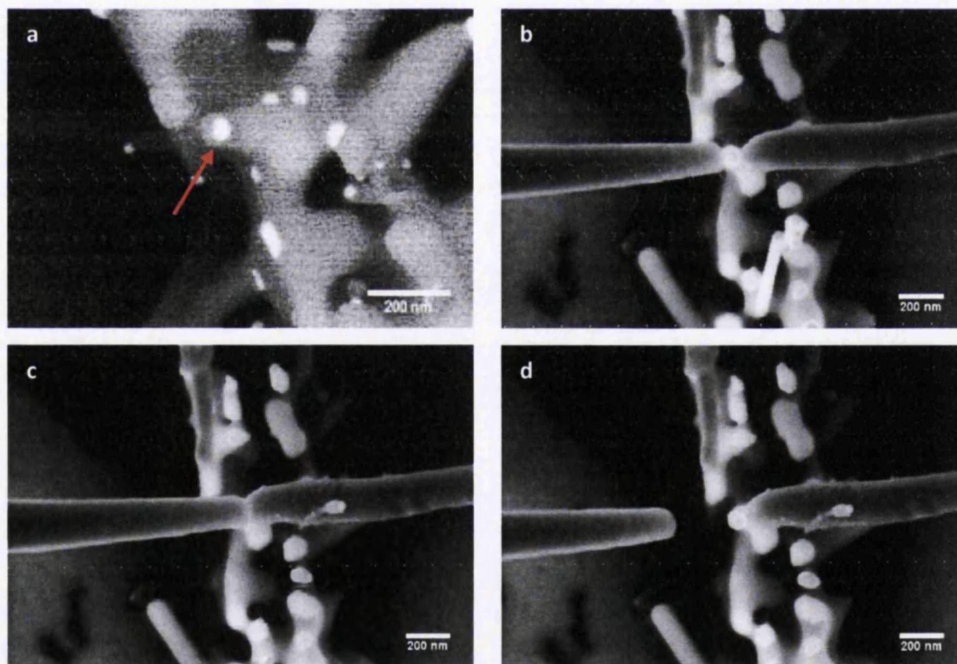

Figure 59. Images depicting the process of identifying a catalyst tipped NW and two-probe measurement, left-to-right fashion from the top-left. **a)** the NW with a 'bright' Au particle on the top facet is identified by SEM and BSE. **b)** the same NW is then identified in the Nanoprobe and the probe tips are brought in to test the contacts side-to-side across the NW. **c)** one probe is then raised above the NW and lowered onto the Au particle using a small applied bias and real-time current monitoring, once contact is achieved an I-V sweep is taken. The probe is then physically raised and lowered in similar fashion to repeat the measurement several times. **d)** probes are then removed and the catalyst particle is identified on top of the NW

4.11 Summary of the Experimental techniques

Zinc Oxide NW growth, like any other crystal growth, is not an exact science. However in order to explore and characterise the NWs it was necessary to control the NW growth to create samples of sufficient quality for application to devices and also allow characterisation with the described techniques. SEM provided the immediate characterisation of the NW growth samples which was used to assess the alignment, quality and morphology of the product. Optimum but typical samples were selected for further TEM analysis to examine bulk crystal structure. TEM allows imaging using phase contrast of the atomic lattice planes and to reveal the structure of the Au contact interface at a resolution of approximately 0.25nm. Combined with EDX and HAADF a thorough compositional analysis of the NWs was completed. However, as described in Chapter 2 catalyst metal contamination can greatly hinder some NW materials, such as silicon. Only two techniques are capable of imaging single impurities within crystalline materials which are aberration corrected HAADF-STEM and Atom Probe tomography. Atomic resolution of HAADF-STEM made it possible to study the NWs at an atomic level and to examine the catalyst particle interface with depth sectioning techniques that is not possible with most metal contact structures e.g. nanocontacts on a planar substrate. This was necessary to assign the appropriate analysis to the electrical measurements which take advantage of the nanoprobe system. The nanoprobe allows measurements of the true NW resistivity NWs without patterned contacts and surface modifying processing steps in UHV free from environmental effects.

Electrical contact on the nanoscale can be greatly affected by many problems such as barrier inhomogeneities, defects, edge effects and dopant atoms. However the thorough characterisation of the NWs and the contact interface has allowed us to form sound arguments and single out the most appropriate explanations for the two-probe results of Au deposited and catalyst particle contacts on ZnO NWs. This body of work is able to reveal the behaviour of the catalyst Au contacts and deposited Au contacts with measurements that are free from confusing contributions that originate from conduction through the substrate and patterned contacts processing. Both influences can result in very low currents due to contamination, scattering and long conduction paths with multiple interfaces. We measure the current across the Au-NW interface with local probe measurements free from all of these potentially detrimental effects.

Chapter 5

5 ZnO Nanowire Growth and Contact fabrication results

NW growth experiment results of ZnO NWs by vapour phase Au catalysed and catalyst-free methods are detailed in this chapter. Also covered here are the experiments tailoring the Au catalysed growth to achieve distinct Au particle growth tips along with the fabrication of Au contacts on non-catalysed NWs. The major tools of characterisation were Scanning Electron Microscopy (SEM) and Backscatter Electron (BSE) imaging which provided the typical representations that are given to cover the major aspects of progress. The products from experiment to experiment, especially for non-catalysed NWs, were variable and to avoid unnecessary detail and to gain the most useful knowledge from the experiments strong trends with experimental parameters are reported. Trends in experiments of lesser success are briefly stated. The major aim of growth experiments were to achieve perfectly aligned arrays of NWs, suitable for devices with high areal density and inform morphology, or suitable for measurement purposes with low areal density or a specific NW size.

5.1 Previous work

The growth experiments built upon previous work by the author during his MRes project that investigated catalysed and non-catalysed growth on ZnO solution based seed layers.[203] Previously the seed layer was formed on single crystal Silicon wafer and achieved arrays of aligned ZnO NW growth. Formation of ZnO seed layers from solution was the major achievement along with growth on non-lattice matched substrates, this technique is implemented here to grow vertically aligned arrays of NWs on conducting substrates such as metals and oxides. Solution based seed layer deposition involves dissolving Zinc Acetate into ethanol and dispersing on a clean substrate and annealing in air to form ZnO, the method is discussed in Chapter 4. In this chapter experiments specifically investigate:

- catalytic growth on lattice matched Sapphire and GaN
- non-catalytic NWs using solution- and plasma-assisted ZnO seed layers on metals and ITO
- non-catalysed growth on bare roughened a-plane Sapphire.

Details of the sample and experiment preparation and procedures are detailed in Chapter 4. All SEM and BSE images were taken at 30° sample tilt or top-down, geometrical considerations can show in the tilted perspective the NWs were in fact double the projected length.

5.2 Catalysed ZnO nanowire growth

Catalysed ZnO NW growth utilises Au catalyst that is deposited on the substrate before the growth experiment. The Au film (~1-6nm thickness) breaks up into nanoparticles at the growth temperature which capture the source Zn vapour. Saturation of Zn on the particle surface or in the particle bulk initiates growth and a NW is formed atom by atom. Using a catalyst provides increased control over the growth product relative to non-catalysed NW growth. For this reason 40 experiments were required in total to tailor the growth for all subsequent experimental measurements that included:

- Very thin NWs (<20nm diameter)
- Long NWs (4-6μm) of various diameters (40-100nm) for four-probe electrical measurements
- Arrays of vertical low density NWs

All experiments required distinct Au catalyst growth tips to be present on the NWs to ensure they had grown by catalytic means rather than by a vapour-solid process. This requirement ensured the growth method was distinct from the catalyst free growth modes which could still contribute in these experiments. A complete table of experimental growth parameters along with the experiment numbers is included in Appendix A-1. The major aims for catalysed growth were control of the NW array density, NW length, NW diameter and the presence of Au growth tips that had to be identified with BSE imaging.

5.2.1 Growth tapering

Samples positioned further from the source exhibited shorter and thinner NWs. Eventually the growth product tapered to nothing where the furnace temperature was cooler. A temperature gradient from the furnace centre, where the source is located, decreases away from the hottest zone. Moving away from the source reduces the local Zn vapour concentration that was observed through all experiments as overgrowth at the sample boat front, then a region of good high density growth ~1cm from the front, and then growth

diminished to nothing at the boat rear. The tapering regions towards the boat rear proved most useful for nanoprobe measurements of free standing wires (Figure 60a). Along with thick Au depositions (~4-6nm) many high aspect ratio NWs with distinct Au tips could be found. The catalysed NWs in this region varied greatly in length 1-3μm and diameter 20-100nm. The longer NWs were usually >60nm diameter with distinct Au tips. Many Au particles of size range 10-100nm diameter were found spread around the base growth as seen with BSE images (Figure 60b). The variation in length and low density of NWs allowed good probe access for contact measurement. A distance of 1cm downstream of the low density NW samples very little growth was found on the substrates.

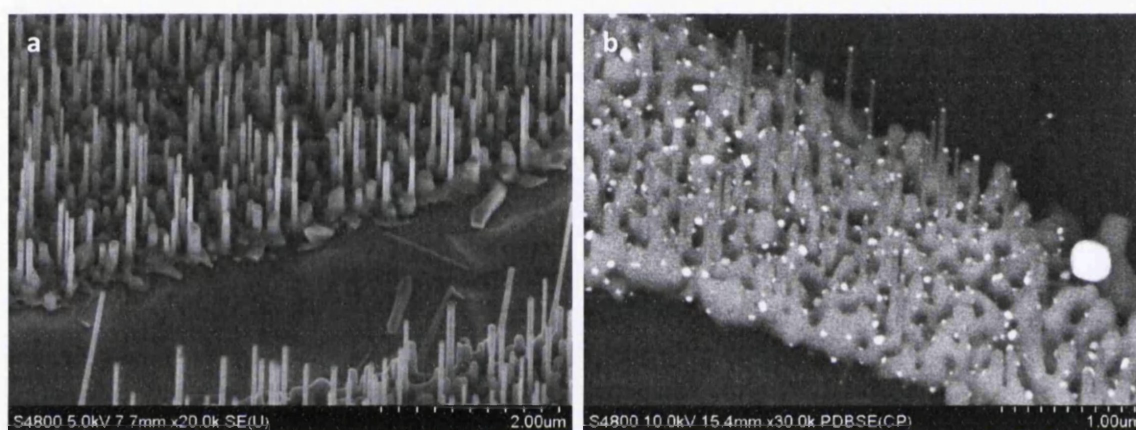

Figure 60. Growth diminishes away from the source. **a)** the cooler region (~12cm from source centre of Experiment 35) along with a large amount of Au provided NWs of various lengths, mostly with Au particles at the tip. The sprawling base growth makes these ideal for electrical measurements on free standing NWs, however, **b)** a large number of Au nanoparticles were located on the undulating base growth. The base crystal growth provided electrical connection to ground on insulating substrates like sapphire.

5.2.2 Thin nanowires with distinct Au catalyst particles

It was found when growing NWs suitable for the four-probe measurements that the diameter was usually >60nm. The higher furnace temperatures initially used generate greater concentrations of Zn vapour that produces thicker NWs, presumably the vapour – solid mechanism of lateral growth increases with the greater flux of Zn vapour. Therefore specific experiments were conducted to achieve thin NWs long enough (>4μm) for four-probe measurements, i.e. long with distinct Au tips (Figure 61a and b) but of diameter as small as 30-60nm. Growing NWs of aspect ratio ~100 required the reduction of the growth temperature to ~900°C and a thick Au catalyst deposition ~6nm (Figure 61a and c). The large amount of Au encouraged the catalytic process whilst the lower vapour pressure restricted the thickening of the NWs. Long growth times of up to 120mins were required to

achieve lengths suitable for multiple separation four-probe measurements ~4-6μm at these fine diameters. Experiment 35 (Figure 61a) and 34 (Figure 61c) were the most appropriate examples with NWs of this requirement on sample 2 (1cm intervals) in the boat. Using less Au (~4nm) on Experiment 34 produced thinner Au NWs in a similar region.

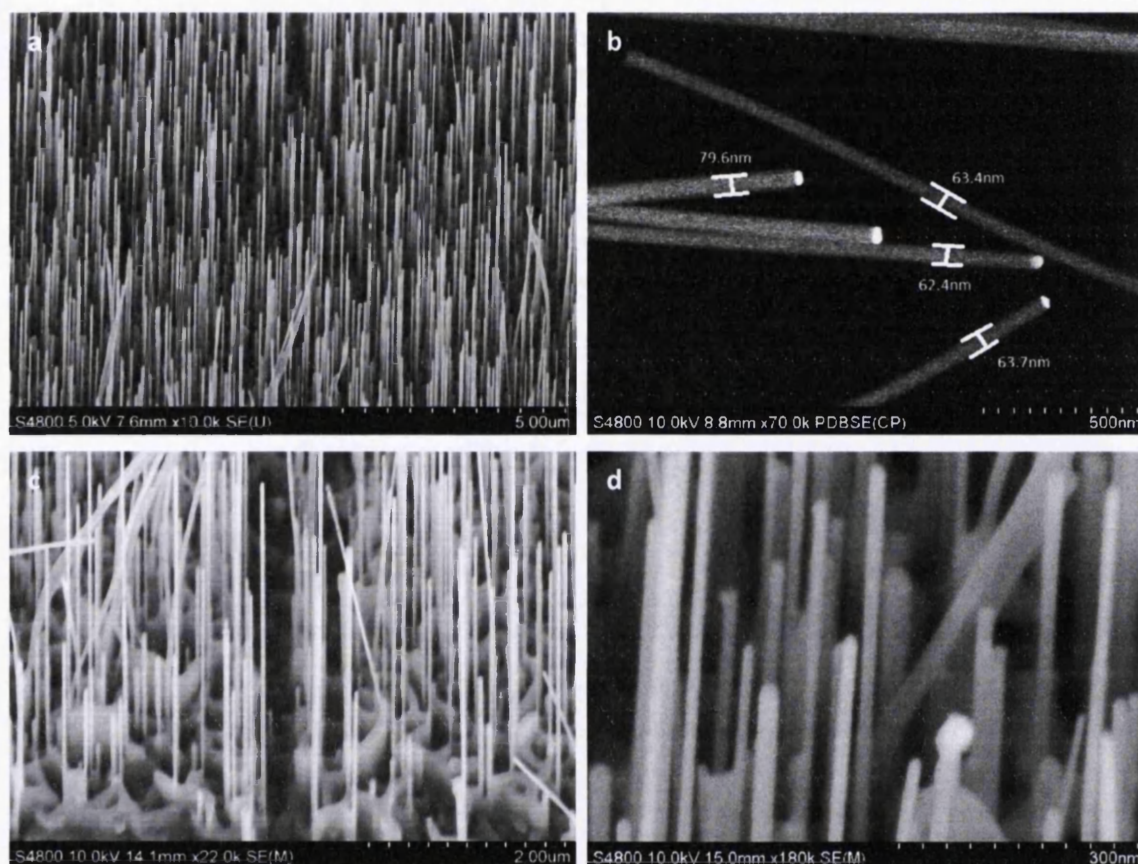

Figure 61. SEM images depicting the change in NWs as the amount of Au catalyst was reduced. **a)** Long growth times with a thick (6nm) Au catalyst layer at low temperatures gave very long NWs (Exp. 35) with distinct Au tips as shown in **b)** a BSE image. **c)** less Au (4nm) produced smaller nanoparticles to initiate growth and then subsequently thinner NWs (Exp. 34), maintaining a low vapour pressure resulted in a high aspect ratio. **d)** growing for a short time produced NWs ≪20nm diameter, although they did not have time to grow as long.

Growth was a trade-off between time and temperature (source vapour pressure) with all other parameters being equal. Longer growth times at lower temperature tended to produce thin NWs, but when Au tips were present they still grew very long Figure 61c. By reducing the growth time (~35mins) the amount of growth decreased and very thin NWs (Figure 61d) with Au tips were present (not shown). Experiment 33 was typical of the NWs grown for high-resolution HAADF that required NWs of maximum 20nm diameter. With shorter growth times the region of good growth moved towards the source slightly – this

was a symptom of the furnace 'hot' zone spreading further over time as the entire apparatus insulation heated up.

Au tipped NWs tended to grow long and thin, dominated by catalytic growth. While rods usually where the Au tip was not present and may have fallen off, may have continued to grow in a vapour-solid driven growth mode so they grew outward as well as upward. These rods were short because they did not have a catalyst particle to preferentially attract vapour at the NW tip.[118] The Au particles that were not located on NWs had a random size dispersion which at the very least is due to the deposited Au film separating into nanoparticles when heated[125] if melting didn't occur. The particles were then mobile on the surface capturing source vapour as they moved adding to the growing base layer[117]. The base layer was shown with TEM to be all crystalline and of the same crystal orientation as the NWs (the base layer is examined in detail with cross-sectional TEM in Chapter 6).

5.2.3 Short growth time for atomic imaging samples

For atomic HAADF imaging it was necessary to produce NWs as thin as possible, at the most 20nm diameter, to increase the detection intensity of heavy element atoms. Therefore a number of experiments concentrated on this of which Experiment 33 (Figure 61d) was the last. To achieve the very thin NWs it was necessary to use short growth times ~35mins. Below this, <30mins little growth was observed, it appeared to take this long for the sample and source to reach the minimum temperature (Experiment 32 ran for 30mins Figure 62a) for growth and then the additional 5mins allowed very fine NW growth Figure 62b and c. Also a medium thickness of Au ~4nm encouraged prominent Au particles at the tip (necessary again for HAADF imaging) but not so large that thicker NWs were prevalent. Reducing the time to ~25min with more Au ~6nm provided very short stubby thick growth (Experiment 27 NW diameter 50nm) which eventually sprouts thicker NWs (diameter 30-50nm) when growth is continued to 35mins. Again, the more Au catalyst provided the thicker the structures but until the 30mins is reached no NWs strike up. With samples grown at times <35mins and at these low temperatures it was required for the sample to be very close (~2-3cm) to the source. With more initial Au the growth tips also tended to become larger (Figure 62d displays Experiment 29 with a thick initial 6nm Au catalyst layer).

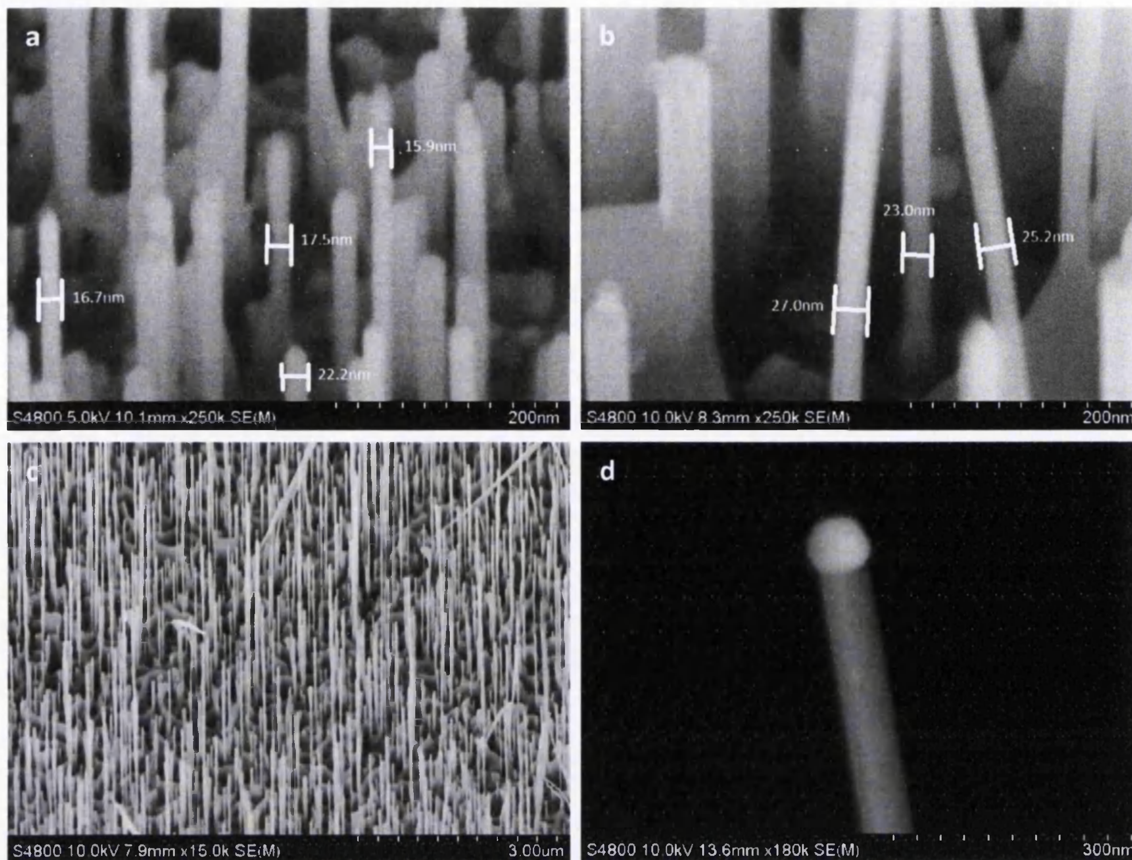

Figure 62. SEM images depicting the critical influence of growth time. With all other parameters the same, **a)** Experiment 32 of growth time 30mins had very thin NWs just beginning to grow, **b)** Experiment 30 with only 5mins extra growth had NWs that are still thin but overall the growth is larger, **c)** and the fine wires sprout up, **d)** using more Au (~6nm) results in large Au particles and generally thicker NWs

Deposition of 6nm Au provided NW growth of diameter 30-50nm in the early stages which then increased in length rather than diameter for long growth times up to 120mins when a low furnace temperature was used. This demonstrates the dominant role of the catalyst on NW growth when it is present at the NW tip, the NWs only thicken slightly with the long growth times in comparison to a very large change in length (~5μm). The long growth times however contribute to the base growth which grows large with time forming undulating random shapes (the base layer is examined in detail with cross-sectional TEM in Chapter 6).

5.2.4 Growth of nanowalls

The base growth can be tailored in similar fashion to the NWs by varying the growth parameters. The exact mechanism of growth is not known but is likely a process of both vapour-solid and catalysed growth which can be influenced by the vapour flux and quantity of Au. Similar control over the base growth as NW morphology is possible that can range from very little base layer to large interconnected wall type structures between NW

outgrowths. Locating the samples near or on the source boat (facing the sample down at the source material) exposed it to very high concentrations of Zn vapour, this resulted in overgrowth of the base and a thick layer of Nanowalls[214] grew at the bottom of the NW array. High Zn vapour concentrations along with a thick Au layer (~6nm) and longer growth time (45mins), produced thick NWs but not necessarily very long (~1-2um) (Figure 63a).

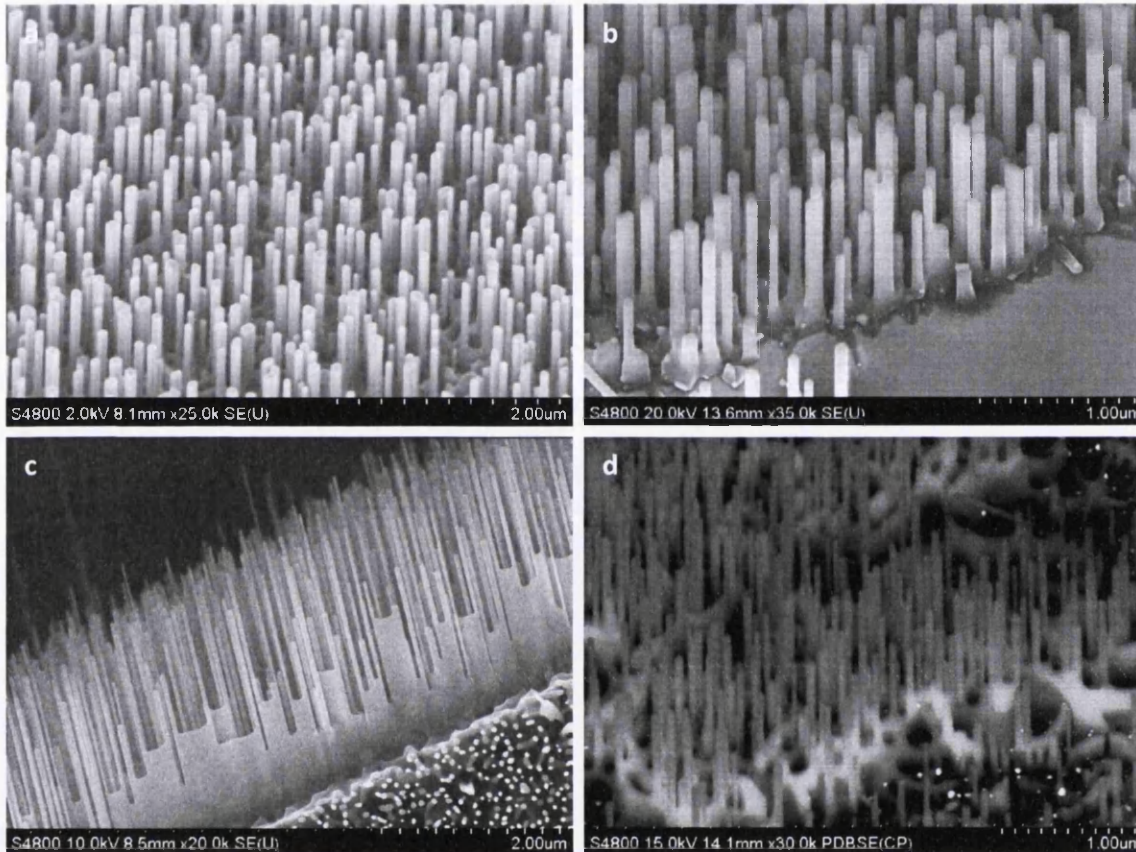

Figure 63. **a)** High vapour pressure very near the source created thicker NWs with few Au tips and a substantial base growth layer (Experiment 23), **b)** simply by turning the sample to face upward reduced the base growth and individual NWs grew from the substrate, **c)** reducing the amount of Au gives excellent NWs but with very extensive walls Experiment 11, and, **d)** BSE image of Experiment 12 showed very little Au present on the nanowalls or the NWs that suggested at least in the latter stages of the experiment catalytic growth was not the dominant mechanism (2nm Au catalyst layer).

Locating the sample, on or very near the source encouraged the nanowall growth due to the greater Zn vapour concentration and the increased trapping across the entire substrate which was covered by a relatively high concentration of Au nanoparticles. By reducing the temperature to 880°C, and also the concentration of Zn vapour, the nanowall growth was reduced to a minimum even when the sample was coincident with the source. Alternatively, turning the sample to face up from the source Figure 63b reduced the impact of high

concentrations of Zn vapour. Introducing more source material also increased the wall growth.

The growth of walls and NWs, rather than thick rods, was encouraged when a smaller amount of Au was used (~2nm) with high temperatures to create a high Zn vapour concentration, the typical growth product is shown in Figure 63c and d. The higher source temperatures required the sample substrates to be positioned further from the source to maintain the growth temperature of ~850°C. Figure 63d shows there is no Au on the NW tips and very little Au near the tops of the nanowalls. This indicates the wall and NW growth was initiated by Au but continued in addition to catalytic growth. The NWs still grew with a good aspect ratio (~20) and perfectly aligned with very high density. Even though no Au was present near the top of the growth the initial quantity of catalyst had a bearing on the growth morphology. NWs depicted in Figure 63c and d could be excellent for devices because the small amount of Au would minimise the impact on charge transport through the base layer which is substantial and robust. Larger quantities of Au produced an undulating base growth rather than a wall structure that was covered and embedded with Au particles, which is shown in Chapter 6. We have shown here that even with a catalyst other growth modes contribute which was more apparent at higher vapour concentrations and is displayed by a lack of catalyst growth tips on the NWs.

5.2.5 Substrate lattice match

In Chapter 2 we introduced the physical concepts that govern crystal growth and the importance the substrate has on the development of the NW structure and alignment. The majority of growth on non-lattice matched substrates was performed with non-catalysed growth as this worked best with ZnO seed layers. However, catalysed NW growth of different crystal cuts of Sapphire were experimented with. Growing uniform NWs on non-lattice matched substrates by catalytic means proved too difficult to achieve (no seed layer used). Instead of NWs the experiments produced a variety of shapes or very little growth. Experiments with c-plane Al_2O_3 displayed the effect of a poorly matched substrate on the growth orientation. NWs grew at a tilt angle close to the 51.8° which aligns the ZnO (0002) with Al_2O_3 $(10\bar{1}4)$ (Figure 64a) that have a plane spacing of ~2.51Å and ~2.55Å respectively.[80] Instead, α-Al_2O_3 or GaN were ideal substrates for vertical NWs and both have

benefits such as sapphire is relatively cheaper while GaN provides good electrical properties, Figure 64b.

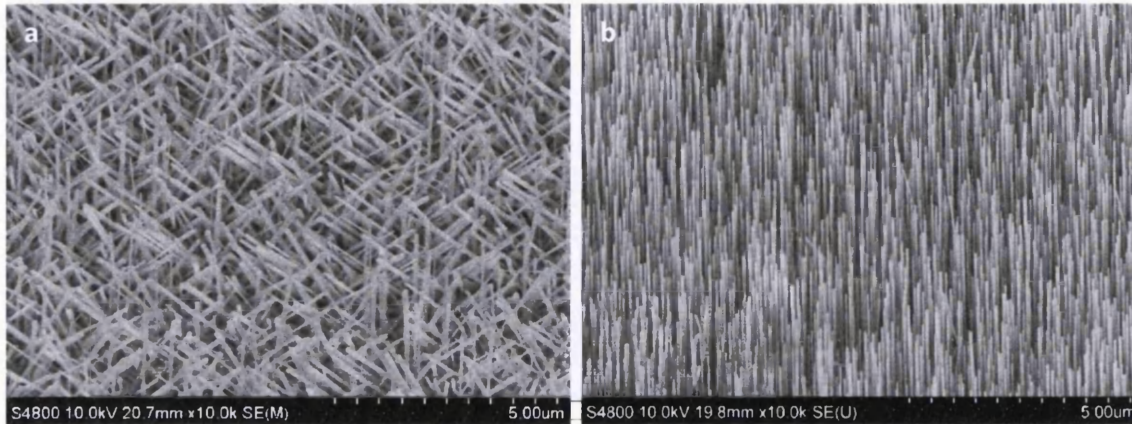

Figure 64. The influence of the substrate on NW tilt. **a)** c-plane sapphire provided NWs tilted at 51.8° to the substrate consistent with the crystallographic misalignment of the substrate for NW growth, **b)** however this is easily overcome by using a lattice matched substrate such as GaN which provided vertically aligned NWs in high density arrays, these NWs though did not have Au particles at the tip, from experiment 7.

Unsuccessful attempts were made to enhance the control over the growth with Au colloids spin coated on the sample that was tested at various growth temperatures on Si, no NWs were achieved. This method may have more success on lattice matched substrates such as sapphire with experimentation of colloid size.

5.2.6 Catalysed growth conclusions

36 growth experiments were necessary to achieve the desired NW attributes for all of the measurements detailed in Chapter 6 and 7. This included arrays of long NWs (>5μm) with distinct Au tips and an average NW diameter within each array ranging from 40nm to 100nm, these were used for transferring to four-probe measurement substrates. Two-probe measurements required shorter NWs and of much lower density. It was possible to grow the arrays with a sprawling base growth, (this provided an electrical path to ground on $\alpha\text{-}Al_2O_3$) but with low density NWs with distinct Au catalyst tips riding on the top facet, this acted as the top contact. The low density allowed easy probe access to contact the NWs from base to tip, the shorter length prevented the NWs from sticking together under beam exposure. The variation in growth characteristics displayed the good control that was possible with catalysed NW growth – largely due to generating enough Zn vapour at the same temperature at which optimum growth occurs. This removed temperature gradients across the sample, the most distinct influences on the growth product are summarised in Figure 65. The major benefit of the Au catalyst was to capture very low levels of Zn vapour and

grow NWs with relatively low gas flow rates – coupling this with the higher chamber pressure gave much reduced flow effects such as turbulence. It was even possible to grow high quality arrays of NWs with the sample placed on the source (facing up or down) at the furnace centre. In this orientation growth occurs even at 880°C but there is still debate whether the Au nanoparticles are actually liquid at these temperatures[125], although it has been shown that little alloying of the Au particle with Zn occurs which prevents any eutectic melting. With no eutectic melting an Au particle of 33nm should not melt until ~1031°C and the growth must proceed by a Vapour-Solid-Solid method (VSS).[125] When a solid particle catalyses growth there must be an epitaxial relationship between the solid particle and the growing crystal.[103] It is unclear without melting how a 6nm layer of Au would form into small nanoparticles without melting but it must break up and a surface liquid layer is possible. The relationship between the catalyst tip and NW is examined in detail by TEM and high resolution STEM in the Chapter 6.

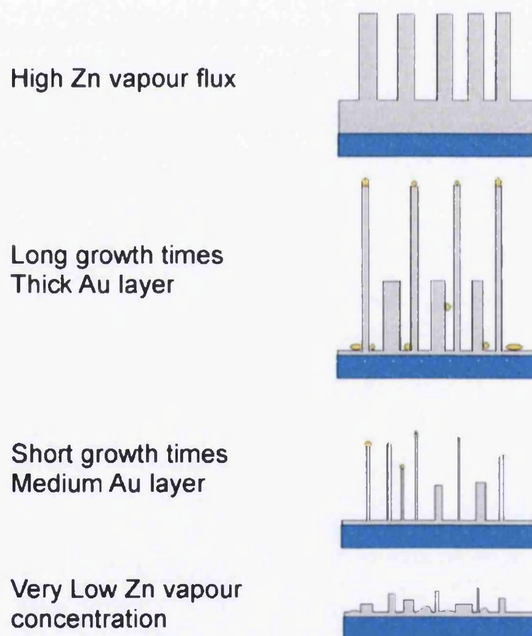

Figure 65. Drawing depicting the major influences on the catalysed growth product and the typical features that are displayed.

The variation in length and diameter across the arrays was accentuated when a thicker (>4nm) deposition of Au was used. In this instance the NW growth proceeded in the majority with Au catalyst tips. However Au particles were observed to 'fall off' the top facet and could be found at various positions on the NW sides Figure 66a.[58] To achieve NW arrays

of uniform diameter and length Figure 66b much thinner (1-2nm) depositions of Au initiated growth, but NWs grew without the aid of a catalyst particle at the tip. Without a substantial initial layer of Au, NWs were observed to have no Au at the tips and only small quantities of particles were found around the base growth layer.

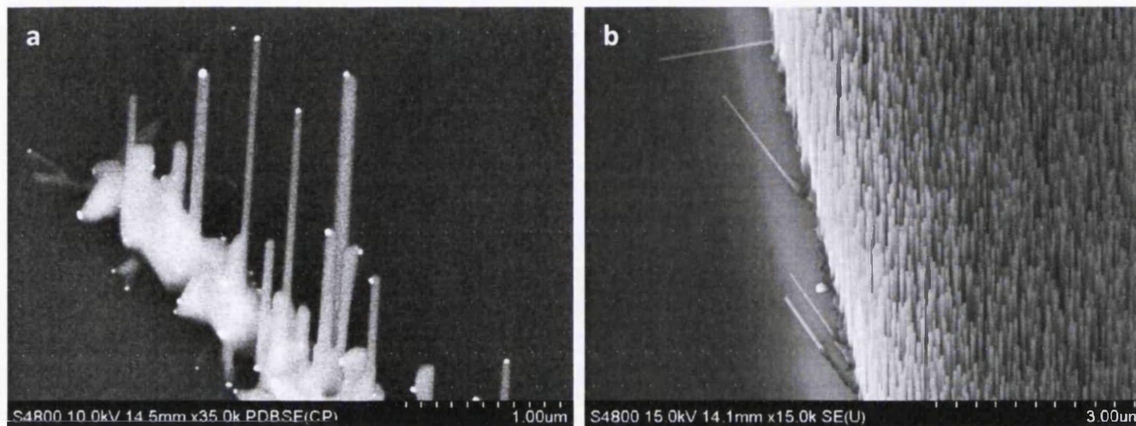

Figure 66. **a)** BSE image of Experiment 35 which showed the catalyst particle at various stages of dismount from the (0001) top facet of the NW. **b)** thin initial layers of Au catalyst provided more uniform arrays ideal for device fabrication, however there was no Au present on the NW tips which maybe a hindrance for contact formation.

5.3 Non-Catalysed NW growth

The advantages of this growth method were the superb quality NWs, excellent arrays of high density perfectly aligned and very long NWs, all of which may have had a maximum range of 20 nm in diameters. It was possible to produce uniform arrays covering samples as big as 1cm^2. However repeatability was difficult, repetition of the same parameters could produce very different results and structures, with NWs being the most desirable. Due to this, many experiments were performed at similar conditions, and so instead of examining each experiment general trends and optimum results are presented, knowing these can be achieved. The majority of experiments were run with similar parameters however further details of parameters of the experiments referred to here are listed in Appendix 1-B. Growth experiments centred on the substrates of roughened sapphire (section 5.3.1) and ZnO seed layers deposited on non-lattice matched substrates (section 5.3.7). The relationship of growth parameters, the substrate and the growth products were similar for sapphire and ZnO seed layers and many of the observations are relevant to both.

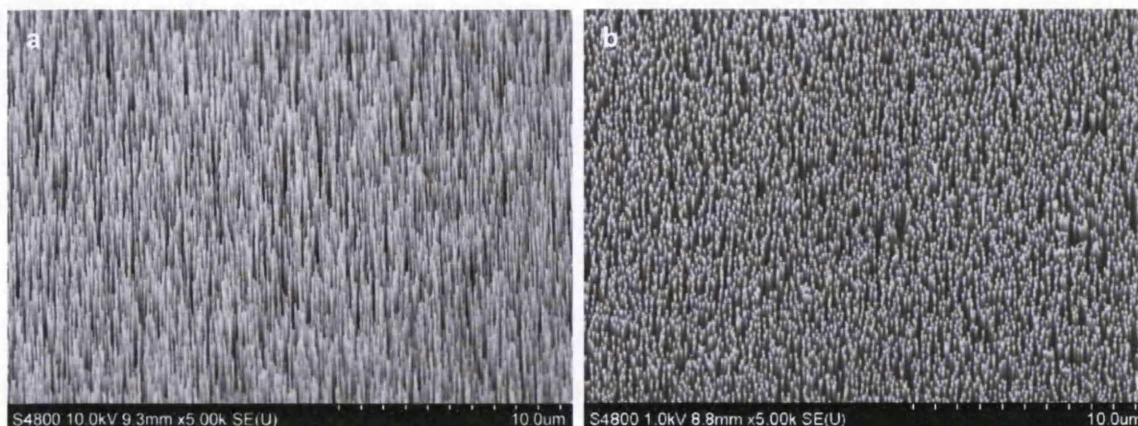

Figure 67. **a)** Experiment 211 produced excellent NWs over a large area, similar experiments however do not always produce this quality, **b)** Experiment 198 showing equally good NWs of uniform length ~7μm and uniform diameter 100nm.

5.3.1 Roughened α-Al_2O_3 for ZnO NW growth

Sapphire provides an almost ideal lattice match for ZnO growth (see Chapter 2) and offers the means for growing non-catalysed NWs by a simple etching of the surface with NaOH solution (described in Chapter 4). This removes variability in substrate quality from the growth which can confuse the assessment of other parameters. Growing NWs on α-Al_2O_3 therefore provides an ideal means to assess the current state of the growth experiments and the overall relationship with growth parameters.

Using a-plane sapphire with minimal processing was an excellent, method for aligned NWs (Figure 67), and the insulating properties were overcome by the thick epitaxial layer that was found at the base. The only processing was to expose the sapphire to an etchant which was then washed away.[111] This removed a major variable when analysing the results and NWs were assessed on morphology and alignment, with long (~5μm) perfectly vertically aligned NWs being considered ideal. Many of the proceeding observations apply to growth on all substrates attempted.

5.3.2 Low density vertical NWs for two-probe measurement

Non-catalysed NWs usually grew at high density over the entire substrate and are not easy to pattern because the control over growth site that a catalyst gives was not available (Figure 67). Aligned NWs grew close together and are the same length, in the high quality arrays very few sites across the substrate allowed easy probe access. This was partially overcome by fracturing the sample to expose a clean sharp edge. However for nanoprobe measurements (see Chapter 4) the density of the growth made it extremely difficult to

contact individual NWs from base to tip without touching the probe tips to neighbouring structures. Therefore, low density vertical NWs were required that could be individually contacted with multiple probes on a fractured sample edge.

The arrays that were most useful for two-probe measurements of bare and deposited Au contact were grown in Experiment 216 (Figure 68a) and were generally grown at a furnace temperature of 1050°C that is typical of many of the experiments and a source-sample boat separation of 23cm. Samples in the front half of the boat had low density vertical long NWs and a diameter within the range of 40-100nm. The sample boat created a turbulent flow that shielded the samples from the full extent of ZnO precipitation. However, achieving the low density was far easier on etched Al_2O_3 than on other substrates. A likely explanation is the etching process controlled the areal density of nucleation sites and this combined with reduced local vapour pressure allowed only a small number of NWs to grow, although this was difficult to prove by varying the etch time.

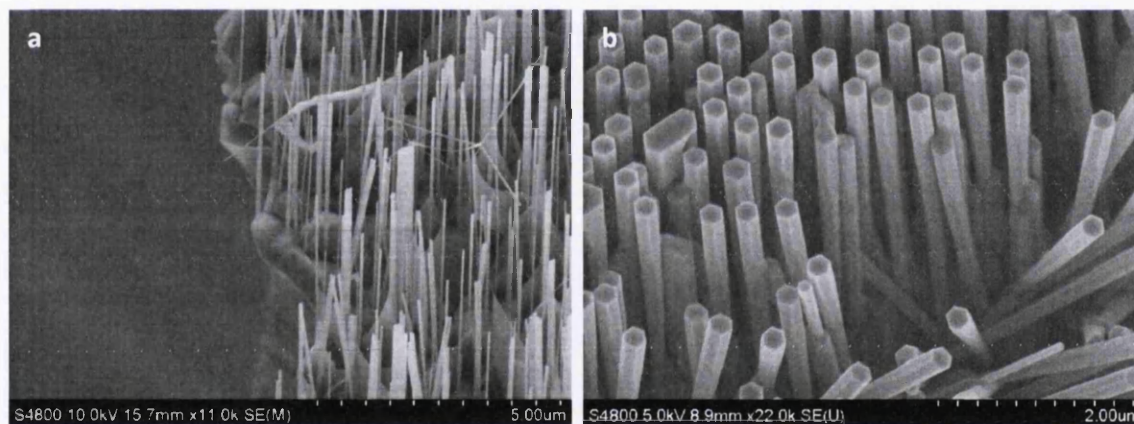

Figure 68. **a)** Low density vertical NWs allow good probe access along a cleaved edge, the NWs are long and vertical however other structures are evident that can interfere with measurements, it was difficult to avoid growing these when aiming for low density NWs by the catalyst-free method. **b)** the high density of growth in cooler regions and the tapering effect that can cause NWs to merge together

5.3.3 Changing growth morphology and the sample temperature

Within the furnace there exists a temperature gradient (the apparatus is explained in full Chapter4) from the maximum at the furnace centre where the source material is located that drops rapidly along the furnace tube. The location of the substrate for non-catalysed growth is in a region of very steep temperature gradient which can drop 300°C along the length of the sample boat (8cm). A main effect of the gradient was a change in the growth structure as samples were placed further downstream. The upstream portion of the sample

boat usually had a region of thick disordered growth due to the turbulence caused by the boat catching the fast gas flow. This could be reduced by using a boat with a small recess of the same depth as the sample. After the poor quality growth, which usually covered approximately the first 1cm of the boat, NWs of varying quality grew for a region of up to 2-3cm and then the NWs begin to taper in shape. They did not get thinner toward the top, but thicker, and the top could easily double the diameter of the root (Figure 68b). This was seen as a regular growth feature. Eventually the top could become so chunky that they almost merged into a single film with a NW type structure at the base.

Another regular feature in the cooler regions of the sample boat was a large, undulating and irregular base growth out of which NWs sprouted, usually where the tapered NWs grew. These NWs may still have been very well aligned and uniform in size, however, this feature appears to have no use at present.

5.3.4 Growth time and source vapour

The overall thickness of structures was influenced by the initial source quantity and the chamber pressure. However, long growth times (>60mins) created no additional growth as the source was completely depleted, all ZnO was consumed in this time regardless of initial quantity. Therefore increasing the source quantity resulted in a greater flux of Zn vapour and faster ZnO growth which generally resulted in thicker NWs (Figure 69a). Using shorter growth times resulted in thinner shorter NWs, i.e. less growth occurred. Similar to catalysed growth it required >30mins for growth to be initiated and even at 45mins growth was thin.

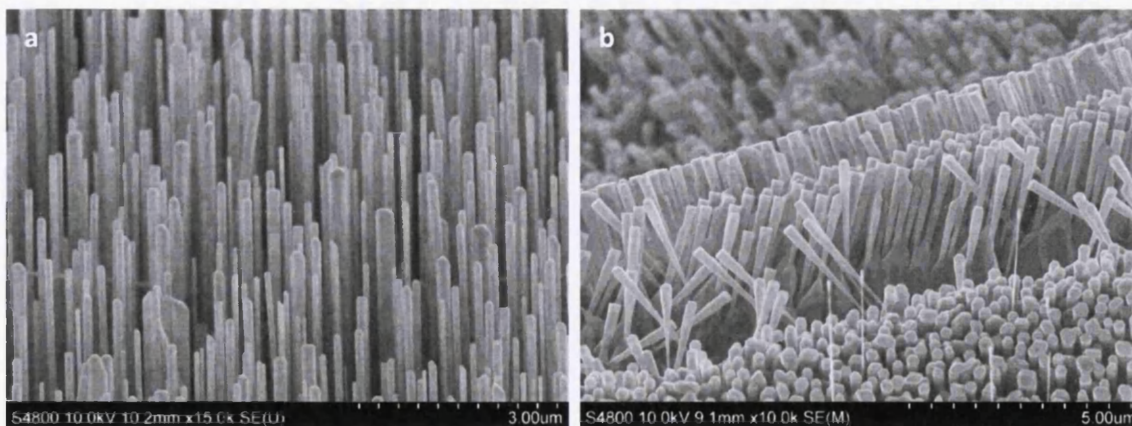

Figure 69. **a)** Crystal overgrowth occurred when the precipitation of ZnO increased, shown here is the effect of an increase of source material to 1g, NWs were of excellent quality, very long but many had grown in thickness rapidly due to the additional flux of ZnO with many NWs diameter 300nm. **b)** Growth in the cooler regions (~500°C) formed tapered NWs, increasing the pressure chamber also caused structures to grow in a three-dimensional sense merging together, shown here at the sample edge of Experiment 207 grown at pressure 2.8mbar.

Increasing the pressure effectively increased the deposition of ZnO onto the sample area because flow rates were reduced and precipitation at the growth site was more abrupt. Higher pressure led to crystal overgrowth, where structures grew outwards and started to form uniformly hexagonal films, this form of overgrowth generally occurred in the cooler regions (Figure 69b). Reducing the source particle size was an alternative method for creating greater flux of ZnO[215], however this had little effect on the overall quality of growth, as long as high purity graphite powder was used.

5.3.5 Nanowire diameter

Non-catalysed NW growth lacks the influence of a catalyst to encourage growth along the preferential [0001] growth direction. Growth dynamics are then highly dependent on the Zn vapour concentration that has a large influence on the rate at which the crystal facets grow. The balance of growth between the (0001) facet and the side $\{10\bar{1}0\}$ facets determines the aspect ratio of the NW structure and the thickness was observed to increase from the front of the boat to the rear. Commonly at the front of the boat NWs had diameter 100nm and increased to >200nm near to the rear. However, there was little control on the actual NW diameter in the best region, this was influenced by pressure, ZnO flux and to a great extent by flow effects which were hard to control but could be reduced by aerodynamic shaping of the alumina boat. It is most likely the substrate and the initial surface roughness had an effect to influence the diameter and areal density of the NW growth. Although no relationship with etching time was revealed a further study could investigate the roughness with AFM studies of pre-growth substrates.

5.3.6 Base epitaxial growth layer

It was observed early in the experiments that a substantial base growth was present with all high quality NW arrays. Closer inspection of the layer was possible with the experiments that provided low density arrays that revealed the NW root. At the root or base of a NW a hexagonal relationship with the base layer/substrate was revealed by the growth structure that developed into a NW (Figure 70a). It is likely this layer and structure started to develop early in the growth once the source began to evaporate, and as the sample heated up to full

temperature then NWs started to grow, i.e. a temperature lag ~30mins.

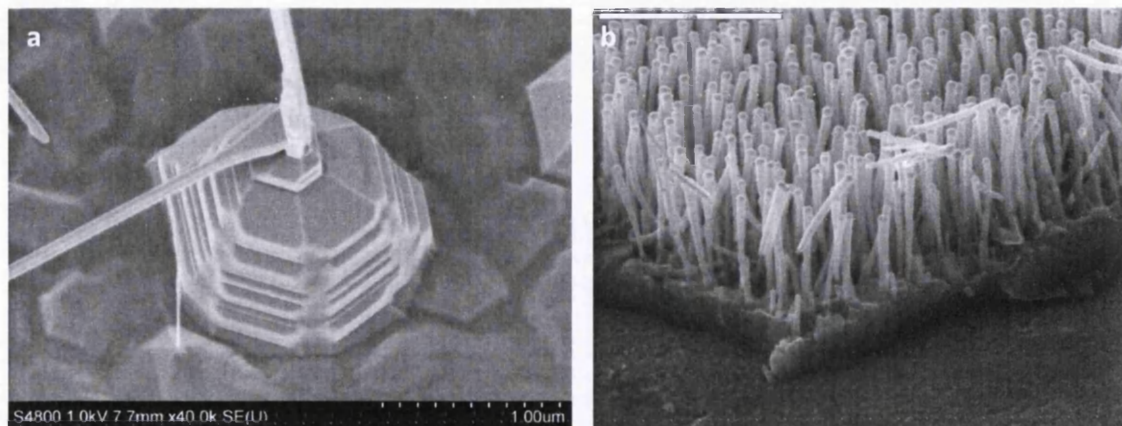

Figure 70. **a)** Experiment 199 produced some excellent nanowires but only in small patches which allowed the inspection of the NW root, we can see here the hexagonal growth pattern of the crystal which developed into a NW, the NW may have sprouted when conditions in the chamber reached the correct balance. **b)** When high quality arrays of NWs grew the base growth was always a thick and uniform layer which did not appear to be formed of isolated crystallites and instead was one continuous layer from which NWs grew, the relationship with good NW growth suggested this layer is epitaxial. These NWs have had metal deposited on top of the NWs that grew from a solution seed layer on Si-Cr-W substrate.

The low density arrays obviously had less growth and so we are in fact looking more at the individual NW structure rather than at the base of an array (Figure 70a). Structure and morphology of the base growth with full dense arrays is different, all of the root growth has merged into one continuous layer that can reach up to 1μm in thickness (Figure 70b). This is likely to be an epitaxial layer although this is not proven for non-catalysed NWs (the base growth of catalysed NWs is shown to be epitaxial in Chapter 6).

5.3.7 Metal and conducting substrates

NWs on sapphire provide excellent quality but the insulating properties of Al_2O_3 restrict the possible applications of the arrays. Conducting substrates such as metals, conducting semiconductors or oxides are attractive to provide a uniform electrical conduction path to the entire NW array. This reduces scattering that can occur in the NW base layer and provide efficient charge transfer as part of a device circuit. For this reason growth on metals with very high melting points was investigated and made possible by the use of solution deposited seed layers (see Chapter 4).

Solution seed layers were formed by drop casting Zinc Acetate dissolved in ethanol on the metal substrate and annealing at 350°C. The seed layer acted as a nucleation site for the ZnO NW growth which occurred at a temperature much lower than catalysed NWs. A local growth temperature of ~600-650°C was optimum. At this temperature Zn and ZnO

precipitates out of the growth atmosphere and was deposited on all surfaces. The ZnO seed layer acted to encourage aligned growth of NWs, rather than random structures with no preferential alignment such as on bare metal or non-lattice matched surfaces.

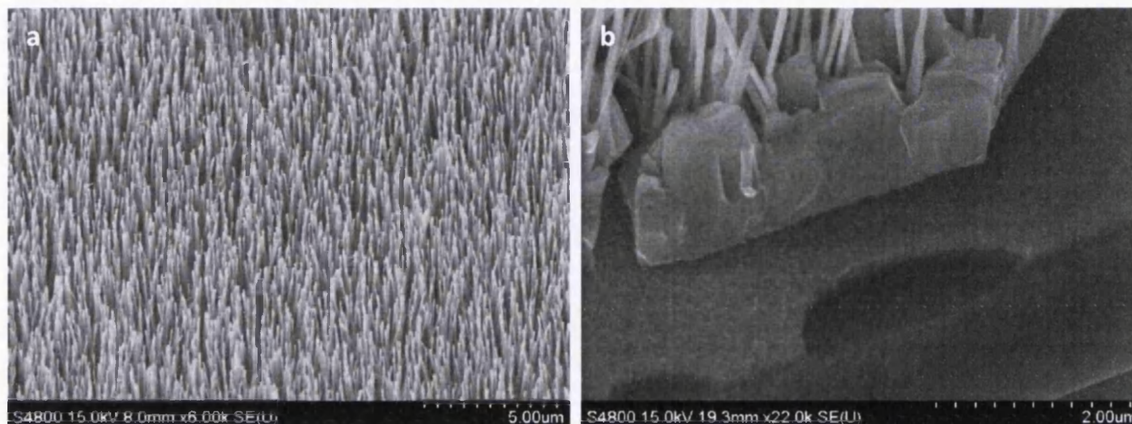

Figure 71. **a)** Nicely aligned and very uniform NW array, grown using a solution derived seed layer on Si-Cr-W substrate, experiment 179. **b)** A thick base growth developed on the seed layers which was topped by dense NWs, the tungsten layer is also displayed on top of the Chromium and Silicon substrate.

Several schemes of metal were tried on Silicon $\langle 111 \rangle$ substrate. The most successful was Silicon, 50nm Cr, 200nm W and then solution based layers seed annealed on top (Figure 71a), also shown is the thick base growth that occurred when using ZnO seed layers on top of metal layers (Figure 71b). The silicon required thorough solvent cleaning, oxidation Piranha clean and then HF to expose the virgin Si surface. Chromium and W were then deposited sequentially by plasma assisted physical vapour Deposition. The chromium acts as a wetting layer to adhere the tungsten, which would otherwise peel off during the high temperature growth. Several other schemes of conductive layers were attempted which included ITO, Nb, Cr and W, on all layers good NWs were grown using the solution seed layer method. The full scheme of Si-Cr-W-ZnO proved the most robust and repeatable, although ITO showed equal promise and has many advantages such as transparency and semiconducting properties. The Indium has also been shown to diffuse into ZnO NWs creating an n^+ layer.[216]

5.3.8 ZnO Seed Layers and metal buffer layers

Seed layers were used to buffer the ZnO NW growth from the substrate lattice mismatch. The most successful seed layer was the solution based method. Plasma assisted physical vapour deposition (PVD) seed layers from a pure ZnO target were also extensively investigated, however NWs comparable to roughened substrates or solution seed layers

were never achieved. Many combinations of in-situ heating up to 350°C, Oxygen concentration, substrate material, thickness and deposition rate were tried. The main investigation centred around PVD seed layers on Si of which were tried $\langle 111 \rangle$ $\langle 100 \rangle$ and $\langle 110 \rangle$ wafers, however it was very difficult to obtain a c-axis orientated seed layer due to the very large mismatch with Si (Figure 72b). To overcome this many attempts at buffer layer[108,217] formation (Ti, Al, Cr and W and combinations of these) were attempted with the most successful being very thin layers of Al deposited (5-20nm) on HF exposed Si $\langle 111 \rangle$. Thin layers of ZnO (~10-20nm) were then deposited after the Al and the sample annealed (up to 900°C) post deposition in air. The phase and composition of the compound formed was unclear but it is likely the thin Al would oxidise rapidly before the annealing temperature reached the melting point. Such a thin layer may have turned completely to Al_2O_3, whether this could have formed a phase compatible with aligned NW growth is unknown, however

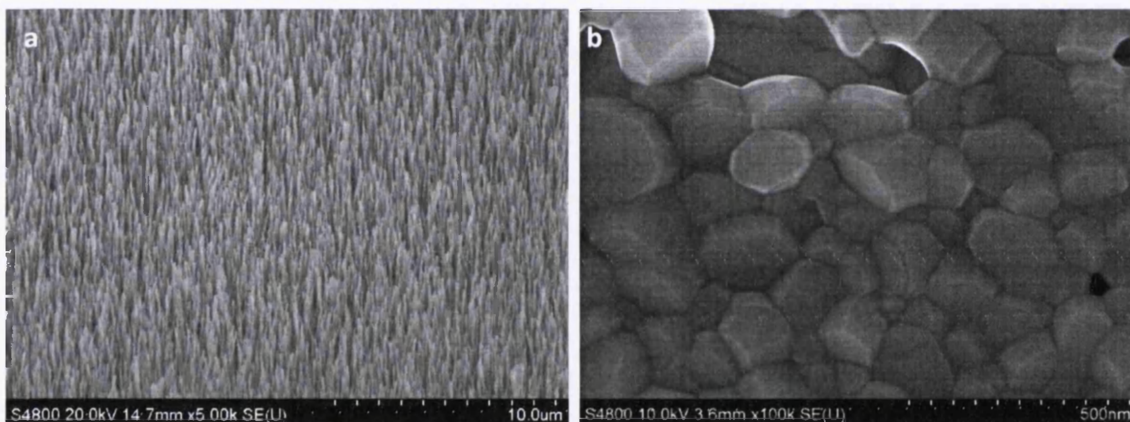

Figure 72. **a)** SEM image which shows the best NWs achieved with buffer layer-seed layer combination with ~20nm Al and ~20nm ZnO plasma Ar-ion deposited with the inclusion of 10% O_2 during ZnO deposition and post deposition 1hour anneal in air at 700°C. **b)** After annealing the PVD seed layer, large crystallites formed but the random orientation was difficult to control, this determined the alignment of the NWs

this produced the best results (Figure 72a). Figure 72b shows a thicker ZnO deposition and the reason for misaligned NW growth is due to the random orientation of the crystallites.

Cross-sectional TEM could reveal the details of this layer although it is likely Al would have diffused from the buffer layer into the ZnO base growth. Al diffusion could be very beneficial for devices because the resistivity would be reduced with Al acting as an n-type dopant. Similar buffer layers have been shown by Wang et al and Lee et al to produce aligned growth, one of which is AlN[218,219], however the electrical properties of this are not conductive and a better alternative maybe Titanium or Tungsten Silicide[220] of which one

phase is hexagonal. It may be possible to rely on the substantial base growth of the array for device conduction, especially if Al diffusion acts as a n^+ dopant, in which case insulating buffer layers and substrates could be used.[216]

A very interesting result of the PVD mounting system was a region under the sample fixing which often produced well aligned and dense NWs. It was unclear if this was due to roughening of the substrate by the screw, or a combination of metal atoms and nanoparticles nucleating growth in such a way that it could grow NWs which were independent of the substrate crystal structure. Figure 73 shows the growth under this region that occurred on plain $\langle 111 \rangle$ Silicon.

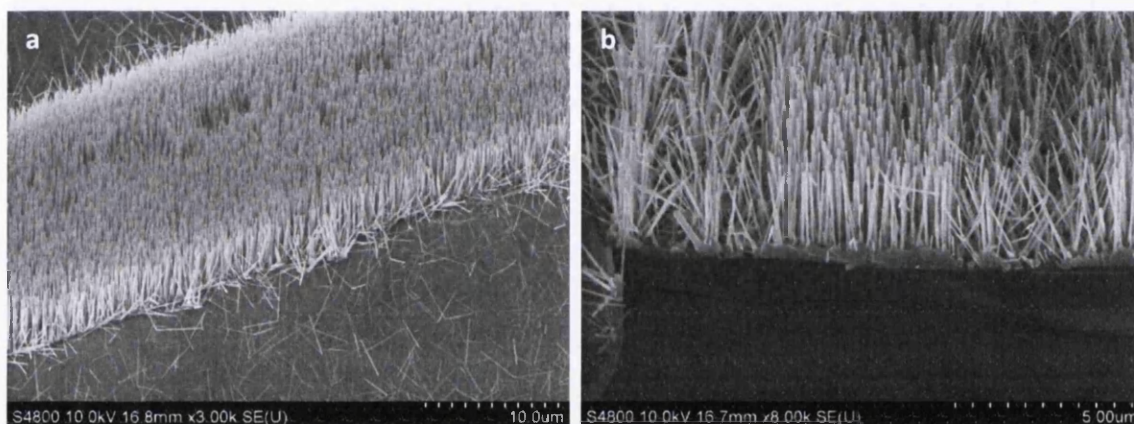

Figure 73. **a)** Excellent alignment was regularly achieved with the NWs located in the screw fixing region, many attempts were made to uncover the secrets of this but no attempt produced NWs of this quality over a large area. **b)** The cross-sectional SEM image shows a similar area, the base growth is substantial but growth quickly disappears suggesting some local roughening of the surface, this thick base growth always occurred with high quality well aligned catalyst-free NWs.

5.3.9 Au contact deposition

Non-catalysed NWs lack a top contact; this must be fabricated as a separate step to NW growth. Two techniques can achieve the deposition of metals as contacts that are thermal evaporation and plasma assisted PVD. Au contact formation was initially attempted by plasma assisted PVD. It was possible to achieve individual metal particles on the tips of each NW and with further deposition these tips grew and would eventually combine to form a metal layer. This was achieved without resist processing techniques to protect the NWs. However, the PVD deposition was found to coat metal onto the NW side as well as the top. PVD is considered a multi-directional coating technique whereas evaporation more uni-directional. For this reason evaporation was eventually used to form individual contacts to the NWs to reduce the side deposition[221] that could influence two-probe measurements.

Au contact formation by evaporation was completed with final Au contact thicknesses estimated to be in the range 10-50nm. TEM analysis was conducted on NWs that were shown to have Au of 10-20nm thickness and this was correlated to the deposition parameters, further depositions were in multiples to obtain Au of thickness up to 50nm. The thinnest coating of 10nm is shown Figure 74a. NWs that were slightly tilted from vertical were metal coated on the uppermost facing sides, this was undesirable for two-probe measurements.

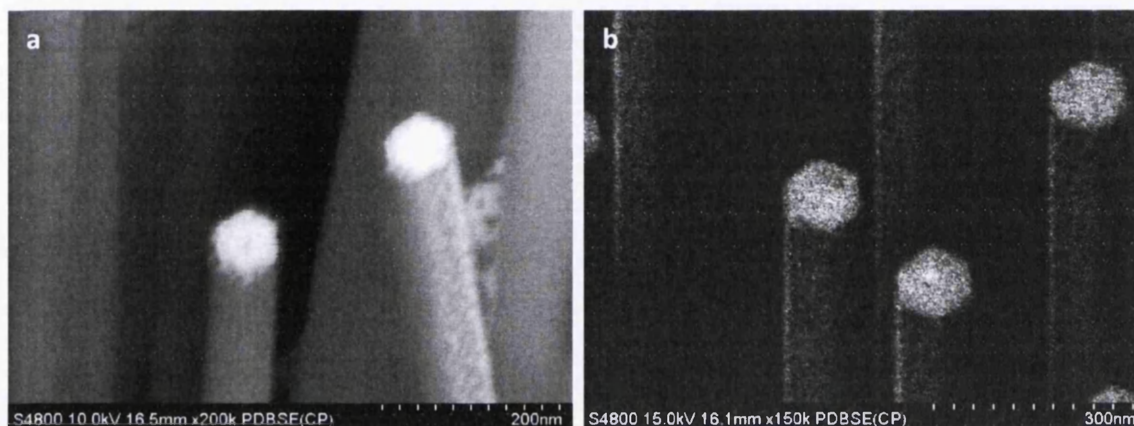

Figure 74. **a)** BSE image of a 10nm evaporated Au contact on ZnO NWs, the well aligned NW shows very little Au on the side whilst the tilted NW displays Au coating the uppermost faces. **b)** A deposition of 20nm Au on perfectly aligned NWs gives a substantial Au pad on top of the NW but still leaves some side deposition highlighted by the backscatter image.

To minimise the side coating problem only perfectly vertical NWs were measured in the nanoprobe to ensure minimal Au on the side, shown in Figure 74a. However, very small Au particles were detected on the side facets of a large proportion of NWs but the Au did not form a continuous layer. With the thicker Au depositions some Au was detected on the NW sides even on well-aligned NWs as shown in Figure 74b. This most likely will have been a problem of Au deposition onto a sample that was not perfectly orthogonal to the deposition direction which was very difficult to correct experimentally with the current apparatus. Using BSE imaging to highlight the Au it was possible to determine the extent of the side deposition which never formed a continuous layer (Figure 74b). The Au contacts and the Au coating on the side facets is investigated in detail with TEM in Chapter 6.

5.3.10 Metal-Semiconductor-Metal structure

With continued deposition of metal by PVD it was possible to create a complete contact layer across the tops of the NW arrays. NWs grown on conducting metal substrates then in effect became a metal-semiconductor-metal device structure. The continuous ZnO base

layer separated the planar substrate metal from the deposited metal. Metal coatings initially formed large particles on the tips (Figure 75a and b), and as more metal was added the particles increased in size (Figure 75c) and eventually formed a complete layer once approximately 1μm of metal had been deposited (Figure 75d). Thinner depositions still tended to coat Au on the NW side and so evaporation was used for the much thinner contacts that were suitable for two-probe measurements.

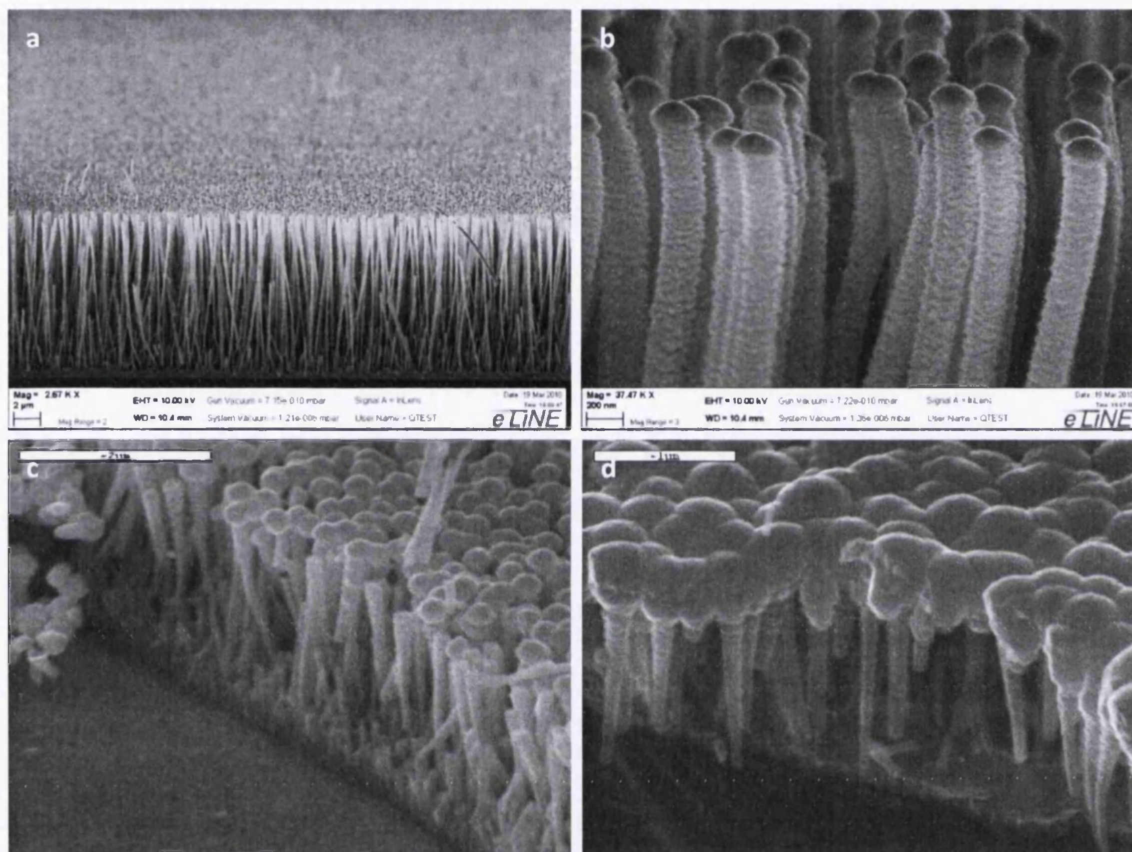

Figure 75. **a)** The SEM image shows very long catalyst-free NWs with small metal particles at the tips. The metal was deposited by PVD, **b)** with closer inspection the metal can be seen to form a spherical particle on the NW tip and also to create a fluffy coating on the NW sides, this deposition was measured by SEM to be 170nm on planar Si. **c)** Increasing the deposition amount to approximately 500nm planar equivalent creates large particles at the NW tip which start to merge. **d)** Further deposition forms a complete film across the NWs.

5.4 Conclusions

The non-catalysed method of NW growth produced excellent NW arrays which formed a robust and substantial base layer that interconnected all of the structures. For vertical array devices this structure is ideal, and it may be possible to tailor the electrical properties by seed layer or growth source material doping and particular substrate selection. Solution seed layers provided the best method for growing large area arrays on non-lattice matched

substrates such as metals. Post growth contact formation was achieved by either metal evaporation or PVD, with evaporation being the preferred option for contacts to individual NWs for two-probe measurements, however some Au was still observed on the NW sides. This could in future be reduced with a very accurate sample positioning and mounting system for the evaporation chamber. We have shown both vapour phase methods with and without Au catalyst produced high quality arrays and control of the morphology was possible.

The growth experiments were successful; they achieved the high quality samples necessary for all of the electron microscopy and electrical measurements and provided NW arrays that are very suited to device fabrication. Tailoring the features of each array made the measurements in Chapters 6 and 7 possible and enabled successful techniques to be developed to capture high quality data from the nanometre scale structures. Au catalysed growth provides the greatest control of the NWs and the arrays, however we have seen the Au catalyst can contaminate the base growth which may interfere with electrical conduction, this is investigated further with TEM in Chapter 6. Non-catalysed NWs can overcome any potential catalyst contamination problems and growth can be nucleated with a very simple, clean and reliable process of surface roughening. The difference in growth control is exhibited by the number of experiments completed for both growth methods; approximately 220 experiments for non-catalysed growth were needed to ensure samples for all of the nanoprobe measurements whilst only 36 catalysed growth experiments provided nanoprobe samples and NWs suitable for high resolution electron microscopy. Chapter 6 that follows next characterises the NWs using electron microscopy to uncover the details of the crystal structure, the material composition and the role of Au at the NW tip and around the base growth.

5.5 Unusual structures

Some interesting images of unusual growth structures that the catalyst-free method produces are shown.

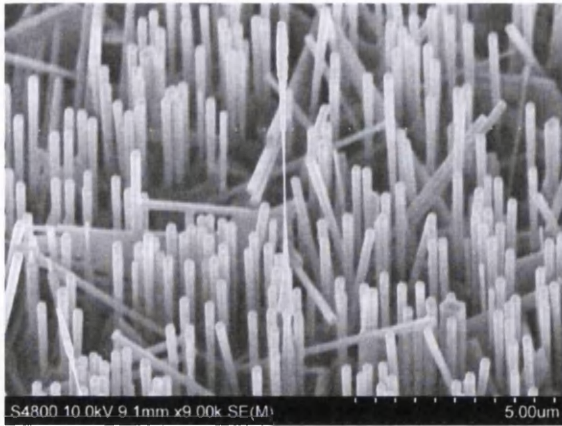
S4800 10.0kV 9.1mm x9.00k SE(M)
5.00um
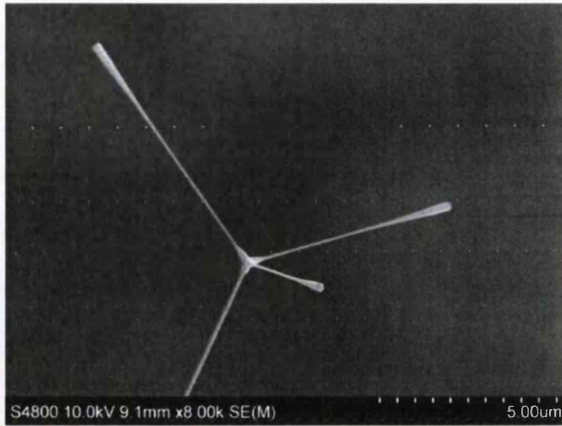
S4800 10.0kV 9.1mm x8.00k SE(M)
5.00um
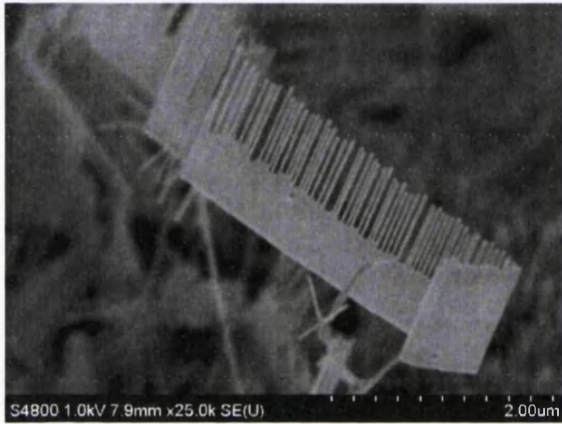
S4800 1.0kV 7.9mm x25.0k SE(U)
2.00um
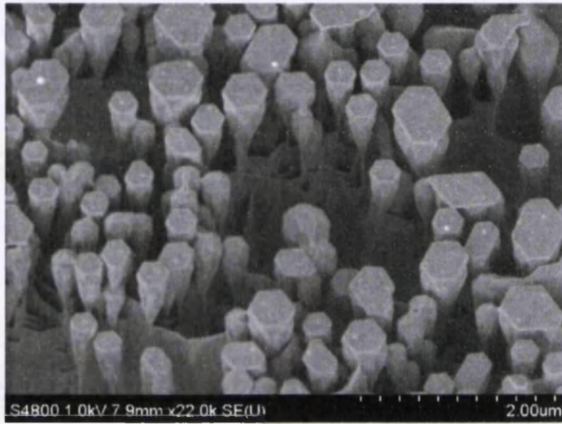
S4800 1.0kV 7.9mm x22.0k SE(U)
2.00um
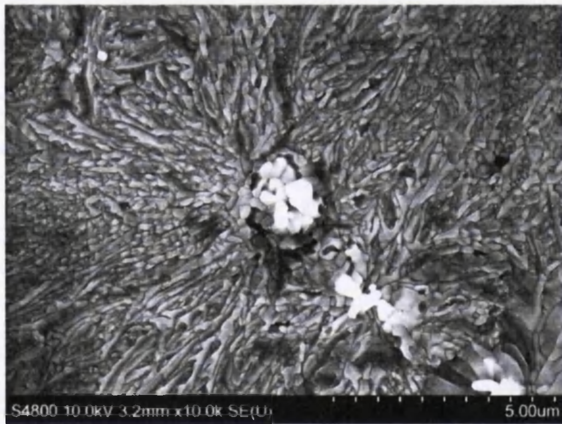
S4800 10.0kV 3.2mm x10.0k SE(U)
5.00um

Chapter 6

6 Electron Microscopy Analysis of ZnO nanowire structure

This chapter details the crystallographic characterisation of ZnO NWs grown by vapour phase and hydrothermal methods and also the structural analysis of Au contacts to catalysed and non-catalysed vapour phase NWs. Detailed crystallographic analysis was vital to perform before electrical measurements could be analysed and interpreted. The crystal structure of the semiconductor and any anomalies such as defects and contamination had to be thoroughly assessed to apply the most applicable principles and theories to the measured properties of the NWs and the Au contacts. Defects that may originate from the growth process such as phase and grain boundaries or atomic contamination from metal catalysts can all severally hinder the electrical properties and induce defect energy states, charge trapping and charge scattering. Crystallographic orientation also can have a major impact on electrical properties even in perfect single crystals, this is displayed by the effective electron mass that can differ depending on the crystallographic direction.[5] Therefore is was necessary to thoroughly investigate the NWs with transmission electron microscopy techniques.

The initial characterisation was undertaken with Transmission Electron Microscopy (TEM) at Leeds University with the help of Michael Ward. TEM analysis led into a more detailed inspection of the atomic lattice of vapour grown NWs, particularly those grown with Au catalyst, with high-resolution Scanning Transmission Electron Microscopy (STEM) and High Angle Annular Dark Field Imaging (HAADF) at SuperSTEM with Quentin Ramasse. The STEM-HAADF analysis completed detailed inspection of the NWs structure, a search for heavy element contamination and the structural quality of the Au interface formed by catalyst particles. To complement the HAADF imaging simulations were performed by Demie Kepaptsoglou and Quentin Ramasse to investigate the likely intensity one Au atom may have in a host ZnO matrix.

6.1 ZnO nanowire structure by imaging and diffraction

ZnO NWs from high quality arrays were transferred directly to carbon film coated copper TEM grids without the use of intermediate solvent dispersions. This preserves the NW

surface and reduced the likelihood of contamination problems. In order to reveal the NW lattice the NWs lying flat on the carbon film were rotated to the most accessible zone axis which would align the longitudinal and lateral planes. The single crystal quality and orientation were initially established by in-depth TEM analysis.

Lattice images were used to inspect the ZnO NW lattice and the bright field technique was used to image the NW morphology. NWs were tilted close to the Bragg angle such that the lattice planes were distinguished and at least (0001) were aligned with the beam. During the tilting and diffraction analysis of the samples signs of defects were searched for. Typical signs such as dark lines of intense contrast and fringes were analysed by tilting the specimen through large angles to ensure any defects that were not invisible in the normal orientation could be found. No defects were found in any of the ZnO NWs and all of them were of single crystal quality. The lattice images (Figure 76) show the uninterrupted (0001) lattice planes of ZnO. Intense strain contrast was common along the NW length because the high aspect ratio structure was suspended on the thin holey carbon film.

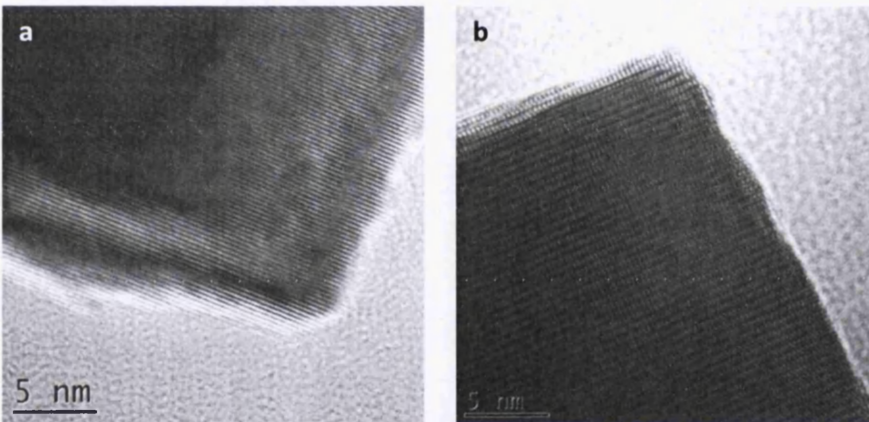

Figure 76. **a)** 0001 lattice planes of a non-catalysed NW with single crystal defect free quality, **b)** a lattice image of a hydrothermal NW with the (0001) lattice and the $(10\bar{1}0)$ lattice aligned onto zone axis $[\bar{1}2\bar{1}0]$.

Structurally all NWs were parallel from the base to the tip and not tapered, as shown in Figure 77. Catalysed NWs however showed some local variation of necking just below the catalyst particle and a disordered meniscus around the particle base. The NWs had minimal surface roughness and were very smooth except for those grown by hydrothermal methods which showed a large variation in surface quality, Figure 77b. This could have been due to post-growth etching of the surface by the growth solution. Although a more likely explanation was growth variation in the particular hydrothermal process because surface

corrugation is not universal in the batch and it has been seen as a result of certain vapour growth techniques.[18] Hong et al showed corrugations introduced surface trap states and/or defects which can affect the electrical properties of the NWs.

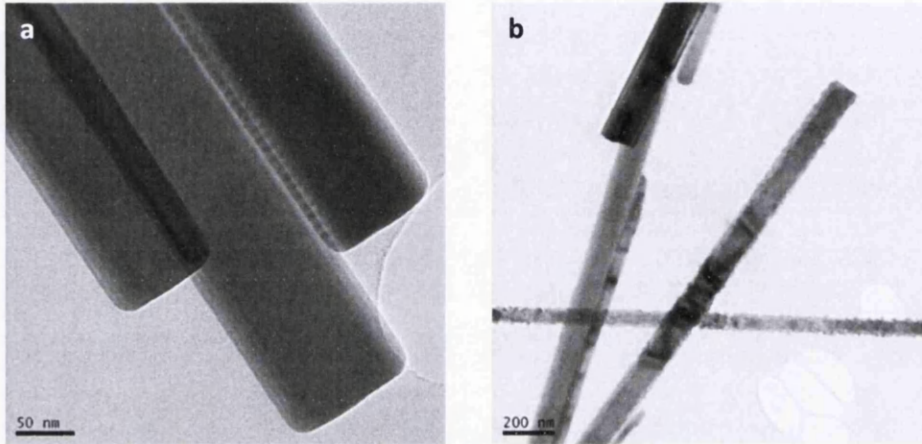

Figure 77. **a)** Bright field image of Non-catalysed NWs with uniform diameter, fringes from the thickness variation at the NW edges and overlapping NWs can be seen. **b)** Hydrothermal NWs with uniform diameter but considerable roughness/corrugation variation, strain contrast can be seen in the middle NW and the top NW is close to the Bragg angle.

The defect analysis was limited to diffraction contrast variations with tilt angle and observation of diffraction patterns. In the NWs imaged no crystallographic defects were found. The diffraction patterns displayed the crystal structure of the NWs through interpretation of the zone axis that the beam was aligned with.

6.1.1 Indexed Diffraction patterns

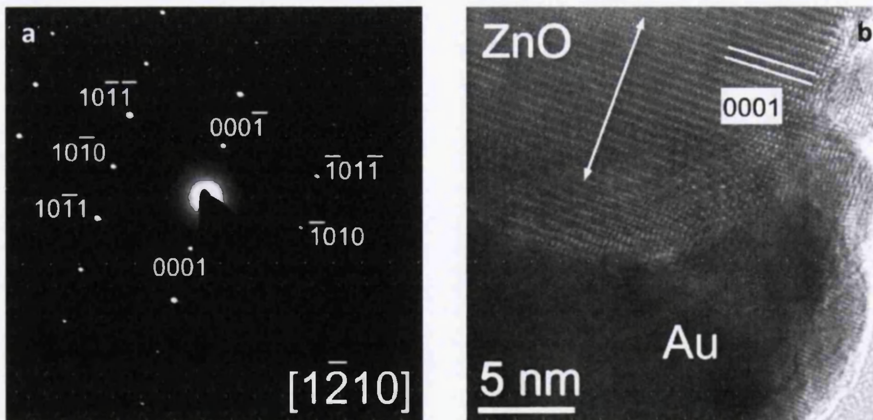

Figure 78. **a)** Indexed diffraction pattern showing the ZnO NW was single crystal with 0001 growth direction giving a hexagonal cross-section as previously seen in SEM images. **b)** the 0001 planes labelled on the TEM lattice image.

The first example in Figure 78 shows the indexed diffraction pattern of a non-catalysed ZnO NW. Figure 78a shows the appearance of a forbidden reflection {0001} in the $\left[1\bar{2}10\right]$ zone

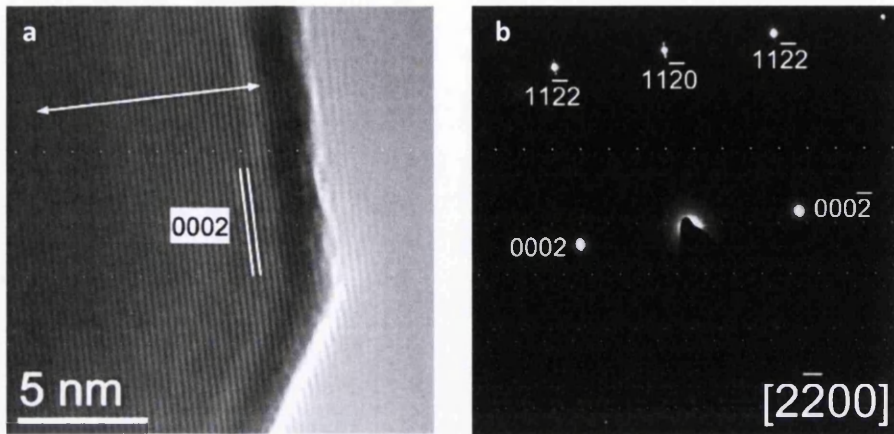

Figure 79. **a)** Lattice image of a ZnO NW with beam parallel to planes of the $\left[2\bar{2}00\right]$ zone axis. **b)** diffraction pattern showing the zone axis configuration and the absence of the 0001 reflection.

axis diffraction pattern for the hexagonally close packed crystal structure which is the basis of the wurtzite structure of ZnO. It is shown below that the forbidden reflections of 0001 do not appear in all sample orientations (Figure 79) and instead the 0002 planes must be used to index and measure the lattice and diffraction images. The angle of 58.8° from the (0002) to the $\left(11\bar{2}2\right)$ is close to the standard result[88] of 57.8° of the $\left[01\bar{1}0\right]$ zone axis which is symmetrically and crystallographically equivalent to the $\left[2\bar{2}00\right]$ zone axis (shown in Figure 79b) of the hexagonal structure.

Diffraction patterns - Catalysed NWs

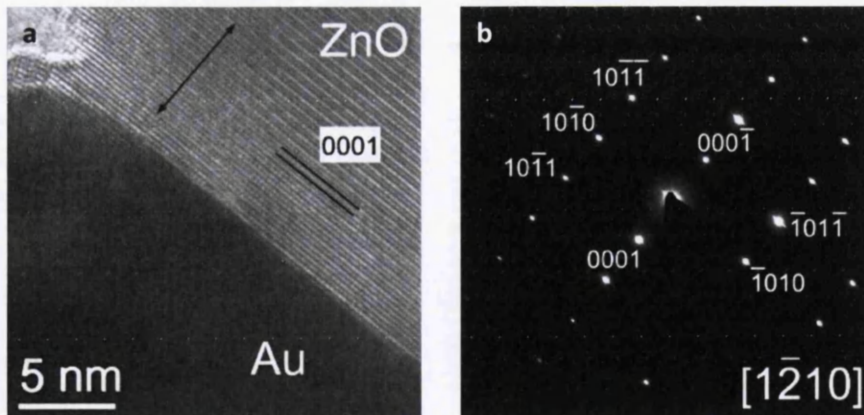

Figure 80. **a)** Lattice image of catalysed sample 16 NW with a Au catalyst particle showing the (0001) lattice planes and abrupt interface. **b)** Diffraction pattern showing the zone axis, lattice spacing and growth direction as the non-catalysed sample.

This analysis for sample Catalysed 16 was consistent with all Au catalysed NW samples displaying single crystal quality with no obvious defects, Figure 80. The zone axis $\left[1\bar{2}10\right]$ is

the same as the non-catalysed sample above with the same growth direction [0001] and the lattice image in Figure 80a shows the Au catalyst particle forms an abrupt interface with the NW.

Diffraction patterns – Au Catalysed Nanobelt

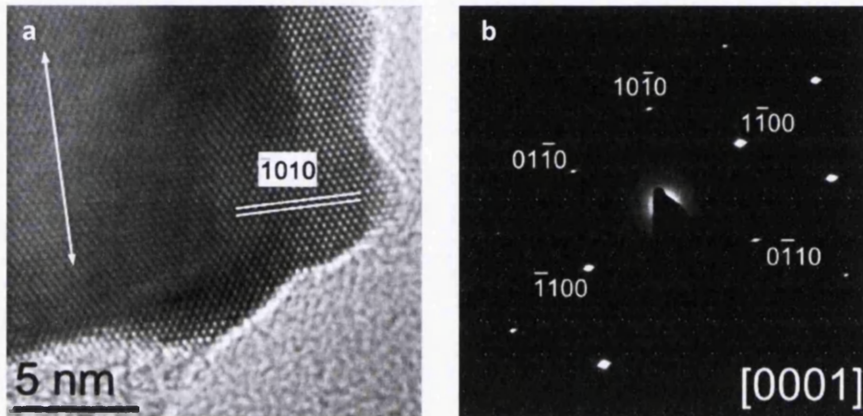

Figure 81. **a)** Lattice image of a ZnO Nanobelt with a different growth direction to the NWs. **b)** diffraction pattern confirming the structure

A ZnO Nanobelt grown by catalytic methods has a different crystallographic growth orientation and is presented here for comparison only in Figure 81. This nanobelt has a structure with a rectangular cross-section that the polar surfaces dominate because the c-axis [0001] is perpendicular to the growth direction displayed by the arrow in Figure 81a.

Diffraction patterns - Hydrothermal

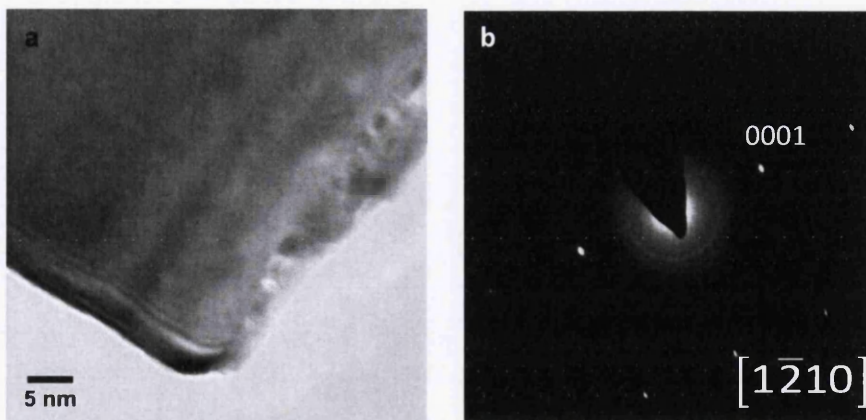

Figure 82. **a)** lattice image of a hydrothermally grown NW showing considerable surface roughness but the lattice is unbroken to the surface. **b)** diffraction pattern indicating the [0001] growth direction and crystallographic equivalence to the other NWs

Hydrothermal NWs grown by the high-temperature high-pressure method showed large variations in diameter and length and in some cases with considerable surface roughness

shown in Figure 77b. The NWs however were single crystal with no amorphous layer and the unbroken lattice extends to the surface even in the rough areas, shown in Figure 82a. Crystallographically the hydrothermal NWs were equivalent to the vapour NWs grown with and without Au catalyst, shown by the diffraction pattern in Figure 82b.

6.1.2 Atomic Lattice imaging with high resolution HAADF

The STEM analysis concentrated on atomic resolution high angle annular dark field (HAADF) imaging of catalysed ZnO NWs and non-catalysed NWs as a comparison. Simultaneously recorded HAADF and bright field (BF) images were taken in most cases but the analysis concentrated on the HAADF images due to the ease of interpretation and atomic compositional information. Therefore a brief discussion on the c-axis lattice spacing is included along with a more in-depth discussion of the lateral crystal spacing of the columns to confirm the zone axis that is displayed. The images were not filtered in the majority of cases and are the raw captured data. The lateral planes are depicted as 0002 planes.

Firstly identifying the correct orientation of the NWs on the film was important. Consistently in the scan images there was a non-linearity in the x-direction. The extent of this distortion was determined from the c-axis NW lattice measurement which was thoroughly determined from the TEM diffraction and lattice analysis. The distortion was present due to the pixel size in the x-direction being slightly different to the y-direction. This originates from the beam scan directions not being exactly orthogonal. Therefore dimensions discussed here are scaled according to the x-axis distortion calculated from the c-axis measurement. As we are mainly interested in the zone axis and Au lattice spacing this was sufficient.

Figure 83 shows high-resolution HAADF images of a catalysed ZnO NW located on a major zone axis which allowed not only the distinct (0002) planes to be resolved but also those of the longitudinal planes. HAADF transmission imaging is direct bulk analysis with no additional diffraction analysis but the atomic resolution allows the zone axis to be determined from lattice measurements and fast Fourier transform (FFT) image analysis. The zone axis looking directly at the side facet of the ZnO NW was the most accessible, rotation to the zone axis looking at the apex of the side facets proved to be too far for the stage tilt range.

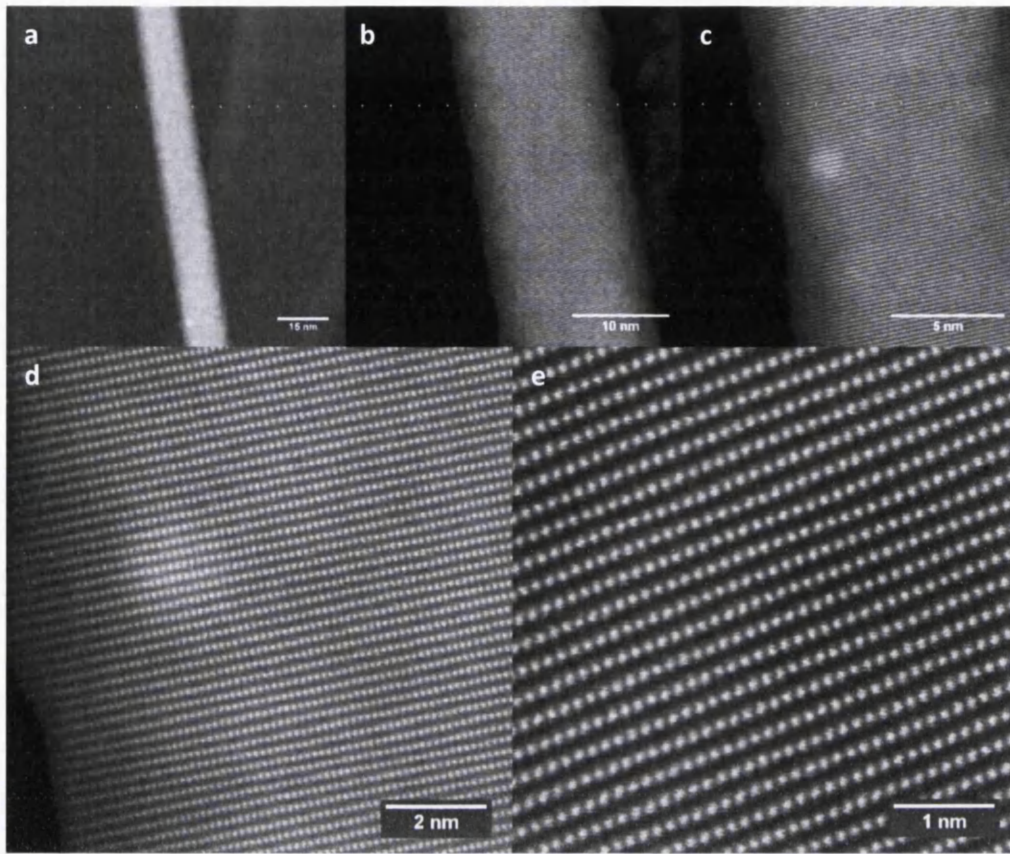

Figure 83 HAADF-STEM images at 100kV of a catalysed ZnO NW located on a major zone axis. **a)** a thin NW is located overhanging the carbon film. **b)** a 35nm wide scan of the wire reveals the (0002) lattice planes. **c)** a 20nm scan with a 5nm scale bar revealed the individual Zn atomic columns in the (0002) planes. **d)** a 10nm wide HAADF scan distinctly revealed the Zn atoms of the NW on the zone axis. **e)** high-resolution HAADF image of the individual Zn atomic columns of a [0001] orientated ZnO NW, the resolution allowed direct measurment of the atomic column spacing.

Performing FFT analysis on Figure 83d and e the 'diffraction spots' gave an average of ten manual measurements of the repeated patterns. The laterally extending planes normal to the longitudinal axis had a spacing of approximately 0.251nm (std. dev. 0.0015) and the lateral plane spacing was 0.145nm (std. dev. 0.0005). As we see the lateral planes were close to orthogonal with the image scan x-axis that was strongly affected by the distortion in the x-axis scan changing the measured lateral plane spacing (lateral columnar spacing) more than the longitudinal spacing. Several other images with the NW longitudinal axis parallel to the image x-axis revealed an approximate reduction of the FFT calculated plane spacing by a factor 0.23/0.26. Using this ratio we see the actual lateral spacing of the atoms in Figure 83 was approximately 0.163nm. These atoms were clearly resolved by the microscope showing the resolution was better than the centre-centre atomic column spacing of 1.6Å, to achieve this resolution the sample and microscope had to be very stable.

The atomic arrangement revealed a simple rectangular lattice projection in this NW orientation. The NWs have been shown by TEM to be single crystal of the wurtzite structure. By examining the wurtzite structure (Figure 84a) scaled to the ZnO lattice parameters of $a = 3.25\text{Å}$ and $c = 5.21\text{Å}$ it was apparent the longitudinal spacing was half of the c-axis i.e. the (0002) spacing.[5] The lateral spacing of 1.6Å was approximately half the a-axis as depicted in Figure 84b.

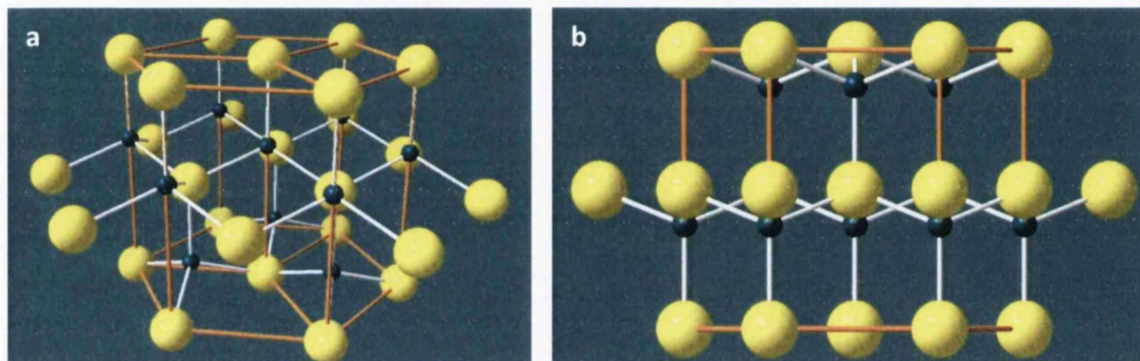

Figure 84. **a)** Wurtzite structure of ZnO. **b)** lattice structure facing the side facet of the Wurtzite structure of a [0001] grown ZnO NW looking down the $[01\bar{1}0]$ zone axis equivalent to the HAADF image, the horizontal axis is the equivalent of the a-axis in this image. The wurtzite crystal images were generated by the Diamond software.

Examination of the structure in Figure 84b reveals the ZnO unit cell has planes parallel to the c-axis with a spacing of 1.63Å and planes with the c-axis normal of spacing 2.61Å. This confirmed the orientation of the NW lying flat on the carbon grid with the beam normal to the side facet of the NW. The zone axis imaged here was the $[01\bar{1}0]$ as indicated by the standard crystal structure diffraction patterns[88] when comparing the angles and measurements taken from FFT analysis. The interlocking close packed structure of the hexagonal system provided the repeated rectangular pattern of Zn atoms in this orientation. Figure 84 indicates the close proximity from this perspective of the O atoms to the Zn atoms and thus the influence in the HAADF or bright field imaging was not detectable. The direct imaging of the atomic columns can reveal defects such as dislocations through misalignment of the atomic lattice.[207] No defects were found which is consistent with the TEM analysis.

Rotating to an alternative zone axis to increase the spacing of the interstitial cavities proved to be beyond the tilt range of the stage. Looking at the wurtzite structure from a side apex would have provided a staggered spacing of minimum 1.88Å between plane and nearest atomic column and a maximum of 2.82Å between neighbouring (0002) atomic columns. This

alternative orientation is the $[2\bar{1}\bar{1}0]$ zone axis (alternatively expressed as $[1\bar{2}10]$) which views the apex of two $\{01\bar{1}0\}$ side facets, this and the zone axis imaged here are the only two zone axis which display the 0002 or 0001 planes. Unusually $[1\bar{2}10]$ zone axis was frequently accessible with TEM however only NWs orientated on $[01\bar{1}0]$ zone axis were found during the STEM analysis. This may have been a result of baking the STEM grid sample at 120°C that allowed the NWs to relax on the carbon film.

Figure 83a depicts the NW overhanging the carbon film into free space. A bright region can be seen on the NW structure coinciding with the carbon film edge. The bright region in the images was contamination that appeared when imaging through the carbon film and was mostly avoided so as not to confuse it with impurities in the NW. A high Z-number cluster is shown in Figure 85 on the carbon film at the exit surface of the NW, this was determined by under-focussing the beam, and so focusing through the NW. This was likely to be a Au cluster dislodged or transferred to the carbon from the substrate during the preparation process. However it gave an idea of the intensity that was expected from Au impurities.

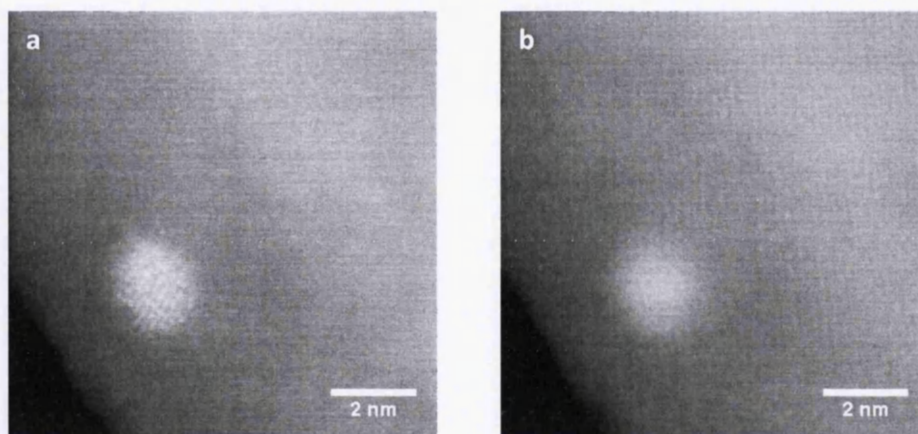

Figure 85. **a)** HAADF image under-focus on a nano-cluster below the NW, with a Z-number far greater than the ZnO NW appearing bright and with some crystalline structure. **b)** over-focus condition showing the intensity and structure of the foreign atom cluster was lost and the sensitivity to the focal point showed the necessity of focal sectioning

6.2 Metal contact structural analysis

Contacts of Au were formed on non-catalysed NWs by Au evaporation onto vertical arrays and catalysed NWs were grown purposely with distinct Au tips as described in Chapter 5. The analysis is based on TEM images which is included here and then follows onto STEM

analysis of the catalysed NWs. Each wire was rotated to a zone axis such that the (0001) planes were diffracting and the beam was parallel to the Au-NW interface.

6.2.1 Non-catalysed Au capped nanowires

The Au was evaporated in varying amounts by adjusting the quantity of Au wire source material. Due to the variable surface of a NW array the deposition thickness had to be measured by TEM to allow interpretation of the two-probe electrical measurements (Chapter 7) that were completed with Au of different thicknesses. The interface must be abrupt because the NWs have flat (0001) facets at the tip (Figure 77) and the samples were not annealed.

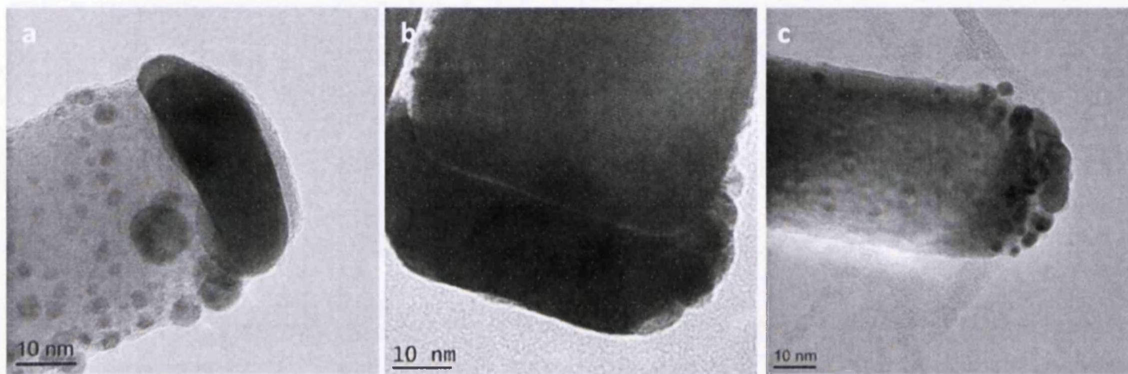

Figure 86. **a)** TEM lattice image of the deposited Au cap, average pad thickness of the sample was 12nm, Au particles were seen on the NW side. **b)** a 20nm Au deposition with an average pad thickness of 19nm, the meniscus effect was very apparent as the Au deposition increased. c) image showing the polycrystalline nature of the Au cap

The alignment of the NW array was crucial to obtain an even Au pad on the NW tip and minimal coverage on the NW side facet. The Au formed a pad on the NW tip and with increased Au thickness a meniscus type effect was seen where the Au thinned around the NW edge (Figure 86a and b). The pad always covered the entire width of the top facet which was equal to the NW diameter because the NWs maintained parallel sides. The thickness of the pad on aligned NWs was fairly uniform but was formed of multiple Au nanoparticles of various sizes; the nanoparticles are highlighted in Figure 86c. The Au did not have any crystallographic alignment with the NW and appeared to have random orientation but this was difficult to assess as nanoparticles overlapped. The shape of the Au contact pads was uniform and conducive to physical contact and probe measurements, the densely packed nanoparticles formed a robust layer, Figure 86a and b. Also apparent were small individual nanoparticles that spread around from the top to the side facet spreading the contact Au

layer. Figure 86 shows approximate depositions of 12nm and 20nm, later depositions were completed as multiplies of these.

6.2.2 Catalysed nanowire Au particle

The Au particle and the catalysed NW had a complex relationship during growth. Symptoms of the complex variations included single (Figure 87a) and poly-crystalline Au particles, various size particles relative to NW diameter and Au particles on the top (0001) facet or on the NW side (Figure 87b). The NW diameter varies within arrays but not monotonically with catalyst particle size. This may have suggested in some cases the Au was depleted during growth reducing its size and giving a thick wire but small Au particle at the end.

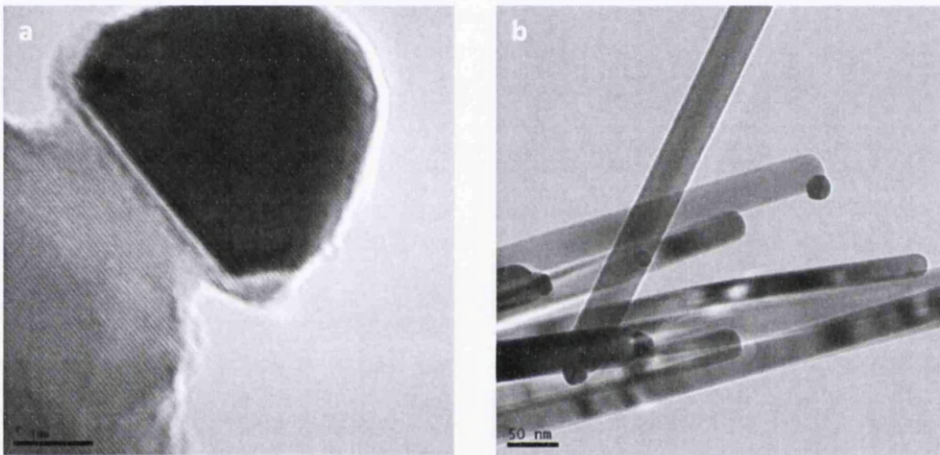

Figure 87. **a)** Lattice image of a single crystal catalyst Au particle tip on ZnO NW with a growth meniscus and neck. **b)** ZnO NWs with catalyst particles of various sizes in various positions on the NWs

The Au particles formed an approximate hemispherical shape. Also apparent was a distinct ZnO growth meniscus around the edges of some Au particles. This growth lip appeared to be randomly orientated until order was established at the uppermost complete NW (0001) facet. The Au hemisphere was conjoined with the top (0001) flat facet of the NW and the meniscus suggested the epitaxial addition of ZnO from the surface of the Au particle. The images show the interface was abrupt with no substantial interfacial layer and lay parallel to ZnO (0001).

The typical hemispherical shape of the Au particle can be seen in Figure 87a. Later calculations for two-probe electrical measurement analysis (Chapter 7) required the interface diameter between the Au particle and NW, this had to be estimated from top-

down SEM images. Therefore the analysis here gained statistics of the Au particle diameter against thickness and interface diameter.

Three different Catalysed samples were measured with 24 NWs measured in total giving the average particle depth as 58% of the diameter with a standard deviation of 6%.The ZnO NWs were seen to thin down at the neck and the interface width was measured to be on average 83% of the maximum particle diameter with standard deviation of 6%, but this excluded the growth meniscus effect. These results justified an approximate hemispherical model of the Au particle with the flat edge completely in contact with the NW. An important result was the particle diameter was on average only 63% of the NW diameter with a standard deviation of 9% but with outliers having particles far less than 45% of the NW diameter.

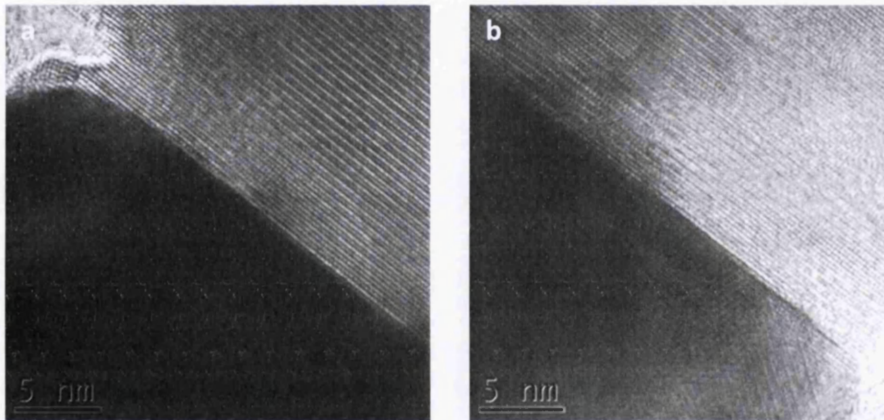

Figure 88. **a)** Lattice image showing the disordered growth meniscus at the edge of the Au particle. **b)** planes of various orientations in the Au particle suggested in this case the particle was polycrystalline.

The Au particle formed an abrupt interface with the ZnO (0001) plane at the NW tip. It was not possible to state that the interface was completely atomically abrupt as TEM is a two-dimensional representation of a three dimensional bulk sample. The interaction of the beam with the atomic lattice made it difficult to assess the exact atomic interface although the images showed a distinct contrast difference between the lattice planes of the ZnO and Au. This interface was investigated further by high-resolution STEM imaging in section 6.4. It is possible to build a three dimensional data block using tomography which would reveal more of the interface structure.

Figure 87 and Figure 88 have lattice periodicity (measured by line profiles) that revealed the ZnO 0002 spacing to be 0.266nm and the Au spacing to be 0.242nm on average over the

particle. Spacing measurements were similar near the interface with no indication of lattice distortion. The measured ZnO spacing was approximately half of the (0001) spacing of 0.52nm.[5] Some Au particles were single crystal (Figure 87a) whilst other particles had planes at various orientations which suggested a polycrystalline structure (Figure 88b). Lattice images revealed polycrystalline Au particles had several orientations and defects such as twinning (Figure 88b), however there still remained in the dominant grain (the particle was usually composed of only a small number of grains with one grain making up most of the particle) alignment at the interface with ZnO (0001). The hemispherical shape was maintained in both crystalline cases. The single crystal lattice planes of the Au particle agreed with the {111} spacing of Au which aligned with the ZnO (0001). This alignment is necessary for an epitaxial relationship between the particle, especially when single crystal, and the NW. This provided evidence for the Vapour-Solid-Solid growth mode which

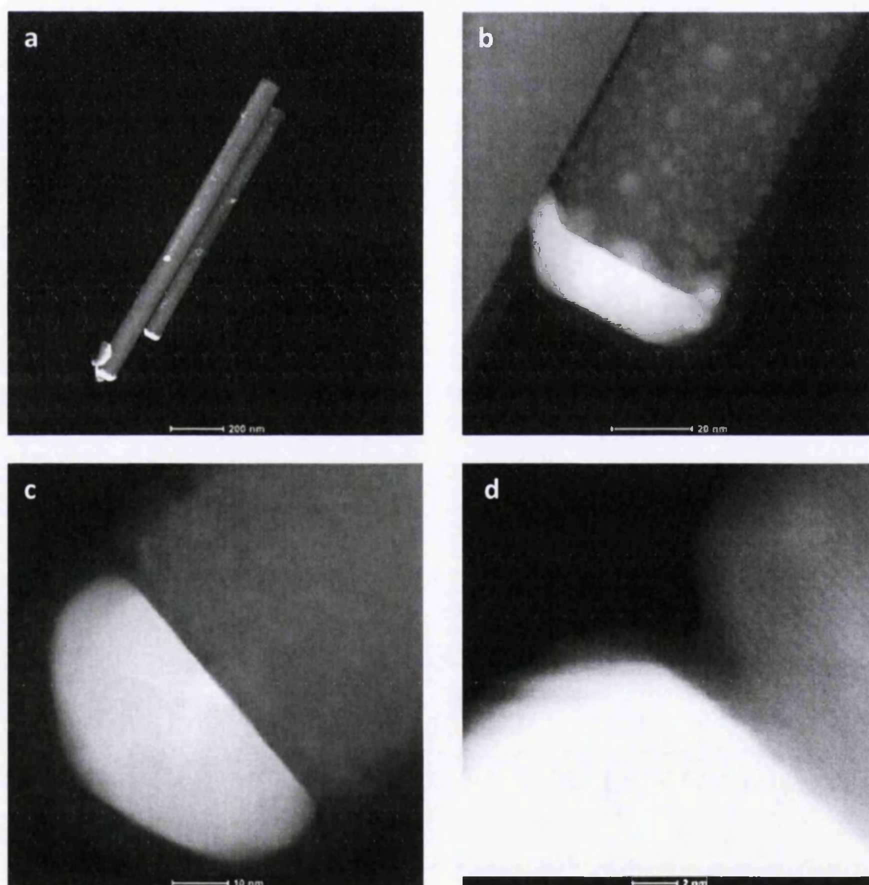

Figure 89. **a)** Low magnification HAADF image of two non-catalysed NWs capped by a 20nm Au deposition. **b)** HAADF image of the Au cap and distinct Au clusters on the NW side facets, both images showed clearly the high Z-number clusters coated the sides of the NWs but they did not form a continuous layer. **c)** HAADF image of a catalysed NW with a bright high Z-number Au particle, the very abrupt interface with the NW and no Au on the sides. **d)** high magnifcation HAADF image achieving close to the best resolution of the microscope.

occurs with solid catalyst particles rather than liquid, this is discussed in more detail in section 6.5.[58,103,125]

6.2.3 TEM High Angle Annular Dark-Field (HAADF) imaging

HAADF imaging in the Tecnai TEM used an annular detector in STEM mode that collected electrons incoherently scattered through relatively large angles. The scattering power of an atom is roughly proportional to Z^2.[90] HAADF analysis was used to identify the Z number variation in the ZnO NWs with Au caps and to identify Au present on the side facets. This was performed with TEM in scanning mode which reduced the resolution to 0.5nm from 0.25nm in normal imaging mode. HAADF imaging was particularly useful for confirming the presence of deposited Au on the non-catalysed NWs and confirming small particles on the side facets after the evaporation process were Au, shown in Figure 89a and b. The Z-number contrast imaging was capable of identifying compositional variations, for example the Au catalyst particle and the abrupt interface in Figure 89c, and a particular advantage is atomic planes appear bright in the image, in the full resolution high quality version of Figure 89d the (0001) planes can be seen.[90] The technique is capable of very high resolution which is dependent on the probe size. In this case contrast difference between lattice planes was achievable.

6.3 Nanowire Compositional analysis

TEM Energy Dispersive X-ray (EDX) spectroscopy analysis was used to confirm the elements present in the ZnO NWs, the Au particle on the catalysed NWs, and the Au coated non-catalysed NWs. The spectra of a catalysed NW stem and catalyst particle are displayed in Figure 90a and b respectively. Similar results were obtained for the non-catalysed deposited samples even though Au nanoparticles were present on the side facets which showed the limits of detecting small concentrations of elements. Therefore the HAADF imaging , for example Figure 89d, must be used to identify the particles on the NW side facets as Au. It can be seen there was no Zn detected in the Au of the NW crystals suggesting no alloying had taken place. However this was limited by the accuracy of EDX which was around 1%. The results show local information can be achieved with EDX when using thin samples, spot EDX was used here; no stray signals were collected from the neighbouring material when scanning the Au particle or the ZnO NW. The proportional amounts were obscured by the presence of Carbon, Oxygen and Copper signals that originated from the surrounding

sample grid and carbon film, this is a normal feature when performing EDX in a TEM. The relatively weak signal of Oxygen represented by the atomic mass difference between Zn and O made quantitative analysis of the atomic ratio in the NW difficult and no further analysis was attempted because the necessary accuracy could not be obtained.

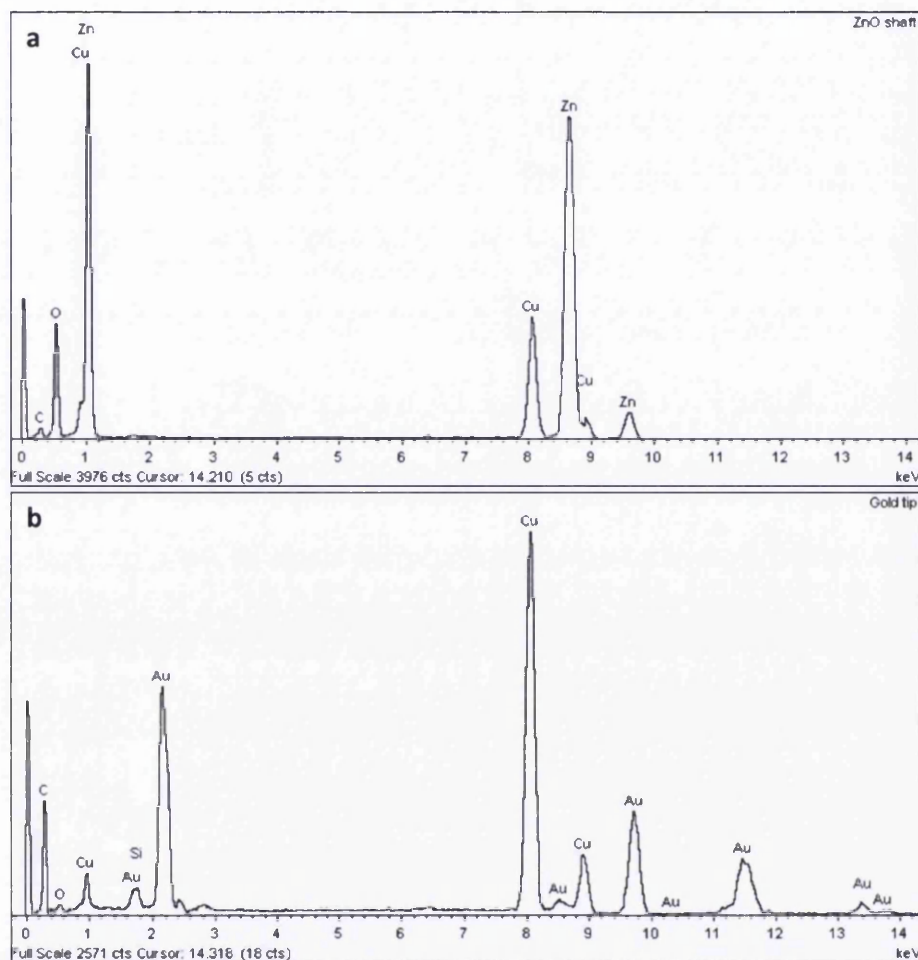

Figure 90. **a)** EDX spectra of the catalysed ZnO NW crystal. **b)** EDX spectra of the Au catalytic particle

6.4 Catalytic Au contamination and the Au-ZnO interface by high resolution HAADF

Identifying possible Au contamination of the catalysed NW was crucial for the correct assessment of the Au catalyst particle – NW interface, especially when concerning the electrical properties and the potential energy landscape in Chapter 7. It was shown in section 6.1.2 a high resolution STEM-HAADF image of a ZnO NW with all of the atomic columns of the same intensity, Figure 83e. No bright spots were apparent when focussing in the central horizontal plane of the NW. The lack of Au or other high Z-number impurities in

the NW stem was consistent with the analysis of 12 catalysed NWs ranging from 15-30nm in diameter. NWs only with distinct Au catalyst particles were thoroughly searched using HAADF and naturally this concentrated on the region near the Au tip. The interface was shown to be abrupt. To describe the interface as atomically abrupt was difficult without 3-D tomography but the 2-D representation of HAADF imaging indicated this.

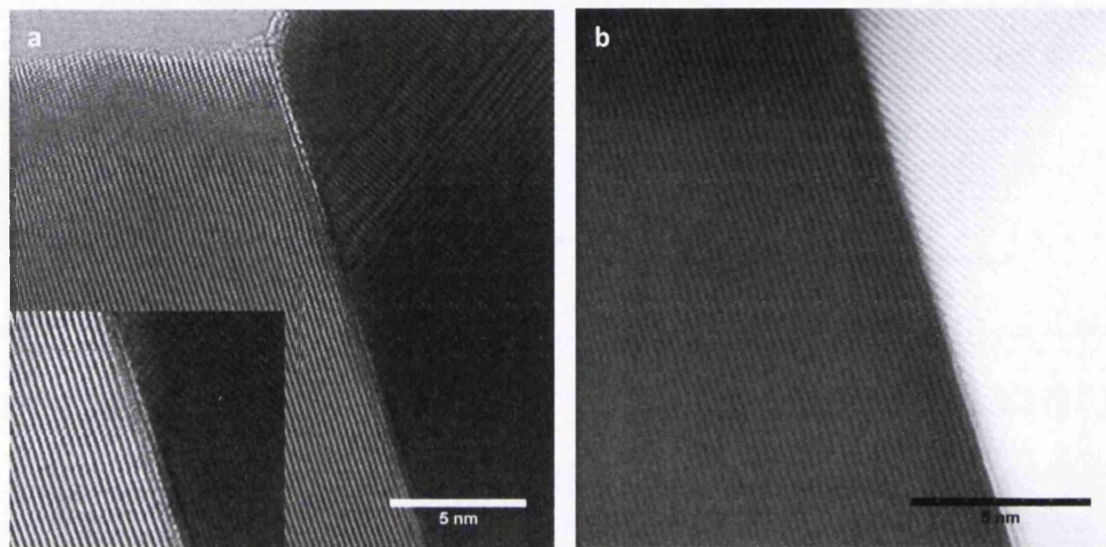

Figure 91. **a)** Bright-field image of a 30nm diameter NW and the Au catalyst tip, the intimate relationship was evident but the interface region suffered from phase interference especially with two crystal orientations (displayed in the inset) of the Au particle which confused the image. **b)** corresponding HAADF image at higher magnification showed the (0001) of ZnO and a polycrystalline Au with a crystallite displaying {111}.

Concentrating the analysis on the Au particle to NW interface showed the crystalline nature of both materials Figure 91. The Au tip had two different crystal orientations, shown in the bright field image of Figure 91a and is highlighted in the inset, this displays the alignment of one crystallite with the ZnO (0001) (this is also seen in the high resolution version of Figure 92). The corresponding HAADF image in Figure 91b overcomes the confusing phase phenomena of the bright-field image near the interface region and displays the distinct ZnO and Au lattice with no interfacial region. The high resolution HAADF images in Figure 92 display the Zn atomic columns with no contrast variations and the abrupt interface with the Au particle. No interdiffusion of Au into the ZnO was apparent and Au atoms were not seen close to the interface in the ZnO. A linescan across the atomic columns reveals that all of the

Zn columns were equal in intensity Figure 93.

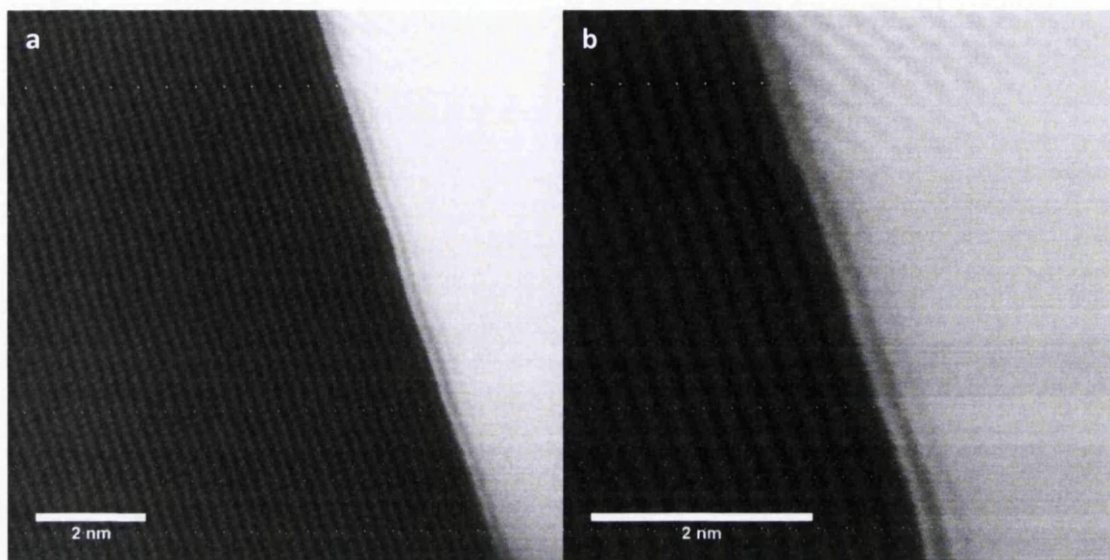

Figure 92. High magnification HAADF images of the NW tip interface. **a)** two different orientations of Au are seen in the catalyst particle the interface is abrupt with no interfacial layer. **b)** magnifying further shows the individual atoms of Zn next to the abrupt Au interface

The intensity profile of a HAADF image can reveal variation in the relative intensity of neighbouring columns which may indicate changes in sample composition or thickness. The equal intensity of the Zn columns indicated similar composition and the sudden intensity increase at the interface showed there is no interfacial layer. The interface between the ZnO and Au was abrupt, however the first Au column on the profile appeared less intense, this is an effect of the catalyst particle shape.

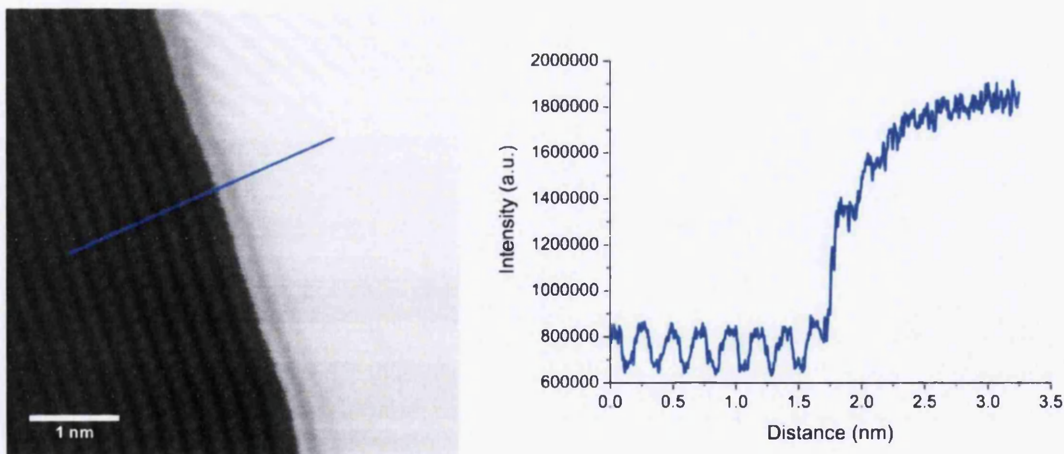

Figure 93. Graph showing the line intensity profile across the Zn columns to the abrupt Au interface and particle. The equal intensity of Zn atoms indicated the average Z-number of each column was the same and high Z-number impurities such as Au were not present.

6.4.1 Depth sectioning with HAADF STEM

To examine the interface further and ensure Au atoms were not hidden within the bulk or on the surface of the NWs the crystal was 'cut' into sections by focussing the probe at different depths. Through-focal series were conducted for all wires and sectioned into at least 8 images. A series of images are shown in Figure 94 from the initial focal point at the NW centre to a plane 15nm above and below resulting in the blurred over- or under-focussed condition. This analysis was also conducted on NWs as small as 15nm diameter with large distinct Au tips. High-resolution high magnification images are shown in Figure 92 of the interface. The intensity profile of the interface shown in Figure 93 indicated the equal intensity of the Zn atoms and an abrupt Au interface but whether this was a three dimensional atomic abruptness was not possible to infer even with through-focal series which limited the influence of atoms outside the depth of field (in this case a few nanometres).

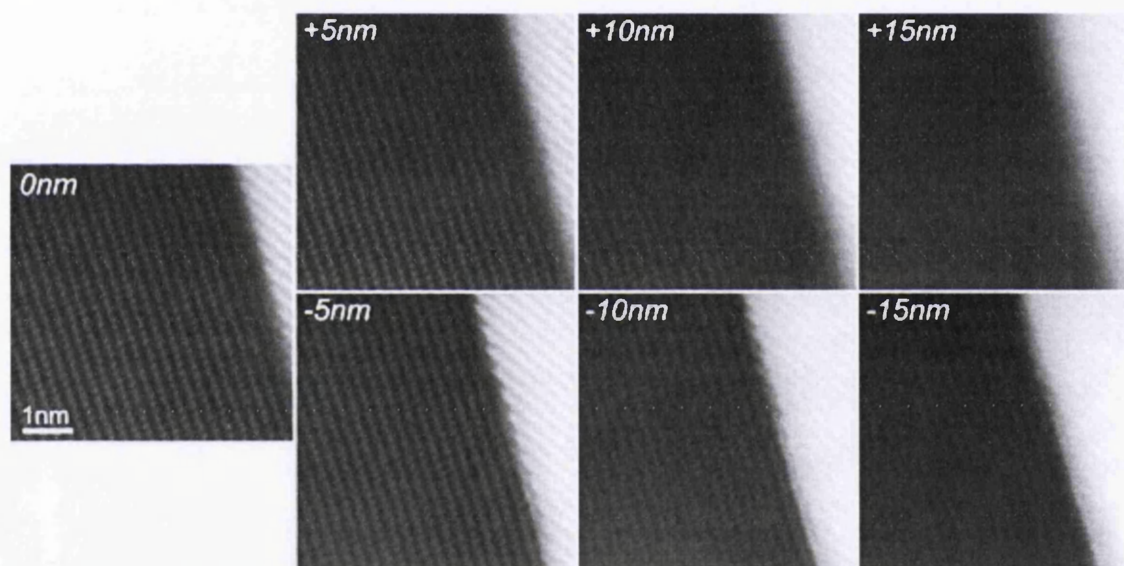

Figure 94. On axis through-focal series. HAADF images of a ZnO NW oriented on the $[01\bar{1}0]$ zone axis and the ZnO-Au interface starting with focus on the NW centre through to the overfocus condition 15nm above. No bright spots were seen in the ZnO matrix near the interface or in the bulk.

The correction of aberrations up to 5th order allowed the use of very large probe convergence angles (here 31 mrad semi-angle) that provided a very shallow depth of field (a few nm). Although due to complex optical reasons the depth resolution is limited[222] the technique is useful for the observation of point defects and spatially limited impurities[15,134,140,223] and was used in an attempt to reveal impurities buried within the

sample depth (Figure 94). Through-focal series were recorded both along the NWs zone axis or tilted away from channelling conditions. Figure 94 and Figure 95 show members of the series, for the on axis and off-axis alignments respectively, which revealed no distinct bright atomic signals. This was consistent with all NWs when located on a zone axis or tilted away from the zone axis by a few degrees which can help to detect impurities in challenging materials.[136]

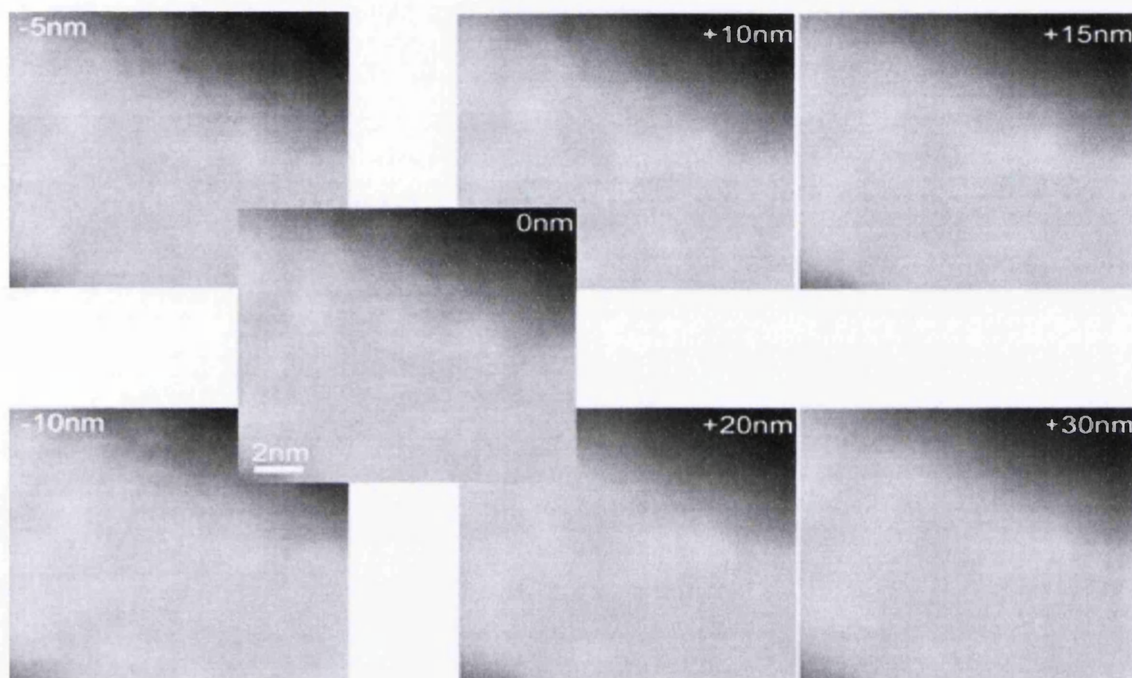

Figure 95. Off axis through focus series. HAADF though focus images of a ZnO NW tilted away from channelling conditions.

It was possible Au atoms may have been located interstitially which can make them difficult to detect[212] when imaging on a zone axis. To overcome this and in an attempt to reveal these atoms HAADF imaging was conducted on tilted and randomly orientated NWs. The NWs slightly tilted away from the major zone-axis still displayed the (0002) lattice but no bright signals were detected.[136] Further tilt was used and in this random orientation bright specks were occasionally seen to run across the image while scanning. Closer inspection did not reveal any bright impurities and this anomaly was increased beam damage and sputtering of the NW because of the greatly reduced beam channelling. The Z-number contrast imaging overall was only slightly hampered by beam damage and the hexagonal shape of the NWs presented a sample with variable thickness near the edges which may have helped to detect Au atoms. It was possible Au atoms were very mobile within the ZnO

matrix and moved when scanned, a good indication that this was not happening and no Au was present were the equivalent HAADF images, imaging effects and lattice measurements that were obtained on non-catalysed NWs of diameter 20-60nm. However to be certain simulations were used to investigate the detectability of Au in the NWs, described later in section 6.6.

6.4.2 Control Experiment of non-catalysed ZnO NWs

Although some very local contrast variations were observed in the HAADF images of the catalysed NWs, these were merely due to statistical noise and/or limited surface roughness. This was identified by comparing two images acquired in identical conditions of the side of a NW grown without Au catalyst Figure 96a and a similar image for a NW grown with Au catalyst Figure 96b. Minute local intensity fluctuations were evident in both micrographs but the fact that the images were otherwise perfectly comparable was a further indication that no Au impurities were incorporated into the NW during growth.

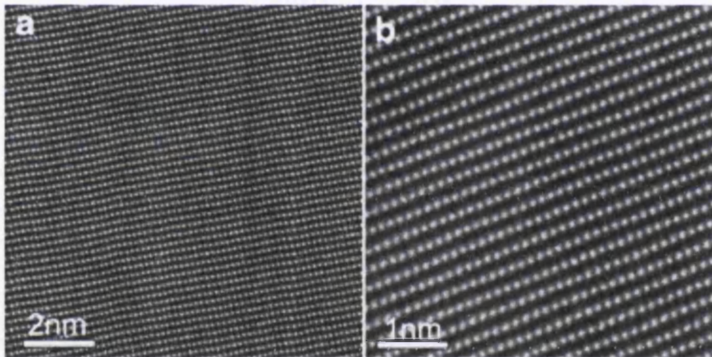

Figure 96. **a)** HAADF image of a ZnO NW grown without Au catalyst and, **b)** HAADF image of a ZnO NW grown with Au catalyst. Both images were recorded in identical conditions, with both NWs oriented on the $[01\bar{1}0]$ zone axis.

6.5 Au Catalyst Particle and the Growth Mechanism

Although some Au particles displayed several crystal orientations and appeared polycrystalline other Au particles were single crystal (Figure 97). FFT analysis of the Au tip revealed ~2.37Å lattice spacing. The face centred cubic structure of Au investigated with a 'stick and ball' model (Diamond v3.2 software) and comparison of measured lattice spacing's and angles to standard results[88] the particle was likely close to the $[011]$, $[\bar{1}12]$ or $[\bar{1}23]$ zone axes and displayed the $\{111\}$ spacing of 2.35Å. This lattice spacing was also revealed during TEM analysis of other single crystal Au particles and the major crystallites in polycrystalline particles. This confirms the Au particle when in a single crystal state aligns

the Au{111} with the (0001) of ZnO. The relationship $Au(11\bar{1})||ZnO(0002)$ was described by Brewster et al using diffraction and it is a common feature for Au catalytic particles on the (0001) of ZnO NWs.[58]

Initially it was unclear whether the Au was liquid during growth and crystallised on cooling or whether some crystal relationship held during the growth process. Assuming the VLS model is accurate the poly-crystalline or single crystalline structure of the Au particle should develop on cooling and should be an alloy of Au-Zn. However it was unlikely that alloying of Zn and Au occurred[125], confirmed by TEM-EDX and the lattice spacing's were consistent with a pure Au crystal. However, HAADF, EELS and EDX are unable to distinguish alloying at very small concentrations, but no alloying is consistent with published results.[58,125] The alignment of the Au and ZnO lattice shows an epitaxial relationship that may have held during growth with a solid Au particle and growth driven by surface diffusion.[125] The growth meniscus revealed by TEM around the edge of the Au particles provided further evidence that surface diffusion was the dominant mechanism. A solid particle with no alloying and an epitaxial relationship with the NW fits the model for Vapour-Solid-Solid growth.[58,103,125]

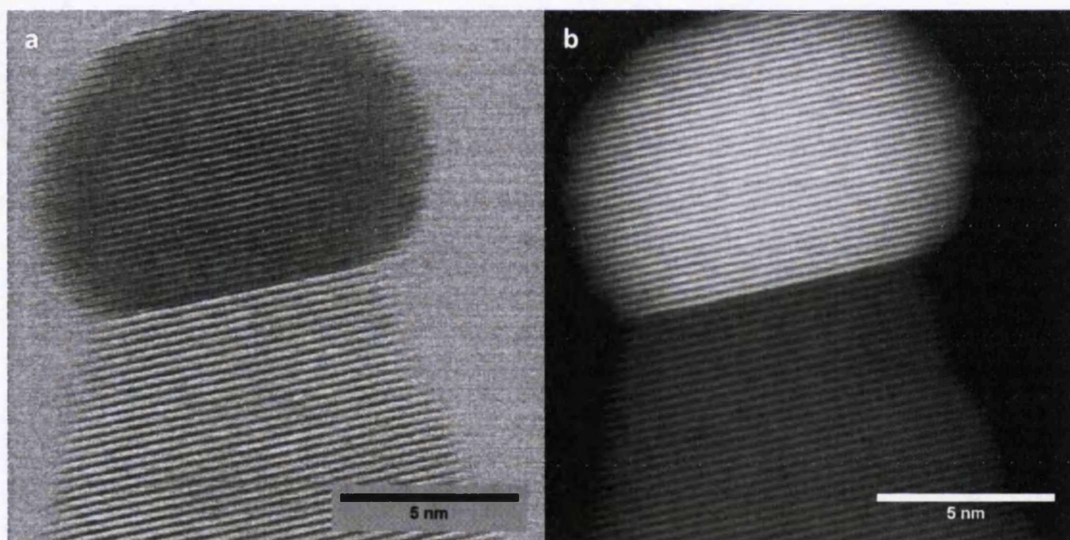

Figure 97. **a)** bright-field image with phase contrast of the uninterrupted lattice planes of the Au particle joined to the ZnO NW. **b)** corresponding HAADF image highlighting the compositional difference and single crystal quality of both the tip and the NW.

6.6 HAADF Imaging Validation

The major factor governing the intensity of atomic columns in the HAADF image was the average Z-number in the depth of field. If the Z-number of a foreign atom was not great

enough in comparison to the host columns the excess intensity may go unnoticed. Filtering the image can enhance the intensity of columns by removing the noise[15], for example, by using a bandpass filter unwanted frequencies can be removed from the image and by tailoring the passband the 'sample signal' is left. The 1024x1024 pixel images were filtered with the bandpass filter tool in ImageJ software that filters the large structures down to 40 pixels and small structures up to 3 pixels. This enhanced the low frequency point occurrence of atomic columns and individual signals of foreign high Z-number atoms. This premise is displayed in Figure 98 using a NW overlapped by another wire and close to the carbon film. After numerous imaging scans of the wire bright spots appeared, this is sputtering of material from the NW lying on top. Similar distinct effects were not seen on any individual NWs.

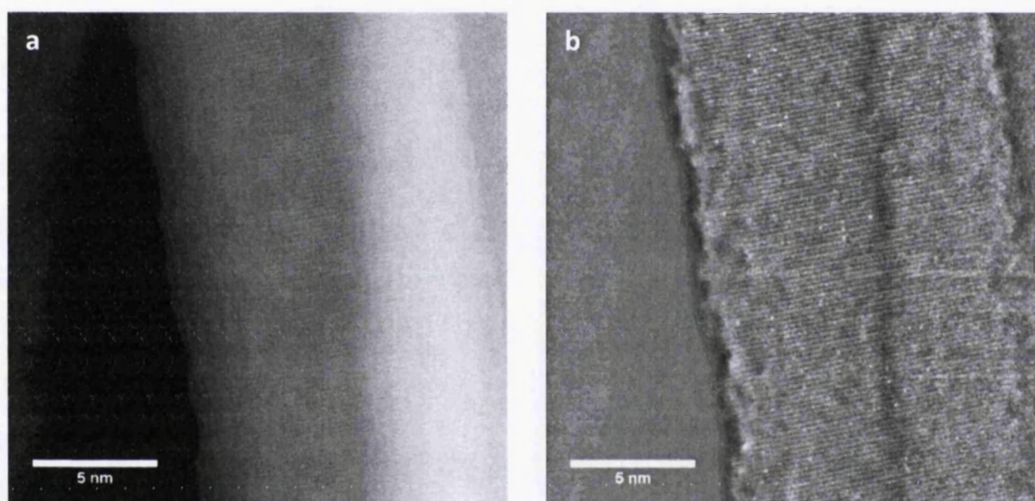

Figure 98. **a)** Raw HAADF image of two overlapping NWs with bright spots apparent in the image. **b)** Bandpass filter of image enhances the spots of greater Z-number although in this case this is unlikely to be Au and more likely beam damage of the overlapping NW.

Increasing the magnification (Figure 99a) showed some of the bright spots were in line with the ZnO (0001) planes and a line intensity profile (Figure 99b) of the unprocessed image revealed the distinct increase in intensity at one of these points. These points were in the size range of single atomic columns and were likely be one or two additional atoms sputtered from the neighbouring NW or transferred from the carbon film. As these spots were spread randomly and were not found on any other wire or near a catalyst tip it is unlikely these were native Au catalyst contamination. However it was necessary to validate

the HAADF imaging.

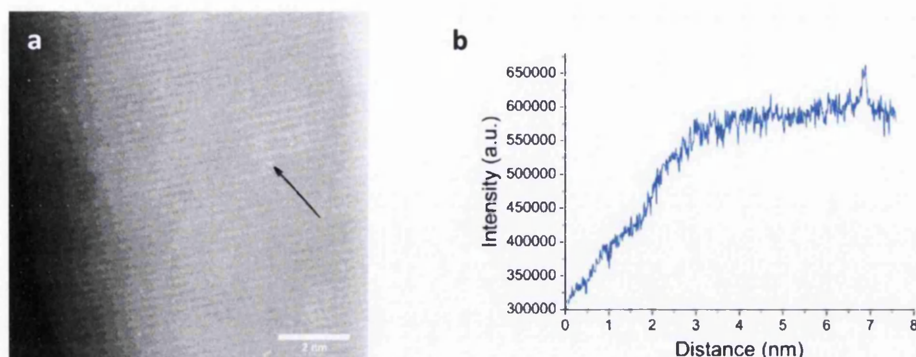

Figure 99. **a)** Unfiltered raw image showing the bright beam damage more clearly. **b)** line profile from the edge of the NW along the (0001) lattice plane and the distinct jump in intensity of the bright spot, also of note is the approximate linear increase of the intensity along the side facet of the NW and the increasing intensity relationship with thickness

6.6.1 Estimating intensity increases

A simple method for estimating the increase in intensity of an atomic column containing a foreign atom is to assume screened Rutherford scattering and an intensity according to $Z^{1.7}$.[15] A ZnO NW of approximately 20nm diameter in the orientation as seen here $[01\bar{1}0]$ has Zn atoms spaced every ~5.63Å within an imaged atomic column. This provided approximately 35 Zn atoms in the central depth of the NW and a simple calculation of the relationship with $Z^{1.7}$ and substituting in one Au atom roughly estimates an excess intensity of 14%. This assumed the entire column contributes equally without the influence of focal depth which would greatly increase the local intensity excess near Au atoms.[15,140] The rough calculations were built upon with multi-slice simulations.

6.6.2 The effectiveness of imaging with a small tilt off-axis

GaAs NWs of similar diameter and placed in a similar configuration as the ZnO NWs imaged here have been shown by Bar-Sadan et al to have Au impurities in the bulk by HAADF-STEM.[136] Imaging of the impurities in the GaAs NWs was improved by tilting 3° away from the zone axis to reduce background signal from the host matrix. An electron beam aligned with a crystal zone axis is channelled along the atomic columns which increases the high-angle scattering of the host material within the column. By tilting slightly away from the zone axis the channelling effect is reduced and the excess intensity of individual impurities increases dramatically over the greatly reduced background. As a comparison, Ga has atomic number 31 and As of 33 and that presented a greater challenge to detect Au 79 in

the bulk than it does in the ZnO matrix of Zn at 31 and O at 8. Oxygen gives little high angle scattering and it cannot be imaged next to the Zn columns.

A criteria for the detectability of an impurity in a crystalline sample was set by Voyles et al[212] of $Z_{dopant}/Z_{host} \geq 3$ for reliable detection, although this neglected dynamical diffraction[136] and the sensitivity, stability and resolution of fifth-order aberration corrected STEM. Therefore on the same principles the ratio of Z_{Au}/Z_{Zn}=2.63 is sufficient[136] when orientated on-axis, and with slight tilt this ratio is stretched allowing imaging in materials as challenging as GaAs. To detect the Au atom the probe must be focussed near to the impurity.[136,140] The improved depth of field combined with a slight tilt from a zone axis produces a very strong signal from the impurity which is enhanced by a substantial reduction in the background signal.

The detection limit of the impurities is determined by the noise which depends on the electron dose and the host matrix. Noise is increased by an amorphous surface layer and contamination but these were not observed during analysis.[136] When the impurity signal intensity rises above the signal and background 'noise' of the host matrix it can be detected which was aided by using very thin samples. The background signal can also reduce the intensity of interstitial impurities to a point where they can't be detected[136,212] which can also be overcome by tilting slightly off axis but this again did not reveal Au impurities in any ZnO NWs. However to overcome the difficulty in proving something isn't there it was necessary to show further that it was indeed possible to detect singular Au atoms when on-axis.

6.7 QSTEM: HAADF simulation

Slabs of ZnO of various thicknesses were created for the simulations using the microscope conditions used for the experiments. The slabs were aligned along the $[01\bar{1}0]$ zone axis with a flat entrance and exit surface. The thicknesses of the slabs were chosen to correspond to the experimental conditions and sample morphology. Single Au atoms were then substituted for a Zn atom at various depths within the slab (along the beam propagation

direction), without any additional relaxation of the lattice.

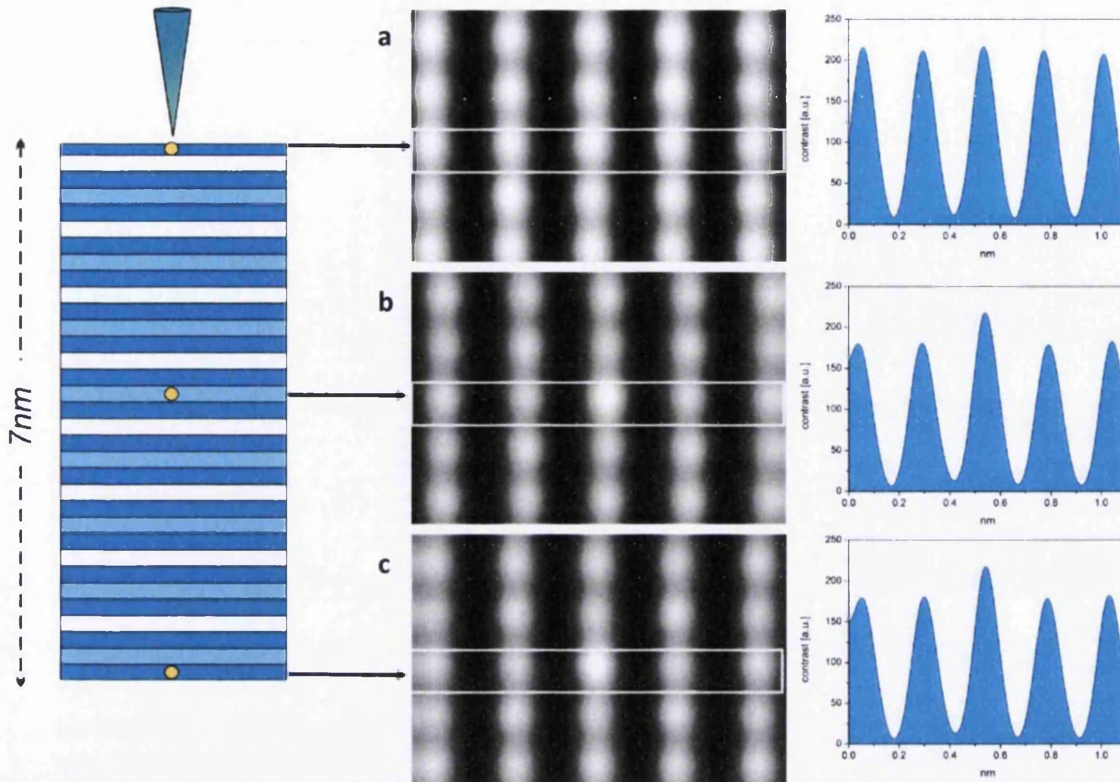

Figure 100. HAADF image simulations of a slab 7nm thick, with one Au impurity atom placed at **a)** the entrance surface, **b)** middle and **c)** exit surface of the slab.

Slabs of thickness 7 nm (Figure 100) and 14 nm (Figure 101) were simulated with single Au atoms embedded in the bulk or on the surface. In the 7 nm slab, the Au impurity atoms were placed at the entrance surface, in the middle of the slab, and at the exit surface (. a, b and c respectively). While the presence of the impurity atom at the entrance surface did not change the contrast significantly (increase ~2%), placing the Au atom in the middle or exit surface of the slab increased the contrast in both cases by ~20%. In the 14 nm slab the Au substitution was placed at the entrance surface, 3.5 nm from the entrance surface, in the middle of the slab, 10.5 nm from the entrance surface and at the exit surface (Figure 101a-e respectively) when the impurity atom was placed at the exit surface of the slab the contrast increase was approximately ~15%, while it dropped to ~3% when the atom was placed further in the bulk of the sample.

The simulations show the validity in the conclusion that no Au atoms contaminate catalysed ZnO NWs and even in the most challenging configuration, when on-axis, Au impurities would have been very prominent. Au atoms would be detectable at most points in the

thinner NWs (~15nm diameter), and in the thicker NWs (~25nm diameter), especially when near the exit surface or near the edges of the side facets that thin to an apex.

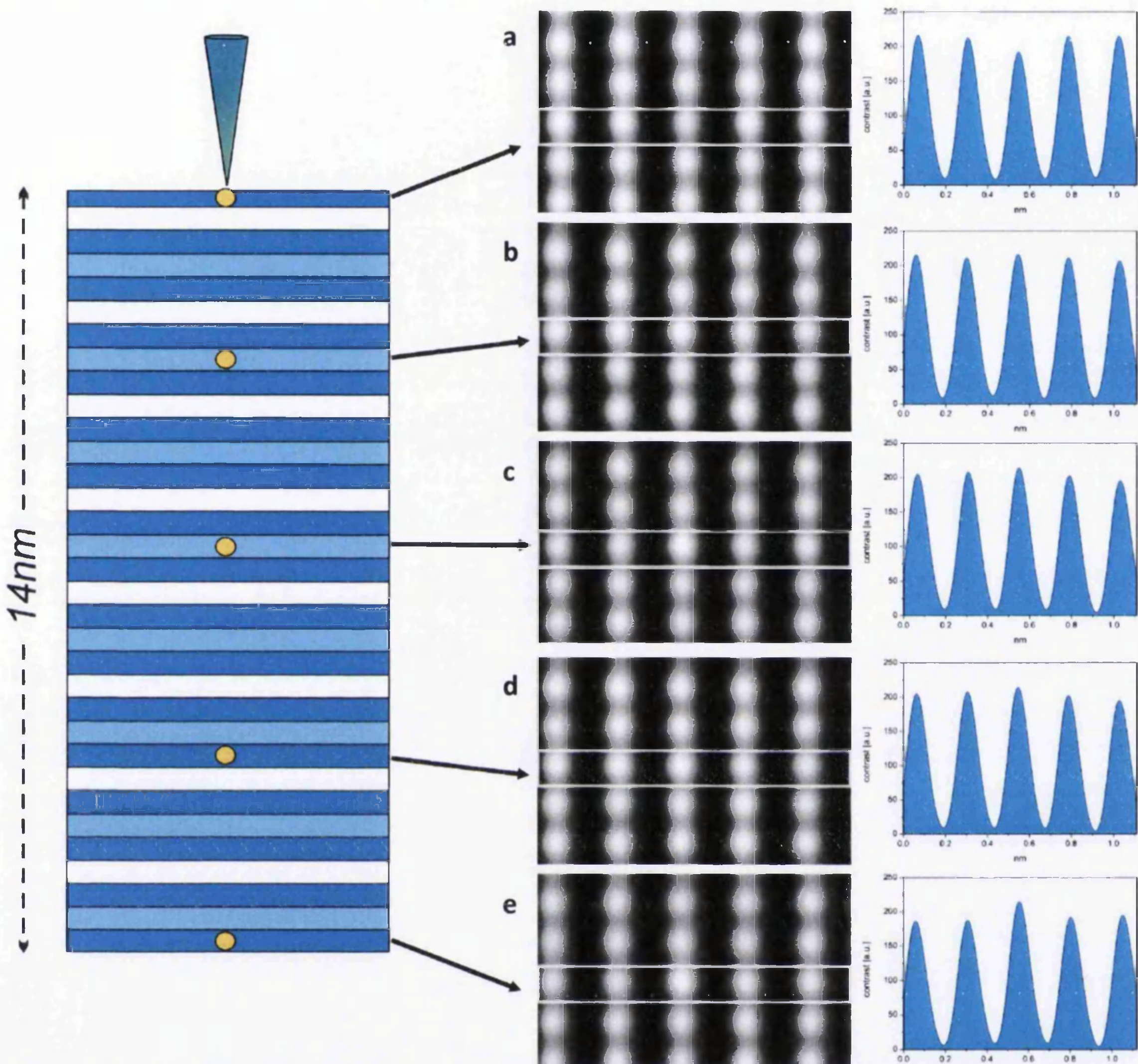

Figure 101 HAADF image simulations of a slab 14nm thick, with one Au impurity atom is placed at **a)** the entrance surface, **b)** 3.5 nm from the entrance surface, **c)** in the middle of the slab, **d)** 10.5nm from the entrance surface and, **e)** at the exit surface of the slab.

6.8 FIB cross-section Nanowire array analysis

Once a high level of confidence in the lack of Au within the NWs was achieved it was necessary to investigate the Au catalyst relationship with the base growth. The milling of a NW array cross-section was intended to observe the crystallographic nature of the base layer and the position of Au catalyst particles. By using a focussed ion beam (FIB) thin samples of <100nm were milled from each array. During this process the array was coated with an amorphous carbon-platinum matrix to protect and reinforce the sample. The initial ~50nm platinum coating is seen in Figure 102a as a dark layer across the growth that was

embedded in the light contrast e-beam deposited amorphous carbon, capped by the darker ion-beam deposited layer. The main objective of the analysis was to investigate the base crystal growth that occurs at the bottom of the upright NWs and the relationship with catalyst particles. Other points of interest were the NWs and the intersection with the base crystal growth, the substrate interface and the crystallographic quality of the entire array. This quality is highly important for array devices which hope to transfer charge efficiently through this layer.

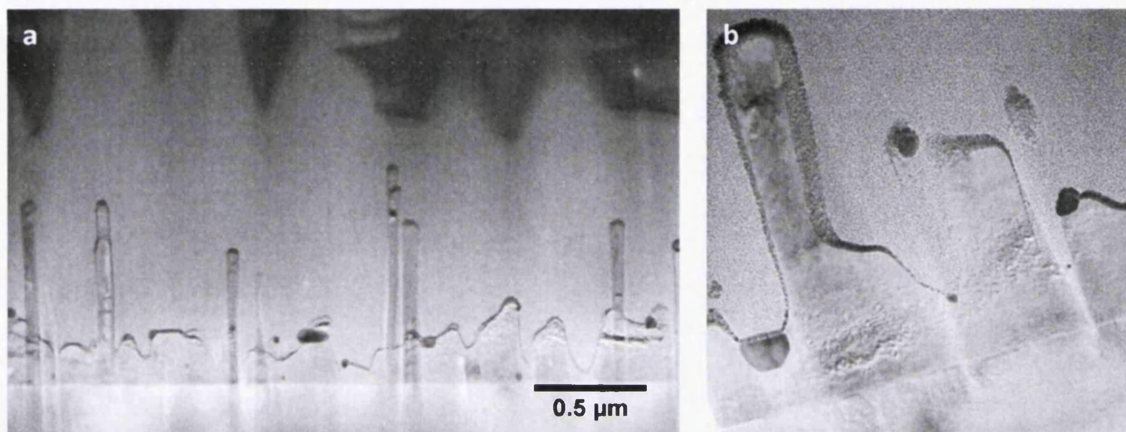

Figure 102. **a)** Bright field span of sample Cat 34-3 and the lumpy nature of the base ZnO growth. **b)** Cat 36-3 the base growth segments and adjoining NWs are all one crystal with no obvious boundaries.

Three samples were analysed Cat 34-3, 36-3 and 36-4 to assess the change in growth with different amounts of Au catalyst and different sample positions in the furnace. A typical cross-section is shown Figure 102a that depicts the Al_2O_3 substrate, the ZnO NW array and the dark regions from the deposited platinum. The gold catalyst particles were distinct. A close-up image (Figure 102b) shows the segments of base ZnO growth and sprouting NWs were all one ZnO crystal with no inherent boundary. Undulating growth mounds appeared and even NWs without a Au particle at the tip. The Au particles were randomly scattered and of various sizes and shapes. Figure 102b appeared to show an Au particle embedded within the ZnO matrix. This random scattering and inclusion of Au within the ZnO could form large depletion regions detrimental to any conduction. A similar particle is displayed in Figure 103a along with the compositional analysis from TEM-HAADF and EDX linescan Figure 103b and c.

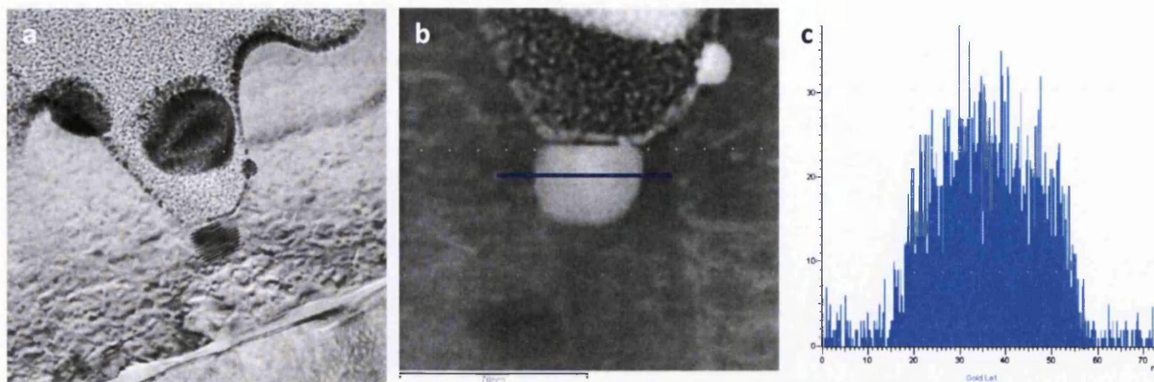

Figure 103 **a,** Au particles on sample Cat 34-3 with the bottom particle embedded in the ZnO and moire fringes from the overlapping crystalline materials, **b,** the corrresponding HAADF image of the same Au particle, **c,** EDX linescan of the particle and the Au element intensity, location identified by blue line in HAADF image

The specimens were aligned on a zone axis of the sapphire substrate and the ZnO was seen to diffract strongly indicating good alignment of the two layers (Figure 104). The base growth was of crystalline hexagonal ZnO and formed an epitaxial relationship with the hexagonal a-plane Al_2O_3. Although no diffraction patterns were taken of the base growth the lattice spacing was that of the (0001) or (0002) planes measured from FFT analysis. Although no defects were found in the NWs considerable defects were seen in the base growth, particularly edge dislocations. Several regions of strong contrast fluctuations occurred but it was difficult to ascertain the true nature of these effects. The preparation method can dislodge material and there was ambiguity in the depth of overlapping features as the depth of field is large in TEM.

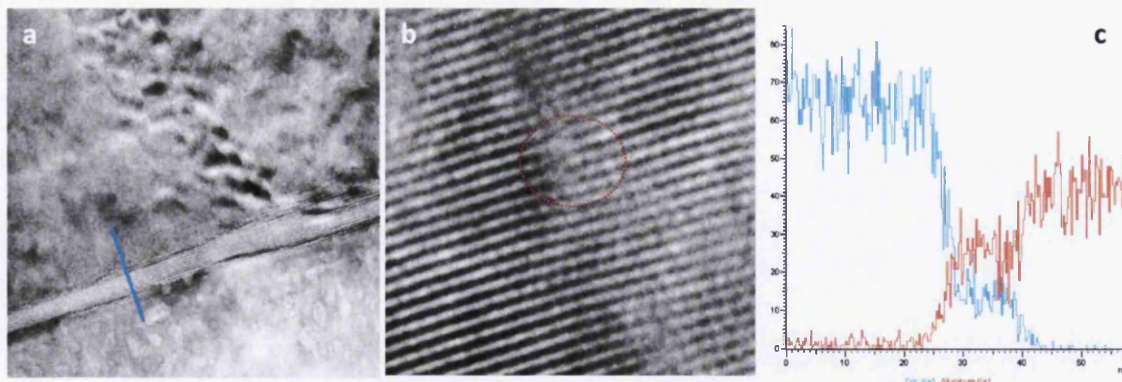

Figure 104. **a)** Lattice image looks at first like a boundary in the ZnO but the lattice planes continue uninterrupted across the entire ZnO layer of Cat 36-3. **b)** enlarged section of the ZnO lattice image showing a heavily faulted region with edge dislocations similar to this throughout the base growth of each sample. **c)** EDX linescan indicated in the lattice image across the interfacial layer, the blue Zinc line and red Aluminium line indicate more diffusion of the Zn into the Al_2O_3.

Figure 104a shows the (0002) lattice planes with a spacing of ~0.26nm which were continuous across the ZnO layer in the image even though it appeared initially that some

boundary existed. The fringe effect could have been due to unknown thickness variations, for example cavities within the ZnO growth. Prevalent edge dislocations were found throughout the ZnO base layer Figure 104b. The ZnO base however did not exhibit substantial phase or grain boundaries and was a continuous crystalline growth but the layer was disjointed by line defects and the lateral spread of growth clusters across the substrate. The size of the base growth and growth clusters were controlled by the growth parameters and the initial quantity of Au catalyst as discussed in Chapter 5. Apparent in the lattice image was an interfacial layer between the ZnO base and the sapphire substrate.

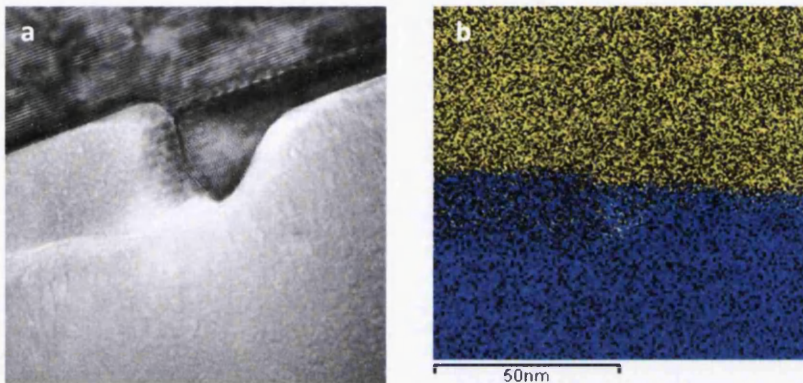

Figure 105. **a)** lattice image of a boundary within the interfacial layer of two different phases. **b)** corresponding EDX map shows yellow zinc diffusing more on the left side of the boundary

The linescan in Figure 104c and images of the interfacial layer (IL) indicated an abrupt and flat boundary between the ZnO and the IL. Several orientations of the IL were seen across the sample Figure 105a. The EDX results Figure 104c and Figure 105b indicated Zn has diffused into the polished Al_2O_3. During EDX scanning the intensity of Zn was greater due to the greater atomic mass and the characteristic high energy x-rays were preferentially detected and emitted. The intensity of the Al signal is much greater within the IL compared to Zn which indicated Zn diffusion across the boundary although due to the stronger signal of Zn atoms it was difficult to assess whether Al had diffused into the ZnO matrix. Al is a common n-type dopant and significant diffusion could greatly enhance electrical conduction through the ZnO base layer, Scanning Auger Electron Spectroscopy could determine this. The presence of Au on and within the base growth along with the many defects suggests the base layer alone should not be relied upon for long conduction paths in a NW array device, for example on an insulating substrate. This may explain the small currents typically

reported from NW tip and through the base growth with conducting AFM experiments, discussed fully in Chapter 3.[188]

6.8.1 Comparing three FIB sections of catalysed nanowire arrays

FIB sections were taken from three catalysed arrays and each expressed a permutation in the growth parameters. Experiment 36 sample 4 (Figure 106c) was downstream of sample 3 (Figure 106b) by one centimetre with both samples having ~8nm Au deposition. Experiment 34 sample 3 (Figure 106a) used the same experimental parameters as Experiment 36 sample 3 but with a shorter growth time of 80mins and less Au (~4nm). This was expressed in the greater base growth with more Au particles apparent in the latter section, however the NWs look similar. From the TEM images we can see the length of NWs and size of the base growth decreased as the temperature of the sample reduced.

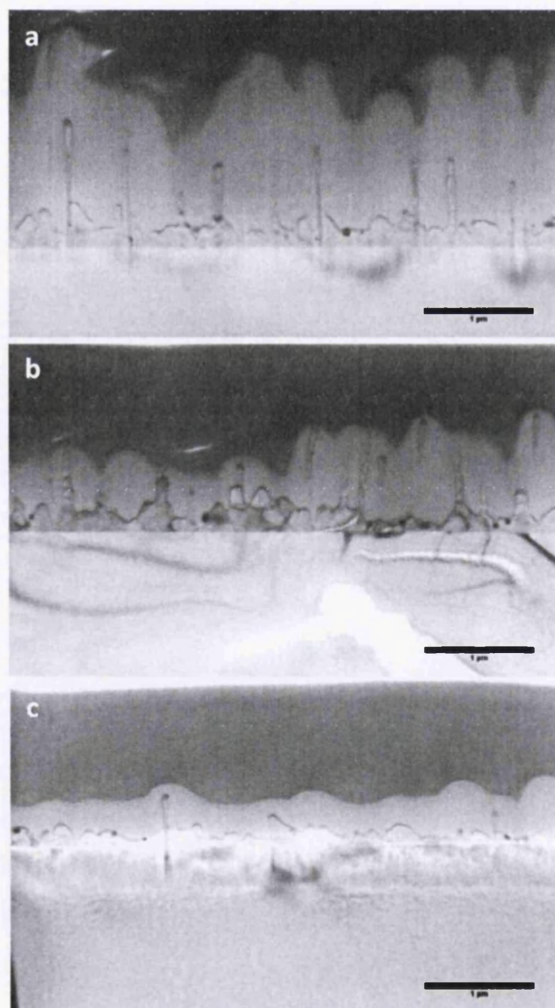

Figure 106. **a)** Cropped FIB cross-section bright field image of Experiment 34 sample 3. **b)** cross-section of Experiment 36 sample 3 and, **c)** sample 4, all the scales bars are 1um.

Apparent from all sections was the variation in Au size and the random dispersion across the base layer. It was possible the Au may act as a mobile particle, or at least with a liquid surface once at temperature, and moved across the sample surface. Particles that become pinned can concentrate growth into a wire, whereas mobile particles can randomly add material to the base growth as they move.

6.9 Conclusions

ZnO NWs have been characterised as high quality single crystals with little variation in bulk structure across growth methods, this was very important to determine before analysing the electrical measurements. Depositing Au contacts created a cap on the NW (0001) top facet which thinned around the edges. Sporadic Au nanoclusters from the deposition process appeared on the sides but do not form a continuous layer. Catalysed growth displayed a random dispersion of Au particles that appeared to contribute to the undulating base growth which was defective with many point defects such as dislocations. The catalyst particle had at least partial alignment of Au {111}||(0001)ZnO which suggested an epitaxial relationship. An interfacial layer occurred at the ZnO-Al_2O_3 interface which signified some interdiffusion of Al and Zn which could effectively n^+ dope the base layer. No interfacial layer was revealed by TEM at the NW-Au interface which appeared abrupt.

The Multi-slice simulations showed that in the conditions used for our experiments, the presence of a single Au atom near the surface of a 7 nm thick slab of ZnO would generate a contrast increase of ~20%. The conditions of the STEM-HAADF experiments should have therefore allowed the detection of Au impurity atoms if they were present even when on a zone axis, in particular on the sides of the NWs where the overall material thickness is reduced. Also it was discussed that even for the less favourable case of Au embedded within ZnO, tilting away from a zone axis can improve the visibility of impurities[136]. The HAADF images without aligning them along a specific crystallographic direction showed no additional contrast and all recorded images were in fact similar to those taken on a control sample where the NWs were grown without any Au catalyst. Aberration-corrected instruments using large probe convergence angles (here 31 mrad semi-angle) allow depth-slicing techniques to exploit the reduced depth of field (2-4 nm) which can reveal impurities buried within the sample depth, in particular at point-defects[15,140,223]. However, through-

focal series recorded both along the NWs zone axis or tilted away from channelling conditions showed no trace of heavy metal impurities or point defects in any NW. When the entire analysis of the NWs and interface quality were taken into consideration the lack of Au within or on the surface of the ZnO NWs was not surprising. The Au atoms in Silicon NWs are concentrated at defects which is common for impurities in defective crystals.[15,133] The defects have the effect of incorporating the Au directly from the liquid phase during growth suggesting a strong relationship between growth direction, defect structure and contamination frequency.[133] As the ZnO NWs here display no defects through STEM and TEM analysis, along with a seemingly low solubility[224] of Au in ZnO, no Au contaminates the bulk or surface of the single crystal NWs. This is advantageous for electronic devices and tailoring the NW and interface properties. Evidence showing the epitaxial alignment of the Au particle lattice with the ZnO NW and no alloying on either side of the interface reveal the growth mechanism as Vapour-Solid-Solid.

The insolubility of Au in the catalytically grown ZnO NWs makes them possibly unique, whereas Silicon[15], GaAs[136] and InAs[137] are hampered by Au catalyst incorporation. Along with the interface quality and the ability to grow NWs with a variation in catalyst particle size the ZnO NWs do provide unique opportunities for electronic devices. Ge NWs[17] analysed by atom probe tomography appear to be free from Au catalyst impurities and this method would provide valuable evidence to reinforce the HAADF results of ZnO.

Chapter 7

7 Nanoprobe Results

ZnO NWs from three growth techniques have been shown in the previous chapter to be structurally equivalent with similar morphology. No defects were found in the bulk of the NW crystals and limited surface roughness was found only on a proportion of the hydrothermally grown NWs. This chapter extends the characterisation to electrical measurements comparing the bulk resistivity of the three NW types that allows the comparison of Au deposited and Au catalyst particle end-contacts. These measurements were achieved with the nanoprobe system in ultra-high vacuum (UHV).

7.1 4-probe measurements

16 catalysed, 14 non-catalysed and 10 hydrothermally grown NWs were measured with the Nanoprobe system. Multiple four-probe measurements were taken on each NW lying flat on insulating SiO_2. Firstly, the four probes were placed onto the NW and the contact between each tip was tested with an I-V sweep that was usually linear between the outer tips and the inner tips with current in the micro-amp range. Contacts sometimes needed slight adjustment but under normal conditions good contacts were established on the NWs of >50nm diameter. Measuring thin NWs of <50nm diameter required the AC etched tips provided by Omicron because they were more flexible and avoided damage to the NWs.

7.1.1 Experimental variation and technique

The greatest measurement interference came from beam deposition on the early experiments where substrates had not been thoroughly cleaned. This was noticeable by a permanent dark rectangle in the regions of high magnification SEM images where the electron beam had been concentrated. Thoroughly cleaning the measurement substrates with a Piranha solution avoided this problem. Beam charging effects tend to dissipate and were not noticeable in these experiments. A good contact to the NW was considered to be linear I-V sweeps between probe tips and a current that roughly scaled according to probe separation and Ohm's law. The current was typically of the order of $1\mu A$ at $1V$. A four-probe measurement was then taken with a bias on the outer probes between $\pm 0.4V$ up to

$\pm 1V$. The inner measurement probes sense the voltage drop across the particular section of NW.

An ideal four-probe measurement on a catalyst-free NW is shown in Figure 107a. The resistance scales linearly with probe separation as expected from Ohm's law. The x-axis error bars depict the difference between the inner and outer span of the sense probes. Figure 107b shows the individual I-V measurements of the first and fourth four probe measurements and the outer two-probe measurement of the source tips. Each of the I-V measurements are linear and scale according to separation indicating low-resistance Ohmic contact of all four-tips. The scaling of the two- and four-probe I-V aids accurate and reliable measurements even though a four-probe measurement is theoretically independent of contact resistance. Unequal contacts at each tip can provide non-linear I-V and unreliable four-probe measurements.

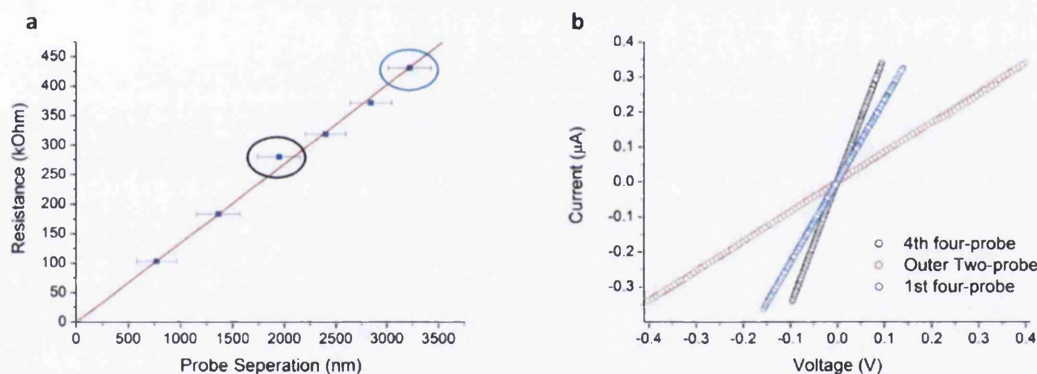

Figure 107. **a)** Graph of six four-probe measurements on a non-catalysed NW of diameter 86nm. The inner probe separation is measured from in-situ SEM images and the error bars represent the uncertainty of these measurements i.e. the width of the probes in the SEM image. A linear fit is applied passing through zero obeying Ohm's law and no contact resistance. The gradient scaled by the cross-sectional area of the NW gives the resistivity 0.08Ωcm. **b)** graph showing individual measurements, blue data depicts the first in the series of the six four-probe measurements (blue circle in **a)**), black data the fourth measurement in the four probe I-V series (black circle in **a)**) and the red data is the two-probe I-V of the outer source tips.

In most cases five of more separate four-probe measurements were taken on each wire. The diameter of the wire was taken as the average diameter measured from five line profiles using ImageJ software as shown Figure 108. At 50% of the maximum grey value intensity of the line profile a measurement is taken. The SEM has a resolution of 5nm and so the error in the diameter measurement is considered to be ± 2.5nm.

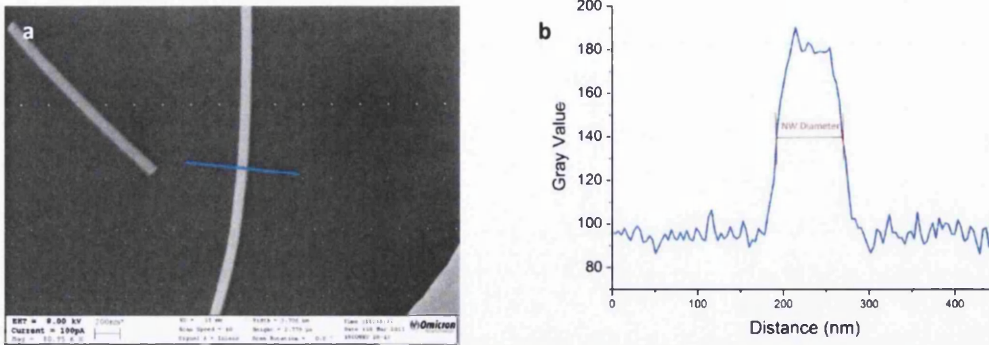

Figure 108. **a)** In-situ SEM image of a non-catalysed NW indicating the position of the line profile. **b)** the line profile taken at 50% of the maximum gray value intensity.

The data was analysed using MATLAB, to plot the two- and four-probe I-V data. The gradient of an individual four-probe measurement represents the resistance at that particular separation of the sensing tips $R=(\partial I/\partial V)^{-1}$. Multiple resistance measurements on the same NW along with measured probe separations and errors are plotted on the resistance-separation curve Figure 107a. MATLAB was used to fit the linear relationship to the data points and pass through zero to fit Ohm's Law which still holds in NWs.[26,64]

Data was analysed using Matlab to fit the resistance to the separation with the ordinary least-squares solution of the linear system. This fitting was achieved with the routine 'lscov' that provides a least squares fit for the two input variables and intercept $y=0$. This minimises the sum of the squared errors and outputs the gradient and the standard error which are respectively NW resistivity and the standard error which is the overall $\pm$error in ρ.

7.1.2 ZnO Nanowire Resistivity

In this manner the 40 NWs were measured and analysed against growth method, diameter, length, probe positioning (proximity and order of positioning), deformation on the substrate and whether a catalyst particle was present at the end of the catalysed NWs. The only apparent relationship identified is with diameter which shows for all growth methods resistivity increases with decreasing diameter.

Figure 109 shows a range of resistivity of two-orders of magnitudes for each growth method and the magnitude for each is similar. The values range from 0.02-3Ωcm which is far less than the bulk resistivity of 59800Ωcm[(41)] which suggests a higher carrier concentration or

mobility in the NWs.[17] The spread of these measurements is very small compared to several publications which span a range of 10^{-3}-$10^{5}\Omega cm$.[50]

In terms of these measurements the growth methods are equivalent which suggests the relatively high concentration of Oxygen and lower temperatures in the non-catalysed growth process has little effect on the electrical properties, also the hydrothermal process appears equivalent. Structural TEM analysis of each wire type showed equivalent crystallographic structure and the majority of NWs had smooth surfaces (See Chapter 6). All of the NWs are deemed to be crystallographically similar with comparable surfaces and morphology which excludes a substantial variation in surface scattering behaviour.[225,226] Some hydrothermal NWs did exhibit substantial surface roughness but there was a range from rough to smooth. These corrugations that can happen during growth[18] did not appear to have a critical effect on the four-probe measurements as the rough textured structures were avoided during measurements. The same spread and magnitudes of resistivity were found on all NWs.

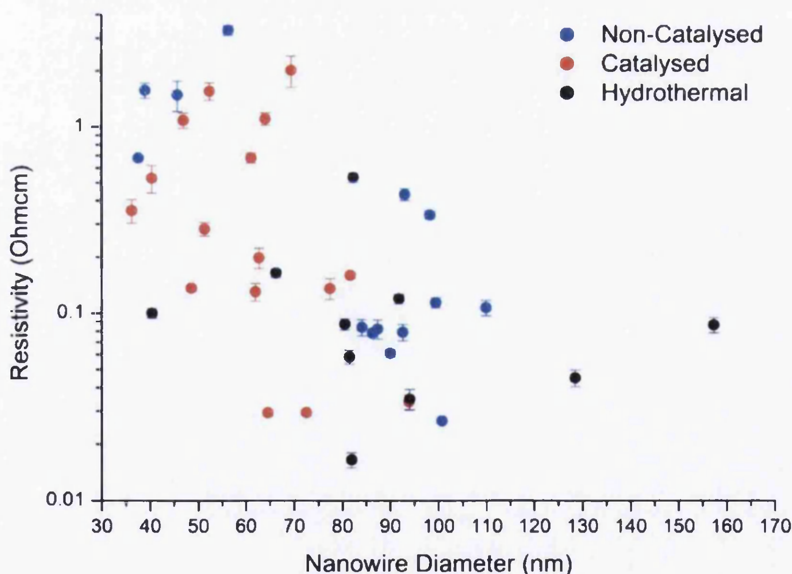

Figure 109. Resistivity plot against NW diameter showing the multiple separation 4-probe measurement of 16 Catalysed, 14 Non-Catalysed and 10 hydrothermal NWs. The y-error bars indicate the standard error of the least squares linear fit and the x-error bars $\pm$2.5nm are omitted for clarity. The graph shows an increasing resitivity with decreasing diameter for all NW growth methods.

The variation in conductivity could be due to crystallographic defects, stoichiometric differences affecting doping levels such as Zn interstitial and O vacancies, catalyst or

impurity contamination and surface states, defects or dielectric mismatch.[5,18,154] Environmental factors during preparation and measurement can introduce surface adsorbates and trap states that can dominate the surface sensitive structures.

TEM and STEM did not reveal any structural defects in any NWs and only reveal single crystal defect free NWs (Chapter 6). TEM is based on interference effects which makes point defects such as edge dislocations difficult to uncover. HAADF which does not rely on interference effects is very useful for detecting defects in crystals although point defects they can still be difficult to expose even with atomic resolution STEM-HAADF.[207] However after thorough analysis of NWs from diameter 10-100nm at several tilt orientations no point or structural defects were found in any NW by STEM-HAADF and TEM. Surface defects on a single NW basis are very difficult to directly assess but this can be inferred from electrical measurements as we discuss next.[17,18] Stoichiometric differences may contribute, again these are not directly detectable, but the influence maybe seen through an overall influence on doping level. Doping levels can be estimated with gated FET measurements.[17,18] Bjork et al however assume Si NWs from the same CVD growth experiment are all the same doping concentration, we show here for ZnO NWs this cannot be the case.[154]

STEM-HAADF was used to detect contaminating atoms based on the large Z-number of the Au catalyst used in catalytically grown NWs. No bulk or surface Au atoms were detected and the NWs compared identically to non-catalysed NWs. It is unclear whether Au atoms in ZnO NWs would act as acceptors, as in Ge NWs[17], but if so they would reduce the- n-type conductivity in the catalysed NWs, which is not seen here overall. It is likely some doping variations exist in the NWs even within an array and the equilibrium concentration is influenced significantly by surface defects and states.[17] The influence of surface states increases as the diameter of the structure decreases, and an increase in the surface-volume ratio which is expressed as an increase in resistivity.

Bulk defects and substantial surface corrugation/roughness are not prevalent enough to influence the resistivity to such an extent as the 4-probe results depict. Growth impurities are less likely because the variation in resistivity occurs across all growth methods, this also reduces the possibility of incorporation of the same bulk impurity species from each procedure. The resistivity range measured can be considered as an inherent property of the

NWs and would have to be designed into any device. However the equivalence of the growth methods increases the options for device fabrication. It is possible with surface passivation surface states could be tempered and electrical properties may find a common datum.[17,93] Similarly, a chemical surfactant has been shown by Djurišić et al to quench the PL green emission in ZnO tetrapods indicating the surface defects that can be a source of mid-bandgap states were passivated.[227]

7.1.3 Diameter dependence

Although bulk stoichiometric differences and unintentional doping may lead to differences in carrier concentration they do not explain diameter dependent properties[228,229], as we see here. The increasing resistivity with decreasing diameter suggests an increasing surface-over-bulk influence. Stoichiometric ZnO consists of a one-to-one ratio of Zn^{2+} and O^{2-} ionically bonded. At the surface of the crystal some of these bonds are free and along with defect sites they can greatly affect the NW properties. Intrinsic surface states are responsible for inducing energy levels in the band gap and can result in Fermi-level pinning which can greatly affect contact barrier formation and surface depletion layers.[94] Dangling bonds, surface defects and adsorbed ions can all cause surface depletion or accumulation.[93]

Surface defects can induce states additional to intrinsic surface states and remove more charge from the bulk and the subsequent screening of the trapped surface charges produces local surface band bending, Figure 110a.[230] As the density of these defects and states is related to surface area any surface roughness or corrugation can increase this effect.[18] Surface states which induce an acceptor like surface charge, (as seen with oxygen adsorption capturing electrons to form O_2^- on ZnO[92] depicted Figure 110b) have been estimated to deplete carrier concentration in the bulk of 45nm diameter ZnO NWs with only an effective channel area of only 25% of the physical diameter depending on the initial concentration.[231] The surface states can have such an influence that they can determine the carrier type in some NWs.[17]

The increasing influence of surface trap states as the NW diameter decreases helps to explain the increasing size-dependent resistivity. Surface state/defect dominance enhances surface-recombination which is the source of deep-level luminescence and quenches band-band recombination by acting as a trap for charge carriers.[232] Band-band recombination

produces UV luminescence but the origin of emission in the visible range is due to the creation of defect energy levels in the band gap thus providing a measure of defects and surface quality.[18] One possible route to overcome this is surface donor doping which provides electrons to occupy the defect energy levels.[150]

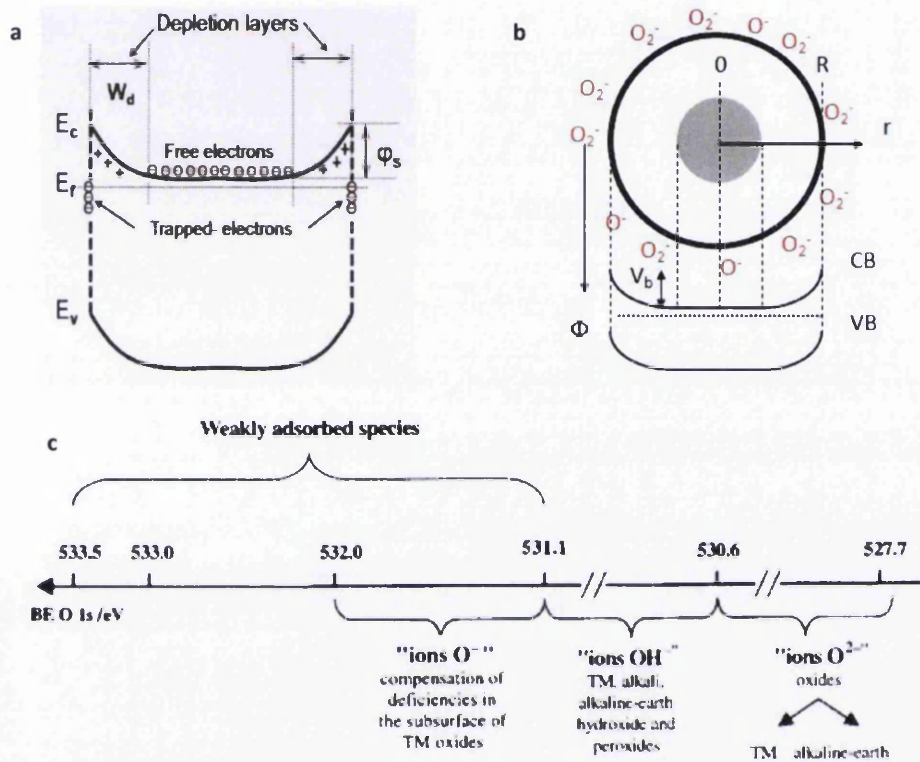

Figure 110. **a)** Diagram depicting the surface depletion resulting from trapped carrier electrons at the surface mid-band energy levels associated with surface states and defects, reproduced[18]. **b)** The radial band bending effect on a NW of surface trap states that occur as a result of Oxygen adsorption to dangling bonds and defect sites. **c)** Binding energy of Oxygen indicating loosely and tightly bound species.

As the NW diameter decreases the trap states remove or scatter charge and result in a depletion region which consumes more of the channel and the effective conductive area reduces, Figure 110a.[18] Pacification of the surface states or additional surface doping can return or compensate the trapped charge.[17] This can be achieved with solvents[93], etching[17], chemical bonding[153] or could even be an unintentional effect of fabrication beam deposition and adsorption of gases from atmosphere[230,233].

Even though the samples here are bare NWs not subjected to any processing and measured in UHV the surface states still influence the NW surface and bulk. The density of these surface states has a major impact on the measured resistivity and contributes to the range

of magnitudes measured here. Logically, regardless of the surface state density, passivating the surface could reduce all NWs to a similar conductivity.[154]

It is possible this has been seen with Focussed Ion Beam (FIB) patterned ZnO four-probe contacts.[51] Tsai et al used the FIB contact patterning technique which uses a platinum-hydrocarbon based precursor gas and Ga^+-beam for depositing the contacts which provided 3 NWs measured at 0.031, 0.037 and 0.047Ωcm[51]. FIB does not rely on exposing the NWs to harsh solvents but deposition of carbon is extensive and the implantation of gallium ions is unavoidable.[92] An earlier similar comparative study with e-beam contacts shows resistivity of 0.019-0.15 Ωcm for four NWs. This does require exposure of the NW to harsh solvents as part of the patterning process as well as electron beam deposition.[41]

The surface modification effect was highlighted by Liao et al by the enhancement of conductivity merely by vacuum which removes some loosely bound gaseous species such as oxygen and hydrogen and also water moisture.[94] The dangling bonds and defect sites at the surface act as adsorption sites for gas molecules. For example oxygen adsorbing on the surface gives $O_2(g) + e^- \rightarrow O_2^-$ and water moisture $2H_2O(g) + O_2 + 4e^- \rightarrow 4OH^-$ forming 4 negatively charged hydroxyl groups.[94] Each of these common atmospheric adsorbates act as electron acceptors trapping charge carriers from the bulk and reducing the concentration of free charge carriers creating a potential variation.[94]

A concentration of the trap states as low as $10^{10}cm^{-2}$ (~200 states per NW) can have a marked reduction on the conduction channel.[18,94] Measuring the NWs in UHV reduces the influence of gaseous species substantially but does not remove those that are tightly bound such as chemi- and physi-sorbed H_2O see Figure 110c.[230,234] Maffeis et al used XPS to reveal hydroxyl groups are removed from NWs when annealed in UHV but return when maintained at ambient temperature even in the UHV chamber.[234] Even so, the overall influence on band bending by surface defects and intrinsic states should be greater in comparison to adsorbed species in UHV due to the removal of the majority of loosely bound gases and moisture.

UHV In-situ heating of the sample could remove most of these surface ions and molecules which may free the dangling bonds and defects. Four-probe measurements would then reveal the effect of intrinsic surface states on the conduction properties. Introducing

different gases could then isolate the individual influence on the NWs and the reactions with the surface.

7.1.4 Resistivity Magnitude variation

The variation in resistivity magnitude should be an inherent property of the NWs, rather than a symptom of an unequal modifying effect, as all NWs were processed in a similar and minimal fashion. All were exposed to air after growth, transferred to the substrates and then measured in UHV. The spread therefore is likely explained by variations in surface state density and/or doping variations. The density of surface states can be influenced by surface morphology and/or surface defects. The wires measured here were smooth surfaced except the Hydrothermal NWs that showed a range of smooth-to-corrugated texture. Therefore substantial surface morphology which can greatly affect the density of dangling bonds[153] is not expected to be a major influence on the properties across the NWs measured here.

After exposure to atmosphere, binding of atmospheric gaseous species and moisture to free dangling bonds influences carrier concentration and the conductive channel. This is very likely to affect measurements but when the material is returned to vacuum the loosely bound species (such as those physi-sorbed or with weak ionic bonds) are removed and the surface is again not totally consumed by atmospheric conditions. This effect is shown by ZnO gas sensors that become more conductive when exposed to vacuum[235] indicating a substantial variation in surface state density can still play a major role in our experiments because the surface is not saturated with adsorbed species. Chemisorbates such as hydrogen bonding to oxygen form hydroxyl groups on the surface that also result in band bending and these will still have an effect because they are very difficult to remove due to the strength of the bond.

Dielectric mismatch between the NW with the surrounding medium has been shown by Bjork et al to cause donor deactivation at the surface of Si NWs.[154] Coating the NWs with a dielectric material that reduced the dielectric mismatch with the NW suppressed the increasing resistivity with decreasing NW diameter. Increasing resistivity was shown to occur for NWs of equal doping concentration and other factors such as size-dependent dopant incorporation and mobility were experimentally disproved. Measurement results we present here for ZnO NWs show a spread in magnitude and an increase with decreasing diameter. The dielectric mismatch of vacuum to ZnO is just the relative dielectric constant of

ZnO of 8.66 which is constant for all of the NWs measured; for this reason donor deactivation cannot be the reason behind the magnitude spread although it may contribute to the relationship with NW diameter. Donor deactivation in the Si NWs with a native oxide surface layer had a dielectric mismatch of approximately 4:1 for SiO_2:air [(236)], and for ZnO: vacuum it is 8.66:1. Because of this the ZnO NWs measured here may experience a greater effect of donor deactivation than the Si NWs. However, the surface sensitivity of ZnO especially to gases present in Air such as Oxygen and the large diameter range of the sampled ZnO NWs would suggest the magnitude spread is mostly a factor of doping and the increase in resistivity is an increasingly important surface depletion. ZnO NW depletion is likely to be mostly dependent on the chemisorbed and physisorbed surface species but also with an element of donor deactivation. The extent of the influence of adsorbed gas species could be measured in UHV by in-situ heating and subsequent exposure to different gases and surface passivation by different solvents. To reveal the isolated behaviour of dielectric donor deactivation in ZnO NWs would be difficult as a surface oxide layer does not exist and a mixture of influences exist on the surface such as trap states and donor deactivation. Coating the ZnO NWs with another material may reduce the dielectric mismatch but would also alter the surface states. Whereas, the Si NW has the trap states at the Si-SiO_2 interface and the dielectric mismatch on the oxide surface, coating the surface doesn't affect the interface trap states. The depletion of ZnO due to exposure to gases and moisture is well documented and is a major reason for the surface depletion of the ZnO NWs measured here. Variability in the surface state density may also contribute to the resistivity spread, however, the equal preparation and mostly smooth surfaced NWs suggests doping to be the dominant factor.

NWs measured here were loaded into the UHV chamber for at least 12 hours before measurements. This should remove most loosely bound gases and water and provide equal surface preparation for all NWs. The surface depletion layer influencing the conduction is then dependent on the surface state density that create a surface potential and a space charge layer will extend into the NW a distance dependent on doping levels. Hong et al[18] estimated the surface depletion due to trap states for a NW, of diameter D, embedded in a

dielectric Figure 111b in terms of the effective channel diameter $D_{eff} = D - \left(\frac{N_t}{N_D}\right)$ which highlights the influence of the density of surface traps N_t and the doping density N_D.

This model is not entirely accurate for the experimental setup used here as the ZnO NWs were placed flat on SiO_2 dielectric in vacuum. Depletion in ZnO NWs exposed to vacuum occurs at surfaces due to trapped charges as we have seen, and also at interfaces particularly for semiconductors with materials such as dielectrics or metals. The NW surfaces exposed to vacuum during measurement presents a greater dielectric mismatch than the SiO_2 substrate, for this reason the substrate effect is expected to be small on the measurements. There is nothing to suggest the density of trap states would be greater at the NW substrate interface than at the NW-vacuum interface. ZnO NWs have a hexagonal shape that means a maximum of 1/6 of the NW surface is in contact with the substrate and the depletion is expected to be approximately symmetrical as depicted in Figure 111b.

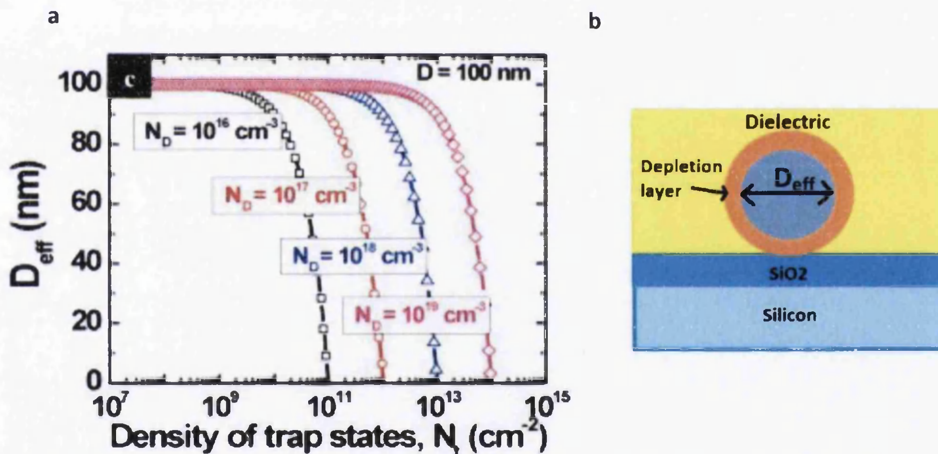

Figure 111. **a)** Effective conduction diameter of a NW embedded in dielectric plotted against surface trap state density and n-type doping density, reproduced[18]. **b)** Diagram depicting the radial depletion of a nanowire by the surface interface trap states when embedded in a dielectric, the effect of the SiO_2 interface is proposed to be negligible on D_{eff}.

The simple relation for effective diameter does however reveal the overall importance of the doping and trap density. Large variations in effective diameter D_{eff} can occur with relatively small fluctuations in N_t and N_D as shown in Figure 111a. This explains the magnitude spread in resistivity measured here and the insensitivity to growth method and morphology. Doping concentrations and surface trap state density control the resistivity of the NWs but the combined effect blurs the influence of each contribution. The surface depletion indicates the most conductive ZnO NWs measured have little or no surface

depletion layer, this variation in surface depletion also explains the difficulty in forming good contacts to some NWs whilst others are very easy with good contacts immediately achievable. The flat lying configuration allows more pressure to be applied to form better contacts, however in the free standing configuration used for two-probe experiments later in the work (Section 7.2) means only high conductivity NWs with little surface depletion are easily contacted.

7.1.5 Four Probe experimental variations

Resistance against separation graphs exhibited 3 individual characteristics, a linear fit to Ohm's law, a linear fit with data spread around Ohm's law (Figure 112a) and linear but with increasing resistivity as the probe separation decreased Figure 112b and c.

Measurements that do not fall exactly on the Ohm's law trend have all measurements within the same magnitude and within natural experimental spread around the 'ideal'. The variation of spread from Ohm's law has no link with NW length, NW diameter, sensing probe positioning order, probe proximity or size, to the quality of measurement. Assuming the substrate is homogenous the variation must be due to either, unequal contacts which would give non-linear I-V and an inaccurate measurement, contamination and beam deposition, or variations in NW properties along the length. These three factors are interlinked and are difficult to separate.

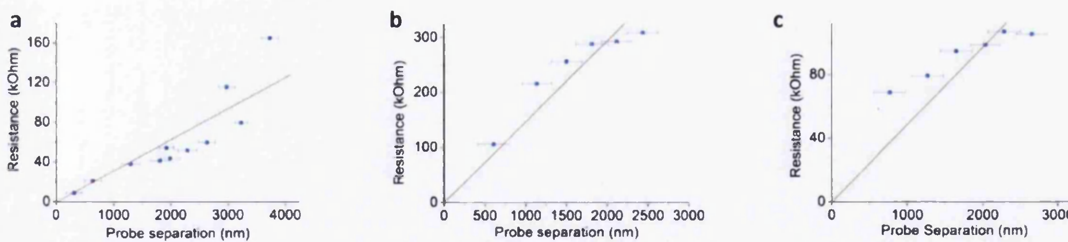

Figure 112. **a)** Resistance against separation graph of Hydrothermal NW showing a spread of data points around an Ohm's law fit average resistivity of 0.015 Ohm.cm, fit gradient resistivity of 0.016 Ohmcm and fit error of 0.0015 Ohm.cm. **b)** Resistance separation graph of a non-catalysed NW with increasing resistivity as the probe separation is decreased due to carbon deposition the average resistivity is 0.124 Ohm.cm the fit gradient resistivity of 0.113 Ohm.cm and fitting error of 0.007 Ohm.cm. **c)** Catalysed NW with increasing resistivity and average resistivity of 0.040 Ohm.cm, fit gradient resistivity of 0.034 Ohm.cm with fitting error of 0.0031 Ohm.cm.

Non-linear four probe I-V were discarded and for good quality measurements the outer two-probe voltage was seen to scale approximately with the inner probe tip voltage. Initial experiments did suffer from carbon deposition due to the high magnification SEM images

used for initial probe positioning. Inhomogeneous NW properties were not considered to be a problem as no junctions were observed in I-V measurements or with electron microscopy.

Carbon deposition is considered to be the major experimental factor affecting measurements. Carbon deposition rate is unknown but depends on the sample cleanliness. Deposition was 'visible' during scanning of the SEM when using contaminated samples. This contamination was found to originate from the lithographically patterned substrates and once these were cleaned properly with a Piranha etch no problems were encountered. It has been seen with certain measurements when a 'high mag' image is taken of the NW a rectangle remains on the substrate in the image, which indicates carbon deposition or charge retention. The resistivity in a small number of cases is seen to increase as the probe separation is decreased see Figure 112b and c. When one probe is located on the deposition site it is possible the contacts maybe unbalanced, but individual I-V are linear. This effect on the properties is likely to be due to influence of a carbon layer on the NW inducing additional surface depletion. This effect does not however affect the overall spread of resistivity's and only results in an error of the fit to Ohm's law. The value of the gradient resistivity is close to the average measured resistivity which is greater by 9.7% for Figure 112b and 17% for Figure 112c which is expressed in the resistance against diameter plot error bars by the standard fit error which is 6% and 9% respectively of the fit gradient. Increasing resistivity only affected 4 wires in total with no relation to resistivity. Remaining measurements were considered as a spread around Ohm's law or near ideal. The level of error does not affect the magnitude relative to the overall spread in the entire sample range and this spread must be considered accurate.

7.1.6 Important experimental factors for future work

The sequence of sensing tip movement does not appear to affect the measurement which indicates the wire is not altered by the probes or electrical current. Carbon deposition can hinder measurements and when it is extensive measurements can be impossible because of the difficulty in forming good contacts. These contamination problems can be easily avoided by rigorous cleaning.

Good and equal contacts were necessary for reliable measurements. It was crucial to test the I-V between tips before a four probe measurement was conducted. Although tungsten of work function $\Phi \sim 4.5$eV can likely form an Ohmic contact to ZnO of electronegativity

χ~0.42eV the low resistance contacts are aided by the high-field at the sharp tip. The key to the experiments detailed here and two-probe experiments are the linear 'Ohmic' contacts, readily achievable and limiting any band bending and depletion of the NW by the probe contacts. Suitable contacts were considered to be those which show linear I-V, an outer tip two-probe I-V that scales to the inner two-probe I-V and of current magnitude >100nA at 0.5-1V. Contacts are easily adjusted to improve contact. Although no direct correlation with doping was attempted contact formation was more difficult on some wires more than others. This is thought to be a thicker surface depletion layer making contact formation more difficult most likely a result of lower doping and perhaps surface state density.

Stiff DC etched tips are suitable for thicker NWs diameter >50nm and make forming a good contact easy as pressure can be applied with the tip. Thinner more flexible AC etched tips are necessary for thinner NWs to avoid cutting the NW although balanced contact formation is more difficult as considerable pressure cannot be applied.

7.2 2-probe interface measurements

Two probe measurements were conducted on free standing NWs. Catalysed NWs with distinct Au particles at the tip, as shown in Figure 113, were compared to non-catalysed NWs with and without an evaporated Au cap on the top facet.

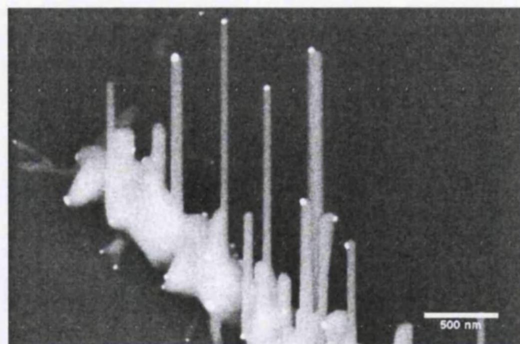

Figure 113. Backscatter electron image at 45° of the actual NWs measured in two-probe experiments with distinct Au particle tips. A large aspect ratio is evident for all NWs measured in the two-probe configuration made possible by precise control of the probe tips.

Bare non-catalysed NWs were measured as a common datum. In the case where linear I-V measurements and microamp current were not initially observed it was required to current anneal the tips together. This usually provided more current on the NW but the I-V were not always linear and in some cases good contacts to certain NWs were very difficult or

impossible. In the free standing configuration applying pressure to the wire is more difficult than when lying flat. On occasions opposing the tips to apply pressure achieved a good initial contact in the side-to-side configuration. After some manipulation good near-linear low-resistance I-V are possible but not on all NWs. Once the initial contact is formed one tip can be moved to the next position for measurement. Various two-probe configurations are shown in Figure 114 of a non-catalysed sample along with the relevant I-V measurements. All non-catalysed samples were grown under the same conditions.

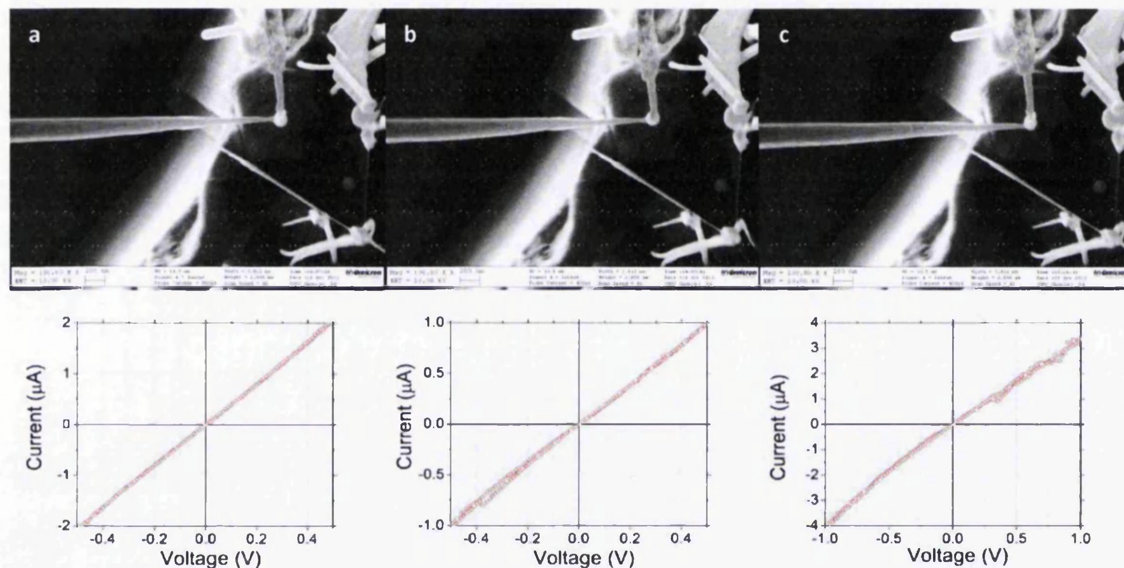

Figure 114. Series of In-situ SEM images of sample non-catalysed 216a, a two-probe measurement of a bare non-catalysed NW and the corresponding I-V measurements. **a)** Firstly the probes are placed on the side, **b)** once good contacts are established one tip is placed on top and, **c)** then the tip is placed again on the side. The I-V graphs indicate in each instance a low-resistance contact is formed between the NW and both tips, the current scale is micro-amps. Measurements like these are highly dependent on clean probe tips.

The current passing through the wire was of the order of one micro-amp at 1V similar to four-probe measurements that indicated good Ohmic contacts were formed. This level of current was used to assess the contacts. Divulging useful conductivity data from the two-probe measurements is difficult due to the inaccuracy in measuring the vertical separation and the two-probe technique which inherently suffers from the influence of contact resistance at both tips that can vary for each measurement. It is noted that it was not possible to form good contact with all NWs, this is thought to be as a result of changes in surface depletion region. NWs of greater doping will have smaller depletion regions which made good contacts easy to form. Therefore the conclusions from the four-probe data

indicate the NWs used for two-probe measurements had minimal surface depletion with the balance on the side of high doping levels in the NWs over the surface charge. This was consistent with all NW arrays and growth methods. This effect is most noticeable with free-standing NWs as significant pressure is difficult to apply, unlike the flat lying four-probe technique which could be manipulated to improve the contact resistance.

7.2.1 Non-Catalysed NWs with Deposited contacts

These measurements spanned across several samples of NWs with diameters up to 300nm with Au depositions of ~12-52nm thickness. The same measurement procedure indicated for bare NWs in Figure 114 was followed for all NWs. The top contact measurement was repeated at least twice with the probe tip lifted and replaced. Many NWs with diameters of 40-300 nm from five different arrays (different experiments but the same parameters) were measured and of these 24 had linear or near linear I-V across the top contact. Other NWs measured indicated no barrier at the Au but were hindered by poor side contacts, the I-V resembled a Schottky contact although the polarity of the measurement showed the barrier is on the NW side. In these instances two good contacts in the side-to-side configuration were difficult and the I-V would indicate one low-resistance and one high-resistance contact. Figure 115 shows three typical I-V measurements of NWs deposited with 52nm, 35nm and 19nm Au respectively left to right. No I-V measurement indicated a substantial barrier at any Au thickness or NW diameter.

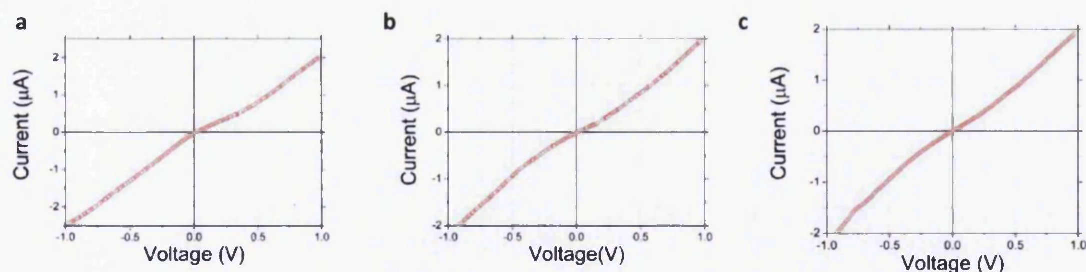

Figure 115. Current-Voltage sweeps in two-probe configuration, **a)**, **b)** and **c)** correspond to catalyst-free NWs with Au contacts of thickness 52nm, 35nm and 19nm on NWs of diameter 110nm, 95nm and 92nm respectively. Nearly linear I-V were measured for all deposited contact thicknesses on NWs of diameters 40-300nm. Current data can only be compared qualitatively due to the difficulty in positioning the probe tips on the NW side below the interface in the top-down SEM view, and characterising the interface size.

The four-probe results show the validity in comparing two-probe contact measurements of different ZnO NW growth types. With similar conductivity properties the contact behaviour of catalysed and non-catalysed NWs can be evaluated together. Non-catalysed wires show a spread in resistivity which is likely due to trap states and doping variations. The carrier

density of the semiconductor is extremely important in the physics of metal-semiconductor contacts. However as a wide range of metal depositions, wire diameters and NW arrays were measured any surface and carrier influence should have been sampled. Little variation was found in the deposited contact I-V characteristics of the top contact. All of the NWs which formed good contacts with the probe tips exhibited low-resistance I-V with current of micro-amps and linear or near linear I-V. The near linear characteristic of the I-V indicate several mechanisms at play in the interface and the slight 'bump' in reverse bias indicates a weak barrier is present but easily overcome.

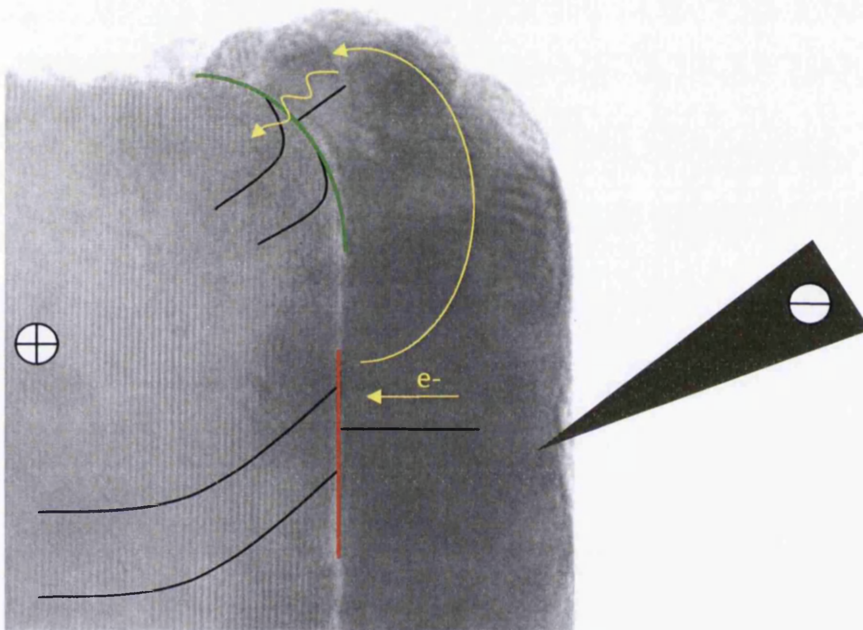

Figure 116. The concept of a deposited Au contact presents the problem of thinning of the metal at the top facet edges. Under the reverse bias condition electrons maybe presented with a substantial barrier formed by Au-ZnO. Electrons seeking the path of least resistance find the barrier can be penetrated with enhanced tunnelling due to the local metal nano particle size and disordered agglomerate form of the deposited Au especially near the edges. These effects distort the contact size to much less than the characteristic length scale of the system, in this case the NW diameter. This allows tunnelling even with heavy deposition of Au on the top facet.

Au is known to form a substantial barrier with ZnO displaying strong rectifying characteristics (barrier height of planar contacts on ZnO (0001) are in the range 0.6-0.71eV[5]). The effective barrier of these NW contacts has deteriorated from a large barrier which must be due to the contact structure and preparation methods. Exposing the NW to air was unavoidable and although thermal evaporation in high vacuum is standard procedure it is usually onto clean surfaces. The preparation methods did expose the NW to

air particularly the species of O_2 and H_2O which bind to the NW surface and form a surface adsorbate layer that was present during Au deposition.

Another likely cause for the low-resistance in reverse bias is the structural properties of the Au pad. TEM (Chapter 6) revealed the pad consists of multiple nanoparticles dispersed and agglomerated on the top facet and around to the NW side facets. The Au holds no crystallographic alignment with the ZnO or amongst nanoparticles. At the ZnO top and side interface there are many nanoparticles that may introduce the tunnelling characteristics of small contacts.[60,61] As the deposition thickness increases instead of 'filling the gaps' between nanoparticles and creating a more substantial contact barrier more individual nanoparticles are added to the contact pad. Due to the nanoparticle size the local electric field increases introducing localised edge effects[21] at the grain boundaries creating an inhomogeneous barrier and the total effect is the depletion layer across the contact is thinned enough to allow substantial tunnelling[60], depicted in Figure 116.

Structural inhomogeneity exists on the (0001) facet of ZnO. The (0001) facet is more catalytically active than the oxygen terminated and negatively charged $(000\overline{1})$. Because the growth of NWs is a reaction process the top facet of a vertical NW in an array is the positive Zn^{2+} (0001).[237,238] The (0001) top facet is a stable polar surface without major surface reconstruction but has been shown to have many surface defects such as step edges which act as nucleation and adsorption sites. The polar field that exists in the c-orientated NW due to the charged (0001) and $(000\overline{1})$ is stabilised by a change in surface charge.[71] This is achieved with a non-stoichiometric (0001) surface with O-terminated step edges.[71] The polarity of the ionically bonded wurtzite ZnO NWs requires a stabilising reduction in charge of the positive Zn terminated (0001) top facet by ~1/4 with negative Oxygen steps and islands.[71] The Oxygen steps on bare (0001) form triangular islands of up to 34Å in side length which is a substantial area for a 500Å wide contact. In contacts of large ideality factors a region of low barrier height can dominate the total current.[239] These surface defects may drive interface properties that induce local variations in trap density and influence their energetic location (possibly within the bandgap), resulting in lateral barrier inhomogeneity.[240]

Although the surface charge is stabilised the (0001) surface has atomic scale holes and islands of single atomic plane step height.[71] This roughness over the top facet will increase surface states and adsorption of foreign atoms and molecules from air, particularly O_2, O and H_2O induced hydroxyl groups. Adsorbates are unlikely to be removed before Au deposition and will remain as a thin layer within the contact.

Adsorbates induce a substantial density of inner-band states on the bare ZnO surface in addition to intrinsic surface states. These surface states find an equilibrium charge level when compensated by ZnO charge carriers. Charge is depleted from near the surface even in the bare condition leaving a net positive space charge in the ZnO beneath the surface resulting in band bending. This may partially screen the ZnO from the electric field induced by Au deposition. Au deposition may also result in additional metal induced gap states and eventually an equilibrium charge level is found that may lead to further band bending. A high density of surface/interface states can result in the amount of charge in the depletion region and barrier height becoming independent of the metal work function.

A common case includes a thin interfacial layer which 'decouples' the system enough to exclude substantial influence by the metal on the surface states.[55] The extent of the interfacial layer is dependent on preparation methods, in the case of catalysed NWs there appears to be no layer at all, we cannot however exclude this for the deposited contacts which are subject to bound gaseous species even though the material is inert Au and ZnO.

The contact as a whole under no bias must be electrically neutral including the charge held by the surface states. With surface, defect, adsorbates and metal induced gap states the density of states could be very high with pinning of the barrier to the neutral surface charge level. Adsorbates contribute by changing the barrier to one that is very different to an intimate contact and current does not experience the large barrier usually formed between Au and ZnO. The resulting Fermi-level pinning combined with the structural properties of the Au contact contribute to an Ohmic-like conduction.

7.3 Catalyst Particle Interface (CPI) measurements

Catalyst NWs were measured in Omicron Germany taking advantage of the finer flexible AC etched tips and the high resolution (3nm) SEM to pinpoint catalyst particles before and after

measurement. Identifying the Au particles in-situ is vital to ensure the metal is present and the probe tip actually contacts only the Au particle. Sample Cat 35-3 was used for these measurements.

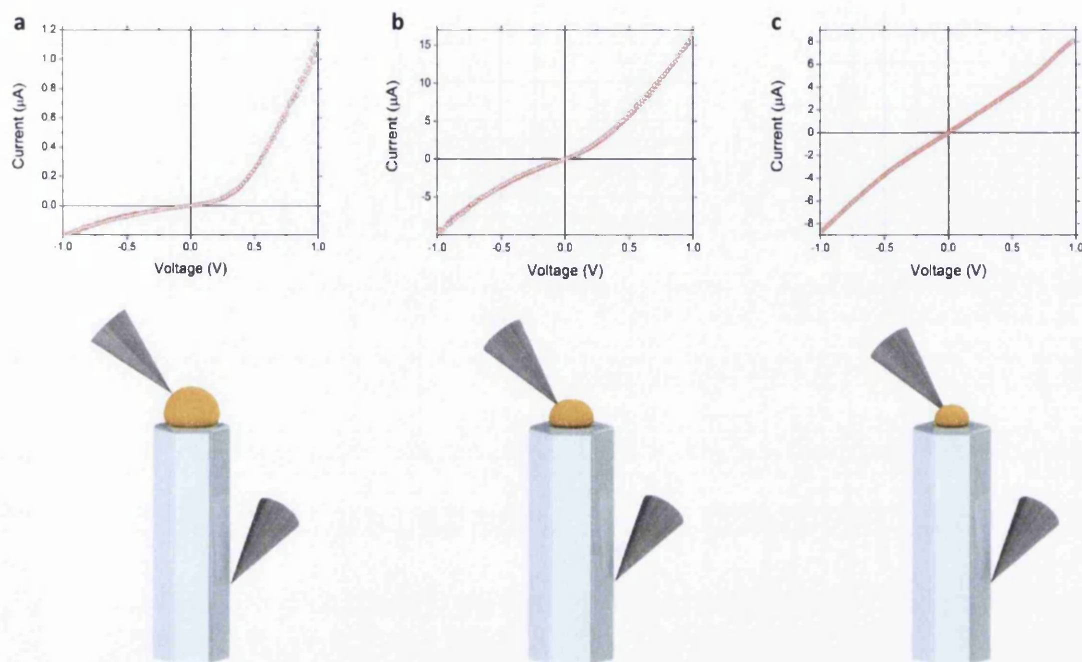

Figure 117. Current-Voltage sweeps in the two-probe configuration. **a)**, **b)** and **c)** correspond to catalysed NWs of diameter 73, 79 and 73nm with particles of diameter of 59nm, 47nm and 37nm respectively as depicted by the scaled 3-D drawings. Current data can only be compared qualitatively due to the difficulty in positioning the probe tips on the NW side below the interface in the top-down SEM view, and characterising the interface size.

Figure 117a-c shows the two-probe measurement results of the catalysed NWs with decreasing Au particle sizes of 59nm, 47nm and 37nm diameter respectively. The results indicate a decreasing potential barrier as the particle size decreases. Diameters of the particles were measured from 5 secondary electron (SE) and backscatter electron (BSE) top-down images for each particle taking into consideration the TEM images (Chapter 6) that revealed a catalyst particle that can be approximated as hemispherical in shape. By measuring the Au particle diameter with multiple SE and BSE micrographs on the exact NWs used in the 2-probe contact experiments the interface width was estimated as the measured diameter.

7.3.1 Schottky behaviour

The rectifying catalysed NW Au contact displays Schottky behaviour. Performing basic analysis and applying thermionic-emission (TE) theory[55] for the case of V greater than 3kT/q we have

$$J_{TE} = A^{**}T^2\exp(-q\phi_e / kT)\exp(qV / nkT)$$

where T is the temperature of 298K or RT, ϕ_e is the effective barrier height, V is the applied voltage, n is the ideality factor and A** is the modified Richardson constant. A** for n-type ZnO is dependent on the effective mass of an electron m_r and this varies according to the crystallographic direction in which the electron travels. Here current flows approximately parallel to [0001] and for bulk wurtzite ZnO m_r has been calculated between 0.14-0.3 (average 0.21) and experimentally values obtained are 0.21-0.3 (average 0.25) [67]. A** can be determined experimentally by plotting functions of saturation current and temperature, without this exact value A** we can only qualitatively argue the nature of the contacts. A** is dependent strongly on electric field and can vary greatly with morphology and in practice extracted constants may be far from the theoretical value due to barrier inhomogenities.[239] It has been shown by Dhananjay et al that A** maybe two orders of magnitude lower than the theoretical value for planar Au contacts on sputtered ZnO thin films[69]. As relatively large variations in A** have the same effect as a small change in ϕ_b[(55)] for our qualitative analysis of the nano-Schottky diodes using the theoretical Richardson constant for ZnO of $32\times10^4 Am^{-2}K^{-2}$ is reasonable, although investigation of this constant in NWs would present a very relevant study.

The contact area was estimated from TEM images which allowed the current density J to be calculated. Then the ideality factor and the effective barrier height were calculated from the linear region of the LnJ-V plot, Figure 118a black line. A linear region displays the voltage range where an exponential relationship which the current density holds. It is noted the less rectifying contacts do not display a linear region, and thus no exponential relationship, and similar LnJ curve shapes that reflects the near linear I-V characteristics.

Figure 118b displays the same current density data plotted on a log scale to indicate the magnitude of the current density at positive bias for each contact. The deposited contacts (Figure 115) show very similar current densities that increase slightly with decreasing NW

diameter and deposition thickness. The rectifying catalysed contact shows similar current density magnitude at 1V but slightly less at lower bias revealing the potential barrier presented by the built in voltage of the contact. The two catalysed NWs with 'small' particle contacts show a huge increase in current density indicating the potential landscape formed by the NW and NW-Au combined system has changed significantly. The slight rectification of Figure 117b shows a slight barrier is present and this is indicated by the lower current density at smaller positive bias than the 'nanoisland' contact of Figure 117c.

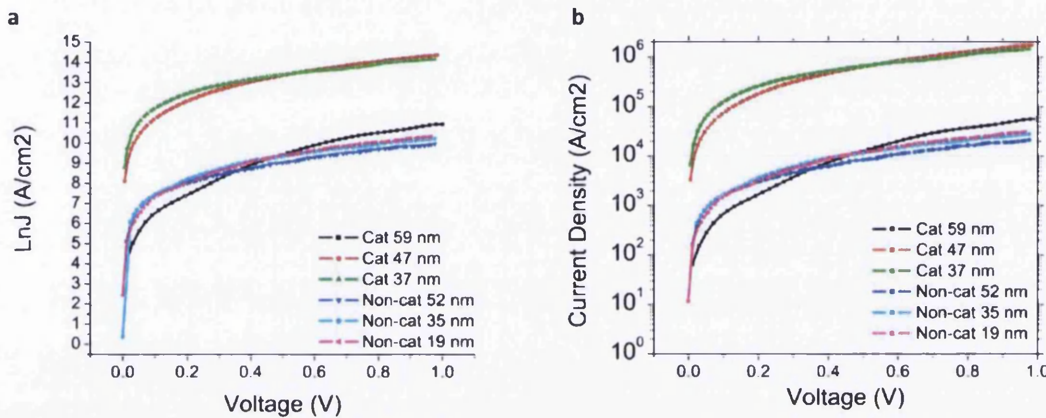

Figure 118. **a)** Plot of the natural log of the current density J against the forward bias voltage V for each contact of Figure 115 and Figure 117, the rectifying contact of Figure 117a is the only curve to display a linear region between 0.1-0.3V which is used with Thermionic Emission theory to estimate the barrier height by extrapolating to the y-axis. **b)** Forward bias current density plotted on a log-scale to show the much greater magnitude of current density on the two 'small' catalyst particle contacts. The deposited and 'large' Au particle contacts have very similar current density although the nature of the contacts varies the shape of the curve.

Applying thermionic emission theory to the rectifying catalysed contact of Au diameter 59nm gives an approximate barrier of 0.25eV and ideality factor of 5-6. By taking natural the log of J_{TE} the straight line region gives an experimental value for the ideality factor which is the gradient $d(\ln J)/dV$. By applying the straight line equation y=mx+c we find $c = J_0 = A^{**}T^2 \exp(-q\phi_b/kT)$ and $m = q/nkT$. It should be stressed that the analysis is far from ideal with large values of n. LnJ against V displays a linear region over approximately 0.2V, this again shows the contacts are very different from planar contacts when thermionic emission theory is usually a much better fit and ideality factors close to one are readily achieved with clean and intimate contacts. Although the thermionic emission does not describe the entire transport mechanism for this barrier the thermionic emission component can still be substantial and is very pertinent in the case of one-dimensional nanostructures where the depletion region can extend significantly into the semiconductor.

Thermionic emission current does not depend on the depletion width and if the barrier can be surmounted electrons can still conduct through into the structure.

7.3.2 Deviation from Thermionic Emission

Tunnelling may likely be a better fit, for example in the form of Thermionic Field Emission, but in order to gain good insight reliable values for the properties of ZnO NWs such as permittivity[229] and donor level are required. The shifting balance of properties can have considerable effect as we have seen with the four-probe measurements. Scanning Conductance Microscopy has been used by Yang et al to show the dielectric constant of a ZnO structure decreases from 9 to 2.5 as the diameter is reduced from 300nm to 100nm attributed to a weakening surface dielectric effect.[229] However the crystal measured cannot be classed as a NW with strong tapering of the morphology and the size is above the NWs considered here. (Frequency dependent measurements of the dielectric function for NWs of 15-60nm diameter have been performed using Electron Energy loss Spectroscopy and will be analysed as further work, until this work is completed we have to assume a bulk permittivity). Without directly measuring the dopant concentration and permittivity we must use published data of a realistic doping level $10^{17}\,cm^{-3} < N_d \leq 10^{18}\,cm^{-3}$ (18) that allows estimation of the important parameter in tunnelling theory

$E_{00} = \frac{h}{4\pi}\left[\frac{N_d}{m^* \varepsilon_s}\right]^{1/2} = 18.5\times10^{-15}\left(\frac{N_d}{m_r \varepsilon_{sr}}\right)^{1/2}$ eV where $m^*\left(=m_r m_e\right)$ is the effective mass of electrons in the semiconductor and $\varepsilon_s(=\varepsilon_{sr}\varepsilon_0)$ is the permittivity. Taking the bulk permittivity of ZnO $\varepsilon_{sr} = 8.66$ (5), $N_d = 10^{18}\,cm^{-3} = 10^{24}\,m^{-3}$ and $m_r = 0.24$ (23) we have $qE_{00}/kT = q\times1.28\times10^{-2}/kT \sim 0.5$ or $qE_{00} \sim 2kT$ and according to Rhoderick and Williams[55] transport enters the TFE regime in forward bias when $qE_{00} \sim kT$. This is independent of anomalies in the potential barrier that may exist due to contact size or edge effects. We have to surmise that TFE is a strong possibility although Thermionic emission when $kT \gg qE_{00}$ may still be substantial in bulk ZnO diodes of this doping level.

A simple means to assess the effect of the onset of TFE on the interface transport is to consider it as a reduction in barrier height. The expression requires details of the depletion region, such as the width, which are complicated in one-dimensional structures by the interplay of the NW surface and contact depletion regions.[21] However, by assuming the

diffusion potential V_d is the difference in work functions at the barrier $\sim 0.65eV$ and using the expression given by Rhoderick and Williams[55] we find

$\Delta\phi \approx (3/2)^{2/3} (E_{00})^{2/3} (V_d)^{1/3} \approx 0.06eV$ which shows a substantial reduction in effective barrier height is likely due to thermionic-field emission even in forward bias.

This neglects any bias dependence of the diffusion potential and so in reverse bias, with increasing $|V_d|$ it is much easier to enter the TFE regime. This can occur even in non-degenerate semiconductors as the electrons tunnel from the metal and for ZnO $N_d \sim 10^{17} cm^{-3}$ the main reverse bias transport mechanism can be TFE[241]. We have shown here with approximations that tunnelling can have a major influence on the transport properties but this still neglects the scale of the contacts which can lead to significant variations in the potential landscape.[16,60,242] Poor reverse bias characteristics are associated with tunnelling especially at the edge of metal contacts due to the crowding of the field lines which decreases the barrier width because of the increased field strength.[55,165]

The effective barrier calculated from the fit of TE to the data is much lower than planar Au-ZnO contacts (typically 0.6-0.7eV[5]) which is due to the 'small' size of the contacts and NWs. The largest Au catalyst particle has a diameter of 59nm and the small interface width constricts the lateral spread of the potential barrier.[60,63] The hemispherical shape of the particle concentrates the field lines around the particle edges which can enhance edge leakage and tunnelling. Sakurai et al used E-beam patterned Au contacts on flat lying ZnO NWs and measured over a temperature range of 200K (which allows the use of generalised Norde theory) to determine the barrier height of 0.4eV at 300K with n=1.2[150]. Contacts to flat lying NWs can have a much greater contact area than the free-standing NW configuration measured here, however as we have seen lithography can result in contamination of the device.

Assuming the donor density in each NW measured here is the same for deposited and catalytic contact schemes we may see effects of image force lowering, a non-homogenous barrier height as well as possible Fermi level pinning. However the catalysed Au interface is very different to the deposited contact which suffers from surface adsorbates and non-uniform Au structure. Usually forward biased ZnO Schottky barriers with $N_d < 10^{17} cm^{-3}$

experience an image force effect that is negligible although the lowering can be important in the case of a high field in the depletion region such as in reverse bias or at the edge of a contact.[55] In these cases the image force reduces the effective barrier height and width especially for potential barriers that are already narrow.[60] In forward bias the effect of image force lowering can be taken into account in the thermionic emission theory by a bias dependence of the effective barrier height ϕ_e in terms of the ideality factor which is constant when $\frac{\partial \phi_e}{\partial V}$ is constant[55], however the influence of this effect is likely to be small in comparison to the effective barrier reduction (~0.4eV) measured[194,201] and alternate explanations are necessary which we explore next.

7.3.3 The catalyst interface and CPI size dependence

Contacts to nanostructures are a hot topic with a recent article discussing contacts as either end-bonded or as side-bonded.[19] Side-contacts are typically lithography patterned on flat lying one-dimensional nanostructures. End-bonded can be contacts such as catalyst particles or end fused hetero-structures. It has been revealed by Leonard et al. that there is size dependent behaviour of the current transport across the Catalyst particle contact in relation to NW diameter. Contacts were shown to increase in current density and become less 'ideal' Schottky barriers as the Ge NWs were reduced in diameter, Figure 119.[21] The contact was measured with a single STM probe placed on the NW tip and measured through the n^+ doped substrate. The size of the catalyst particle was not considered to deviate from the NW diameter. We show here the overriding size-dependence is related to the catalyst particle size and not solely the NW diameter.

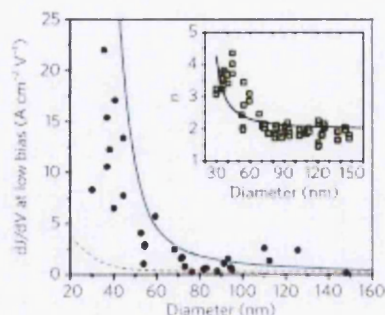

Figure 119. Graph showing the diameter dependence of Ge NWs. As the diameter decreases the zero bias conductance density increases and the contact becomes a less ideal exponential fit shown by the increasing ideality factor n for a generic temperature dependent exponential form, inset. Reproduced[19].

The conductance density at low bias of the ZnO catalysed contacts measured here displayed in Figure 117a-c at low forward bias (0.05V) is estimated as $4.14\times10^{3}\,\mathrm{Acm^{-2}V^{-1}}$, $3.43\times10^{5}\,\mathrm{Acm^{-2}V^{-1}}$ and $6.61\times10^{5}\,\mathrm{Acm^{-2}V^{-1}}$ respectively for the 59nm, 47nm and 37nm size particles. The magnitude of the low bias conductance is very high compared to the Ge NWs and indicates the non-ideal rectification properties even for the large 59nm Au particle. The current density increases dramatically as the particle decreases in size and the potential barrier is reduced. These values of low bias conductance density and the leaky reverse I-V shape indicate tunnelling becomes more prolific as the size decreases, although thermionic emission could be extensive if there is only a small potential barrier height or barrier inhomogeneities.

7.3.4 Potential barrier and the Interface structure

It has been shown theoretically by Leonard et al that end-bonded contacts to one-dimensional nanostructures can provide "unpinned" behaviour and the barrier can be described well in terms of the metal work function and no interface dipole.[243] The I-V characteristics then fit well to ideal thermionic emission with little reverse leakage contrary to planar contacts. Pinning still occurs but is localised to within 2nm of the interface after which the barrier is dictated by the metal work function and semiconductor ionisation potential.[243] However results here show significant reverse leakage and large deviation from forward bias thermionic emission. This is most likely due a significant variation in electric field at the particle edges and a reduced depletion region. Pinning may or may not have a substantial effect although the extent of pinning is dependent on the interface atomic-structure and must be very different from the deposited contacts.

Tung has written extensively on barrier inhomogeneity[163,164] to describe deviation of planar contacts from thermionic theory. The oxygen terminated defect step edges and islands on the Zn^{2+} (0001) top facet provide a physical source for inhomogeneity due to the differing bonds between Au-Zn and Au-O. Gaseous adsorbates are unlikely as the catalyst is present throughout the growth. Tung et al have shown barrier inhomogeneity of $NiSi_2/Si(100)$ leads to a large reduction in barrier height of 0.4eV compared to $NiSi_2/Si(111)$.[164] This large variation is considered to be a result of an intrinsic mechanism based on the interface atomic structure and not through Fermi-level pinning. However large barrier heights are

always reported for Au contacts on ZnO (0001) and barrier inhomogeneities if present must only have a minor effect.[5] Also the intimate contact between the catalyst particle and ZnO NW which is bonded on an atomic level with no observable defects or interfacial compounds reduces defect and interface states that can lead to inhomogeneities.

Metal-induced gap states are likely which can still induce pinning although the variation in barrier height of reported values of Au-ZnO[5] contacts suggests strong pinning is not a common feature.[193,244] The potential reduction in density of mid-gap states of the clean intimate contact should reduce the influence of Fermi-level pinning although locally[164] this may vary. The variable and defective nature of the (0001) facet alone may induce local barrier height variations[242,245] and for the contact size these regions could cover a substantial effective area. However the interaction, stabilisation and bonding that is present with an intimate solid Au interface that is present during crystal growth must affect the balance that is appropriate for a free surface of ZnO (0001).

The HAADF analysis in Chapter 6 of the Au catalyst particles show they form an abrupt interface with the NW and no discernible interfacial layer or substantial diffusion of Zn into the catalyst particle. Particles are alternatively polycrystalline in nature or single crystal with a lattice spacing of 0.237nm close to the spacing of the Au {111}||(0001) planes, in agreement with Brewster et al[58]. Polycrystalline catalyst particles have been observed to consist of two crystallites and there is evidence in all cases of crystallographic alignment between at least one crystallite and the NW. The particles in all structural cases are one particle and not several nanoparticles conjoined.

The high quality and bonding at an atomic level of the physical interface surpasses even a UHV prepared contact because it has never been exposed to anything other than the Au. The ZnO and Au catalyst particle interface is clean and intimate, can be considered free from inhomogeneities and provides a large potential barrier 0.6eV typical of Au-ZnO. These conclusions are supported by detailed microscopy analysis and comparison to relevant literature which allows greater confidence in attributing size dependent behaviour on particular transport phenomena.

7.3.5 Characteristic length scale and depletion region

When the length scale of metal-semiconductor interfaces is reduced tunnelling becomes increasingly important.[60,61,246] Increases in current density far greater than expected by simple geometry considerations are seen in STM experiments on contact nanoislands.[61] The doping density in the semiconductor has a major influence on the barrier thickness. However, the ZnO NW typical carrier density of $10^{18} cm^{-3}$ has less influence at the length scales (considered to be contact radius) of the contacts measured here because the morphology rather than the material properties allows tunnelling to become a major transport process, Figure 120a.[60]

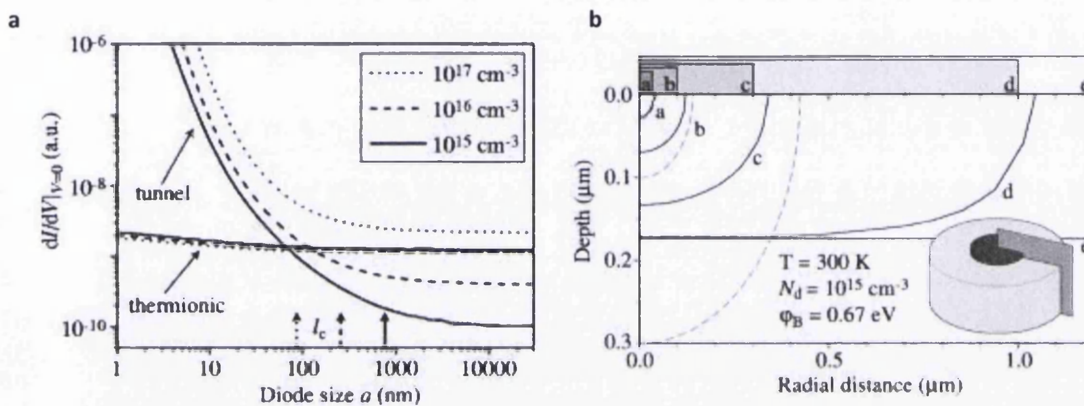

Figure 120. **a)** Modelled contributions to the zero bias differential conductance of tunnelling and thermionic emission. For a diode of radius less than 100nm the tunnelling regime is substantial. **b)** The numerically calculated FWHM of the depletion region of several nanosized contacts on a planar semiconductor.Reproduced[60].

The Schottky barrier thickness becomes a function of the diode size[60], shape and semiconductor dielectric properties[194,195] and reverse bias leakage can increase to the point where it can equal forward bias current as the potential barrier is easily penetrated. The rectifying catalysed contact, Figure 117a, displays $dI/dV|_{V=0} \approx 1.25\times10^{-7}\Omega^{-1}$ and the nanoparticle diode of diameter 60nm is shown to have a substantial tunnelling contribution in Figure 120a. The graph indicates NW doping is greater than $10^{17} cm^{-3}$.

Smit et al[60] numerically solve the Poisson equation for the nanocontact on a planar semiconductor system that can be assessed in terms of a characteristic length scale l_c (radius of contact area). Below l_c the contribution of tunnelling and the barrier thickness and shape become more dependent on the contact size and independent of the doping unlike conventional potential barriers. The concept is shown with a depletion region that becomes equal in size to the contact radius for the planar diode with a finite metal contact size in Figure 120b, and is applied specifically to the material properties of ZnO in Figure 121. The

expression in terms of the equation $l_c = \sqrt{2\varepsilon_s V_s / q N_d}$ plotted against doping density N_d for the relative dielectric constant, $\varepsilon_s = 8.66$ the bulk value of ZnO.

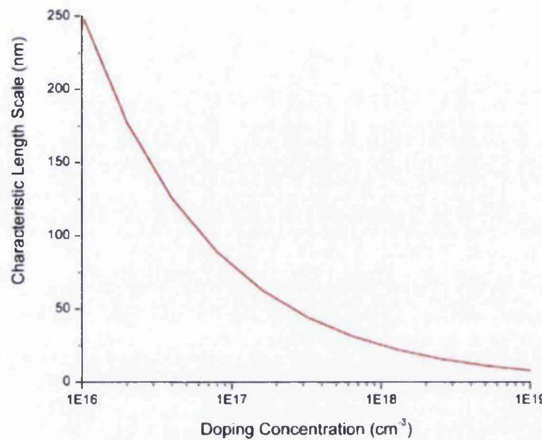

Figure 121. Plot of the characteristic length scale of a diode with a radius below which the barrier FWHM (barrier width) no longer depends on the carrier concentration. Instead, independently the size and morphology of the contact forms a 'thin' barrier of FWHM equivalent to diode radius (Figure 120b) and tunnelling then becomes a substantial transport process. This concept is applied in this graph to ZnO for the bulk value of the dielectric constant and a measured value for 100nm diameter ZnO NWs.

The total potential drop across the space charge region V_s is defined by $V_s = (\phi_b - \phi_s)/q - V$ and for estimation we assume the zero bias condition V=0 and a Fermi level near the conduction band such that $\phi_s = E_c - E_f \approx 0$ which gives a potential drop equal to the barrier height and $V_s = 0.65V$. This indicates even when neglecting edge effects the 'large' catalyst particle of 50nm diameter (25nm radius) will experience tunnelling through the depletion region as a dominant transport process at moderate doping levels. Below the characteristic length scale of the system the FWHM of the barrier becomes equal to the diode radius and as thermionic emission is relatively independent of barrier thickness the tunnelling contribution increases and the total conduction through the contact increases rapidly. This is characterised by the shape of the I-V curve changing as the contacts become smaller with an increase in reverse bias current and more linear forward bias.

The current density across the catalysed contacts increases dramatically which is a result of the change in contact configuration from a nanoparticle similar in diameter to the NW to one where the nanoparticle is much smaller than NW. The former is more like a linear system[194] and the latter more like a nanoparticle on a planar semiconductor surface[60,195]. The width of the depletion layer for a linear system, such as a NW, decreases substantially

from the conventional planar diode and decreases again dramatically for the nanoparticle on a surface.[194] Both cases allow substantial tunnelling increase as the depletion region decreases and as such this affects the current density across each contact. These models however neglect any surface conduction, edge effects, or transport though a contact-size restricted depletion region as shown in Figure 120b.

7.3.6 Isolating the influences on the interface transport

Experimental measurements by Smit et al and Song et al looking at contact islands less than 30nm diameter show at the top end of this size range I-V characteristics of lower effective barrier heights than the bulk equivalent, but still exhibit rectification behaviour.[61,197] Although surface leakage through surface states has been shown by Dickie et al to have considerable influence on nanocontacts of diameter 30-70nm (exposure to different gases[199] can quench these states) in our case these may result from exposure to air creating possible surface state conduction[167]. The surface state leakage around the nanocontacts can provide an Ohmic like conduction path which dominates when the contact is in reverse bias and the potential barrier of the interface prohibits current flow.[167,199] This results in a linear reverse bias I-V relationship, with leaky characteristics, and the easy forward biased barrier still may obey thermionic emission. Surface leakage would be expected to obey a relationship with the circumference of the contact and not with the area as the case is for 'conventional' transport mechanisms (square of contact diameter). For the deposited contacts and the 'large' catalysed contact this relationship would be approximately linear with the NW diameter. Although it is difficult to conclude whether surface leakage contributes to the conduction in the catalysed NWs the greater data set for deposited contacts allows further discussion later (section 7.5). However, the catalysed NWs were all prepared equally and the change from rectifying to Ohmic behaviour occurs independently to the NW sizes and so the total influence of surface conduction is expected to be minor. To isolate this as surface conduction would need further investigation by repeating the measurements with annealing to remove loosely bound species and subsequent exposure to gases such as O_2.

Modelling of a NW with an end-bonded contact covering the entire facet combined with surface depletion of the NW (as we have seen is appropriate for Ge and Si NWs but not ZnO) decreases the effective conductive core resulting in an increased effective contact barrier

height, this is due to the combined depletion effect, depicted Figure 122a.[201] The nature of the behaviour of the contact formed is entirely dependent on the extent of the combines depletion that extends from the contact further into the NW. This serves as a model for the deposited contacts (Figure 122d) and somewhat the large catalyst contact as depicted in (Figure 122b). For the smaller catalyst particle contacts the depletion due to the metal-semiconductor interface is smaller and because the NWs are much larger than the contact the overlapping depletion effect is much reduced (Figure 122c). This allows the small catalyst particles to act more like nanoislands on a plane and for tunnelling to be the dominant transport process. However as previously stated the surface depletion for the measured NWs is expected to be very small.

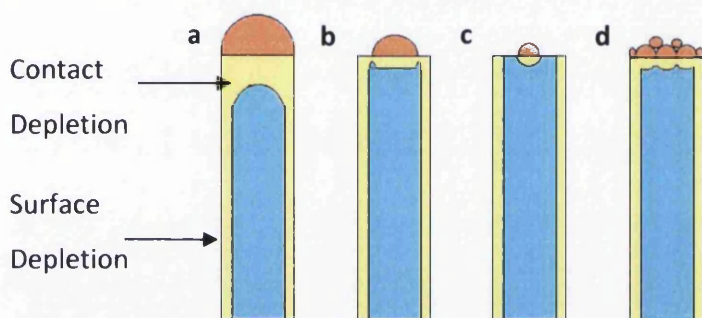

Figure 122 Schematic diagram depicting the combination of depletion from surface effects and the metal contact of catalysed **a)-c)**, and, **d)** Au deposited catalyst free NWs.

Single probe measurements on vertical catalysed Ge NWs show increasing contact conductivity and ideality factors greater than two as the NW diameter is decreased below 60nm (Figure 119), however no dramatic rise is seen until <50nm NW diameter which is far below the size of catalytic NWs measured here. Talin et al[247] state that tunnelling must be discounted as the mechanism behind increased conductivity as the depletion region increases with decreasing NW diameter [21,200]. However these models assume the contact is the same diameter as the NW and covers the complete end facet; they do neglect any size variation of the catalyst particle. Our results here show size dependent behaviour on similar sized NWs with different particle sizes, the extent of the depletion region is evident in the current passing through each contact but transport cannot be described by conventional mechanisms, and as we show tunnelling in the edge region must be considered.

The deviation from thermionic emission of the large catalyst particle is a result of the onset of Thermionic Field Emission (TFE) and Field Emission (FE) which becomes substantial due to

the size of the particles and the small depletion regions. The catalyst contacts measured here are in a domain between end-bonded NWs and nanoparticles on an infinite plane. The measurements see effects of a large barrier height coupled with edge tunnelling with conduction around a complicated depletion system of the metal-contact potential field which is simplified below.

7.4 Modelling Au-ZnO Catalyst Particle Contacts

The catalysed NW contacts as we show here display I-V behaviour that spans conduction regimes from Thermionic Field Emission (TFE) to Field Emission as the contact depletion region is confined by the contact size. To explain this we need to examine the interface. We have shown the interface to be abrupt, free from any interfacial layer and stray Au atoms that may have diffused into the NW bulk which may interfere with the potential landscape[16]. These facts allow confidence in assigning a value to the interface potential energy barrier height of 0.65eV[(5)] similar to that of clean vacuum formed Au-ZnO(0001) contacts. The next step is to characterise the shape and size of the NWs. We have shown the Au particles to be approximately hemispherical in shape which defines the contact area. Fitting thermionic theory to the large catalyst particle results in very large ideality factors and a very low effective barrier height, this theory does not fit the system well. Small nanoisland contacts are well known to deviate substantially from 'ideal' behaviour as a result of their finite size and mechanisms involving the increasing influence of surface and edge effects.[16,61,167,168,199] The edges of contacts tend to concentrate the field lines[55,165] locally increasing the field across the contact in the edge regions which has been modelled as a central 'normal' region of the contact and an edge annulus with reduced contact potential[63]. When the barrier height is constant the increased field at the edges will contract the depletion region similar to the effect of increasing the semiconductor doping. This provides a simple method to assess the current contribution through the edge and central regions which are simply summed according to area similar to the case of SBH inhomogenities[63]. In this analysis series resistance is ignored to simplify the effects and so the results are only considered in forward bias and at low voltages.

7.4.1 Depletion regions

The depletion of the surface due to surface trap states can be estimated in a similar manner to that of a conventional Schottky barrier.[18] The surface potential ϕ_s produced by surface

states and adsorbed ions acts like a potential barrier and the associated depletion width $W=(2\varepsilon_{ZnO}\phi_s/qN_D)^{1/2}$ which gives a value of 10nm when $N_D=10^{18}cm^{-3}$ and $\phi_s=0.1eV$. A substantial conductive core still remains and this may provide a reasonable estimation for some of the NWs measured by the four-probe technique.[18] However, the NWs measured by the two-probe technique in the free standing configuration formed good Ohmic contacts with the probe tip with relative ease. Forming good contacts can be very difficult in the free standing configuration and the reason for this is thought to be the extent of the surface depletion. It would seem likely for the free standing NWs that were readily contacted with minimal probe force had a minimal surface depletion which indicates a doping level at the high end of the doping range. Therefore a considerable surface depletion is not considered to be a factor in the analysis.

The metal-interface of the 59nm, 47nm and 37nm contacts is of a size where the depletion region becomes comparable to the radius and takes a parabolic shape.[60] Figure 121 shows for ZnO bulk parameters the characteristic length scale is ~25nm i.e. the contact radius needs to be below this before the depletion width scales with contact size. The 'large' 59nm catalyst particle is on the cusp of this regime and therefore we assume the conventional depletion approximation to estimate the depletion width at 25nm, calculated from $W=\sqrt{2\varepsilon V_d/qN_d}$. However, similar to a contact on a plane the parabolic shape of the depletion region is only marginally wider than the contact in the interface plane and in this edge region the depletion layer is thin, for example the smallest contact in Figure 120b. This thin edge region can be used to model edge effects without a complicated numerical solution to the Poisson equation which would need to include the high fields at the contact edges plus the finer details of the NW and contact shapes.

7.4.2 Transport mechanisms

The main transport mechanisms usually considered are TE, TFE and electron-hole recombination in the space charge region. Applying the standard equations[55] for recombination we can see the term is dominated by $J_{r0}=qn_iW/2\tau$. The intrinsic carrier concentration for ZnO[(248)] is low at $n_i<10^6cm^{-3}$ and the contact depletion region of $\sim 25nm$ provides only a small depletion region and the recombination current is insignificant. As stated the size of the NWs were above the size range for end-bonded NWs[(21)] where the

combined depletion extends a long way into the NW which may allow surface related recombination as a plausible mechanism. This mechanism is also very unlikely in ZnO due to the hole concentration which is many orders of magnitude lower than Ge.

7.4.3 Catalytic Au Contact modelling

The model of Smit[60] details a depletion region that scales with contact size. Below the characteristic length scale the depletion width (W) at the contact centre becomes comparable to the contact radius, unlike a bulk contact where W is determined by material properties. For small contacts the depletion region is confined by the contact edges with a small extension into the semiconductor βR, see Figure 123.

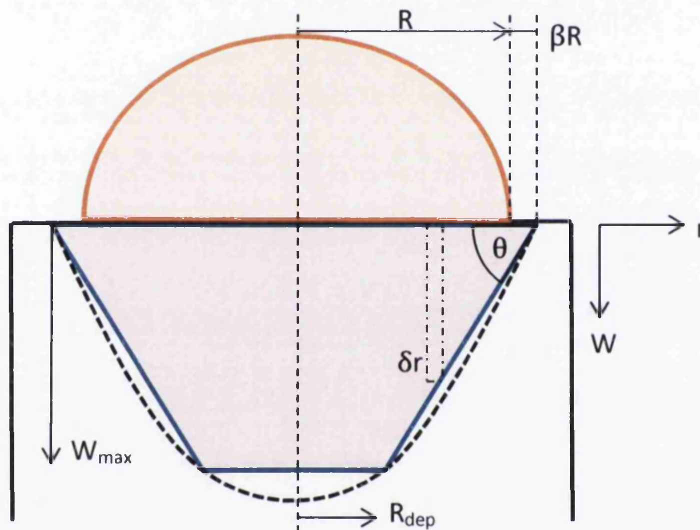

Figure 123. Diagram depicting the model used to approximate the parabolic depletion width of small contacts.

To model the transition from the rectifying 59nm contact to the Ohmic 37nm contact, a trapezoidal depletion shape is assumed for simplicity with maximum radius R+βR. Splitting the depletion region into small segment rings around the contact centreline of width δr, the depletion width is either the maximum depletion width W_{max} or a linear function of radius. From geometrical considerations W can be calculated from the angle $\tan\theta = W_{max} / (R - R_{dep})$.

Therefore, between a radius of R_{dep} and (R+βR) the depletion width is $W(r) = (R - r)\tan\theta$.

The current through one segment ring of width δr in terms of the current density J is $\sim 2\pi r J \delta r$ when δr becomes very small. To fit the data the current flowing across the entire contact is calculated with

$$I_{total} = 2\pi \int_{0}^{R_{dep}} J_{W_{max}} r dr + 2\pi \int_{R_{dep}}^{R} J(r) r dr$$

which expresses the variable depletion width in terms of r through the current density term J(r). The current is summed from the contact centre r=0 to the contact edge R where the depletion width thins to $\beta R \tan\theta$. As we have seen TE and Rec are negligible due to the large SBH, the large bandgap and the small intrinsic carrier concentration of ZnO. The dominant transport mechanism in this instance is tunnelling however the model was intended to investigate this mechanism further and analyse the regions of the contact that dictated the I-V characteristics. The most accessible analytical tunnelling expressions define terms for Thermionic Field Emission (TFE) and Field emission (FE) and were derived by Padovani and Stratton[96]. The tunnelling current through a finite size segment ring (of width δr) of the depletion region was numerically calculated with the current density of the form[96,97]

$$J_{TFE} = J_s \exp\left(\frac{V}{E_0}\right)\left[1 - \exp\left(-\frac{qV}{kT}\right)\right]$$

where $E_0 = E_{00} \coth\left(\frac{qE_{00}}{kT}\right)$ and the saturation current specific to TFE is

$$J_s = \frac{A^{**} T q \exp(q\xi / kT)\{\pi E_{00}(\phi_b - V + \xi)\}^{1/2}}{k \cosh(qE_{00} / kT)} \exp\left(-\frac{(\phi_b + \xi)}{E_0}\right)$$

The tunnelling parameter $E_{00} = \frac{h}{4\pi}\left(\frac{N_d}{m^* \varepsilon_{ZnO}}\right)^{1/2}$ is dependent on the donor concentration N_d, m^* the electron mass in the semiconductor and the permittivity of ZnO is ε_{ZnO}. E_{00} is an energy that is very important in tunnelling theory. The depletion width is calculated from the geometrical considerations W(r) and then using the standard depletion approximation

$W=\sqrt{\frac{2\varepsilon_{sr}\varepsilon_0 V_{bi}}{qN_d}}$, N_d and E_{00} can be calculated. This does not represent the 'bulk' doping of the ZnO but allows the representation of a 'thin' barrier in the tunnelling expressions.

Applying only TFE alone does not provide the current densities to match experiment and the expression breaks down in the edge region due to the narrow depletion widths, therefore we must turn to FE. FE is appropriate for degenerate semiconductors with the Fermi level above the conduction band minimum (CBM) where $\xi>0$. For ZnO the n-type material becomes degenerate when the doping is greater than $3.4\times10^{18}cm^{-3}$. This was calculated from a Fermi level position coincident with the CBM $\xi=0$ in the expression $\xi=\ln\left(\frac{N_d}{N_c}\right)\frac{kT}{q}$, where the effective density of states in the conduction band is $N_c=2\left(\frac{2\pi m^* kT}{h^2}\right)^{3/2}$ for $m_{ZnO}=0.24^{(23)}$ $N_c=3.5\times10^{18}$ cm^{-3}. To be consistent it is assumed $\xi=0.01eV$ throughout the analysis which corresponds to the doping density $N_d=3.4\times10^{18}$ cm^{-3}. For Au catalysed NWs grown on Sapphire a doping density of 1.2×10^{18} cm^{-3} can be expected[18] in which case $\xi=0.026eV$ below the CBM. The approximation of doping degeneracy in the NWs to satisfy the tunnelling expressions is not considerable because the wires measured here are expected to have high doping densities because of the ease with which Ohmic contacts were formed with the probe tips, this is not often the case in the free standing configuration. Further measurements on flat lying NWs have shown Ohmic contacts with the probe tips are more readily formed to the most conductive NWs which have minimal surface depletion and high doping concentrations.[18,154] In the free standing configuration the flexibility of the NWs increases the difficulty of forming good Ohmic contacts and only the most conductive NWs were selected to provide reliable contacts. Additionally, a Gaussian spread of electrons around the Fermi-level, often assumed in analytical solutions of transmission probability[96,97], still infers a large concentration of electrons at energy levels above the CBM even if the Fermi level is slightly below.

FE takes the same form as TFE, however it is expressed in terms of E_{00} ($E_0 \sim E_{00}$ at high doping levels) and the J_s term specific to this mechanism

$$J_{FE} = J_s \exp\left(\frac{V}{E_{00}}\right)\left[1-\exp\left(-\frac{qV}{kT}\right)\right]$$

where

$$J_s = \frac{2\pi q A^{**} T E_{00} \exp(-\phi_b / E_{00})}{k\left[\ln\{2\left(\frac{\phi_b - V}{\xi}\right)\right]\sin\left[\frac{\pi kT}{2qE_{00}}\ln\{2\left(\frac{\phi_b - V}{\xi}\right)\right]}$$

Padovani and Stratton specify a maximum temperature range for FE defined by

$kT < \left[(2qE_{00}\xi)^{-1/2} + (2qE_{00})^{-1}\ln(4\phi_b/\xi)\right]^{-1}$ which requires E_{00}>0.14eV at 300K. This excludes the majority of the contact other than near the very edge. However this restriction must be relaxed because the model does not use the 'bulk' semiconductor doping and instead models a depletion region dependent on the contact size and not material properties. FE is appropriate not only at low temperatures and high doping concentrations but also in high electric fields that produce narrow depletion regions such as those experienced at the contact edge.[55,165] The expressions by Padovani and Stratton provide the most accessible and interpretable means of assessing tunnelling currents without a full numerical solution of the transmission coefficient for each contact.

Tunnelling is frequently said to transition from TFE to FE when $qE_{00}/kT \gg 1$ [(55,97,98)] and contacts become Ohmic by tunnelling at values of E_{00} when $E_0 \sim E_{00}$ which occurs within an error of less than 1% when $qE_{00}/kT>2.7$.[98] At values much greater than $qE_{00}/kT=2.7$ the 'cosh' term in the TFE expression rapidly becomes large and TFE calculated currents start to decrease, this is in spite of the depletion region becoming very narrow i.e. the TFE term breaks down. In this instance FE becomes the process of conduction as a result of the contracted depletion region and highly n-type material properties. Similarly, values of E_{00} such as $qE_{00}/kT<2.7$, lead to a negative 'sin' term in the FE J_s expression and the mechanism must be TFE. FE can only apply to larger values of E_{00} which represents high doping levels, or in this instance a narrow depletion region <5.3nm in width.

Applying the analysis as a summation of current from the contact centre to the contact edge, with a geometrically dependent W which in turn determines E_{00} in the TFE and FE

terms we have an expression that can be numerically calculated,

$I_{total} = 2\pi \sum_{i=1}^{10R} J(i)\left(i*\frac{R}{10R}\right)\left(\frac{R}{10R}\right)$ where the step size is expressed as $\frac{R}{10R}$ =0.1nm and the equality above for E_{00} was used as the cross-over point from TFE to FE.

7.4.4 Depletion region model optimisation

To fit the experimental data for each contact it was necessary to write a Matlab program that optimised the values of β, R_{dep} and W (see Appendix B for the full code). The maximum depletion width W_{max} for the 59nm contact was set by the standard depletion approximation for the properties of ZnO doping of $10^{18}cm^{-3}$ and barrier height 0.65eV that provides a depletion width of 25nm from the standard depletion approximation. This depletion width is applied to the largest 59nm diameter contact because it is above the scaling range proposed by Smit. However the smaller contacts are below the characteristic length scale of the system (Figure 121) and the depletion width scales with contact radius, i.e. the 47nm contact W_{max}~23.5nm and the 37nm contact W_{max}~18.5nm. The Matlab program was then written to optimise the remaining variables within ranges $0 \leq R_{dep} \leq R$, $\beta \geq 0.01$ and W_{max} with a small tolerance for each contact. This allowed the program to optimise the depletion shape which is approximated as a trapezium using a differential evolution routine. The fitting results and the optimised shapes are shown below.

7.4.5 Depletion region fitting results

The best fit for the 59nm contact, shown in Figure 124, is a wide trapezoidal shape that approximates the parabolic shape shown by Smit (Figure 120b). The depletion overhang at the contact edge is minimal, β=0.011, R_{dep}=27.2nm and W_{max}=24.8nm.

99.9% of the current at very low bias is shown by the model to be in an edge region of width <1nm and the currents are very small <1nA. At greater forward bias 0.25V the majority (~60nA) of the current flows in an edge region of the contact with an annulus of width ~13nm (~56% of the contact area). The depletion region contracts with increased forward bias and the tunnelling current spreads across the contact, at even greater bias the tunnelling current eventually dominates across the entire contact.

At 0.25V within the 99.9% current tunnel window the depletion region spans from the maximum 25nm to a minimum of 3nm at the contact edge. The values of E_{00} range from

0.0278eV to 0.1044eV which represents the artificial doping levels of $1x10^{18}cm^{-3}$ to $6.6x10^{19}cm^{-3}$ respectively. These values neglect the bias dependence of the depletion width and represent the inputs for the TFE and FE terms that are dependent on the applied bias. As a comparison the bias dependent values of W_{bias} range from 19.6nm at the inner most region of the tunnel window to 2.4nm at the contact edge at a bias of 0.25V. Transition from TFE to FE occurs at a depletion width of 4.5nm which is very close to the contact edge where FE was expected to dominate.

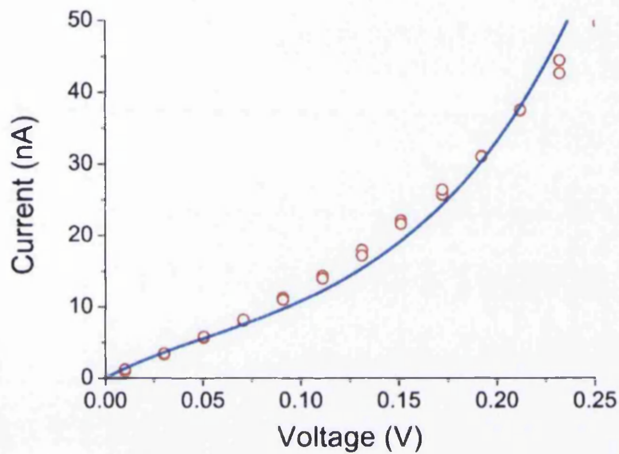

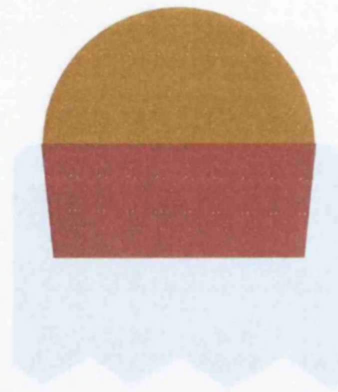

Figure 124. The Graph shows the low bias experimental current voltage measurement of the 59nm Au contact (red dots) and the corresponding optimised fit for a trapezoidal depletion region approximation. The depletion shape provided the necessary current to match the data when applying Thermionic Field Emission and Field Emission as the dominant transport mechanisms through the barrier that has a large Schottky barrier height.

Smaller contacts exhibited a change in transport behaviour becoming more conductive and less rectifying. This change is expressed in the depletion region taking a triangular shape, shown in Figure 125, to allow more tunnelling current which is a product of the optimised fitting routine that provided the parameter values for the 47nm contact of β=0.10 and R_{dep}~0nm with W_{max}=21.8nm.

99.9% of the very low bias current across the 47nm contact is within an edge region of width 3.7nm (~15% of the contact area) and the current is much larger (~50nA) than the 59nm contact, the smaller contact is more conductive. When the bias is increased to 0.25V the current (~2.4μA) flows within a region of ~7nm width (~30% of the contact area). The depletion region contracts with increased forward bias and expands the tunnelling current window that covers a greater proportion of the contact and increases the total current.

Within this window at 0.25V the range of E_{00} was 0.0448eV to 0.1608eV which represents artificial doping of $1.04 \times 10^{19} cm^{-3}$ to $1.57 \times 10^{20} cm^{-3}$ and the depletion region scales from 7.75nm to 2nm respectively. Again the transition between TFE and FE occurs when the depletion region is ~4.5nm.

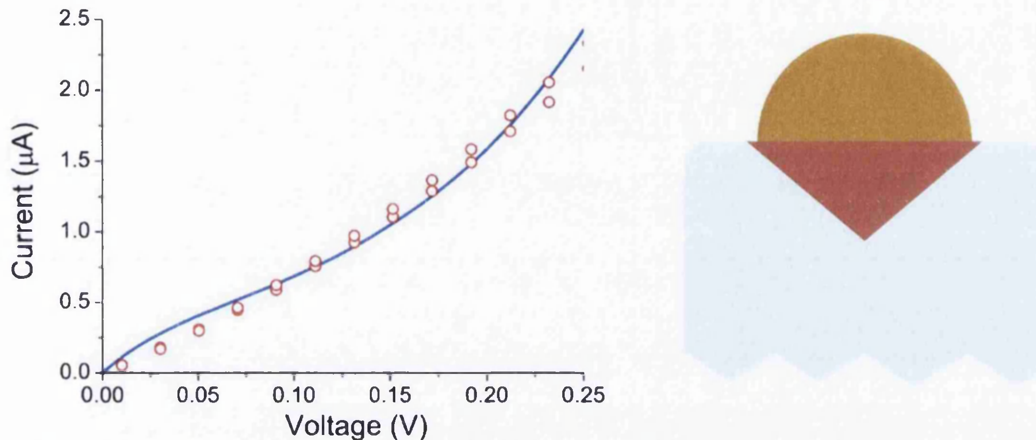

Figure 125. Graph showing the low bias experimental current voltage measurement of the 47nm Au contact (red dots) and the corresponding optimised fit for a trapezoidal depletion region approximation. This depletion shape provides the necessary current when applying Thermionic Field Emission and Field Emission as the dominant transport mechanisms and the change from trapezoidal to triangular shape represents the large increase in conductivity of the contact below the characteristic length scale when edge effects increase.

Linear I-V characteristics of the 37nm display an Ohmic contact with depletion parameters of β=0.1095 and R_{dep}~0nm with W_{max}=19nm with a triangular depletion shape, shown in Figure 126. A transition to purely Ohmic behaviour of the 37nm contact occurs with a similar value of β for both of the small contacts. The value of β actually represents a smaller absolute value of the overhang of 4.1nm for the 37nm contact compared to 4.7nm for the 47nm contact. This coupled with the smaller depletion width maximum increases the tunnelling current around the contact edge. In comparison, the actual value of the current is less because the contact is only 60% the size of the 47nm contact, however, the current density is greater for the 37nm contact in the bias regime considered for the model.

The 99.9% current tunnel window increases from an annulus of width 3.7nm, near to zero bias, to 5.9nm at 0.25V and again opens up with applied bias. Within this window at 0.25V E_{00} ranged from 0.0446eV to 0.1707eV which represents artificial doping of $1.15 \times 10^{19} cm^{-3}$ to $1.77 \times 10^{20} cm^{-3}$ where the depletion region decreases from 7.34nm to 1.88nm. Again the transition occurs when the depletion region is ~4.6nm. The smaller values for the depletion width within the tunnel window are due to the smaller relative value of βR which introduces

more FE into the overall current. The increased FE current provides a more linear I-V characteristic with little resistance to the current flow as the barrier becomes transparent to electron transport in the edge region.

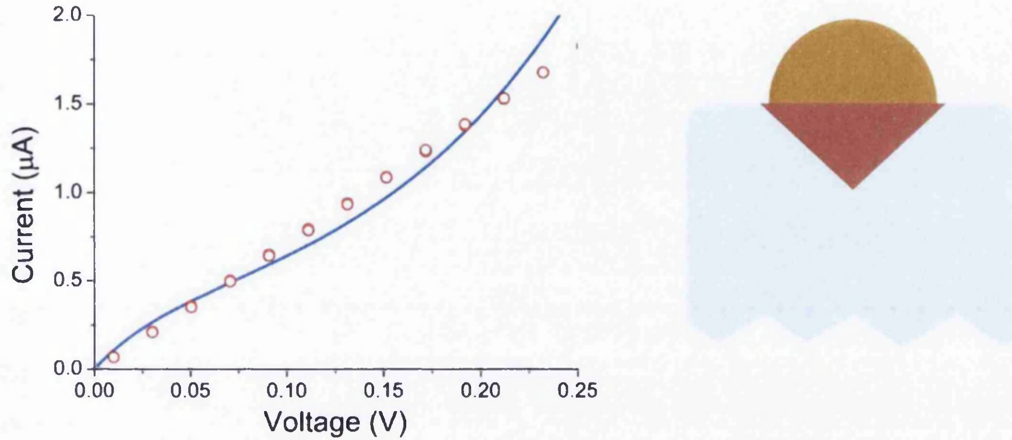

Figure 126. Graph showing the low bias experimental current voltage measurement of the 37nm Au contact (red dots) and the corresponding optimised fit for a trapezoidal depletion region approximation. The transition to pure Ohmic behaviour is a result of the reduced depletion size which encourages more tunnelling across the contact.

7.4.6 Summary of fitting results

Modelling results showed as the contact size decreased relative to the wire the contact became more conductive and less rectifying. This transition was expressed by applying TFE and FE theory to a depletion region that changed its shape as the contacts became smaller. Greater current measured in the smaller contacts was calculated by approximating the depletion region as triangular. A change to a triangular shape provided the transition to a narrow edge-induced depletion region necessary for more FE tunnelling current that can produce an Ohmic contact. An optimised depletion region for the large 59nm contact similar was similar to that predicted by Smit with a full and nearly semi-circular depletion region shape, approximated as a trapezoid. A 59nm contact on a ZnO NW of typical doping concentration is in the regime above the characteristic length scale which predicts the depletion width is governed by material properties although the shape is confined by the small particle size – it is not infinite in area and the lateral spread is limited to a size slightly larger than the contact interface. The 47nm and 37nm contacts are below the characteristic length scale and the depletion regions scale with the contact radii. A triangular depletion approximation was the most appropriate model with a depletion region that thinned considerably towards the edge of the contact which allowed tunnelling to dominant in these

regions. To fit the data a combination of TFE and FE was required to provide the current densities necessary to match the experiments. At zero bias the tunnelling window only exists at the very edge of the contact, as expected from the high-field at the contacts edge, but the window increased and became much larger dispersing the current across the contact area as the bias and total current increased. Tunnelling increased as the contact and depletion region decreased in size - the system is interdependent and is dominated by tunnelling. This model should apply to all small contacts with large and homogenous Schottky barriers.

7.4.7 Validity of the Model

Approximating the depletion region as a trapezoidal depletion model provided the fit to the experimental data. Two prominent features in each fit are apparent, the shape of the fit does not exactly match the experimental data, and the fit is only for low bias.

Fitting deviates rapidly from the experimental data at larger bias because the series resistance was excluded in the model. Series resistance is normally included as a term that reduces the voltage drop across the interface in the current density expression specifically $V-IR_S$ is substituted for V. R_s is the series resistance of the circuit included in the measurement other than the interface of interest. The majority of this is the NW and the contact resistance at the Ohmic contact on the NW side. R_s can be determined from the linear part of an I-V curve at voltages above the SBH (in this case 0.65V). For the 59nm contact the resistance at 1V is ~830kΩ which could be taken as the series resistance. However including this in the model is difficult. The model splits the contact into small segments with each potentially having different transport mechanisms, in this case FE or TFE. Series resistance only applies to the entire circuit i.e. the current flowing through the entire contact and the NW. The model calculates the current through a small annulus of width δr and the total current is a sum of each small segment; this does not allow the possibility of introducing the $V-IR_S$ term into the current density expressions. Each segment experiences a different barrier thickness that was modelled as a changing value of E_{00} and N_d. This provided in the edge regions proportionally much greater currents to those in the contact central region, in the edge region the value of IR_s becomes very large. The voltage drop on the contact segment $V-IR_S$ becomes disproportionally small near the edge damping

the edge effect. This masks the proportions of transport mechanisms across the contact and the extent of the edge conduction.

Other reasons for the ill fit at large bias are the terms of FE and TFE neglect effects of image force lowering which can have an enhanced effect on the effective barrier height and barrier width especially with narrow barriers[60]. To include this effect would require a more precise calculation of the transmission probability at voltages near to the SBH. This may also include electron tail lowering which can induce an even larger decrease of the SBH and the assumption of the standard parabolic depletion width approximation becomes important and considerable. The tail lowering becomes more important for tunnelling transport and by neglecting it the contact resistance can be overestimated.[162]

The shape of each fit is determined by the proportion of TFE to FE and the local value of E_{00}. Three separate models were tested and the trapezoidal depletion region provided a model which is adaptive and fits both the rectifying and Ohmic contacts. Also tested were a step depletion model which used a central region with a barrier width which scales with the contact radius and a narrow 1-2nm annulus with a contracted depletion region. This model required only TFE in the central and edge regions for the 59nm contact. The smaller contacts required the introduction of FE in the edge annulus, however as the depletion region in this region was required to be very thin to achieve the experimental current magnitude the term for FE produced a poor fit. The calculated values of J_s in the annulus were very large which produced high curvature in the low bias regime.

The numerical solution of Poisson's equation by Smit et al[60] depicts a depletion region which could be approximated as semi-circular for contacts of radius less than 50nm and the depletion width is dependent on contact size. Using this approximation the depletion region was split into segments and N_d used to model the deceasing depletion width from contact centre to edge in the FE and TFE terms. In this model the contacts were dominated by tunnelling in the peripheral regions where the depletion width is narrow. This created a problem with the semi-circular depletion model which confined the region of 'narrow' depletion (<5nm) to a very small area of the contact. The depletion region border at the contact edge is almost perpendicular to the interface and the depletion region rapidly becomes too thick for tunnelling. This required very small and diminishing values of β

almost producing a 'singularity' at the contact edge where the depletion region becomes very thin <0.5nm. Fitting the three contacts with this single model based on a depletion region that scales with the contact radius in a semi-circular shape crowded the majority of the tunnelling current into a few angstroms width near the contact edge. This is a result of tunnelling being negligible with depletion widths greater than ~8nm.To provide the current magnitudes of the smaller contacts the model over estimates the influence of FE in the edge regions with very large values of J_s and the model could not approximate the experimental data for all three contact variations.

The trapezoidal model provided the correct current magnitudes for each contact at low bias with realistic values of β, depletion width and the 99.9% tunnelling window. The shape of the fit however is approximate, but we have shown the dominant transport mechanism for small contacts to be tunnelling. TE and recombination are negligible and most tunnelling occurs at the contact edge where the depletion region thins considerably due to edge effects. The thin region near the contact edge was revealed by Smit, however at doping concentrations above those considered by Smit ($>10^{17}cm^{-3}$) the high field at the contact edge contracts the depletion region further and tunnelling through the depletion region increases at the contact edge. Here we have demonstrated the importance of edge tunnelling for nanocontacts using well established tunnelling terms without the complexity of 3D numerical calculations. The terms for TFE and FE however are in themselves approximate and are appropriate for macroscale contacts which can be considered in one-dimension with no lateral variation in barrier. Edge effect and barrier inhomogeneities must be considered as three-dimensional barrier systems which can vary on a nanometre scale as revealed by Im et al with Ballistic Electron Emission Microscopy (BEEM) experiments[242] on Schottky diodes with a high coverage of shallow barrier height patches.

The tunnelling terms of FE and TFE are based on a simple barrier shape, this is essential for providing an analytical solution which is practical to use, hence the popularity of the expressions. To provide accessible and useful terms for Schottky barrier tunnelling Padovani and Stratton use the barrier transmission probability provided by the one-dimensional Wentzel-Kramers-Brillouin (WKB) approximation which applies a semi-classical exponential as the wavefunction. The potential barrier is modelled as a parabolic function of distance from the interface and the one-dimensional time-independent WKB transmission

probability for the barrier is a function of potential energy.[96,97] The approximation required the terms for FE and TFE to have specific regimes where they are applicable, they are approximations for tunnelling at the Fermi-level or at a greater thermally excited level.

The FE temperature range discussed (section 7.4.3) specifies for large metal-semiconductor contacts the temperature at which the majority of charge carriers are located near the Fermi-level and the depletion region is narrow enough for tunnelling transmission. However in small contacts the depletion region is not the same across the contact and the width varies due to the additional effect of the high field created at the edge region. This is not an effect of semiconductor doping contracting the depletion region. However to simulate this effect with the FE and TFE terms we must artificially increase E_{00}. The tunnelling model of Padovani and Stratton and Crowell and Rideout assume Gaussian distribution of electrons around the Fermi-level or at a thermally excited level above. This creates a spread of electrons and many are available above and below the specific energy level. In the case here the edge effect induces a very narrow depletion region which allows tunnelling at all energy levels in the CB and the effect is enhanced with forward bias which compresses the depletion region further. The potential barrier which is independent of material parameters, as shown by Smit, is determined by contact size and the edge effect which negates the temperature validity range set out by Padovani and Stratton. The FE temperature range is dependent on E_{00}, ϕ_b and ξ and by varying E_{00} to simulate a three-dimensional depletion with one-dimensional theory the temperature equality must be ignored. E_{00} in this model does not relate to the bulk semiconductor properties as specified in large contact FE and TFE theory.

The FE term has a large influence on the shape of the total calculated current. This shape is determined in the exponential term by the factor q/E_{00} and the current magnitude is largely influenced by the value of J_s. The value of E_{00} therefore dictates both the value of J_S and the shape of the fit. In this model E_{00} was determined by the doping concentration calculated from the standard depletion approximation for each segment of the changing depletion width. N_d was locally determined by the value of β and the slope angle which provided the control in the model to match the experimental data. To produce a near linear output from the FE exponential E_{00} was required to be very large, and also N_d, along with a very thin local depletion. The large value of E_{00} also produces a large value of J_S (which is proportional E_{00}).

Therefore a balance between current magnitude and shape was found by the fitting parameters.

The analysis of the Ohmic 37nm small contact could equally be expressed by a contact resistance, however to express the transition of I-V behaviour with transport phenomena we have fit one model to each contact. Fitting exponential functions to a linear I-V is not ideal although the model provides an excellent explanation for the transition seen. However the expressions of FE and TFE are limited because they do not give an explicit theory for tunnelling of non-alloyed non-degenerate semiconductor Ohmic contacts where emission can occur at the CBM, which is a possibility for the NW contacts measured.[162] Also quantum-mechanical reflections are ignored in the FE expression which can have a probability of as much as 50% to scatter electrons back into the semiconductor when emitted at the Fermi-level. These would be included in the transmission probability in a full numerical solution of the contact. and may represent a large reduction in current which can lead to Ohmic contact currents being overestimated that may increase the influence of FE in our model.[162]

Regardless of these simplifications the fits produced show an approximation to the depletion region and the contact behaviour and demonstrate that tunnelling dominates the contact in the peripheral regions. This determines the transition from rectifying to Ohmic as the contact decreases in size and the edge induced field effect on the depletion region intensifies.

To correctly simulate the transport across small contacts on NWs it is necessary to solve the Poisson equation for a realistic potential barrier of the contact including size scaling effects. However to reveal something new it is also necessary to include the enhanced electric field because of the high curvature at the contact edge which will act to locally pinch-in the depletion region and to include semiconductor surface states around the contact that may induce surface depletion or accumulation as an additional influence. The SBH can be considered constant over the entire contact which was revealed by the high quality of the interface. The depletion region then becomes a three-dimensional landscape and Poisson's equation must be numerically solved. The transmission coefficient could then be calculated for the depletion region in a one-dimensional fully quantum mechanical calculation[60,249]

with all electrons at energy levels below the SBH maximum contributing to the tunnelling current.

It is proposed the current densities observed reflect a very high electric field at the particles edge which locally compresses the depletion region opening a tunnelling window. With increasing forward bias the window increases in size and electrons can effectively tunnel through the barrier similar to n^+ regions used for Ohmic contacts Figure 127.

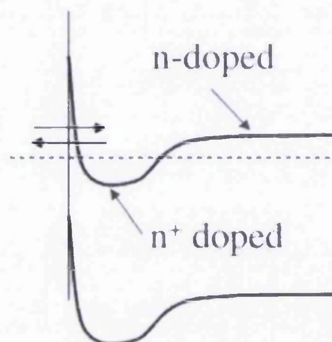

Figure 127. The band diagram for a highly doped n+ region near the interface for an n-type contact. The Fermi level is below the conduction band but tunnelling can still occur due to the extreme band bending near the interface, the potential barrier becomes virtually transparent to tunnelling current.

Tunnelling in this case does not require a bulk degenerate semiconductor (Figure 127), as required for theoretical FE, but even with a Fermi-level slightly below the CB the contact is altered by the induced electric field of the n^+ region and not the bulk properties of the semiconductor. This is where the FE model of Padovani and Stratton and the experimental data differ, the electric field driving the contact is beyond that of the applied or built–in voltage for planar contacts and is not totally dependent on bulk material parameters. This is the effect of the high electric field at the particle edge and the contact-size dependent depletion region, as the particle size decreases the influence of the Au-ZnO potential barrier on tunnelling current is reduced.

7.5 Catalytic and deposited Au Contact comparison

The study by Leonard et al[21], Figure 119, is the most relevant work to the contact measurements taken here. Pinning of the Au-Ge bulk interface Fermi level is well established and the barrier height of the NW-Au contact is assumed by Leonard et al to be the same. The main result shows increasing current density and ideality factor with decreasing NW diameter contrary to the expected decrease in conductivity stemming from

the increasing influence of surface depletion in smaller NWs, the modelled depletion is shown in Figure 128.

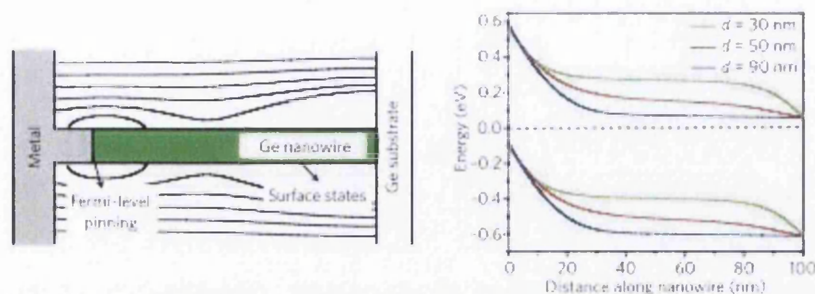

Figure 128. End-bonded model for Ge NWs in the presence of strong Fermi-level pinning which fixes the barrier to 0.59ev regardless of contact or NW size. The contact covers the entire NW diameter and when the is decreased the combined effect with surface states increases the depletion width along the NW. Reproduced[19].

By solving the Poisson equation for an end bonded NW Leonard et al show for a contact that covers the entire end facet in the presence of strong Fermi-level pinning coupled with the influence of surface states on the NW sides, the contact depletion region increases in width with decreasing NW diameter. This is critical for the hypothesis of electron-hole recombination in the depletion region which is the only mechanism that can fit the increasing depletion size with increasing current density. This model relies on the catalyst particle covering and contacting the entire NW end facet which is inappropriate for catalysed ZnO NWs. A diameter dependent recombination time is also required to fit the data shown depicted in Figure 119. For conventional planar diodes solving the Poisson equation shows the depletion width becomes smaller with diode diameter and eventually becomes thin enough for tunnelling to dominate as the size decreases below 100nm, Figure 120.[60]

To postulate on the transport mechanisms which contribute to the contacts measured here we can construct a graph similar to Figure 119, which compares the low bias conductance with Au contact diameter. The contact diameter for deposited contacts is the NW diameter, whereas the catalyst contact is the diameter of Au particle. Although the exact vertical position of the probes is not known to allow quantifiable comparison of each contact, the majority of measurements had the probes within one coarse piezo-step of the NW tip i.e. ~1μm separation.

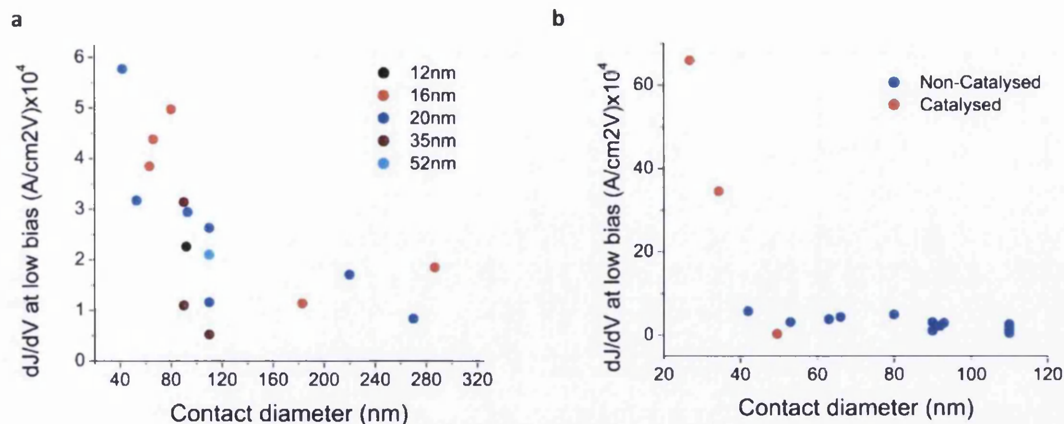

Figure 129. **a)** Small-bias conductance density of the deposited ZnO-Au contacts against Au contact diameter, the graph shows a similar relationship to Figure 13. **b)** the major difference however is the current density of the Catalysed NWs increases in similar manner but independent of a change in NW diameter with the two smallest contacts on NWs of diameter 79nm and 73nm.

The results for the catalysed NWs measured here show the increasing current density can be correlated to the metal contact size and independently from the NW. Figure 129a depicts the same increasing trend with decreasing diameter as revealed by Leonard et al[21]. The magnitude of the low bias conductance density of deposited contacts also increases as the NW diameter decreases for NWs from 300 to 40nm diameter.

This may suggest the influence of surface leakage which can form an Ohmic like conduction path around the potential barrier.[167,168,199] This conduction mechanism could stem from surface state conduction of intrinsic states, adsorbed O_2^- ions and other gases coupled with the Au nanoparticles on the NW side facets which uniformly, but not continuously, covers some of the NW side facets. When coupled with Fermi-level pinning due to the adsorbates at the interface both the forward and reverse bias appear near linear. Surface leakage should, like all surface related mechanisms, obey a linear relationship with contact diameter (from the circumference) and the conductance density would then increase $(dJ/dV) \propto 1/d$ as shown in Figure 130a. Scaling of the conductance density occurs according to the circumference in relation to the nanocontact area. Surface related electron-hole recombination does not fit with the expected small depletion region of the disordered nanoparticle form and the linear I-V characteristics.

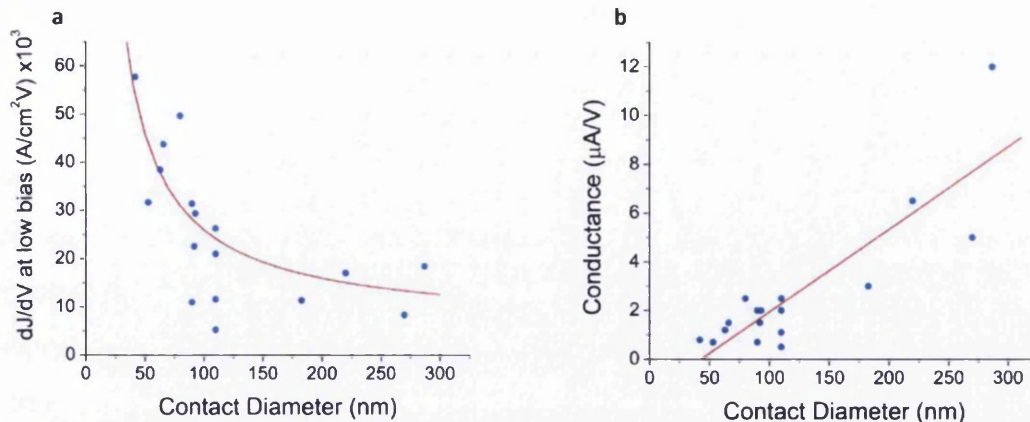

Figure 130. **a)** The conductance density of the deposited contacts with a surface related estimated fit proportional to the inverse of the diameter, a similar fit has been used to explain surface related electron-hole recombination in Ge NWs[21] however this could also apply to surface leakage from the contact and NW bypassing the potential barrier in reverse bias which provides more Ohmic like conduction[199] and, **b)** a linear like increase of conductance with diameter.

The spread in values is largely due to inaccuracy of probe positioning however the results of Figure 130a provide a reasonable fit to the circumference. The least squares linear fit of the conductance against diameter (Figure 130b) may indicate a point of transition where the conductance tends to a minimum as the NW approaches 35nm.

The role of surface leakage has been attributed to the reduction in conductivity of clean contacts exposed to residual gases over time.[62] The slow adsorption of gases is shown to reduce the conductance density of nanoisland Schottky contacts by modifying the surface state conduction and leaving only conduction through the space-charge region. The surface properties are altered by the slow exposure to gases, however consideration for surface depletion is not given which could deplete the semiconductor beneath the nanoisland and reduce the conductivity. All of the NWs here have been exposed to atmosphere and were not initially 'clean' surfaces and will have a surface depletion layer even under the deposited contacts. This does not discount possible surface conduction and surface leakage as influential mechanisms for all of the contacts. Although surface depletion is evident – a surface related conduction mechanism is also apparent, although this does not govern the catalytic Au contact behaviour.

The non-catalysed NWs measured here are close to the end-bonded NW model system, Figure 128, however the current density increase is seen at a larger NW diameter, perhaps revealing a greater extent of the surface depletion. The recombination model relies on a decreasing recombination time scale (such that $(dJ/dV) \propto 1/d$) as more surface

recombination contributes with decreasing diameter. Electron-hole recombination is more frequently associated with large Schottky barrier heights and semiconductors of relatively small bandgap as the case is with Au-Ge, but not with the large bandgap of ZnO.[247] The nanometre scale contacts, relatively small depletion regions and low intrinsic carrier concentration make the number of recombination centres small which reduce the likelihood of recombination as a significant conduction mechanism[16,62]. Although, recombination centre's on the surface may have increasing effect. The transport process around the barrier is not clear but it appears likely there is a substantial surface influence on the two-probe results, and we can conclude the surface influence of nanostructures affects not only the bulk properties of the material but also the contacts formed. Surface conduction provides a bypass when the current is against the reduced barrier which is formed by the disordered Au nanoparticle contact pad and pinning at the interface from surface adsorbates.

7.6 Conclusions

The four-probe results show increasing NW resistivity with decreasing diameter as a surface depletion layer consumes greater proportions of the conductive channel. The surface depletion region that is a major influence on the NW resistivity's and spread is explained by a balance of trapped surface charge and initial NW n-type doping. We have also shown NWs of different growth methods have similar resistivity characteristics. It was possible to uncover these properties because the NWs were measured without intermediate processing that will change or passivate the surface effect e.g. no processing to disperse the NWs or to fabricate contacts. Considerable surface roughness that can increase the trap state density was shown not to be a common characteristic of the NWs; the majority were smooth surfaced. The spread and increase with diameter in resistivity occurred independently to substantial differences in surface morphology. Our consistent measurement and preparation methods therefore allow an assumption that the surface trap state density of the NWs is approximately similar and the resistivity spread is more influenced by the NW doping. This increases the likelihood that doping variations from NW to NW are significant. However, the four-probe measurements allowed the conclusion that the NWs measured in free-standing vertical configuration had reliable contacts because they had little or no

surface depletion. Therefore, the NWs discussed in the two-probe measurements were at the high end of ZnO NW doping range.

Increasing resistivity with decreasing diameter does not appear to agree with two-probe measurements of the deposited Au contacts on non-catalysed NWs that show increasing conductance density with decreasing diameter. A combined depletion of the contact and surface impinge further on tunnelling current as the NWs decrease in size. For clean and intimate Au-ZnO contacts a large barrier is formed and at room temperature thermionic emission would not contribute significantly to the current. However, for the deposited contacts the I-V characteristics show in forward bias a near linear relationship and the nanoparticle structure of the contacts suffers from grain boundaries, nanoparticles forming around the contact edge and probable Fermi-level pinning due to adsorbed species. The structural characterisation of the deposited contacts shows a metal layer composed of many nanoparticles that in the absence of pinning would each form a narrow or low barrier easily tunnelled through or surmounted. These features all greatly affect the potential barrier that provides restriction to current flow and the transport across the barrier is simultaneously tunnelling and thermionic emission. Reverse bias displays a small barrier observable in the I-V characteristics (Figure 115) that is easily overcome with increasing reverse bias and the complete I-V curve is near linear. The barrier is bypassed in the reverse bias by a surface conduction mechanism, likely to be a combination of Au deposits and surface state conduction. Surface conduction becomes more influential in the I-V characteristics as the diameter of the NWs decreases and the conductance density increases. Deposited contacts provide repeatable and consistent behaviour desirable for Ohmic contact and charge injection with a metal that can also be used for rectifying contacts.

Contact measurements of the large 59nm catalyst particle that covers most of the top NW facet had similar current density to the deposited contacts. The smaller depletion regions of the smaller catalyst particles allow much greater current density due to the thinner barrier and increased tunnelling. Tunnelling occurs as a result of the contact depletion that no longer depends on the bulk semiconductor properties and presents a very thin barrier near the contact edge. The depletion width is influenced by the particle size and edge effects that effectively reduce the barrier and the extent of the depletion region to allow the overall conduction to be dominated by TFE and FE.

Decreasing the catalyst particle interface relative to the NW decreases the size of the depletion region.[60,201] The difference in size between the NW and the particle decouples the depletion region from the NW surface and the interface becomes more like a nanoparticle on a planar semiconductor[60,194,195] which allows substantial tunnelling and very high current densities.[60,62] NWs are known to exhibit extraordinary current densities before failure for example, gold NWs[250] of 55nm diameter failed at $5x10^8Acm^{-2}$, NiSi NWs of various sizes reputably failed >$3x10^8Acm^{-2}$ and Au catalyst contact on Ge NWs exhibited current densities (extrapolated to 1V) of >$5x10^6Acm^{-2}$. This compares $2x10^6Acm^{-2}$ at 1V for the 37nm catalyst particle and the very short total measurement time of 1 second avoids errors generated by Joule heating.[250]

Surface related mechanisms, combined with the main transport mechanisms of thermionic emission and tunnelling, apply to ZnO NWs with deposited contacts. Surface conduction did not have a significant influence in the measurement of the catalysed Au contacts and the change in behaviour from rectifying to Ohmic occurred independently of NW size. This rules out any noticeable in influence of surface conduction, and we have shown instead, the transport is dominated by tunnelling. A contact-size dependent barrier allows significant tunnelling in the region of the contact edge that becomes most influential below the characteristic length scale (~25nm contact radius) of the system. The regime investigated here furthers our knowledge of NW and nanoscale contacts beyond recent work by Leonard et al and Hu et al who consider only contacts of the same size as the NW.[21,200]

Catalysed NW contacts of rectifying or low-resistance Ohmic nature are possible by controlling the Au particle size and for contacts below ~60nm in diameter the depletion region allows tunnelling to dominate and current densities can be very high. Both contact schemes demonstrate methods for controlling the contact characteristics for vertical NW arrays without substantial processing.

Chapter 8

8 Conclusions

ZnO NWs from initial growth experimentation and optimisation have been thoroughly characterised both structurally and electrically. The major finding in the results is the size dependence of Au catalyst particle contact transport behaviour and NW electrical properties that are dominated by the surface. Structural characterisation revealed the high quality of NWs from vapour phase and hydrothermal growth that translated to similar measurements of NW resistivity. We have confirmed as far as possible that no Au catalyst contaminates ZnO NWs, and in this respect they are in advantage against commonly used Silicon or GaAs NWs. Within the limits of atomic resolution HAADF the interface of the catalyst particle and the NW is abrupt, clean and intimate, with no Au diffusion, interfacial layers or roughness. TEM and STEM reveal the ZnO is epitaxial with the Au catalyst which is solid during growth. Using fabrication and contamination free nanoprobe measurements in UHV the transition of rectifying to Ohmic contacts is dependent on contact size and not the contact materials or structural variations, even when a large potential barrier is present. Au can form an Ohmic contact to a ZnO NW when the particle is <40nm in diameter, above this the contact becomes more rectifying as the particle increases in size, at 60nm diameter the contact is strongly rectifying. We have shown this with the application of the nanoprobe on free standing as-grown catalysed ZnO NWs.

The four-probe results show increasing NW resistivity with decreasing diameter as a surface depletion layer consumes greater proportions of the conductive channel, this fact does not appear to agree with the increasing conductance density of the deposited contacts. The combined depletion of the contact and surface should impinge further on tunnelling as the NW decreases in size. An inverse relationship with the NW diameter shows the increasing conductance density must be related to the surface which has greater influence on the smaller NWs combined with the main transport mechanisms of thermionic emission and tunnelling which overcome the weak barrier. On the basis of experimental evidence it was postulated the deposited contacts were dominated by the presence of strong Fermi-level pinning and a metal layer composed of many nanoparticles each forming a thin barrier that

is easily tunnelled through or surmounted. Thermionic emission and tunnelling can combine and easily overcome the weak barrier in forward bias. The size dependence of the conductance density and near Ohmic-like I-V characteristics suggests a surface conduction mode that bypasses any interface barrier but still produces a slight deviation from linear behaviour at low reverse bias.

The NW with the large 59nm catalyst particle covering most of the top facet shows similar current density to the deposited contacts. Smaller depletion regions of the smaller catalyst particles allow much greater current density due to the thinner barrier and increased tunnelling. For each contact the depletion width is influenced by the particle size and edge effects which effectively reduce the barrier and the extent of the depletion region allowing the overall conduction to be dominated by TFE and FE. As the catalyst particle interface becomes smaller relative to the NW the depletion region decreases in size.[60,201] The difference in size between the NW and the particle decouples the metal-induced depletion region from the surface state-induced depletion region and the potential energy barrier becomes more like a nanoparticle on a planar semiconductor[60,194,195] which allows substantial tunnelling and very high current densities.[60,62]

The 59nm catalyst contact is rectifying and the smaller contacts become more Ohmic. Catalysed NW contacts of rectifying or low-resistance Ohmic nature are possible by controlling the particle size – we have shown with a simplified but effective model of the size-dependent depletion region that tunnelling dominates near the edge of the contact and current densities can be very high. Both contact schemes demonstrate useful methods of contact formation to vertical NW arrays without complicated fabrication techniques and we have categorically identified and explained a regime of NW contact behaviour that is dependent on tunnelling.

8.1 ZnO nanowire growth

Vapour-phase growth of vertically aligned NWs (discussed in Chapter 5) was tailored for device fabrication and nanoprobe measurements. Extensive experiments were conducted with non-catalysed NWs, and although consistency is difficult, excellent NW arrays were achieved on metals, ITO, and roughened Sapphire. It was possible with some control to alter the growth product from a dense array to low-density vertical NWs suitable for two-probe

measurements in Chapter 7. Metal contact formation was achieved with plasma assisted PVD and thermal evaporation. Entire metal layers can be formed on the NWs that can act as a contact plane to an array, and the base metal layers as a back contact. Individual contacts to NWs can be fabricated by thermal evaporation of small quantities of Au as shown in Chapters 5 and 6.

Catalysed growth provides greater control and the Au tips, when in place, act as suitable as-grown electrical contacts. The growth experiments revealed the Au tips were not always on the NW tips and this provided some criteria for selecting structures for two-probe measurements. When Au tips are not essential, perfect arrays of dense NWs can be achieved over large areas. Excellent arrays of NWs by catalysed and non-catalysed growth methods are possible on numerous substrates, even with considerable lattice mismatch.

8.2 Transmission Electron Microscopy

TEM study of the NWs showed they are single crystal and defect free. NWs from catalysed, non-catalysed and hydrothermal methods are crystallographically equivalent growing along [0001]. This is important when comparing electrical properties. Detailed study of the cross-sectional characteristics of catalysed arrays revealed scattered Au particles and a substantial base growth layer. An epitaxial layer of ZnO grows on the a-plane Al_2O_3 but has considerable crystal defects; however, these do not transmit to the NWs. The Au particles which cover a large size range are also found embedded in the ZnO layer and significant depletion regions could result from these nanoparticles.

Au contacts deposited on non-catalysed NWs by evaporation were also examined by TEM. The analysis revealed a thin layer of nanoparticles on top of the (0001) facet of the NWs, nanoparticles wrapping around the edge and a thin scattering on the NW sides. Au particles on catalysed NWs reveal a single nanoparticle, often single crystal, with the {111} lattice planes aligned with (0001) of ZnO suggesting they are epitaxial. Even in polycrystalline catalyst particles some crystallites still hold this relationship.

8.3 Scanning Transmission Electron Microscopy

High resolution examination of the Au particle interface with the ZnO NW is also in agreement with the alignment of the Au single crystal particle lattice with (0001) of the NW. The Au lattice spacing measurements agree with the a-lattice constant of the Au cubic

structure. This alignment must stem from the epitaxy of the ZnO with the Au which strongly suggests the particle is solid during growth, and growth proceeds by surface diffusion of Zn around the Au, via a Vapour-Solid-Solid process.[103,125] A disordered growth meniscus on the Au surface is strong evidence to substantiate this along with the alignment of the Au{111}||ZnO(0001) displayed by the single crystal catalyst particles along with the major crystallites when the Au is polycrystalline.

Au catalyst on ZnO NWs, contrary to many other semiconductor NWs[15,136,137], does not diffuse or become incorporated into the ZnO. No Au was found by atomic resolution high angle annular dark field (HAADF) imaging on the surface or within the bulk of any ZnO NWs. The interface is abrupt with no interfacial layer or diffusion gradient of Au and there is no presence of Zn within the Au particle; no substantial alloying was confirmed by TEM-EDX analysis and HAADF imaging. A structurally homogenous interface with no defects, with quality that surpasses even vacuum formed contacts on atomically clean surfaces, all but confirms the interface as 'atomically' abrupt, 3D tomography studies are required to state this. However, with no alloying, diffusion or interfacial layer the interface can be considered as an ideal intimate electrical contact.

Detecting Au within the ZnO matrix is challenging for HAADF imaging even with the atomic number of Au being much greater than Zn. No excess imaging intensity was found during catalysed NW analysis, as such it was necessary to justify the imaging technique for these particular materials. QSTEM[65] was employed to simulate the presence of single Au atoms at various depths within ZnO slabs. The results showed if the Au was on or near to the exit surface, a substantial image intensity increase would be seen. To cover these possibilities through-focal series imaging depth-sections of the NWs were taken using the distinct advantage of the large convergence angles of aberration corrected STEM. To reduce the impact of beam channelling along the ZnO atomic columns imaging was also performed with tilt slightly away from the zone axis. This however did not reveal considerable atomic intensity increases with images comparable to the control non-catalysed sample.

8.4 Four probe electrical measurements

Having determined the crystallographic equivalence of the NWs from three growth methods comparison of the bulk electric properties could be accurately attributed to surface and bulk

phenomena. 40 NWs from catalysed, non-catalysed and hydrothermal growth displayed the same spread in resistivity and increasing relationship with decreasing diameter. We have shown there is no Au within the NWs which is consistent with the four-probe measurements that showed the NWs had similar resistivity across the three growth methods. The increasing resistivity is attributed to the increasing influence of the surface which suffers from depletion due to the presence of surface adsorbates such as O^-, H^- and O^{2-} which deplete the NW of charge carriers inducing surface band bending. As the overall diameter of the NW decreases the depletion consumes proportionally more of the conductive core restricting current flow. However, as a spread in doping in ZnO NWs is common[18], even in NWs from within the same array, the resulting resistivity is shown to vary from 0.01 Ωcm - 1 Ωcm. The measurements have significantly narrowed the resistivity range of ZnO NWs to an inherent spread symptomatic of the balance in surface and bulk properties. ZnO NWs are conductive and suitable as semiconductor device structures, the surface sensitivity is a means to tailor the properties, or to detect minute levels of atoms or particles.

The Four-probe measurements display a spread of resistivity across NW growth modes which is an expression of the shifting balance between surface trap states and doping density. Fundamentally we have shown the four-probe technique to provide repeatable consistent measurements at several separations on the same NW and these measurements obey Ohm's law.

8.5 Two probe electrical measurements

Two-probe measurements revealed very different transport behaviour across the fabricated and as-grown contacts. Non-catalysed deposited contacts show Ohmic behaviour which is likely a result of Fermi-level pinning at the interface and a surface conduction component that was revealed by a zero bias differential conductance which holds an increasing relationship $\propto 1/d_{NW}$. Current along the easy surface conduction route in reverse bias bypasses any remaining interface barrier and the deposited contacts are then nearly Ohmic in nature.[62,199]

Catalysed as-grown contacts reveal a size dependent behaviour which spans the regime between 'nanoparticle on a plane' and an 'end bonded NW' contact formed by the Au catalyst particle on the NW (0001). The contact becomes less rectifying as the particle

diameter is reduced from 59nm to 47 nm and then becomes Ohmic when of size 37nm. Modelling by Smit et al of such small particles shows the depletion region no longer depends on the semiconductor properties but on the size of the contact. When the contact is reduced in size the depletion region scales with the contact and the transport is driven by the depletion region that is very narrow near the contact edge. Tunnelling is accentuated by the additional edge effects which induce high electric fields that thin the already narrow depletion region. Smit et al showed a restricted depletion region with a small overhang at the contact edge[60]. When the depletion shape is coupled with a high electric field a locally thin Schottky barrier allows a tunnelling window to open in the contact periphery that dominates regardless of the large barrier height. This is modelled with a combination of Thermionic-field Emission and Field Emission near the contact edge in a window that increases with applied bias spreading the current across the contact area. These results greatly influence recent models of the Au-NW contact which rely on surface recombination modes to explain size dependent behaviour[21] or strong rectifying properties on all Au particles for device output[29].

ZnO NWs from the most common growth methods have been thoroughly characterised to allow the interpretation of electrical measurements of resistivity and Au end contacts. The size dependent behaviour of the contacts to ZnO NWs provides the necessary knowledge to fabricate ZnO NW devices with controlled properties and function. This overcomes a major step in producing nanodevices without complicated or difficult processing steps. A nanodevice can be fabricated from a substrate, with contacts, in one-step and with controlled contact properties by controlling the catalyst particle size.

8.6 Further work

There are many interesting and appropriate ways to further the study completed here. Most of these, especially those specific to each technique are listed at the end of each relevant chapter. However to gain a deeper understanding of the ZnO NWs and the measurements made already we can make full use of the nanoprobe and the knowledge of the NWs acquired:

1. Perform back-gated FET measurements with the nanoprobe and correlate to four-probe measurements to investigate the role of doping concentration on resistivity.

These measurements will reveal the extent of doping variation from NW-to-NW and the impact this has on the resistivity magnitude spread measured here. A slightly more challenging experiment could be to expose the NWs to a gas, such as O_2, in the nanoprobe chamber and repeating the above measurements. To gain the most useful information it would be necessary to also perform measurements on the NW after baking in-situ and cooling to remove adsorbed water and gas species, this could be considered a datum point for ZnO NWs. These experiments will reveal the full extent of the surface on the bulk conduction properties and how the doping concentration counteracts the surface depletion. To complete the characterisation conduction mechanisms could be studied at low temperatures.

2. Complete a comprehensive set of experiments detailing the electrical behaviour of Au catalysed contacts with NW size and surface depletion. In their bare, 'as-prepared' state the Au contact measurements should be correlated to the overall NW diameter. Introducing gases into the chamber would allow measurement of the influence surface depletion or accumulation has on the contact characteristics and current magnitudes. Also, again annealing the sample in UHV to remove surface adsorbates would allow measurements in the 'clean' state and low temperature I-V-T measurements could assess properties such as the Richardson constant. A parallel study to simulate the Au contact – NW system by applying the Poisson equation to the case of a contact smaller than the NW diameter would provide a crucial insight[21].
3. A very worthwhile but difficult study would be to apply high resolution STEM to study the effects of large currents on the ZnO NWs and the ZnO NW-Au interface. Studying NWs inspected at the atomic level that have been subjected to I-V measurements we could reveal any local changes in composition or crystal structure induced by the edge effects, large current densities and point contact probe tips. This would require the use of the nanoprobe to initially conduct the measurements of the contacts and then to remove the NW from the array and transfer it to a suitable TEM grid.

Specific experiments for each technique are now briefly listed.

8.6.1 Further work: nanowire growth

- AFM of roughened substrates before every growth and correlate to NW morphology, base layer thickness and etching procedure.
- Detailed cross-sectional TEM study to examine the structure of the base layer and all sub-layers such as metals used to investigate the structural and compositional form.[108]
- Doping of the growth to achieve a p^+ or n^+ base growth, p^+ or n^+ NWs and combinations of these
- Electrical measurement of the metal-semiconductor-metal structure fabricated from NWs and metals deposition
- Control the catalyst particle size with monodisperse Au nanoparticles and tailor the NW diameter with growth parameters. This could be used to refine the NW-Au diameter ratio, contact diameter and therefore the contact behaviour.

8.6.2 Further work: TEM and HAADF-STEM

- 3-D reconstruction tomography of the NWs, Au particles and pads, and the resulting interface
- Scanning Auger Microscopy of the base layer to inspect diffusion of substrate elements into the NW array at low concentration levels
- FIB section analysis of non-catalysed NW arrays to investigate the wetting layer apparent from cross-section SEM
- 3-D imaging reconstruction[133] of the Au catalyst interface and HAADF imaging on different zone axes
- Analyse ZnO catalysed nanostructures of different growth orientations, such as NBs, with different catalyst metals for alloying, interdiffusion and catalyst impurities
- Attempt a cross-section of a NW array for high-resolution HAADF analysis of Au atomic incorporation in the base growth – very difficult due to the contamination created by the FIB process
- High resolution HAADF imaging of defective ZnO NWs and Au
- High resolution HAADF imaging with no initial 120°C bake
- Atom probe tomography of a catalysed ZnO NW

- HAADF imaging and EDX at SuperSTEM of the Au catalyst-NW interface after measurement and characterisation with the nanoprobe

8.6.3 Further work: Four-probe measurements

- Heat the NW samples in-situ to remove adsorbed gases to reveal the intrinsic effect of surface states on conductivity, and then introduce pure gases to measure the effect of surface depletion or accumulation
- Surface treatment, such as with solvents, to investigate the influence on transport characteristics along with surface doping[17] to tailor the surface effect on conductivity
- Measure doping levels of many NWs from one growth with nanoprobe back gated FET measurements and correlate to the NW resistivity
- Low-temperature four probe and contact measurements to investigate transport mechanisms

8.6.4 Further work: Two-probe measurements

- TEM of Au-wire contact that has been measured by the two-probe nanoprobe method to investigate any structural or local changes
- Measure the properties of NWs, such as donor density and dielectric constant to apply more detailed analysis to Schottky measurements along with the
- Measurement of the Richardson constant for a range of NW size
- Using the measured properties of the NWs analyse the catalyst particle interface in relation to size and NW diameter e.g. correlate doping to I-V characteristics
- Contact measurements before and after annealing the sample to remove adsorbed species to assess the effect of surface conduction, expose to different gases before measurement can accumulate or deplete the surface
- Numerically simulate the depletion region of the nano-sized catalyst particles including surface charge, edge effects and the catalyst particle and NW shape. Correlate the results of the full depletion model to experimental measurements. This would involve numerically solving the Poisson equation of the potential landscape in a semiconductor of confined shape with a metal contact on the tip. The NW near the tip has slightly tapered sides to the contacts edge and the contact itself has high curvature near the junction with the NW. By solving the Poisson equation and obtaining a transmission coefficient for the barrier shape the transport properties

can be calculated using one-dimensional quantum mechanics. The key to this is the correct modelling of the barrier and the potential effect of a high field at the contact edge which would locally contract the barrier. This would be a major advance on the work by Smit[60] and Leonard[21].

9 Appendix A – Growth parameter tables

9.1 Catalysed Growth Experiments

The table 9-A below provides parameters details and brief comments on all experiments of Au catalysed ZnO growth, these are referred to in the main text by experiment number.

Number	Furnace temp (C)	Source Quantity (g)	boat separation (cm)	Lead sample position (cm)	Growth time (mins)	Au deposition time (s)	Best Nanowire rating (1-5)	Density	NW position from CL (cm)	Comments on best growth	Other comments
36	905	1.6	4	0.5	120	30	5	High	10	V. Long >>6um 30-60nm	Au only on 2-3um NWs at 11cm
35	890	1.6	4	0.5	120	24	4	high	10	4-6um 30-60nm	Sample 3 two-probe measurements, much lower density various lengths and diameters
34	905	1.6	4	0.5	80	14	5	high	10	>5um 40nm + short thicker	thin with Au tips
33	905	1.6	4	0.5	35	14	5	med	9.5	very thin 20nm	thin Au tips
32	905	1.6	2	0.5	30	14	4	low	8	d<20nm	Au tips
31 GaN	905	1.6	6	0.5	35	14	3	low	11	d<20nm whips + flags	Au tips
30	905	1.6	2	0.5	35	14	4	low	8	20-50nm	au tips, walls
29	905	1.6	6	0.5	45	24	1	n/a	n/a	n/a	big Au particles
28	905	1.6	2	0.5	35	24	5	low	8	1-2um 30-50nm on walls	Au tips
27	905	1.6	2	0.5	25	24	2	low	7	stumps 30-50nm	
26 Si	930	1.6	0	0	45	colloid	0	n/a	n/a	lumps	
25 Si	930	0.8	0	0	45	colloid	0	n/a	n/a	lumps	
24	900	0.8	0	0	45	colloid	0	n/a	n/a	lumps	
23	900	0.8	0	0	45	24	5	high	0	2-3um 60-100nm	NWs on Walls
22	860	0.8	0	0	45	24	0	n/a	n/a	No growth	
21	880	0.8	0	0	45	24	4	?	0	1um 50-100nm	No walls
20	905	1.6	2	0.5	45	24	1	n/a	n/a	random structures	
19	895	1.6	2	0.5	60	24	5	med	7.5	1.5um	NWs on walls
18	905	1.6	2	0.5	45	24	5	low	7.5	1.5-2um	Au tips
17	895	1.6	2	0.5	45	24	5	low	7.5	1um 30-80	longer NWs Au tips
16	885	1.6	2	0.5	45	24	4	low	7.5	0.5-1.5um	Au tips
15	905	1.6	2	0.5	30	3	0	n/a	n/a	no growth	
14	885	1.6	1	0.5	45	3	0	n/a	n/a		

13	905	1.6	6	0.5	45	8	5	high	11.5	long thin	some Au tips some walls
12	895	1.6	2	0.5	45	8	5	high	7.5	2-3um 50nm	walls
11	905	1.6	4	0.5	45	8	5	high	9.5	1.5um 50-100nm	400nm walls
10 GaN	905	1.6	6	0.5	45	12	2	n/a	n/a	poor	
9 c-Al2O3	955	0.8	10	1	30	12	3	high	16	rods NWs	
8 GaN	890	1.6	5	1	30	12	0	n/a	n/a	no growth	
7 GaN	915	1.6	6	1	45	12	5	high	12	3-4um 30-60nm	walls
6 c-Al2O3	915	1.6	7	1	56	12	3	high	13	2-4um 30-50nm	tilted
5 c-Al2O3	940	1.6	10	1.5	45	12	3	high	16	4-5um 40-70nm	tilted
4 c-Al2O3	955	1.6	10	2.5	45	12	3	high	17.5	>2um 50-80nm	tilted
3 HOPG	955	1.6	10	5.5	30	12	4	low	n/a	rods	optimisation needed good signs
2 c-Al2O3	1005	0.8	14	1.5	30	12	2	low	n/a	poor	
1 c-Al2O3	980	0.8	14	0.5	30	12	2	low	n/a	poor	

Table 9-A Catalysed Growth Parameters

9.2 Non-Catalysed Growth Experiments

The table 9-B provides parameters details and brief comments on all experiments of non-catalysed ZnO growth, these are referred to in the main text by experiment number.

Number	Set temp (C)	Pressure (mbar)	Source (g)	boat separation (cm)	Lead separation (cm)	Growth time (mins)	5)	Density	[illegible] (cm)	etch time (min)	Comments on best growth	Other comments/Preparation
a-Al2O3			325 mesh									
218	1050	1.6	0.8	23	1	60	4	low	30.5	5	>4um 40nm	v. Low density vert NWs, some diagonal growth
217	1050	1.6	0.6	23	0.5	60	5	med	28.5	5	>5um 40nm	Very thin
216	1050	1.6	0.6	23	0.5	60	4	low	30	5	>8um 40-80nm	v.low density vert NWs, plus diagonal
215	1050	1.6	0.6	23	0.5	60	1	high	n/a	5	mess	
214	1050	1.6	0.6	23	0.5	60	1	high	n/a	5	messy thin NWs	
213	1050	1.6	0.6	23	1	60	4	high	31	5	tapered 3um 70nm	cooler region no mess, tapered
212	1050	1.6	0.8	23	0.5	60	4	med	31	5	5um 50-110nm	vert NW, some mess
211	1050	1.6	1	23	0.5	60	4	high	32	5	>7um 60-200nm	Large area mostly huge diameter range
210	1050	1.6	1	23	2	60	3	high	33	30	3um 100nm	tapered

209	1050	1.6	0.8	23	2	120	2	high	32	30	1um 100nm	tapered
208	1050	1.6	0.8	23	2	60	3	med	32	30	3um 100nm	patchy
207	1050	2.8	0.8	23	2	60	3	v high	30	30	>5um >150nm	overgrowth
206	1050	1.6	0.8	23	2	60	2	low	n/a	5	n/a	messy
205	1050	1.6	0.8	23	2	60	2	low	n/a	5	n/a	messy
204	1050	1.6	0.6	23	2	60	5	high	32	30	3um 70nm	uniform
203	1050	1.6	0.8	23	2	60	4	high	31	30	5um 70nm	with diagonal
202	1050	1.6	0.8	23	2	56	4	high	32	10	4um 100nm	small area
201	1050	1.6	0.8	23	2	60	2	v. Low	n/a	10	n/a	v small patches
200	1050	1.6	0.8	23	2	50	3	low	30	10	1um	poor
199	1050	1.6	0.8	23	2	60	4	n/a	31	10	3um	small patches
198	1050	1.6	0.8	23	2	60	5	high	31	10	7um 100nm	large area
Si-Cr-W-ZnO seed			**2-15um**							**Zinc Acetate in 100ml ethanol (g)**		
186	1100	1.5	0.8	23.5	1	52	3	high	32	0.11	2um 80-110nm	5 similar samples
185	1050	1.5	0.8	23.5	1	52	2	high	32	0.11	1.5um 100nm	lumpy
184	1100	1.1	0.8	23.5	3	60	2	high	32.5	0.11	2um 100nm	pointy tips
183	1100	1.6	0.8	23.5	2	60	2	high	33	0.11	2um 150nm	pointy tips
182	1100	1.7	0.8	23.5	2	60	0	n/a	n/a	0.11	no growth	
181	1050	3	0.8	23.5	1	60	1	high	n/a	0.11	mess lumpy	
180	1050	1.7	0.8	23.5	1	60	4	high	31.5	0.11	>10um 120nm	3 v good samples at rear
179	1100	1.1	0.8	23.5	1	60	5	high	32	0.11	8um 80nm	3 excellent samples
178	1050	1.1	0.8	23.5	1	60	5	high	31	0.11	6um 70-100nm	good rear but tapered
177	1050	1.1	0.8	23.5	0.5	45	3	high	31	0.11	2um 40nm	short growth
176	1100	1.1	0.8	23.5	0.5	60	4	high	33	0.11	2um 40nm	short growth

Table 9-B Non-Catalysed growth parameters referred to in the main text

9.3 Appendix B – Matlab Code

The Matlab code is the differential evolution fitting routine used to optimise the depletion region shape with R_{dep}=middep, β=bR and W_{max}=Wmid.

```
%%%%%%%% Tunnel current through 47nm contact
format    short g
clear

load d2.dat

d = d2;

% Voltage range and step size
% S.Vinc = 100;
S.Vmax = 0.25;
% V = linspace(0,S.Vmax,S.Vinc)'; % voltage

% Metal contact radius and Schottky barrier height
S.cont = (47e-9)/2; % contact radius metres
S.phi = 0.65 ; %barrier height eV
%constants
S.q = 1.6022e-19 ; %electron charge
S.Ez = 8.66; % relative permittivity ZnO
S.Ev = 8.85e-12; % permittivity vac
S.mr = 0.24 ; % relative electron mass
S.k = 1.3807e-23 ; % Boltzmann
S.T = 298 ; % temp
S.Ar = 3.2e5 ; %Ar  ZnO Richardson constant
S.Xi = 0.01; % Fermi level above CB
S.MF = 1e10;
S.n = 235;

figure(3)
plot(d(:,1), d(:,2),'o') ;

%perhaps put a minus here
i_d1 = d(:,1) > 0;
d = d(i_d1,:);
i_d1 = d(:,1) < S.Vmax;
d = d(i_d1,:);

figure(4)
plot(d(:,1), d(:,2),'o') ;
S.d1 = d;

V = S.d1(:,1); % voltage
S.V = V;

% Parameters
bR = 0.01 ;% percentage of total depletion radius that overhangs metal contact edge
middep = 20e-9  ;% span of the depletion region in middle of the trapezoidal shape
Wmid = 23.5e-9; % depletion width in middle of trapezoidal shape

P = [bR middep Wmid];
dP = P*0.9;
%%
Regions = repmat(P,2,1);
Regions(1,:) = [0.001 1e-10 21e-9];
Regions(2,:) = [0.2 (S.cont) 24e-9];

S.fname = 'T_current_DE';

P = fit_TC(Regions,S);
```

```
%%
S.V = linspace(0,S.Vmax,100)'; % voltage
Ic = T_current_1(P,S);
figure(2)
plot(S.V, Ic,'r-', d(:,1), d(:,2),'o') ;
xlim([0,S.Vmax]);
grid on
title('tunnel current')
ylabel('Current / A')
xlabel('Voltage / V')

%write out fit I-V data to file
    name='Sample_217_1Spectra #407 fit data';
    fn = strcat('C:\Users\Alex Lord\Documents\Work\Project\Labs\Omicron
measurements\October 2011\Matlab Contact fit\Rowan Optimise\',name);

    IVwrite = horzcat(S.V, Ic);
    save(fn,'IVwrite','-ASCII');

 %%%%%%%%%%%%%%%%%%%%%%%%%%%%%%%%%%%%%%%%%%%%%%%%%%%%%%%%%%%%%

function P = fit_TC(Regions,R)

dims = size(Regions);
I_D = dims(2);
FVr_minbound = Regions(1,:);
FVr_maxbound = Regions(2,:);
I_NP = 30;
I_itermax = 100;
F_weight = 0.5;
F_CR = 0.9;
F_VTR = 0;
I_strategy = 1;
I_refresh = 1;
I_plotting = 1;
I_bnd_constr = 1;
tol = 1e-10;

%-----Problem dependent constant values for plotting----------------
R.I_NP          = I_NP;
R.F_weight      = F_weight;
R.F_CR          = F_CR;
R.I_D           = I_D;
R.FVr_minbound = FVr_minbound;
R.FVr_maxbound = FVr_maxbound;
R.I_bnd_constr = I_bnd_constr;
R.I_itermax     = I_itermax;
R.I_strategy    = I_strategy;
R.I_refresh     = I_refresh;
R.I_plotting    = I_plotting;
R.tol           = tol;
R.flag          = 0;
R.F_VTR          = F_VTR;
R.sampled        = 0;
R.LHC       = 0;

%*********************************************************************
% Start of optimization
%*********************************************************************
[P,S_y,I_nf] = DE_mrb(R);
end
%%%%%%%%%%%%%%%%%%%%%%%%%%%%%%%%%%%%%%%%%%%%%%%%%%%%%%%%%%%%%%%%%%
% Parameters:
%   S              (I)    Problem data vector (must remain fixed during the
%                                  minimization). For details see Rundeopt.m.
%                     ---------members of S_struct-----------------------------------
```

```
%  fname        (I)    String naming a function f(x,y) to minimize.
%  F_VTR        (I)    "Value To Reach". deopt will stop its minimization
%                       if either the maximum number of iterations "I_itermax"
%                      is reached or the best parameter vector "FVr_bestmem"
%                    has found a value f(FVr_bestmem,y) <= F_VTR.
%  FVr_minbound (I)    Vector of lower bounds FVr_minbound(1) ... FVr_minbound(I_D)
%                                        of initial population.
%           *** note: these are not bound constraints!! ***
%  FVr_maxbound (I)    Vector of upper bounds FVr_maxbound(1) ... FVr_maxbound(I_D)
%                                        of initial population.
%      I_D          (I)    Number of parameters of the objective function.
%      I_NP         (I)    Number of population members.
%      I_itermax    (I)    Maximum number of iterations (generations).
%      F_weight     (I)    DE-stepsize F_weight from interval [0, 2].
%      F_CR         (I)    Crossover probability constant from interval [0, 1].
%      I_strategy   (I)    1 --> DE/rand/1
%      I_refresh     (I)   Intermediate output will be produced after "I_refresh"
%                iterations. No intermediate output will be produced
%                                        if I_refresh is < 1.
%
% Return value:     FVr_bestmem      (O)    Best parameter vector.
%                   S_bestval.I_nc   (O)    Number of constraints
%                   S_bestval.FVr_ca (O)    Constraint values. 0 means the
constraints
%                    are met. Values > 0 measure the distance
%                                           to a particular constraint.
%                   S_bestval.I_no   (O)    Number of objectives.
%                   S_bestval.FVr_oa (O)    Objective function values.
%                   I_nfeval         (O)    Number of function evaluations.
%
%%%%%%%%%%%%%%%%%%%%%%%%%%%%%%%%%%%%%%%%%%%%%%%%%%%%%%%%%%%%%%%%%%%%%%
function [FVr_bestmem S_bestval I_nfeval S] = DE_mrb(S)

%-----This is just for notational convenience and to keep the code uncluttered.----
----
fname        = S.fname;
I_NP         = S.I_NP;
F_weight     = S.F_weight;
F_CR         = S.F_CR;
I_D          = S.I_D;
FVr_minbound = S.FVr_minbound;
FVr_maxbound = S.FVr_maxbound;
I_bnd_constr = S.I_bnd_constr;
I_itermax    = S.I_itermax;
F_VTR        = S.F_VTR;

% d = zeros(I_itermax,4);

%-----Check input variables---------------------------------------------
if (I_NP < 5)
   I_NP = 5;
   fprintf(1,' I_NP increased to minimal value 5\n');
end
if ((F_CR < 0) || (F_CR > 1))
   F_CR = 0.5;
   fprintf(1,'F_CR should be from interval [0,1]; set to default value 0.5\n');
end
if (I_itermax <= 0)
   I_itermax = 200;
   fprintf(1,'I_itermax should be > 0; set to default value 200\n');
end

%-----Initialize population and some arrays-------------------------------
FM_pop = zeros(I_NP,I_D); %initialize FM_pop to gain speed

%----FM_pop is a matrix of size I_NPx(I_D+1). It will be initialized------
```

```
%----with random values between the min and max values of the------------
%----parameters----------------------------------------------------------

for k = 1:I_NP

   FM_pop(k,:) = FVr_minbound + rand(1,I_D).*(FVr_maxbound - FVr_minbound);

end

FM_popold     = zeros(size(FM_pop));     %#ok<NASGU> % toggle population
FVr_bestmem   = zeros(1,I_D);            %#ok<NASGU> % best population member ever
FVr_bestmemit = zeros(1,I_D);    %#ok<NASGU> % best population member in iteration
I_nfeval      = 0;                       % number of function evaluations

%------Evaluate the best member after initialization---------------------

I_best_index   = 1;                    % start with first population member
S_val      = feval(fname,FM_pop(I_best_index,:),S);

S_bestval = S_val(1);                  % best objective function value so far
I_nfeval  = I_nfeval + 1;

% d(1,:) = S_bestval;
% d(1,:) = realsqrt(sum(FM_pop.^2,2)');

for k = 2:I_NP                           % check the remaining members

   S_val(k)  = feval(fname,FM_pop(k,:),S);
   I_nfeval  = I_nfeval + 1;

   if (left_win(S_val(k),S_bestval) == 1)
      I_best_index   = k;              % save its location
      S_bestval      = S_val(k);
   end

end

FVr_bestmemit = FM_pop(I_best_index,:); % best member of current iteration
S_bestvalit   = S_bestval;      %#ok<NASGU> % best value of current iteration

FVr_bestmem = FVr_bestmemit;             % best member ever

%------DE-Minimization---------------------------------------------
%------FM_popold is the population which has to compete. It is--------
%------static through one iteration. FM_pop is the newly--------------
%------emerging population.----------------------------------------

FM_pm1   = zeros(I_NP,I_D);   %#ok<NASGU> % initialize population matrix 1
FM_pm2   = zeros(I_NP,I_D);   %#ok<NASGU> % initialize population matrix 2
FM_pm3   = zeros(I_NP,I_D);   %#ok<NASGU> % initialize population matrix 3
FM_pm4   = zeros(I_NP,I_D);   %#ok<NASGU> % initialize population matrix 4
FM_pm5   = zeros(I_NP,I_D);   %#ok<NASGU> % initialize population matrix 5

FVr_rot  = (0:1:I_NP-1);      % rotating index array (size I_NP)
I_iter = 1;

while ((I_iter < I_itermax) && (abs(S_bestval.FVr_oa(1) - F_VTR) > S.tol))

   FM_popold = FM_pop;                        % save the old population
   S.FM_pop = FM_pop;
   S.FVr_bestmem = FVr_bestmem;

   FVr_ind = randperm(4);                     % index pointer array

   FVr_a1  = randperm(I_NP);                    % shuffle locations of vectors
   FVr_rt  = rem(FVr_rot+FVr_ind(1),I_NP);      % rotate indices by ind(1) positions
```

```
   FVr_a2  = FVr_a1(FVr_rt+1);                  % rotate vector locations
   FVr_rt  = rem(FVr_rot+FVr_ind(2),I_NP);
   FVr_a3  = FVr_a2(FVr_rt+1);

   FM_pm1 = FM_popold(FVr_a1,:);               % shuffled population 1
   FM_pm2 = FM_popold(FVr_a2,:);               % shuffled population 2
   FM_pm3 = FM_popold(FVr_a3,:);               % shuffled population 3

   % all random numbers < F_CR are 1, 0 otherwise
   FM_mui = rand(I_NP,I_D) < F_CR;
   % inverse mask to FM_mui
   FM_mpo = not(FM_mui);

%     DE/rand/1
      FM_ui = FM_pm3 + F_weight*(FM_pm1 - FM_pm2);    % differential variation
      FM_ui = FM_popold.*FM_mpo + FM_ui.*FM_mui;      % crossover
      FM_origin = FM_pm3;

   %-----Select which vectors are allowed to enter the new population------------
   for k = 1:I_NP

      %=====Only use this if boundary constraints are needed==================
      if (I_bnd_constr == 1)
         for j = 1:I_D %----boundary constraints via bounce back-------
            if (FM_ui(k,j) > FVr_maxbound(j))
               FM_ui(k,j) = FVr_maxbound(j) + rand*(FM_origin(k,j) -
FVr_maxbound(j));
            end
            if (FM_ui(k,j) < FVr_minbound(j))
               FM_ui(k,j) = FVr_minbound(j) + rand*(FM_origin(k,j) -
FVr_minbound(j));
            end
         end
      end
      %=====End boundary constraints==========================================

      S_tempval = feval(fname,FM_ui(k,:),S);            % check cost of competitor
      I_nfeval  = I_nfeval + 1;

      if (left_win(S_tempval,S_val(k)) == 1)

         FM_pop(k,:) = FM_ui(k,:);  % replace old vector with new one (for new
iteration)
         S_val(k)   = S_tempval;            % % save value in "cost array"

         %----we update S_bestval only in case of success to save time-----------

         if (left_win(S_tempval,S_bestval) == 1)
            S_bestval = S_tempval;                     % new best value
            FVr_bestmem = FM_ui(k,:);       % new best parameter vector ever
         end

      end
   end

   S.err0r(I_iter) = S_bestval.FVr_oa(1); % keep err0r

   %----Output section-----------------------------------------------------------
   % removed
   I_iter = I_iter + 1;
end %---end while ((I_iter < I_itermax) ...

end

function S_MSE = T_current_DE(P,S)
```

```
%%
N_V = numel(S.V);

Ic = T_current_1(P,S);

dy = (S.d1(:,2)-Ic)*S.MF;
F_cost = sum((dy.*dy))/N_V;

%----strategy to put everything into a cost function-----------
S_MSE.I_nc      = 0;%no constraints
S_MSE.FVr_ca    = 0;%no constraint array
S_MSE.I_no      = 1;%number of objectives (costs)
S_MSE.Ic = Ic;
S_MSE.FVr_oa(1) = F_cost;

End

function Ic  = T_current_1(P,S)

%%
N_V = numel(S.V);

bR = P(1);
middep = P(2);
Wmid = P(3);

R = S.cont*( 1 + bR );  % total depletion radius at interface with metal
ang = atan(Wmid/(R-middep));  % angle of depletion trapezoid sides   \_/
t_ang = tan(ang);

Ic = zeros(N_V,1);
qkT = S.q/(S.k*S.T);

n = S.n;   % number of segments the depletion region is split for each voltage step
S.step = S.cont/n;        % the size of each step relative to the metal contact
radius, not the depletion radius at interface
cenwid = round(n*(middep)/S.cont); % number of steps for middle depletion section
where W is constant

i_n = (1 : n)';
S.r = i_n*S.step;

W = ones(n,1)*Wmid;
Wi = i_n > cenwid;
W(Wi) = t_ang*(R - S.r(Wi));

for ii = 1: N_V     % sum over the voltage range

    S.v = S.V(ii);

    Nd = 2*S.Ez*S.Ev*S.phi./(W.*W*S.q) ;  % doping for which  cirrespond to
depletion width W
    S.E00 = (18.5e-15).*sqrt( Nd/(S.mr*S.Ez) ) ;    % tunnelling parameter
    S.E0 = S.E00.*coth(qkT*S.E00);           % Thermionic Field Emission parameter

    % calculate the current for this step

    [v1, v2, Itfe, v3, Ibits] = current_1(S);

    % total current across contact at voltage step
    Ic(ii) = Itfe;

end ; % for i, move on to next voltage step

end
```

```
function [Istep, i_ck, Itfe, Js] = current_1(S)

qkT = S.q/(S.k*S.T);

i_ck = qkT*S.E00 < 2.7;

pvX = (S.phi - S.v)/S.Xi;

%     %calculate the saturation Js term, split into bits
    JsNum = 2*pi*S.Ar*S.T*S.q*S.E00.*exp(-S.phi./S.E00);          % numerator
    JsDen1 = S.k*log(2*pvX);                          %demoninator 1
    JsDen2 = sin(pi*S.k*S.T*log(2*pvX)./(2*S.q*S.E00))    ; %denominator 2
    Js = JsNum./(JsDen1.*JsDen2); %  full FE Js term
    Istep = 2*pi*Js.*exp( S.v./S.E00 ).*( 1 - exp( -qkT*S.v ) ).*S.r*S.step; %

    %TFE applies in regions of larger W, linked to Nd and E00

    t1 = S.q*S.T*S.Ar./( S.k*cosh(qkT*S.E00) );
    t2 = sqrt( pi*S.E00*(S.phi - S.v + S.Xi) );
    t3 = exp( qkT*S.Xi - (S.phi+S.Xi)./S.E0);
    Js1 = t1.*t2.*t3;
    Js(i_ck)  = Js1(i_ck);
    %Full TFE Js term
    %current over area 2pi*r*dr

    Istep = 2*pi*Js.*exp( S.v./S.E0 )*( 1-exp( -qkT*S.v ) ).*S.r*S.step;

    Itfe = sum(Istep);% count total TFE current


end
```

10 References

1. Sandhu, A. Who invented nano? *Nature Nano.* **1**, 87 (2006).

2. Hunter, R. J. *Introduction to Modern Colloid Science*. (Oxford Science Publications: 1998).

3. Kroto, H. W., Heath, J. R., O'Brien, S. C., Curl, R. F. & Smalley, R. E. C60: Buckminsterfullerene. *Nature* **318**, 162–163 (1985).

4. Monthioux, M. & Kuznetsov, V. L. Who should be given the credit for the discovery of carbon nanotubes? *Carbon* **44**, 1621–1623 (2006).

5. Ozgur, U. *et al.* A comprehensive review of ZnO materials and devices. *J. Appl. Phys.* **98**, 41301 (2005).

6. Pamplin, B. R. *Crystal Growth*. (Pergammon Press: 1975).

7. Meyer, J. C. *et al.* The structure of suspended graphene sheets. *Nature* **446**, 60–63 (2007).

8. Bates, D. S. P. Silicon Wafer Processing. (2000). at http://www.engr.sjsu.edu/sbates/images/materials%26plastics/Silicon_Wafer_Processing.pdf

9. Corporation, R. I. Quartz General Material Specification. (2007). at http://www.roditi.com/SingleCrystal/Quartz/QuartzHead.htm

10. Briseno, A. L. *et al.* Patterning organic single-crystal transistor arrays. *Nature* **444**, 913–917 (2006).

11. Stauth, S. A. & Parviz, B. A. Self-assembled single-crystal silicon circuits on plastic. *Proc. Natl. Acad. Sci.* **103**, 13922–13927 (2006).

12. Michalet, X. *et al.* Quantum Dots for Live Cells, in Vivo Imaging, and Diagnostics. *Science* **307**, 538–544 (2005).

13. Iijima, S. Helical microtubules of graphitic carbon. *Nature* **354**, 56–58 (1991).

14. Wagner, R. S. & Ellis, W. C. Vapor-liquid-solid mechanism of single crystal growth. *Appl. Phys. Lett.* **4**, 89–90 (1964).

15. Allen, J. E. *et al.* High-resolution detection of Au catalyst atoms in Si nanowires. *Nature Nano.* **3**, 168–173 (2008).

16. Smit, G., Rogge, S., Caro, J. & Klapwijk, T. Conductance distribution in nanometer-sized semiconductor devices due to dopant statistics. *Phys. Rev. B* **69**, 035338 (2004).

17. Zhang, S. *et al.* Relative influence of surface states and bulk impurities on the electrical properties of Ge nanowires. *Nano Lett.* **9**, 3268–74 (2009).

18. Hong, W. *et al.* Tunable Electronic Transport Characteristics of Nanowire Field Effect Transistors 2008. *Nano Lett.* **8,** 950-956 (2008).

19. Léonard, F. & Talin, A. A. Electrical contacts to one- and two-dimensional nanomaterials. *Nature Nano.* **6,** 773–83 (2011).

20. Léonard, F. & Talin, A. Size-Dependent Effects on Electrical Contacts to Nanotubes and Nanowires. *Phys. Rev. Lett.* **97,** 026804 (2006).

21. Léonard, F., Talin, A., Swartzentruber, B. & Picraux, S. Diameter-Dependent Electronic Transport Properties of Au-Catalyst/Ge-Nanowire Schottky Diodes. *Phys. Rev. Lett.* **102,** 106805 (2009).

22. Wang, Z. L. Zinc oxide nanostructures: growth, properties and applications. *J. Phys. Cond. Matter* **16**, R829–R858 (2004).

23. Fan, Z. & Lu, J. G. Zinc Oxide Nanostructures: Synthesis and Properties. *J. Nanosci. Nanotechnol.* **5**, 1561–1573 (2005).

24. M. H. Huang H. Feick, N. Tran, E. Weber, P. Yang,, Y. W. Catalytic Growth of Zinc Oxide Nanowires by Vapor Transport. *Adv. Mater.* **13**, 113–116 (2001).

25. Baruah, S. & Dutta, J. Hydrothermal growth of ZnO nanostructures. *Sci. Tech. Adv. Mater.* **10,** 13001 (2009).

26. Weber, B. *et al.* Ohm's law survives to the atomic scale. *Science.* **335,** 64–67 (2012).

27. Wang, X., Song, J., Liu, J. & Wang, Z. L. Direct-Current Nanogenerator Driven by Ultrasonic Waves. *Science* **316**, 102–105 (2007).

28. Ajayan, P. M. & Tour, J. M. Materials Science: Nanotube composites. *Nature* **447**, 1066–1068 (2007).

29. Wang, Z. L. & Song, J. Piezoelectric Nanogenerators Based on Zinc Oxide Nanowire Arrays. *Science* **312**, 242–246 (2006).

30. Hollister, M. A., Le, J. D., Guanghua, X., Xuekun, L. & Kiehl, R. A. High Performance ZnO Nanowire FET with ITO Contacts. *Device Research Conference, 2007 65th Annual* 113–114 (2007).

31. Jeong, M.C., Ham, M.H., Lee, S.W., Myoung, J.M. ZnO-Nanowire-Inserted GaN/ZnO Heterojunction Light-Emitting Diodes. *Small* **3**, 568–572 (2007).

32. Ramgir, N. S. *et al.* ZnO Multipods, Submicron Wires, and Spherical Structures and Their Unique Field Emission Behavior. *J. Phys. Chem. B* **110**, 18236–18242 (2006).

33. Cui, J. B. *et al.* Low-temperature growth and field emission of ZnO nanowire arrays. *J. Appl. Phys.* **97**, 44315–44317 (2005).

34. Kim, D. C., Mohanta, S. K. & Cho, H. K. Vertically Aligned Ultraslim ZnO Nanowires Formed by Homobuffer: Growth Evolution and Emission Properties. *Crys. Grow. Des.* **9,** 4725-4729 (2009).

35. Mai, W. *et al.* Vertically aligned ZnO nanowire arrays on GaN and SiC substrates. *Chem. Phys. Lett.* **460**, 253–256 (2008).

36. Lu, M.-P. *et al.* Piezoelectric Nanogenerator Using p-Type ZnO Nanowire Arrays. *Nano Lett.* **9,** 1223-1227 (2009).

37. P. Yang *et al.* Controlled Growth of ZnO Nanowires and Their Optical Properties. *Adv. Func. Mater.* **12**, 323–331 (2002).

38. Xu, S. *et al.* Patterned Growth of Vertically Aligned ZnO Nanowire Arrays on Inorganic Substrates at Low Temperature without Catalyst. *J. Am. Chem. Soc.* **130**, 14958–14959 (2008).

39. Zhao, Q. X., Klason, P. & Willander, M. Growth of ZnO nanostructures by vapor–liquid–solid method. *App. Phys. A.* **88**, 27–30 (2007).

40. Li, Z. *et al.* Cellular Level Biocompatibility and Biosafety of ZnO Nanowires. *J.Phys.Chem. C* **112**, 20114–20117 (2008).

41. Chiu, S.-P., Lin, Y.-H. & Lin, J.-J. Electrical conduction mechanisms in natively doped ZnO nanowires. *Nanotechnology* **20**, 015203 (2009).

42. Xiang, B. *et al.* Rational Synthesis of p-Type Zinc Oxide Nanowire Arrays Using Simple Chemical Vapor Deposition. *Nano Lett.* **7**, 323–328 (2007).

43. Huang, M. H. *et al.* Room-Temperature Ultraviolet Nanowire Nanolasers. *Science* **292**, 1897–1899 (2001).

44. Kaciulis, S. *et al.* Nanowires of metal oxides for gas sensing applications. *Surf. Inter. Anal.* **40**, 575–578 (2008).

45. Cha, S. N. *et al.* High performance ZnO nanowire field effect transistor using self-aligned nanogap gate electrodes. *Appl. Phys. Lett.* **89**, 263102 (2006).

46. Wang, Z. L. Nanostructures of zinc oxide. *Materials Today* **7**, 26–33 (2004).

47. Hou, X. and Zhu, Y. Electronic mechanical and Piezoelectric properties of ZnO nanowires. *Appl. Phys. Lett* **89**, 223111 (2006).

48. Agrawal, R., Peng, B., Gdoutos, E. E. & Espinosa, H. D. Elasticity Size Effects in ZnO Nanowires: A Combined Experimental-Computational Approach. *Nano Lett.* **8**, 3668–3674 (2008).

49. Fan, Z., Wang, D., Chang, P.-C., Tseng, W.-Y. & Lu, J. G. ZnO nanowire field-effect transistor and oxygen sensing property. *Appl. Phys. Lett.* **85**, 5923–5925 (2004).

50. Schlenker, E. *et al.* On the difficulties in characterizing ZnO nanowires. *Nanotechnology* **19**, 365707 (2008).

51. Tsai, L.-T., Chiu, S.-P., Lu, J. G. & Lin, J.-J. Electrical conduction mechanisms in natively doped ZnO nanowires (II). *Nanotechnology* **21**, 145202 (2010).

52. Lin, X. *et al.* Intrinsic current-voltage properties of nanowires with four-probe scanning tunneling microscopy: A conductance transition of ZnO nanowire. *Appl. Phys. Lett.* **89**, 43103 (2006).

53. Chu, S. *et al.* Electrically pumped waveguide lasing from ZnO nanowires. *Nature Nano.* **6**, 506–510 (2011).

54. Woodruff, S. M. *et al.* Nickel and nickel silicide Schottky barrier contacts to n-type silicon nanowires. *J. Vac. Sci. Technol. B.* **26**, 1592 (2008).

55. Rhoderick, E. H. & Williams, R. H. *Metal-Semiconductor contacts*. (Clarendon Press: 1988).

56. Park, W. I. & Yi, G. C. Ohmic and Schottky nanocontacts on ZnO nanorods. *IEE. Conf. Publ.* **2**, 410–413 (2003).

57. Kim, K. *et al.* Contact barriers in a single ZnO nanowire device. *Appl. Phys. A.* **94**, 253–256 (2009).

58. Brewster, M. M., Zhou, X., Lim, S. K. & Gradečak, S. Role of Au in the Growth and Nanoscale Optical Properties of ZnO Nanowires. *J. Phys. Chem. Lett.* **2**, 586–591 (2011).

59. Seifert, W. *et al.* Growth of one-dimensional nanostructures in MOVPE. *J. Crys. Grow.* **272**, 211–220 (2004).

60. Smit, G. D. J., Rogge, S. & Klapwijk, T. M. Scaling of nano-Schottky-diodes. *Appl. Phys. Lett.* **81**, 3852–3854 (2002).

61. Smit, G. D. J., Rogge, S. & Klapwijk, T. M. Enhanced tunneling across nanometer-scale metal–semiconductor interfaces. *Appl. Phys. Lett.* **80**, 2568 (2002).

62. Song, J. Q., Ding, T., Li, J. & Cai, Q. Scanning tunneling microscope study of nanosized metal–semiconductor contacts between ErSi2 nanoislands and Si(001) substrate. *Surf. Sci.* **604**, 361–365 (2010).

63. Carroll, D. L., Wagner, M., Rühle, M. & Bonnell, D. A. Schottky-barrier formation at nanoscale metal-oxide interfaces. *Phys. Rev. B.* **55**, 9792–9799 (1997).

64. Walton, A. S. *et al.* Four-probe electrical transport measurements on individual metallic nanowires. *Nanotechnology* **18**, 065204 (2007).

65. Koch, C. Determination of core structure periodicity and point defect density along dislocation. PhD thesis, Arizona State Univ. (2002).

66. Mofor, A. C. *et al.* Magnetic property investigations on Mn-doped ZnO Layers on sapphire. *Appl. Phys. Lett.* **87**, 062501 (2005).

67. Morkoc, H. & Ozgur, U. *Zinc Oxide: Fundamentals, Materials and Device Technology.* (Wiley VCH: 2009).

68. Sze, S. M. *Physics of Semiconductor devices.* (Wiley-Interscience: 1981).

69. Dhananjay, Nagaraju, J. & Krupanidhi, S. B. Investigations on magnetron sputtered ZnO thin films and Au/ZnO Schottky diodes. *Physica B.* **391**, 344–349 (2007).

70. Kiyoshi Takahashi Adarsh Sandhu, A. Y. *Wide Bangap Semiconductors: Fundamental Properties and Modern Photonic and Electronic Devices.* (Springer: 2007).

71. Diebold, U., Koplitz, L. V. & Dulub, O. Atomic-scale properties of low-index ZnO surfaces. *Appl. Surf. Sci.* **237**, 336–342 (2004).

72. Baruah, S. & Dutta, J. Hydrothermal growth of ZnO nanostructures. *Sci. Technol. Adv. Mater.* **10**, 013001 (2009).

73. Kong, X. Y. & Wang, Z. L. Spontaneous Polarization-Induced Nanohelixes, Nanosprings, and Nanorings of Piezoelectric Nanobelts. *Nano Lett.* **3**, 1625–1631 (2003).

74. O'Mara, W.C., Herring, R.B. & Hunt, L.P. *Handbook of semiconductor silicon technology* . (William Andrew: 1990).

75. Dimitrijev, S. *Principles of semiconductor devices.* (Oxford University Press: 2006).

76. Golubovic, A., Djuric, S. & Valcic, A. The growth of sapphire single crystals. *J. Sehem. Soc.* **66**, 411-418 (2001).

77. Morkoc, H. *Handbook of Nitride Semiconductors and devices*. (Wiley-Vch: 2008).

78. Kyocera Corporation. Single Crystal Sapphire at http://www.kyocera.com.cn/prdct/fc/product/pdf/s_c_sapphire.pdf?q=singlecrystal

79. Fons, P. *et al.* Uniaxial locked epitaxy of ZnO on the a face of sapphire. *Appl. Phys. Lett.* **77**, 1801–1803 (2000).

80. Baxter, J. B. & Aydil, E. S. Epitaxial growth of ZnO nanowires on a- and c-plane sapphire. *J. Crys. Grow.* **274**, 407–411 (2005).

81. Riaz, M. *et al.* Buckling and mechanical instability of ZnO nanorods grown on different substrates under uniaxial compression. *Nanotechnology* **19**, 415708 (2008).

82. Park, W. I., Kim, D. H., Jung, S.-W. & Yi, G.-C. Metalorganic vapor-phase epitaxial growth of vertically well-aligned ZnO nanorods. *Appl. Phys. Lett.* **80**, 4232–4234 (2002).

83. Greene, L. E. *et al.* General Route to Vertical ZnO Nanowire Arrays Using Textured ZnO Seeds. *Nano Lett.* **5**, 1231–1236 (2005).

84. Lee, J.-B., Lee, M.-H., Park, C.-K. & Park, J.-S. Effects of lattice mismatches in ZnO/substrate structures on the orientations of ZnO films and characteristics of SAW devices. *Thin Solid Films* **447-448**, 296–301 (2004).

85. Xu, C. X. *et al.* Network array of zinc oxide whiskers. *Nanotechnology* **16**, 70–73 (2005).

86. Wang, M. *et al.* Seed-layer controlled synthesis of well-aligned ZnO nanowire arrays via a low temperature aqueous solution method. *J. Mater. Sci.* **19**, 211–216 (2008).

87. Chescoe, D. & Goodhew, P. J. *The operation of Transmission and Scanning Electron Microscopes*. (Oxford University Press: 1990).

88. Edington, W. J. *Electron Diffraction in an Electron Microscope*. (Macmillan Press: 1975).

89. Keyse, R. J. *Introduction to Scanning Transmission Electron Microscopy*. (BIOS Scientific Publishers Limited: 1998).

90. Goodhew, P. J., Humphreys, J. & Beanland, R. *Electron and Microscopy and Analysis*. (Talylor & Francis: 2001).

91. Zeghbroeck, B. Van. Principles of Semiconductor Devices. at <http://ece-www.colorado.edu/~bart/book/book/contents.htm>

92. He, J. H., Chang, P. H., Chen, C. Y. & Tsai, K. T. Electrical and optoelectronic characterization of a ZnO nanowire contacted by focused-ion-beam-deposited Pt. *Nanotechnology* **20**, 135701 (2009).

93. Zhang, Q., Qi, J., Huang, Y., Li, X. & Zhang, Y. Negative differential resistance in ZnO nanowires induced by surface state modulation. *Mater. Chem. Phys.* **131**, 258–261 (2011).

94. Liao, Z.-M., Liu, K.-J., Zhang, J.-M., Xu, J. & Yu, D.-P. Effect of surface states on electron transport in individual ZnO nanowires. *Phys. Lett. A* **367**, 207–210 (2007).

95. Tung, R. T. Schottky Barrier Tutorial. at <http://academic.brooklyn.cuny.edu/physics/tung/Schottky/index.htm>

96. Padovani, F. A. & Stratton, R. Field and thermionic-field emission in Schottky barriers. *Solid-State Elec.* **9**, 695–707 (1966).

97. Crowell, C. R. & Rideout, V. L. Normalized thermionic-field (T-F) emission in metal-semiconductor (Schottky) barriers. *Solid-State Elec.* **12**, 89–105 (1969).

98. Kim, T.-J. & Holloway, P. H. Ohmic contacts to GaAs epitaxial layers. *Crit. Rev. Solid State Mater. Sci.* **22**, 239–273 (1997).

99. Vayssieres, L. Growth of Arrayed Nanorods and Nanowires of ZnO from Aqueous Solutions. *Adv. Mater.* **15**, 464–466 (2003).

100. P. X. Gao J. Liu, Z. L. Wang,, J. S. Nanowire Piezoelectric Nanogenerators on Plastic Substrates as Flexible Power Sources for Nanodevices. *Adv. Mater.* **19**, 67–72 (2007).

101. Wan, Q. *et al.* Fabrication and ethanol sensing characteristics of ZnO nanowire gas sensors. *Appl. Phys. Lett.* **84**, 3654 (2004).

102. Young, S. J. *et al.* Nanoscale mechanical characteristics of vertical ZnO nanowires grown on ZnO:Ga/glass templates. *Nanotechnology* **18**, 225603 (2007).

103. Hofmann, S. *et al.* Ledge-flow-controlled catalyst interface dynamics during Si nanowire growth. *Nature mater.* **7**, 372–375 (2008).

104. Oh, S. H. *et al.* Oscillatory mass transport in vapor-liquid-solid growth of sapphire nanowires. *Science.* **330**, 489–493 (2010).

105. Wen, C.-Y. *et al.* Formation of compositionally abrupt axial heterojunctions in silicon-germanium nanowires. *Science.* **326**, 1247–50 (2009).

106. Y. Xia Y. Sun, Y. Wu, B. Mayers, B. Gates, Y. Yin, F. Kim, H. Yan,, P. Y. One-Dimensional Nanostructures: Synthesis, Characterization, and Applications. *Adv. Mater.* **15**, 353–389 (2003).

107. Zhu, Z., Chen, T.-L., Gu, Y., Warren, J. & Osgood, R. M. Zinc Oxide Nanowires Grown by Vapor-Phase Transport Using Selected Metal Catalysts: A Comparative Study. *Chem. Mater.* **17**, 4227–4234 (2005).

108. Lin, Y.-R. *et al.* Buffer-Facilitated Epitaxial Growth of ZnO Nanowire. *Crys. Grow. Des.* **5**, 579–583 (2005).

109. Fang, Y., Wang, Y., Wan, Y., Wang, Z. & Sha, J. Detailed Study on Photoluminescence Property and Growth Mechanism of ZnO Nanowire Arrays Grown by Thermal Evaporation. *J. Phys. Chem. C* **114**, 12469–12476 (2010).

110. Umar, A., Kim, S. H., Lee, Y. S., Nahm, K. S. & Hahn, Y. B. Catalyst-free large-quantity synthesis of ZnO nanorods by a vapor-solid growth mechanism: Structural and optical properties. *J. Crys. Grow.* **282**, 131–136 (2005).

111. Ho, S.-T. *et al.* Catalyst-Free Surface-Roughness-Assisted Growth of Large-Scale Vertically Aligned Zinc Oxide Nanowires by Thermal Evaporation. *Chem Mater.* **19**, 4083–4086 (2007).

112. Geng, C. *et al.* Well-Aligned ZnO Nanowire Arrays Fabricated on Silicon Substrates. *Adv. Func. Mater.* **14**, 589–594 (2004).

113. Fang, F. *et al.* Growth of well-aligned ZnO nanowire arrays on Si substrate. *Nanotechnology* **18**, 235604 (2007).

114. Li, C. *et al.* Effect of Seed Layer on Structural Properties of ZnO Nanorod Arrays Grown by Vapor-Phase Transport. *J. Phys. Chem. C* **112**, 990–995 (2008).

115. Li, S. Y., Lin, P., Lee, C. Y., Ho, M. S. & Tseng, T. Y. Fabrication of vertical ZnO nanowires on silicon (100) with epitaxial ZnO buffer layer. *J. nanosci. nanotech.* **4**, 968–971 (2004).

116. Song, J. & Lim, S. Effect of Seed Layer on the Growth of ZnO Nanorods. *J. Phys. Chem. C* **111**, 596–600 (2007).

117. Kim, D. S., Scholz, R., Gösele, U. & Zacharias, M. Gold at the root or at the tip of ZnO nanowires: a model. *Small* . **4**, 1615–1619 (2008).

118. Pung, S.-Y., Choy, K.-L. & Hou, X. Tip-growth mode and base-growth mode of Au-catalyzed zinc oxide nanowires using chemical vapor deposition technique. *J. Crys. Grow.* **312**, 2049–2055 (2010).

119. Hong Jin Fan *et al.* Template-Assisted Large-Scale Ordered Arrays of ZnO Pillars for Optical and Piezoelectric Applications. *Small* **2**, 561–568 (2006).

120. Jeong, J. S. & Lee, J. Y. Investigation of initial growth of ZnO nanowires and their growth mechanism. *Nanotechnology* **21**, 475603 (2010).

121. Wei, M., Zhi, D. & MacManus-Driscoll, J. L. Self-catalysed growth of zinc oxide nanowires. *Nanotechnology* **16**, 1364–1368 (2005).

122. Zhao, D. *et al.* Buffer layer effect on ZnO nanorods growth alignment. *Chem.Phys. Lett.* **408**, 335–338 (2005).

123. Levin, I., Davydov, A., Nikoobakht, B., Sanford, N. & Mogilevsky, P. Growth habits and defects in ZnO nanowires grown on GaN/sapphire substrates. *Appl. Phys. Lett.* **87**, 103110 (2005).

124. Park, D. J., Lee, J. Y., Kim, D. C., Mohanta, S. K. & Cho, H. K. Defects in interfacial layers and their role in the growth of ZnO nanorods by metallorganic chemical vapor deposition. *Appl. Phys. Lett.* **91**, 143115 (2007).

125. Kirkham, M., Wang, X., Wang, Z. L. & Snyder, R. L. Solid Au nanoparticles as a catalyst for growing aligned ZnO nanowires: a new understanding of the vapour–liquid–solid process. *Nanotechnology* **18**, 365304 (2007).

126. Kodambaka, S., Tersoff, J., Reuter, M. C. & Ross, F. M. Diameter-Independent Kinetics in the Vapor-Liquid-Solid Growth of Si Nanowires. *Phys. Rev. Lett.* **96**, (2006).

127. Dick, K. A. A review of nanowire growth promoted by alloys and non-alloying elements with emphasis on Au-assisted III-V nanowires. *Prog. Crys. Grow. Char. Mater.* **54**, 138–173

128. Adhikari, H., Marshall, A. F., Chidsey, C. E. D. & McIntyre, P. C. Germanium nanowire epitaxy: shape and orientation control. *Nano Lett.* **6**, 318–23 (2006).

129. Wang, G. T. *et al.* Highly aligned, template-free growth and characterization of vertical GaN nanowires on sapphire by metal–organic chemical vapour deposition. *Nanotechnology* **17**, 5773–5780 (2006).

130. Colli, A. *et al.* Low-temperature synthesis of ZnSe nanowires and nanosaws by catalyst-assisted molecular-beam epitaxy. *Appl. Phys. Lett.* **86**, 153103 (2005).

131. Buffat, P. & Borel, J.-P. Size effect on the melting temperature of gold particles. *Phys. Rev. A* **13**, 2287–2298 (1976).

132. Cheyssac, P., Sacilotti, M. & Patriarche, G. Vapor-liquid-solid mechanisms: Challenges for nanosized quantum cluster/dot/wire materials. *J. Appl. Phys.* **100**, 044315 (2006).

133. Hemesath, E. R. *et al.* Catalyst incorporation at defects during nanowire growth. *Nano Lett.* **12**, 167-171 (2011).

134. Oh, S. H. *et al.* Point defect configurations of supersaturated Au atoms inside Si nanowires. *Nano Lett.* **8**, 1016–1019 (2008).

135. Koren, E. *et al.* Direct measurement of individual deep traps in single silicon nanowires. *Nano Lett.* **11**, 2499–502 (2011).

136. Bar-Sadan, M., Barthel, J., Shtrikman, H. & Houben, L. Direct imaging of single Au atoms within GaAs nanowires. *Nano Lett.* **12**, 2352–6 (2012).

137. Perea, D. E. *et al.* Three-dimensional nanoscale composition mapping of semiconductor nanowires. *Nano Lett.* **6**, 181–5 (2006).

138. Krivanek, O. L., Dellby, N. & Lupini, A. R. Towards sub-Å electron beams. *Ultramicroscopy* **78**, 1–11 (1999).

139. Krivanek, O. L. *et al.* An electron microscope for the aberration-corrected era. *Ultramicroscopy* **108**, 179–95 (2008).

140. Van Benthem, K. *et al.* Three-dimensional ADF imaging of individual atoms by through-focal series scanning transmission electron microscopy. *Ultramicroscopy* **106**, 1062–1068 (2006).

141. Perea, D. E., Lensch, J. L., May, S. J., Wessels, B. W. & Lauhon, L. J. Composition analysis of single semiconductor nanowires using pulsed-laser atom probe tomography. *Appl. Phys. A* **85**, 271–275 (2006).

142. Hutson, A. R. Piezoelectricity and Conductivity in ZnO and CdS. *Phys. Rev. Lett.* **4**, 505 (1960).

143. Look, D. C. *et al.* Electrical properties of bulk ZnO. *Solid State Commun.* **105**, 399–401 (1998).

144. Van de Walle, C. G. Hydrogen as a Cause of Doping in Zinc Oxide. *Phys. Rev. Lett.* **85**, 1012–1015 (2000).

145. Janotti, A. & Van de Walle, C. G. Fundamentals of zinc oxide as a semiconductor. *Rep. Prog. Phys.* **72**, 126501 (2009).

146. Polyakov, A. Y. *et al.* Electrical properties of undoped bulk ZnO substrates. *J. Elec. Mater.* **35**, 663–669 (2006).

147. Yuan, G. D. *et al.* p-Type ZnO Nanowire Arrays. *Nano Lett.* **8**, 2591–2597 (2008).

148. Hu, Y. *et al.* Quantitative Study on the Effect of Surface Treatments on the Electric Characteristics of ZnO Nanowires. *J. Phys Chem. C* **112**, 14225–14228 (2008).

149. Mårtensson, P. & Feenstra, R. M. Geometric and electronic structure of antimony on the GaAs(110) surface studied by scanning tunneling microscopy. *Phys. Rev. B* **39**, 7744 (1989).

150. Sakurai, M., Wang, Y. G., Uemura, T. & Aono, M. Electrical properties of individual ZnO nanowires. *Nanotechnology* **20**, 155203 (2009).

151. Park, W. Il, Kim, J. S., Yi, G.-C., Bae, M. H. & Lee, H.-J. Fabrication and electrical characteristics of high-performance ZnO nanorod field-effect transistors. *Appl. Phys. Lett.* **85**, 5052 (2004).

152. Dayeh, S. A., Soci, C., Yu, P. K. L., Yu, E. T. & Wang, D. Influence of surface states on the extraction of transport parameters from InAs nanowire field effect transistors. *Appl. Phys. Lett.* **90**, 162112 (2007).

153. Sun, M. H. *et al.* Removal of Surface States and Recovery of Band-Edge Emission in InAs Nanowires through Surface Passivation. *Nano Lett.* **12**, 3378-3384. (2012).

154. Björk, M. T., Schmid, H., Knoch, J., Riel, H. & Riess, W. Donor deactivation in silicon nanostructures. *Nature Nano.* **4**, 103–7 (2009).

155. Fu, W. *et al.* Ferroelectric gated electrical transport in CdS nanotetrapods. *Nano lett.* **11**, 1913–1918 (2011).

156. Kind, H., Yan, H., Messer, B., Law, M. & Yang, P. Nanowire Ultraviolet Photodetectors and Optical Switches. *Adv. Mater.* **14**, 158–160 (2002).

157. Park, W. I., Yi, G.-C., Kim, J.-W. & Park, S.-M. Schottky nanocontacts on ZnO nanorod arrays. *Appl. Phys.Lett.* **82**, 4358–4360 (2003).

158. Zhao, J., Sun, H., Dai, S., Wang, Y. & Zhu, J. Electrical breakdown of nanowires. *Nano Lett.* **11**, 4647–4651 (2011).

159. Schottky, W. Zur Halbleitertheorie der Sperrschicht- und Spitzengleichrichter. *Zeitschrift für Physik* **113**, 367–414 (1939).

160. Mott, N. F. Note on the contact between a metal and an insulator or semi-conductor. *Math. Proc. Cam. Phil. Soc.* **34**, 568–572 (1938).

161. Bethe, H., A. No Title. *MIT Radiation Lab Rep* **43-12**, (1942).

162. Kupka, R. K. & Anderson, W. A. Minimal ohmic contact resistance limits to n-type semiconductors. *J. Appl. Phys.* **69**, 3623 (1991).

163. Tung, R. Electron transport at metal-semiconductor interfaces: General theory. *Phys.Rev. B* **45**, 13509–13523 (1992).

164. Tung, R., Levi, A., Sullivan, J. & Schrey, F. Schottky-barrier inhomogeneity at epitaxial $NiSi_2$ interfaces on Si(100). *Phys. Rev. Lett.* **66**, 72–75 (1991).

165. Yu, A. Y. C. Surface Effects on Metal-Silicon Contacts. *J. Appl. Phys.* **39**, 3008 (1968).

166. Lepselter, M., P. & Sze, S. M. Silicon Schottky Barrier Diode with near ideal I-V Characteristics. *Bell System Technical Journal* **47**, 195–208 (1968).

167. Dickie, A. & Wolkow, R. Metal-organic-silicon nanoscale contacts. *Physical Review B* **77**, 115305 (2008).

168. Dupont-Ferrier, E., Mallet, P., Magaud, L. & Veuillen, J.-Y. STM investigation of the charge transport mechanisms to nanoscale metallic islands on a semiconductor substrate. *Physical Review B* **75**, 205315 (2007).

169. Kim, H.-K., Kim, K.-K., Park, S.-J., Seong, T.-Y. & Adesida, I. Formation of low resistance nonalloyed Al/Pt ohmic contacts on n-type ZnO epitaxial layer. *J. Appl. Phys.* **94**, 4225 (2003).

170. Wen-Yan, S. & Ching-Fuh, L. Zinc Oxide Nanowires with Ultra-Thin and Low-Resistance Seed Layer. *IEE. Conf. Publ.* 193–196 (2008).

171. Kim, H.-K., Han, S.-H., Seong, T.-Y. & Choi, W.-K. Low-resistance Ti/Au ohmic contacts to Al-doped ZnO layers. *Appl. Phys. Lett.* **77**, 1647 (2000).

172. Akane, T., Sugioka, K. & Midorikawa, K. Nonalloy Ohmic contact fabrication in a hydrothermally grown n-ZnO (0001) substrate by KrF excimer laser irradiation. *J. Vac. Sci. B.* **18**, 1406 (2000).

173. Kim, H.-K., Kim, K.-K., Park, S.-J., Seong, T.-Y. & Yoon, Y. S. Thermally Stable and Low Resistance Ru Ohmic Contacts to n-ZnO. *Jap. J. Appl. Phys.* **41**, L546–L548 (2002).

174. Liang, S. *et al.* ZnO Schottky ultraviolet photodetectors. *J. Crys. Grow.* **225**, 110–113 (2001).

175. Yang, H. S., Norton, D. P., Pearton, S. J. & Ren, F. Ti/Au n-type Ohmic contacts to bulk ZnO substrates. *Appl. Phys. Lett.* **87**, 212106 (2005).

176. Mead, C. A. Surface barriers on ZnSe and ZnO. *Phys. Lett.* **18**, 218 (1965).

177. Mead, C. A. Surface states on semiconductor crystals; barriers on the Cd(Se:S) system. *Appl. Phys. Lett.* **6**, 103–104 (1965).

178. Coppa, B. J., Davis, R. F. & Nemanich, R. J. Gold Schottky contacts on oxygen plasma-treated, n-type ZnO(0001-bar). *Appl. Phys. Lett.* **82**, 400–402 (2003).

179. Simpson, J. C. & Cordaro, J. F. Characterization of deep levels in zinc oxide. *J. Appl. Phys.* **63**, 1781–1783 (1988).

180. Polyakov, A. Y. *et al.* Electrical characteristics of Au and Ag Schottky contacts on n-ZnO. *Appl. Phys. Lett.* **83**, 1575 (2003).

181. Yu, J., Ippolito, S. J., Wlodarski, W., Strano, M. & Kalantar-zadeh, K. Nanorod based Schottky contact gas sensors in reversed bias condition. *Nanotechnology* **21**, 265502 (2010).

182. Wang, X., Ding, Y., Li, Z., Song, J. & Wang, Z. L. Single-Crystal Mesoporous ZnO Thin Films Composed of Nanowalls. *J. Phys. Chem.C* **113**, 1791–1794 (2009).

183. Hong, J.-I., Bae, J., Wang, Z. L. & Snyder, R. L. Room-temperature, texture-controlled growth of ZnO thin films and their application for growing aligned ZnO nanowire arrays. *Nanotechnology* **20**, 85609 (2009).

184. Lao, C. S. *et al.* ZnO Nanobelt/Nanowire Schottky Diodes Formed by Dielectrophoresis Alignment across Au Electrodes. *Nano Lett.* **6**, 263–266 (2006).

185. Harnack, O., Pacholski, C., Weller, H., Yasuda, A. & Wessels, J. M. Rectifying Behavior of Electrically Aligned ZnO Nanorods. *Nano Lett.* **3**, 1097–1101 (2003).

186. Heo, Y. W. *et al.* Pt/ZnO nanowire Schottky diodes. *Appl. Phys. Lett.* **85**, 3107 (2004).

187. Das, S. N. *et al.* Junction properties of Au/ZnO single nanowire Schottky diode. *Appl. Phys. Lett.* **96**, 092111 (2010).

188. Park, W. I. & Yi, G.-C. Ohmic and Schottky nanocontacts on ZnO nanorods. *IEE. Conf. Publ.* **2**, 410–413 (2003)

189. Scrymgeour, D. A. & Hsu, J. W. P. Correlated Piezoelectric and Electrical Properties in Individual ZnO Nanorods. *Nano Lett.* **8**, 2204–2209 (2008).

190. Shao, Z. *et al.* Pt/ZnO Schottky nano-contact for piezoelectric nanogenerator. *Physica E.* **43**, 173–175 (2010).

191. Gao, Y. & Wang, Z. L. Electrostatic Potential in a Bent Piezoelectric Nanowire. The Fundamental Theory of Nanogenerator and Nanopiezotronics. *Nano Lett.* **7**, 2499–2505 (2007).

192. Gao, Y. & Wang, Z. L. Equilibrium Potential of Free Charge Carriers in a Bent Piezoelectric Semiconductive Nanowire. *Nano Lett.* **9**, 1103-1110 (2009).

193. Nishimura, T., Kita, K. & Toriumi, A. Evidence for strong Fermi-level pinning due to metal-induced gap states at metal/germanium interface. *Appl. Phys. Lett.* **91**, 123123 (2007).

194. Zhdanov, V. P. & Kasemo, B. Potential profiles near the Schottky nanocontacts. *Physica E.* **43**, 1486–1489 (2011).

195. Hägglund, C. & Zhdanov, V. P. Charge distribution on and near Schottky nanocontacts. *Physica E.* **33**, 296–302 (2006).

196. Dascalu, D., Brezeanu, G., Dan, P. A. & Dima, C. Modelling electrical behaviour of nonuniform Al Si Schottky diodes. *Solid State Elec.* **24**, 897–904 (1981).

197. Hugelmann, M. & Schindler, W. Schottky diode characteristics of electrodeposited Au/n-Si(111) nanocontacts. *Appl. Phys. Lett.* **85**, 3608 (2004).

198. Gu, Y., Kuskovsky, I. L., Yin, M., O'Brien, S. & Neumark, G. F. Quantum confinement in ZnO nanorods. *Appl. Phys. Lett.* **85**, 3833 (2004).

199. Song, J. Q., Ding, T. & Cai, Q. Mechanism of surface leakage of nanoscale Schottky contacts between $ErSi_2$ nanoislands and Si(001). *Appl. Phys. Lett.* **96**, 203113 (2010).

200. Hu, J., Liu, Y., Ning, C. Z., Dutton, R. & Kang, S.-M. Fringing field effects on electrical resistivity of semiconductor nanowire-metal contacts. *Appl. Phys. Lett.* **92**, 083503 (2008).

201. Sarpatwari, K., Dellas, N. S., Awadelkarim, O. O. & Mohney, S. E. Extracting the Schottky barrier height from axial contacts to semiconductor nanowires. *Solid State Elec.* **54**, 689–695 (2010).

202. Campos, L. C. *et al.* Determination of the epitaxial growth of zinc oxide nanowires on sapphire by grazing incidence synchrotron x-ray diffraction. *Appl.Phys. Lett.* **90**, 181929 (2007).

203. Lord, A. Vertically aligned Zinc Oxide Nanowires grown by vapour transport on single crystal silicon substrate.MRes Thesis Swansea Univ. (2009).

204. Wang, J., Li, Q. & Egerton, R. F. Probing the electronic structure of ZnO nanowires by valence electron energy loss spectroscopy. *Micron* **38**, 346–53 (2007).

205. Robb, P. D. & Craven, A. J. Column ratio mapping: a processing technique for atomic resolution high-angle annular dark-field (HAADF) images. *Ultramicroscopy* **109**, 61–9 (2008).

206. Leeds Electron Microscopy and Spectroscopy Centre faculty of engineering. at <http://www.engineering.leeds.ac.uk/imr/lemas/>

207. Arslan, I. & Browning, N. D. Atomic scale defect analysis in the scanning transmission electron microscope. *Microsc. res. tech.* **69**, 330–42 (2006).

208. Introduction to Spherical Aberration Correction in Electron Microscopes. at <www.superstem.com>

209. SuperSTEM EPSRC National Facility for Aberration Corrected STEM. at <http://www.superstem.com/>

210. Van Aert, S., Batenburg, K. J., Rossell, M. D., Erni, R. & Van Tendeloo, G. Three-dimensional atomic imaging of crystalline nanoparticles. *Nature* **470**, 374–377 (2011).

211. Pennycook, S. J. Structure determination through Z-contrast microscopy. *Microsc. Spec. Holo. Crys. Elec.* **123**, 173–206 (2002).

212. Voyles, P. M., Grazul, J. L. & Muller, D. A. Imaging individual atoms inside crystals with ADF-STEM. *Ultramicroscopy* **96**, 251–73 (2003).

213. Alloyeau, D., Freitag, B., Dag, S., Wang, L. & Kisielowski, C. Atomic-resolution three-dimensional imaging of germanium self-interstitials near a surface: Aberration-corrected transmission electron microscopy. *Phys. Rev. B* **80**, (2009).

214. Ng, H. T. *et al.* Growth of Epitaxial Nanowires at the Junctions of Nanowalls. *Science* **300**, 1249 (2003).

215. Biswas, M., McGlynn, E., Henry, M. O., McCann, M. & Rafferty, A. Carbothermal reduction vapor phase transport growth of ZnO nanostructures: Effects of various carbon sources. *J. Appl. Phys.* **105**, 094306 (2009).

216. Hsu, C.-L. *et al.* Indium-diffused ZnO nanowires synthesized on ITO-buffered Si substrate. *Nanotechnology* **17**, 516–519 (2006).

217. Kwak, C.-H. *et al.* Structural and electrical properties of ZnO nanorods and Ti buffer layers. *Appl. Phys. Lett.* **96**, 051908 (2010).

218. Wang *et al.* Growth of Uniformly Aligned ZnO Nanowire Heterojunction Arrays on GaN, AlN, and $Al_{0.5}Ga_{0.5}N$ Substrates. *J. Am. Chem. Soc.* **127**, 7920–7923 (2005).

219. Lee, S. H. *et al.* Correlation between ZnO Nanowire Growth and the Surface of AlN Substrate. *Crys. Grow. Des.* **6**, 2640–2642 (2006).

220. Wang, L.-M. & Wu, S.-T. Epitaxial Growth of C54 TiSi 2 on Si(001) by Self-Aligned Process. *Jap. J. Appl. Phys.* **37**, 638–642 (1998).

221. Park, W. Il *et al.* Metal-ZnO Heterostructure Nanorods with an Abrupt Interface. *Jap. J. Appl. Phys.* **41**, L1206–L1208 (2002).

222. Cosgriff, E. C. & Nellist, P. D. A Bloch wave analysis of optical sectioning in aberration-corrected STEM. *Ultramicroscopy* **107**, 626–34 (2007).

223. Kisielowski, C. *et al.* Detection of Single Atoms and Buried Defects in Three Dimensions by Aberration-Corrected Electron Microscope with 0.5-Å Information Limit. *Microsc. Microan.* **14**, 469–477 (2008).

224. Borchers, C., Mueller, S., Stichtenoth, D., Schwen, D. & Ronning, C. Catalyst Nanostructure Interaction in the Growth of 1-D ZnO Nanostructures. *J. Phys. Chem. B* **110**, 1656–1660 (2006).

225. Khanal, D. R. *et al.* Decoupling single nanowire mobilities limited by surface scattering and bulk impurity scattering. *J. Appl. Phys.***110**, 033705 (2011).

226. Hong, W.-K., Jo, G., Kwon, S.-S., Song, S. & Lee, T. Electrical Properties of Surface-Tailored ZnO Nanowire Field-Effect Transistors. *IEEE Trans. Electron. Devices* **55**, 3020–3029 (2008).

227. Djurišić, A. B. *et al.* Photoluminescence and Electron Paramagnetic Resonance of ZnO Tetrapod Structures. *Adv. Func. Mater.* **14**, 856–864 (2004).

228. Chang, P.-C., Chien, C.-J., Stichtenoth, D., Ronning, C. & Lu, J. G. Finite size effect in ZnO nanowires. *Appl. Phys. Lett.* **90**, 113101–113103 (2007).

229. Yang, Y. *et al.* Size Dependence of Dielectric Constant in a Single Pencil-Like ZnO Nanowire. *Nano Lett.* **12**, 1919–1922 (2012).

230. Wang, D. *et al.* Surface chemistry and electrical properties of germanium nanowires. *J. Am. Chem. Soc.* **126**, 11602–11 (2004).

231. Jones, F., Léonard, F., Talin, A. A. & Bell, N. S. Electrical conduction and photoluminescence properties of solution-grown ZnO nanowires. *J. Appl. Phys.* **102**, 014305 (2007).

232. Shalish, I., Temkin, H. & Narayanamurti, V. Size-dependent surface luminescence in ZnO nanowires. *Phys. Rev. B* **69**, (2004).

233. Smith, C. S. Piezoresistance Effect in Germanium and Silicon. *Phys. Rev.* **94**, 42 (1954).

234. Maffeis, T. G. G., Penny, M. W., Castaing, A., Guy, O. J. & Wilks, S. P. XPS investigation of vacuum annealed vertically aligned ultralong ZnO nanowires. *Surf. Sci.* **606**, 99–103 (2012).

235. Tarat, A., Majithia, R., Brown, R. A., Penny, M. W. & Meissner, K. E. Synthesis of nanocrystalline ZnO nanobelts via pyrolytic decomposition of zinc acetate nanobelts and their gas sensing behavior. *Surf. Sci.* **606**, 715–721 (2012).

236. Swart, J. ., Diniz, J. ., Doi, I. & De Moraes, M. A. . Modification of the refractive index and the dielectric constant of silicon dioxide by means of ion implantation. *Nuclear Inst. Meth. Phys. Res. B.* **166-167**, 171–176 (2000).

237. Umar, A., Karunagaran, B., Suh, E.-K. & Hahn, Y. B. Structural and optical properties of single-crystalline ZnO nanorods grown on silicon by thermal evaporation. *Nanotechnology* **17**, 4072–4077 (2006).

238. Wang, Z., Kong, X. & Zuo, J. Induced Growth of Asymmetric Nanocantilever Arrays on Polar Surfaces. *Phys. Rev. Lett.* **91**, 185502 (2003).

239. Sarpatwari, K., Mohney, S. E. & Awadelkarim, O. O. Effects of barrier height inhomogeneities on the determination of the Richardson constant. *J. Appl. Phys.* **109**, 014510 (2011).

240. Tumakha, S. *et al.* Defect-driven inhomogeneities in Ni/4H–SiC Schottky barriers. *Appl. Phys. Lett.* **87**, 242106 (2005).

241. Z. Zhang Y. Liu, C. Jin, X. Liang, Q. Chen, L.-M. Peng,, K. Y. Quantitative Analysis of Current-Voltage Characteristics of Semiconducting Nanowires: Decoupling of Contact Effects. *Adv. Func. Mater.* **17**, 2478–2489 (2007).

242. Im, H.-J., Ding, Y., Pelz, J. & Choyke, W. Nanometer-scale test of the Tung model of Schottky-barrier height inhomogeneity. *Phys. Rev. B* **64**, (2001).

243. Léonard, F. & Tersoff, J. Role of Fermi-Level Pinning in Nanotube Schottky Diodes. *Phys. Rev. Lett.* **84**, 4693–4696 (2000).

244. Mönch, W. Barrier heights of real Schottky contacts explained by metal-induced gap states and lateral inhomogeneities. *J. Vac. Sci. B.* **17**, 1867 (1999).

245. Skromme, B. J. *et al.* Electrical characteristics of schottky barriers on 4H-SiC: The effects of barrier height nonuniformity. *J. Elec. Mater.* **29**, 376–383 (2000).

246. Smit, G. D. J., Flokstra, M. G., Rogge, S. & Klapwijk, T. M. Scaling of micro-fabricated nanometer-sized Schottky diodes. *Microelec. Eng.* **64**, 429–433 (2002).

247. Talin, A. A. *et al.* Transport characterization in nanowires using an electrical nanoprobe. *Semicond. Sci. Tech.* **25**, 024015 (2010).

248. Pearton, S. Recent progress in processing and properties of ZnO. *Prog. Mater. Sci.* **50**, 293–340 (2005).

249. Walker, J. S. Exploring one-dimensional quantum mechanics with transfer matrices. *Am. J. Phys.* **62**, 408 (1994).

250. Peng, Y., Cullis, T. & Inkson, B. Accurate electrical testing of individual gold nanowires by in situ scanning electron microscope nanomanipulators. *Appl. Phys. Lett.* **93**, 183112 (2008).